

Electronic Thesis and Dissertation Repository

10-10-2017 10:30 AM

New GPS Time Series Analysis and a Simplified Model to Compute an Accurate Seasonal Amplitude of Tropospheric Delay

Hadis Samadi Alinia, *The University of Western Ontario*

Supervisor: Dr. Kristy Tiampo, *The University of Western Ontario*

A thesis submitted in partial fulfillment of the requirements for the Doctor of Philosophy degree in Geophysics

© Hadis Samadi Alinia 2017

Follow this and additional works at: <https://ir.lib.uwo.ca/etd>



Part of the [Geophysics and Seismology Commons](#)

Recommended Citation

Samadi Alinia, Hadis, "New GPS Time Series Analysis and a Simplified Model to Compute an Accurate Seasonal Amplitude of Tropospheric Delay" (2017). *Electronic Thesis and Dissertation Repository*. 4956. <https://ir.lib.uwo.ca/etd/4956>

This Dissertation/Thesis is brought to you for free and open access by Scholarship@Western. It has been accepted for inclusion in Electronic Thesis and Dissertation Repository by an authorized administrator of Scholarship@Western. For more information, please contact wlsadmin@uwo.ca.

Abstract

Horizontal and vertical deformation of the Earth's crust is due to a variety of different geophysical processes that take place on various spatiotemporal scales. The quality of the observations from space-based geodesy instruments such as Global Positioning System (GPS) and differential interferometric synthetic aperture radar (DInSAR) data for monitoring these deformations are dependent on numerous error sources. Therefore, accurately identifying and eliminating the dominant sources of the error, such as troposphere error in GPS signals, is fundamental to obtain high quality, sub-centimeter accuracy levels in positioning results.

In this work, I present the results of double-differenced processing of five years of GPS data, between 2008 and 2012, for sparsely distributed GPS stations in southeastern Ontario and western Québec. I employ Bernese GPS Software Version 5.0 (BSW5.0) and found two optimal sub-networks which can provide high accuracy estimation of the position changes. I demonstrate good agreement between the resulted coordinate time series and the estimates of the crustal motions obtained from a global solution. In addition, I analyzed the GPS position time series by using a complex noise model, a combination of white and power-law noises. The estimated spectral index of the noise model demonstrates that the flicker noise is the dominant noise in most GPS stations in our study area. The interpretation of the observed velocities suggests that they provide an accurate constraint on glacial isostatic adjustment (GIA) prediction models.

Based on a deeper analysis of these same GPS stations, I propose a model that accurately estimates the seasonal amplitude of zenith tropospheric delay (ZTD) error in the GPS data on local and regional spatial scales. I process the data for the period 2008 through 2012 from eight GPS stations in eastern Ontario and western Québec using precise point positioning (PPP) online analysis available from Natural Resource Canada (NRCan) (<https://webapp.geod.nrcan.gc.ca/geod/tools-outils/ppp.php>). The model is an elevation-dependent model and is a function of the decay parameter of refractivity with altitude and the seasonal amplitude of refractivity computed from atmospheric data (pressure, temperature, and water vapor pressure) at a given reference station. I demonstrate that it can accurately

estimate the seasonal amplitude of ZTD signals for the GPS stations at any altitude relative to that reference station. Based on the comparison of the observed seasonal amplitudes of the differenced ZTD at each station and the estimates from the proposed model, it can provide an accurate estimation for the stations under normal atmospheric conditions. The differenced ZTD is defined as the differences of ZTD derived from PPP at each station and ZTD at the reference station. Moreover, I successfully compute a five-year precipitable water vapor (PWV) at each GPS site, based on the ZTD derived from meteorological data and GPS processing. The results provide an accurate platform to monitor long-term climate changes and inform future weather predictions.

In an extension of this research, I analyze DInSAR data between 2014 and 2017 with high temporal and spatial resolution, from Kilauea volcano in Hawaii in order to derive the spatial and temporal pattern of the seasonal amplitude of ZTD. I propose an elevation-dependent model by the data from a radiosonde station and observations at a surface weather station for modeling the seasonal amplitudes of ZTD at any arbitrary elevation. The results obtained from this model fit the vertical profile of the observed seasonal amplitude of ZTD in DInSAR data, increasing systematically from the elevation of the DInSAR reference point. I demonstrate that the proposed model could be used to estimate the seasonal amplitude of the differenced ZTD at each GPS station within a local network with high accuracy. The results of this study concluded that, employing this model in GPS processing applications eliminates the need for the meteorological observations at each GPS site.

Keywords

GPS data processing, GIA, meteorological data, zenith tropospheric delay, precipitable water vapor, elevation-dependent seasonal amplitude

Co-Authorship Statement

I prepared this thesis in integrated-article format, and I have written the following manuscripts:

1. Samadi Alinia H., Tiampo, K.F., James, T.S. (2017) GPS coordinate time series measurements in Ontario and Québec, Canada, *J. Geodesy*. 91(6), pp. 653-683. DOI 10.1007/s00190-016-0987-5.
2. Samadi Alinia H., Tiampo, K.F, Samsonov, S.V. (2017) Simplified one-dimensional methodology to retrieve the seasonal amplitude of zenith tropospheric delay on GPS data, *Radio Science Journal*. (under 2nd review)
3. Samadi Alinia H., Tiampo, K.F, Samsonov, S.V., González, P.J. (2017) Modeling the elevations-dependent seasonal amplitude of tropospheric delay in GPS height time series using DInSAR and meteorology data, *Geophysical Journal International*. (under review)

The work for these projects was completed under the supervision of Dr. Kristy F. Tiampo and with financial support from the Natural Sciences and Engineering Research Council of Canada (NSERC) collaborative research and development (CRD) grant, “Real-time ground motion tools for seismic hazard management”.

Dr. Thomas S. James produced the graph of viscosity profiles for the Earth models considered in the first paper. Also, he provided the horizontal and vertical crustal velocities from the prediction Earth models GIA-5G and GIA-6G, and Hadis Samadi Alinia applied them in for comparison to the obtained results from GPS processing.

Dr. Sergey V. Samsonov processed the DInSAR deformation map of the area surrounding Kilauea’s volcano in Hawaii. Also, he assisted with interpretation, suggestions and reviewing the second and third papers.

Dr. Pablo J. González assisted with suggestions for and interpretation and review of the third paper.

Acknowledgments

First, I would like to express my special thanks to my supervisor Professor Kristy Tiampo for her extensive support, valuable guidance and standing by me through all my tough times during the completion of my research.

I would also like to extend my gratitude to Dr. Thomas James, Dr. Sergey V. Samsonov and Dr. Pablo J. González for their insightful assistance and guidance.

I offer my sincere thanks to all my friends and staff at Western University especially Marie Schell, John Brunet, Claire Mortera, Jen Heidenheim and Bernie Dunn for their kindness and support.

I need to express my special appreciations to my loving and supportive husband, Mostafa, and my son, Ryan. Mostafa has been a constant source of strength and inspiration. There were times during the past years when everything seemed hopeless, but I can honestly say that it was only his determination and constant love that ultimately made it possible for me to see this project through to the end.

Last but not the least, I would like to extend my special thanks to my parents for allowing me to realize my potential. All the support and encouragements they have provided me over the years was the greatest gift anyone has ever given me. Also, I thank my brother and sister for their dedication, many years of support and standing by me through all my good times and bad.

Table of Contents

| | |
|---|-------|
| Abstract..... | i |
| Co-Authorship Statement..... | iii |
| Acknowledgments..... | iv |
| Table of Contents..... | v |
| List of Tables..... | ix |
| List of Figures..... | xii |
| List of Appendices..... | xviii |
| Chapter 1..... | 1 |
| 1 General Introduction..... | 1 |
| 1.1 Introduction..... | 1 |
| 1.2 Global Positioning System (GPS)..... | 3 |
| 1.2.1 The Space Segment..... | 3 |
| 1.2.2 The Control Segment..... | 5 |
| 1.2.3 The User Segment..... | 6 |
| 1.2.4 Code Pseudo-Range Measurements..... | 6 |
| 1.2.5 Phase Measurements..... | 6 |
| 1.3 GPS Observation Errors..... | 7 |
| 1.3.1 Satellite Clock Error..... | 7 |
| 1.3.2 Receiver Clock Error..... | 7 |
| 1.3.3 Ionospheric Error..... | 8 |
| 1.3.4 Tropospheric Error..... | 8 |
| 1.3.5 Satellite Orbit Error..... | 9 |
| 1.3.6 Receiver Noise..... | 9 |
| 1.3.7 Multipath Error..... | 9 |

| | | |
|-----------|---|----|
| 1.4 | Differential GPS Observations | 10 |
| 1.4.1 | Single Differences..... | 10 |
| 1.4.2 | Double Differences | 12 |
| 1.4.3 | Triple Differences | 13 |
| 1.5 | Ionosphere Delay Modeling..... | 14 |
| 1.6 | Tropospheric delay Modeling..... | 15 |
| 1.6.1 | Refractivity | 16 |
| 1.6.2 | Tropospheric Path Delay..... | 17 |
| 1.7 | Mapping Functions for Zenith Hydrostatic and Wet Delays (ZHD and ZWD) ... | 21 |
| 1.7.1 | Niell Mapping Function (NMF)..... | 22 |
| 1.7.2 | Vienna Mapping Function (VMF) | 23 |
| 1.7.3 | Vienna Mapping Function 1 (VMF1)..... | 24 |
| 1.7.4 | Global Mapping Function (GMF)..... | 25 |
| 1.8 | Modeling the meteorological parameters..... | 25 |
| 1.9 | Noise analysis | 27 |
| 1.9.1 | Maximum Likelihood Estimation (MLE)..... | 28 |
| 1.10 | Purpose of the work | 30 |
| 1.11 | Structure of the thesis..... | 32 |
| 1.12 | References..... | 32 |
| Chapter 2 | | 45 |
| 2 | GPS coordinate time series measurements in Ontario and Québec, Canada | 45 |
| 2.1 | Introduction..... | 46 |
| 2.2 | Background..... | 48 |
| 2.2.1 | Geological Structure and Recent Glaciations | 49 |
| 2.2.2 | Regional Seismicity | 50 |
| 2.3 | Observations and Method | 50 |

| | | |
|-----------|--|-----|
| 2.3.1 | GPS Data and Analysis | 52 |
| 2.3.2 | Comparison of Bernese and NGL Time Series..... | 63 |
| 2.3.3 | ITRF2008 Angular Velocity | 69 |
| 2.4 | GPS Analysis Results | 70 |
| 2.4.1 | Reliability Assessment..... | 72 |
| 2.5 | GIA Models | 73 |
| 2.5.1 | Horizontal Component..... | 75 |
| 2.5.2 | Vertical Component | 86 |
| 2.6 | Conclusions..... | 91 |
| 2.7 | References..... | 93 |
| Chapter 3 | | 102 |
| 3 | Simplified one-dimensional methodology to retrieve the seasonal amplitude of zenith tropospheric delay on GPS data | 102 |
| 3.1 | Introduction..... | 103 |
| 3.2 | Data Preparation..... | 108 |
| 3.3 | Methods..... | 115 |
| 3.3.1 | GPS Processing..... | 115 |
| 3.3.2 | Employing Meteorological Data..... | 117 |
| 3.3.3 | Computing the elevation-dependent seasonal amplitude..... | 123 |
| 3.3.4 | Precipitable Water Vapor..... | 124 |
| 3.4 | Results and Discussion | 125 |
| 3.4.1 | The comparison between GPS-ZTD and MET-ZTD..... | 125 |
| 3.4.2 | The comparison between the elevation-dependent seasonal amplitude of ZTDs | 127 |
| 3.4.3 | The comparison between GPS-PWV and MET-PWV | 129 |
| 3.5 | Conclusion | 131 |
| 3.6 | References..... | 133 |

| | |
|--|-----|
| Chapter 4..... | 142 |
| 4 Modeling the elevation-dependent seasonal amplitude of tropospheric delays in GPS height time series using DInSAR and meteorology data | 142 |
| 4.1. Introduction..... | 143 |
| 4.2. Geologic setting | 147 |
| 4.3. Data..... | 151 |
| 4.4. Amplitude of seasonal troposphere signal | 157 |
| 4.4.1. DInSAR data..... | 157 |
| 4.4.2. Exponential refractivity model | 160 |
| 4.5. ZTD correction to GPS data | 164 |
| 4.6. Conclusion | 170 |
| 4.7. References..... | 172 |
| Chapter 5..... | 181 |
| 5 General Conclusions | 181 |
| 5.1. Summary and Conclusions | 181 |
| 5.2. Future Studies | 185 |
| Appendices..... | 187 |
| A GPS data processing using Bernese V.5 | 187 |
| A.1 References..... | 192 |
| B GPS data processing using GIPSY/OASIS-II software..... | 193 |
| B.1 References..... | 194 |
| C Glossary | 196 |
| D Computer Code | 200 |
| Curriculum Vitae | 220 |

List of Tables

| | |
|---|----|
| Table 1.1. Coefficients of the hydrostatic and wet mapping functions (Niell 1996)..... | 23 |
| Table 1.2. Constant parameters for hydrostatic and total VMF1 (Boehm et al. 2006)..... | 24 |
| Table 2.1. GPS station information for stations from the POLARIS network and those operated by Canadian Geodetic Survey (CGS), Natural Resources Canada. All coordinates are based on WGS84..... | 53 |
| Table 2.2. Mean coordinate differences (relative to ITRF2008 values; Altamimi et al., 2012) and RMS repeatabilities for a selection of the 24 sub-networks for 2012. All values are in millimeters. | 57 |
| Table 2.3. Estimated and predicted velocity of POLARIS stations and the NRCan PARY and ALGO sites from the time series obtained from the two optimal sub-networks. The velocities and their corresponding uncertainties for the three components were calculated from Hector and employing a complex noise model. The seasonal sinusoidal parameters for all three components time series and the spectral indices associated with the power-law noise model are presented below. Predicted velocities are derived from the ITRF2008 angular velocity of the North American (NOAM) plate (Altamimi et al. 2011, 2012). | 62 |
| Table 2.4. GPS sites positions and velocities from the position time series at the NGL website (http://geodesy.unr.edu/). The spectral index of the power law noise for the three components (K_{east} , K_{north} and K_{up}) and the horizontal velocities (in millimeters per year) are corrected for the North American rigid plate motion given by ITRF2008 (Altamimi et al. 2011, 2012). Pennsylvania Department of Transportation (PENNDOT), New York State Department of Transportation (NYSDOT), Ohio Department of Transportation (ODOT), Precision Laser & Instrument (PLI), Connecticut Department of Transportation (CONNDOT), Michigan Department of Transportation (MDOT), Natural Resources Canada, Geodetic Survey Division (NRCan GSD), NOAA Earth System Research Laboratory (NOAA ESRL), and POLARIS. | 76 |

Table 2.5. Reduced chi-square values for a comparison with the different GIA models considered in this study. The fit of the horizontal and vertical velocities to the GIA models is calculated for three different subsets of GPS stations, as noted in the text. 85

Table 3.1. GPS and weather station details, including elevations above mean sea level (msl) and the mean of the atmospheric parameters observed at the meteorological station between 2008 and 2012 together with their rms errors after corrected for the height difference between the weather station and GPS station. The refractivity at each GPS station is computed using Equation 3.8. GPS stations are sorted based on their latitudes. 111

Table 3.2. The partial water vapor decay parameter (λ) obtained from Smith (1966) based on the latitude of the GPS stations. The mean of the ZTDs obtained from MET and GPS data for the time period between 2008 and 2012 for every GPS station. The rms differences between MET-ZTD and GPS-ZTD. The observed seasonal amplitude of the ΔZTD_{GPS} for every GPS station is referenced to station ACTO. The seasonal amplitudes of ZTD are derived from the proposed elevation-dependent model (Equation 12). Correlation coefficients between MET-ZTD and GPS-ZTD time series are computed using Pearson’s approach. GPS stations in this table are sorted based on their latitudes. 114

Table 4.1. SAR datasets used in MSBAS processing: RADARSAT-2 Ultra-Fine 13 and 16 Wide (U13W2, U16W2); time span (in YYYYMMDD format), azimuth θ° and incidence φ° angles, number of available SAR images N , and number of calculated interferograms M for each data set. ASC and DSC in the table stands for ascending and descending, respectively. 152

Table 4.2. GPS stations details 156

Table 4.3. Altitude of the GPS stations from Table 4.2. The length is the distance between the reference station, PUKA, and each station. The modeled seasonal amplitudes between each station and PUKA are estimated from Equation 4.9. The rmse of the residuals is the difference between the observed high-frequency ΔZTD_{PPP} and the modeled seasonal component. The maximum, mean and minimum of the difference between the modeled seasonal variation and ΔZTD_{PPP} for each station are also presented. Stations are sorted based on altitude. 165

Table A.1. GPS station information for stations from the POLARIS network and those operated by Canadian Geodetic Survey (CGS), Natural Resources Canada. All coordinates are based on WGS84. The subscript star is Stations operated by Canadian Geodetic Survey (CGS), Natural Resources Canada..... 188

List of Figures

| | |
|---|----|
| Figure 1.1. The orbital configuration (http://www.gps.gov/systems/gps/space/ , 2017). | 4 |
| Figure 1.2. Transmitting the satellite signals to the receiver on Earth (https://www.novatel.com/an-introduction-to-gnss/chapter-2-basic-gnss-concepts/step-2-propagation/ , 2017) | 5 |
| Figure 1.3. Single Differences between two receivers (Vimal 2013). | 11 |
| Figure 1.4. Satellite-Receiver Double Differences (Vimal 2013). | 13 |
| Figure 1.5. Triple Differences (Davidson 2016). | 14 |
| Figure 2.1. Earthquake distribution with magnitudes between 2 and 6 (1985 to 2013) for a portion of eastern North America. Events of magnitude greater than 2, and shallower than 30 km depth, were plotted. The seismic regions are: Southern Ontario Seismic Zone (SOSZ), Western Québec Seismic Zone (WQSZ), Charlevoix Seismic Zone (CSZ), Lower St. Lawrence Zone (LSZ) and Boothia Ungava Zone (BUZ) (GSC 2015). | 51 |
| Figure 2.2. Location of continuous GPS stations. Stations used in the Bernese processing and sub-network analysis are shown in green (POLARIS) and blue (permanent NRCan). GPS station motions were also estimated from information downloaded from NGL, as discussed in the text, for these sites and for other stations (black circles). See Tables 2.1 through 2.3 for GPS station details. Inset shows enlargement of stations in the Michigan area. | 54 |
| Figure 2.3. Daily position time series plots of five selected sites from the CAMST3 sub-network analysis (Table 2.2). Shown are component time series for three POLARIS sites (ACTO, STCO, and KLBO) and two NRCan sites (ALGO and PARY) (locations in Figure 2.2) for (a) east (positive eastward); b) north (positive northward); and (c) vertical component (positive up). Errors bars for the daily solutions are the standard uncertainties calculated by the Bernese software. The velocities and their corresponding uncertainties calculated from Hector software and employing a complex noise model. | 59 |

Figure 2.4. Daily position time series plots of selected POLARIS sites from a northern sub-network analysis (CAMST7, Table 2.2) for the (a) east, (b) north, and (c) up components. Symbols and labeling are as in Figure 2.3. The velocities and their corresponding uncertainties calculated from Hector software and employing a complex noise model..... 60

Figure 2.5. Comparison of the horizontal velocities for the Bernese (red arrows) and NGL (black arrows) analysis before correction for the plate motions. Error ellipses show 95% confidence interval corresponding to the uncertainties calculated with Hector. 64

Figure 2.6. Observed vertical velocities (in millimeters per year) for the Bernese (red arrows) and NGL (black arrows) analyses derived from observations spanning January 2008 through December 2012. Error ellipses show 95% confidence interval corresponding to the uncertainties calculated with Hector. 65

Figure 2.7. Scatter plot of the computed velocities and their uncertainties in the three components, north, east, and up for the GPS stations in both Bernese and NGL solutions. The velocities and their corresponding uncertainties calculated from Hector software and employing a complex noise model. The horizontal axis shows latitude of GPS stations..... 67

Figure 2.8. Comparison of the (a) east, (b) north, and (c) up position time series for TYNO for the CAMST3 sub-network Bernese analysis to the time series obtained from NGL (<http://geodesy.unr.edu/>). TYNO is a POLARIS station. The velocities and their corresponding uncertainties calculated from Hector software and employing a complex noise model. See Figure 2.2 for location..... 68

Figure 2.9. Comparison of residual horizontal velocities for the Bernese (red arrows) and NGL (black arrows) analysis after removal of plate motions assuming the ITRF2008 North American pole of rotation (Altamimi et al. 2011, 2012). Error ellipses show 95% confidence interval corresponding to the uncertainties calculated with Hector..... 71

Figure 2.10. Viscosity profiles for the five Earth models considered in this study. Profile B (VM1) has a lower mantle viscosity of 2×10^{21} Pa s and upper mantle viscosity of 10^{21} Pa s and is common to both panels. (a) Profiles, A, B, and C, as indicated. (b) Profiles B, D, and E, as indicated. Lithospheric thickness is 120 km, except for Profile C (depth-averaged VM2), which has a thickness of 90 km, and Profile E (VM5a), which has a 40-km thick high-

viscosity layer (10^{22} Pa s) beneath the 60-km elastic lithosphere. The ICE-5G (Peltier 2004) loading history was employed to load all of the Earth models except profile E (VM5a), for which ICE-6G (Peltier et al. 2015) was employed. 74

Figure 2.11. Horizontal crustal velocities predicted for ICE-5G (Peltier 2004) (black arrows) for four different viscosity structures, a) profile A b) profile B (VM1) c) profile C (depth-averaged VM2) d) profile D. The lithospheric thickness is 120 km except for c) depth averaged VM2, where the thickness is 90 km. Residual horizontal velocities for the Bernese (red arrows) analysis after removal of plate motions assuming the ITRF2008 North American pole of rotation (Altamimi et al. 2011, 2012). Error ellipses show 95% confidence interval corresponding to the uncertainties calculated with Hector. 84

Figure 2.12. Horizontal crustal velocities computed by the ICE_6G_C (VM5a) (Viscosity profile E) GIA model (Peltier 2015) (black arrows). VM5a is a three-layer approximation of the VM2 mantle viscosity profile and features a 60 km thick elastic lithosphere underlain by a 40-km thick high-viscosity layer of 10^{22} Pa s. Residual horizontal velocities for the Bernese (red arrows) analysis after removal of plate motions assuming the ITRF2008 North American pole of rotation (Altamimi et al. 2011, 2012). Error ellipses show 95% confidence interval corresponding to the uncertainties calculated with Hector. 87

Figure 2.13. Predicted vertical velocities computed using ICE-5G (Peltier 2004) (black arrows) for four different viscosity structures. a) profile A b) profile B (VM1) c) profile C (VM2) d) profile D. The lithospheric thickness is 120 km except for c) depth averaged VM2, where the thickness is 90 km. Observed vertical velocities (in millimeters per year) for the Bernese (red arrows) analyses derived from observations spanning January 2008 through December 2012. Error ellipses show 95% confidence interval corresponding to the uncertainties calculated with Hector. 88

Figure 2.14. Vertical crustal velocities computed for ICE_6G_C (VM5a) (viscosity profile E) (Peltier et al. 2015). The Earth model VM5a features a three-layer approximation of the VM2 mantle viscosity profile and a 60 km thick elastic lithosphere underlain by a 40-km thick high-viscosity layer of 10^{22} Pa s. Observed vertical velocities (in millimeters per year) for the Bernese (red arrows) analyses derived from observations spanning January 2008

through December 2012. Error ellipses show 95% confidence interval corresponding to the uncertainties calculated with Hector. 90

Figure 3.1. Location of the weather stations in eastern Ontario and western Québec (red triangles), GPS stations (black circles) and weather stations considered in this study (green triangles). Contour lines illustrating elevations are shown in brown and are spaced at 100-meter intervals. 110

Figure 3.2. Vertical profile of the mean partial water vapor pressures (solid red), the mean dew point temperature (dashed blue) and the mean air temperature (solid blue) at the GPS stations. 115

Figure 3.3. Refractivity time series computed from meteorological data such as temperature, air and water vapor pressure (Equation 3.3) observed at the weather stations near the GPS stations and corrected for the height differences with the GPS stations, distributed from southeastern Ontario to northwestern Québec, using Equations 3.1 to 3.3 (Dousa & Elias 2014) (Figure 3.1). 119

Figure 3.4. Vertical profile of the mean refractivity at GPS stations (blue stars). Comparison of the fitted exponential model a) to the values of all eight stations b) to the values of all stations except for that at INUQ and IVKQ c) to the values of all weather stations except MATQ, INUQ and IVKQ; d) to the values of stations INUQ, IVKQ, MATQ and ALGO. The 95% confidence intervals for the calculated exponential fit to the data in each scenario is presented with dashed lines. 121

Figure 3.5. Correlogram of the Pearson’s linear correlation coefficients between all pairs of ZTD time series calculated from the two strategies, using GPS data and meteorological data at all GPS stations. G and M stand for GPS data and meteorological data, respectively. The scale bar represents the correlation coefficient values. The variables from left to right are sorted for the stations from low to high latitude. 126

Figure 3.6. The vertical profile of the seasonal amplitude of the ΔZTD_{GPS} , obtained from the sinusoidal signal fitted to the difference between GPS-ZTD at each station and at station ACTO (red start) overlain with the seasonal amplitudes modeled by using Equation 3.12 for the points at altitudes between 0 and 1000 m msl (blue solid line). 128

Figure 3.7. Comparison between daily GPS-PWV (red) and MET-PWV (blue) time series between 2008 and 2012. 129

Figure 4.1. a) The map in the background is the velocity model (in cm/yr) calculated from the linear regression on the DInSAR data from 2014 to 2017. The brown contour lines shows elevations spaced at 400 meter interval. The positions of sample DInSAR points are shown with red stars. The rift zones of Mauna Loa and Kilauea are shown in purple. A positive velocity value shows uplift. The DInSAR reference location is shown with red circle in the NW corner b) Distribution of the GPS stations inside and outside of the DInSAR data boundary. The map in the background is the ASTER DEM with 30 m per pixel resolution (<http://gdex.cr.usgs.gov/gdex/>). 148

Figure 4.2. Climate data including a) air temperature b) rainfall, c) water vapor computed from the air temperature d) relative humidity e) air pressure computed from the expression proposed by Triplet & Roche (1983) and the ASTER-derived DEM (<http://gdex.cr.usgs.gov/gdex/>). Maps of air temperature, rainfall and relative humidity (<http://climate.geography.hawaii.edu/>; Giambelluca et al. 2014; Frazier et al. 2016) at 250 m resolution. The brown contour lines represent elevations spaced at 400 meter intervals. The windward/wet and leeward/dry side are separated with a dashed line. 150

Figure 4.3. Example of DInSAR height time series of the specified points *a* through *i*, shown in Figure 4.1a. They all are referenced to a point at elevation 3107 m above msl. In addition to the elevation of each point derived from the ASTER Global DEM (GDEM) (<http://gdex.cr.usgs.gov/gdex/>), seasonal amplitudes estimated by fitting a sinusoidal signal to the height time series are given in each plot. Positive values indicate uplift. 155

Figure 4.4. a) Map of the measured amplitudes of seasonal variations of troposphere signal in DInSAR data by adjusting a sinusoidal signal on the height time series of each point. In the raster maps the brown contour lines represent elevations spaced at 400 meter interval. The rift zones of Mauna Loa and Kilauea are shown as dark lines. The inflation areas at Kilauea’s summit are shown as red circles. Separation between dry and wet regions are shown by the dashed line. b) The vertical profile of the measured amplitudes as a function of height (blue) overlain with the modeled amplitudes by employing Equation 4.9 (red). 159

Figure 4.5. a) the hourly time series of the refractivity of atmosphere at the surface of Earth computed from the air pressure, water vapor pressure and temperature time series observed at the weather station MLO1 (in blue). The daily averaged refractivity time series computed from hourly data (in red). **b)** The vertical profile of the refractivity calculated from the atmospheric parameters (air pressure, water vapor pressure and temperature) observed at the radiosonde station PHTO/HILO. The fitted red line is the best fit exponential function. 161

Figure 4.6. (red) $\Delta ZTDPPP$ time series for each GPS station relative to the reference station, PUKA (black) the modeled seasonal variation of ZTD in which the amplitudes estimated by using Equation 4.9. 168

Figure 4.7. Vertical profile of the rmse of the residuals between the seasonal variations obtained from the modeled amplitudes of ZTD obtained from Equation 4.9 and the differenced ZTD, $\Delta ZTDPPP$, obtained by subtracting the ZTD computed for the reference station from the ZTD computed for the other stations. 169

Figure A.1. Detrended position changes time series at station TYNO in eastern Ontario. The pink line corresponds to the best fit annual sinusoidal function. 191

Figure A.2. The computed power spectral density of the residuals for the up component for station TYNO. The fitted white plus power-law noise model is shown by the solid green line. The red “x” is the calculated spectrum for the observations. 192

List of Appendices

Appendix A: GPS data processing using Bernese V.5

Appendix B: GPS data processing using GIPSY/OASIS-II software

Appendix C: Glossary

Appendix D: Compute Code

Chapter 1

1 General Introduction

1.1 Introduction

Ground surface deformation is the result of various geophysical processes. Therefore, employing space-based geodesy techniques such as Global Positioning System (GPS) and differential interferometric synthetic aperture radar (DInSAR) is fundamental in providing high accuracy measurements of the horizontal and vertical components of position changes at various spatial and temporal resolutions. Installation and maintenance of GPS networks is expensive, so that GPS stations often are distributed quite sparsely. As a result, it is important to ensure an accurate configuration of GPS stations and the employment of appropriate methods which can accurately compute the regional vertical and horizontal components of the GPS station positions.

Many studies have been carried out to employ GPS data for measuring surface deformation (Calais et al. 2006), co-seismic displacement (Hudnut et al. 1996), seasonal variations in response to the hydrological and atmosphere loading (VanDam et al. 2001; Dong et al. 2002; VanDam et al. 2012), and motion resulting from glacial isostatic adjustment (GIA) (Sella et al. 2007; Tiampo et al. 2011). In addition, a variety of research has been conducted that uses high spatial resolution DInSAR data for observing ground motion (Zebker & Goldstein 1986; Gabriel et al. 1989; Massonnet & Feigl 1998; Manconi et al. 2010; Samsonov & d'Oreye 2012).

When a radio signal propagates through the tropospheric and ionospheric layers of the atmosphere, its arrival time to the receiver increases or decreases, respectively (Hoque & Jakowski 2012). The induced delays, particularly from the ionosphere and the troposphere layers of the atmosphere, are the dominant source of error in GPS observations and can produce up to approximately 600 meters geo-location error (Celestino et al. 2007). Hence, adequate modeling and elimination of this delay is of great significance in obtaining accurate positioning results. The delay due to the ionosphere layer is dispersive and depends on the frequency of the radio signal. Eliminating this

effect from GPS data can be achieved through the combination of two or three separate frequency signals or by employing other data sources (Shrestha 2003; Katsougiannopoulos 2008; Sokolovskiy et al. 2008; Elizabeth et al. 2010; Kim & Tinin 2011; Liu et al. 2016).

The tropospheric delay is not dependent on the frequency of the propagating signal, and it is widely variable in time and space, mainly reliant on water vapor. Several models and strategies have been proposed for reducing the effect of this delay from GPS data. These methods are either independent from the surface meteorological data (Hopfield 1969; Saastamoinen 1973; Goad & Goodman 1974) or they are based on the high-resolution meteorological observations and low spatial resolution numerical weather prediction models (van Dam et al. 1994; Bevis et al. 1992; Hofmann-Wellenhof et al. 2001; Flouzat et al. 2009; Dousa 2010; Mousa et al. 2011; Li et al. 2014; Pikridas et al. 2014; Yuan et al. 2014).

The tropospheric delay is computed in the zenith direction and can be incorporated into techniques for calculating the amount of precipitable water vapor (PWV), the most important greenhouse gas, in the atmosphere. The monitoring of long term PWV is valuable for weather and climate changes prediction (Jin & Luo 2009; Morland et al. 2009; Pikridas et al. 2014; Bianchi et al. 2016).

In this dissertation, I use GPS data from the POLARIS (Portable Observatories for Lithospheric Analysis and Research Investigating Seismicity) continuous GPS (cGPS) regional network (Eaton et al. 2005) in southeastern Ontario and western Québec and combine them with data from other high-quality sites. This data is processed with different network configurations by employing double-differencing method in Bernese GPS Software Version 5.0 (BSW5.0). Interpretation of the results and comparison with global solutions indicate a more accurate crustal velocity field for the study of regional geophysical processes, and can be used to constrain the GIA prediction models.

I extend the analysis of the GPS data from this region, reprocessed using a precise point positioning (PPP) technique in order to analyze the amount of the error in the GPS height time series and compute the PWV at each station. Inspired by the work of Samsonov et

al. (2014), I propose a method to estimate the elevation-dependent seasonal amplitude of zenith tropospheric delay (ZTD) at GPS stations using meteorological data in an area which does not have significant topography. The proposed model has a good agreement with the seasonal amplitude of ZTD derived from PPP.

I employ the spatially dense DInSAR data to estimate the tropospheric error in a local region and use it to correct a GPS network on the island of Hawaii. Initially, the DInSAR time series in line-of-sight (LOS) direction at each pixel is converted into the vertical component. Then, I derive the seasonal amplitude of ZTDs in the vertical time series of more than one million DInSAR pixels. I propose a simplified one-dimensional exponential function based on the data from a surface weather collocated with the DInSAR reference location, and a radiosonde station, to accurately fit the DInSAR-derived seasonal amplitudes. This model provides an accurate estimate of the seasonal amplitude of local ZTD in GPS data at any location and elevation on the island.

In the next sections, I introduce the details of GPS, GPS processing techniques and different approaches for tropospheric delay modeling.

1.2 Global Positioning System (GPS)

GPS is the fully functional radiometric space-based Global Navigation Satellite System (GNSS) developed by the U.S. Department of Defense for military applications in the 1970's. In 1983, it became available for civilian usage. Since then, its usage has expanded to include estimation of accurate, real-time three-dimensional position and velocity in a common reference system. In addition, it is broadly employed for achieving high precision timing for communication purposes (Misra & Enge 2006). The GPS system is composed of three distinct segments such as control segment, space segment, and user segment, described in detail in the following sections.

1.2.1 The Space Segment

Currently, GPS has a constellation of 31 medium Earth orbit (MEO) satellites launched into six near-circular orbital planes separated by 60° of right ascension and inclination of approximately 55° to Earth's equator (Kaplan 1996). Satellite orbits are located at an

altitude of 20,183 km from the center of Earth (Montenbruck & Gill 2000; Misra & Enge 2006). This satellites organization allows for at least six satellites to be in the LOS simultaneously from almost any point on Earth's surface at any moment. This arrangement also allows that at least four satellites to be observed at least 15° above the horizon (Gao 2008). Figure 1.1 shows the configuration of GPS satellites.

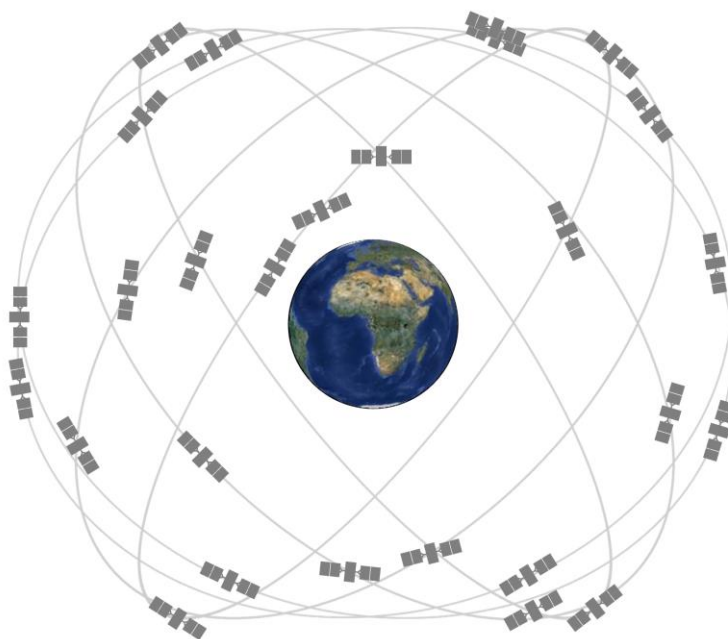


Figure 1.1. The orbital configuration (<http://www.gps.gov/systems/gps/space/>, 2017).

The GPS satellites transmit radio signals to receivers located on Earth. The GPS signal carries C/A (Coarse Acquisition) code and P-code (Precise) by utilizing two frequencies: L1 is 1575.42 MHz and L2 at 1227.60 MHz, respectively. The power source of each satellite is solar panels, and they use a propulsion system for orbit adjustments. The GPS satellites are equipped with accurate rubidium and cesium clocks for highly accurate timing. Each satellite broadcasts a message that allows the receiver to recognize the satellite's position and time and to compute the pseudo-range to that satellite. The pseudo-range refers to the measured range, which is not exactly equal to the actual range between the satellite and receiver, as it contains errors due to the bending of the radio signal as it passes through various layers of the atmosphere (Figure 1.2).

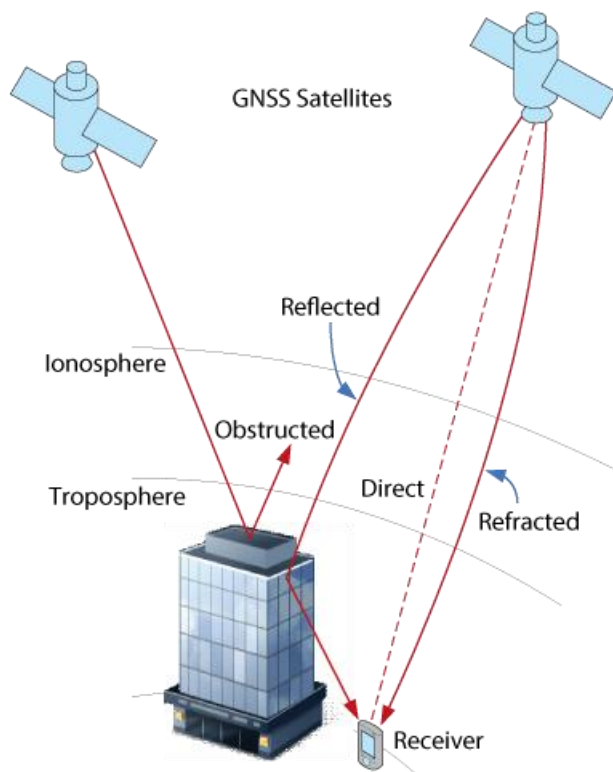


Figure 1.2. Transmitting the satellite signals to the receiver on Earth

(<https://www.novatel.com/an-introduction-to-gnss/chapter-2-basic-gnss-concepts/step-2-propagation/>, 2017)

1.2.2 The Control Segment

Currently, the control segment of GPS systems is composed of one master control station, sixteen monitoring stations located throughout the world and four ground control stations. The master control station is located at Schriever Air Force Base (AFB) in Colorado Springs in the US and collects atmospheric data, range and carrier measurements and satellites signals from the monitoring stations and computes the satellite orbit (ephemerides) and satellite clock parameters (Duquenne et al. 2005). Then the calculated information is sent to one of the four ground stations, and the antenna of the ground station broadcasts that information to the GPS satellite constellation through an S-band signal.

1.2.3 The User Segment

The user segment is composed of receiver technologies for computing local position in the Earth-centered fixed WGS84 reference system and for calculating the receiver clock offset. The GPS applications in the civilian community have expanded as a result of the decreasing cost of accessibility to GPS technology in the recent years.

Code and carrier phase measurements are the two important GPS measurements.

1.2.4 Code Pseudo-Range Measurements

The code pseudo-range measurements are measured at a GPS receiver. The GPS receiver computes the travel time of the signal from a GPS satellite, through the comparison of the pseudo-random noise (PRN) code, generated in the receiver, and the identical code of the arrived signal. Because of the errors in the code pseudo-range measurements, the positioning will be at the low level of accuracy, on the order of a few meters. The measured pseudo-range for a receiver and a satellite can be written as follow:

$$P = \rho + d\rho + c(dt - dT) + d_{ion} + d_{trop} + \varepsilon_p \quad (1.1)$$

where, P is the measured pseudo-range, ρ is the geometric distance measured from the position vector of the satellite and a receiver, $d\rho$ is the orbital error, c is the velocity of light, dt is the error of satellite clock, dT is the error of receiver clock, d_{ion} and d_{trop} are the ionospheric and tropospheric delay, respectively, ε_p is the multipath error and the receiver code noise which can be modelled to obtain high accuracy geodetic results.

1.2.5 Phase Measurements

The phase measurements are computed based on the difference between the carrier phase generated in the receiver and that transmitted from the satellite. To convert the carrier phase to range between receiver and satellite, there is a need to know the number of full cycles and the fractional cycle. The receiver can measure only the fractional part of the carrier phase, and therefore the integer wavelengths remain unknown. To solve for the integer ambiguity and to provide a millimeter level of accuracy of range measurements,

double-differenced of phase method is mostly employed (see Section 1.4.2) (Raquet & Lachapelle 2001).

$$\Phi = \rho + d\rho + c(dt - dT) + \lambda N - d_{ion} + d_{trop} + \varepsilon_{\Phi} \quad (1.2)$$

where, Φ is the observed carrier phase range, N is the integer ambiguity, λ is the wavelength of the carrier wave and ε_{Φ} the multipath error and the receiver carrier phase noise. The other parameters are as defined for Equation 1.1.

1.3 GPS Observation Errors

From Equations (1.1) and (1.2), the GPS measurements consist of various sources of biases and errors, including receiver and satellite clock errors, orbital errors, tropospheric and ionospheric errors, receiver noise and multipath error, each of which must be identified and eliminated for high accuracy positioning.

1.3.1 Satellite Clock Error

Accurate atomic clocks are utilized on the satellites. However, instabilities of up to a few milliseconds, approximately 10 ns, can produce significant inaccuracies, approximately 3 m, in the positioning, such that it affects the accuracy of measuring the range to a satellite. Although the clock error correction is determined at the master control station and the correction coefficients are transmitted to the user together with the GPS signal, they are not accurate enough and the accuracy of the positioning estimates are on the order of ± 2 meter (Hugentobler et al. 2001). For more precise estimates, the accurate information of the satellite clock calculated either by PPP or spaced based augmentation system (SBAS) can be employed. However, differencing approaches which can eliminate the effect of this error from the GPS observables are used in positioning applications (see Section 1.4).

1.3.2 Receiver Clock Error

The receiver clock error relates to the type of clock used in the receiver. To lower the weight of the GPS receivers and lower the cost, less stable quartz crystal oscillators are employed and, therefore, an offset occurs during the navigation. In the absolute

positioning, this error is estimated as an unknown together with the position of the receiver. In the relative positioning, the differencing methods completely eliminate this error from the GPS observables (see Section 1.4).

1.3.3 Ionospheric Error

The ionosphere error is due to the density of the ionized plasma of electrons and is dependent on the total electron contents (TEC) in the ionosphere layer that lies between 50 and 1000 km above the surface of Earth. In this region, the GPS signals are deflected and are exposed to delay in the arrival time. The amount of this delay on the signal changes based on the variation of the ionosphere density. The ionosphere is a dispersive medium at radio frequencies and therefore the effect of delay on a GPS signal is dependent on the frequency of the signal. GPS monitoring stations can calculate the ionosphere correction based on the physical characteristics of the ionosphere and transmit the correction coefficients to the user, but they are not accurate enough, and this delay remains the most significant error in precise positioning. Employing a dual frequency receiver can remove the ionospheric effect by forming linear combination of L1 and L2. This error in the differencing of the GPS observations between sites can be minimized (see Sections 1.4 and 1.5).

1.3.4 Tropospheric Error

The tropospheric error occurs as the signal travels through the lower layer of the atmosphere, below 9-16 km above the surface of Earth. As Figure 1.2 illustrates, the signal is bent as the result of the variability in the refractive index of the troposphere, and therefore the path length of the signal is exceeded and causes a delay in the arrival of the signal. This delay depends on the temperature, pressure and the water vapor content of the atmosphere and highly influences the positioning accuracy. Signals from satellites closer to the horizon are more delayed because the density of the effective parameters is increased. Unlike the ionosphere, the troposphere is a non-dispersive medium, and therefore the effects of this error on the GPS signals are not dependent on the signal's frequency. As a result, dealing with the tropospheric delay becomes a more problematic

issue than that of ionospheric delay, and removing this effect from the signals requires more complex models. Modeling of this error is discussed in detail in Section 1.6.

1.3.5 Satellite Orbit Error

The accurate information about the shapes of the satellite orbits, which is always variable, is significant for the GPS receiver to determine the precise position. The variations of the satellite orbit are continually monitored by the ground stations, and corrections are transmitted to the satellite. Even with the corrections, some small errors remain in the orbit which is due to the errors in the observations at the monitoring stations and causes up to 2.5 m error in positioning (Bauersima 1983). In this case, employing the accurate post-mission orbits, which are given by the National Geodetic Survey (NGS), the International GPS Service (IGS), and the Center for Orbit Determination in Europe (CODE), is essential to calculate precise GPS position.

1.3.6 Receiver Noise

Receiver noise occurs during the processing of the received signal when generating the pseudo-range and phase measurements. These are considered to be white noise because they are time-independent. The magnitude of the receiver noise for the code and phase measurements are not the same, and they are not correlated with each other. The magnitude of the receiver error is approximately 1% of the wavelength of the signal. The maximum error for C/A code measurement and P-code is approximately 3 m and 30 cm, respectively. The amount of this error on the carrier phase is approximately 3 mm. It is worthwhile to mention that that increasing the elevation angle between the satellite and the receiver (up to an approximately 45°) results in decreasing the amount of the receiver noise (Raquet & Lachapelle 2001).

1.3.7 Multipath Error

The multipath error is the result of the arrival of a signal to the receiver after reflection off various objects (Figure 1.2) and is dependent on the neighborhood of high buildings, trees, and the ground. The amount of this error is a few meters, and it is a limiting factor for precise positioning (Larson et al. 2007). To minimize this error in the GPS

observations, receivers are designed to receive the signals above 15° from the horizon. Ray (2000) and Ray & Cannon (2001) proposed a model in which they filter single-differenced measurements of code, phase, and signal-to-noise ratio (SNR) together to calculate the multipath parameter. Their approach results in an improvement of up to 24% in the carrier phase measurements and up to 21% in the code measurements.

In real-time navigation applications, including dynamic GPS attitude determination (Chen et al. 2012; Cong et al. 2015), only one GPS receiver is adopted, and the range to a satellite is computed based on the code pseudo-range measurements approach. In high accuracy positioning applications, the differences of GPS observations which can reduce or eliminate some of the associated errors should be employed (Misra & Enge 2006). Three important approaches for high accuracy GPS positioning are available and they are based on differencing the observations from two or more than two receivers.

1.4 Differential GPS Observations

To further reduce the measurement errors and to achieve sub-millimeter positioning accuracy, the differences of the GPS observations must be made by using two or more GPS receivers. This is because the satellite clock errors, orbital errors and the atmospheric related errors exhibit strong spatial and temporal correlation. In other words, these errors are more similar between the closer receivers and the smaller time difference between the adjacent observations (Misra & Enge 2006).

1.4.1 Single Differences

The single difference method is either the differences of the measurements to a common satellite observed at two stations or the differences of the measurements to two satellites observed at one station. In the former approach, one station has known coordinates and is considered as a reference station and the coordinate of the other station is computed relative to that reference station. In the latter approach, only one receiver, which has unknown position, is involved.

The between-stations single difference method is typically implemented and is shown below:

The single difference between the observations of the two receivers, typically is indicated by Δ , is used to compute the motion of Receiver 2 at epoch t relative to Receiver 1, the reference station (Figure 1.3). As Figure 1.3 indicates, the two stations are observing the same satellite.

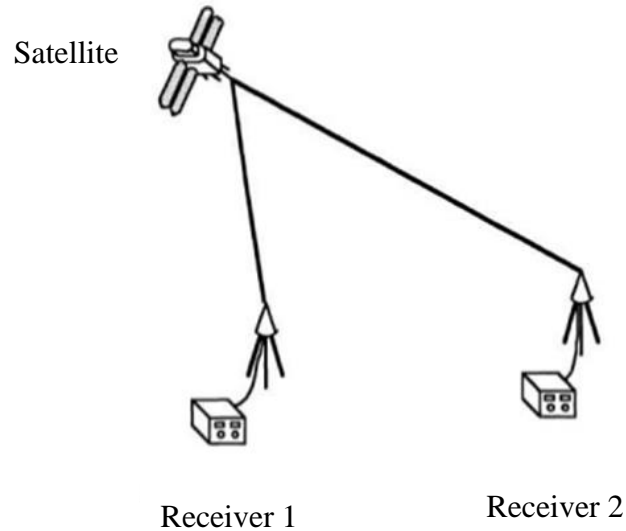


Figure 1.3. Single Differences between two receivers (Vimal 2013).

The single differences for the pseudo-range observations, Δp , and the phase observations, $\Delta\Phi$, can be written as follows (Raquet & Lachapelle 2001):

$$\Delta p = \Delta\rho + \Delta d\rho - c\Delta dT + \Delta d_{ion} + \Delta d_{trop} + \Delta\varepsilon_p$$

$$\Delta\Phi = \Delta\rho + \Delta d\rho - c\Delta dT + \lambda\Delta N - \Delta d_{ion} + \Delta d_{trop} + \Delta\varepsilon_\Phi \quad (1.3)$$

where, $\Delta\rho$ is the single differences for the geometric distance, $\Delta d\rho$ is the single differences for the orbital error, ΔdT is the single differences for the receiver clock's error, Δd_{ion} and Δd_{trop} are the single differences for the ionospheric and tropospheric delays, $\Delta\varepsilon_p$ is the single differences for the multipath error and the receiver code noise for the code observations, $\Delta\varepsilon_\Phi$ is the single difference for the multipath error and the receiver code noise for the phase observations.

As shown in Equation 1.3, in the single difference approach the orbit errors and the local atmospheric errors are reduced and the satellite clock errors are removed. Note that in Equation 1.3, the observations from the Receiver 2 are subtracted from those from the reference station, Receiver 1.

1.4.2 Double Differences

The receiver-satellite double difference is computed by forming the combination of the two single differences between satellites, typically is shown by ∇ , and between receivers, Δ , as follows (Raquet & Lachapelle 2001):

$$\Delta\nabla = \{(\cdot)^{sat2} - (\cdot)^{sat1}\}_{re1} - \{(\cdot)^{sat2} - (\cdot)^{sat1}\}_{re2}$$

$$\Delta\nabla p = \Delta\nabla\rho + \Delta\nabla d\rho + \Delta\nabla d_{ion} + \Delta\nabla d_{trop} + \Delta\nabla\varepsilon_p$$

$$\Delta\nabla\Phi = \Delta\nabla\rho + \Delta\nabla d\rho + \lambda\Delta\nabla N - \Delta\nabla d_{ion} + \Delta\nabla d_{trop} + \Delta\nabla\varepsilon_\Phi \quad (1.4)$$

where, $\Delta\nabla p$ and $\Delta\nabla\Phi$ are the double differences for pseudo-range and phase observations, respectively. $\Delta\nabla\rho$ is the double differences for the geometric distance, $\Delta\nabla d\rho$ is the double differences for the orbital error, $\Delta\nabla d_{ion}$ and $\Delta\nabla d_{trop}$ are the double differences for the ionospheric and tropospheric delays, $\Delta\nabla\varepsilon_p$ is the double differences for the multipath error and the receiver code noise for the code observations, $\Delta\varepsilon_\Phi$ is the double difference for the multipath error and the receiver code noise for the phase observations.

Constructing the double differences leads to the removal of the receiver and the satellite clock errors and it also reduces the orbital errors and the errors due to propagation in the atmosphere. This approach is widely used for accurate static and kinematic positioning.

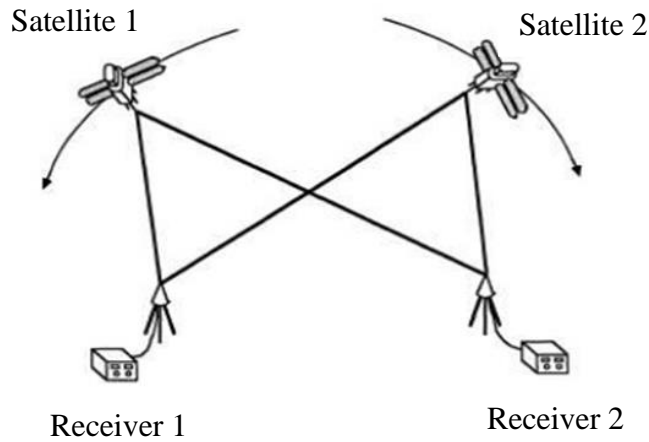


Figure 1.4. Satellite-Receiver Double Differences (Vimal 2013).

1.4.3 Triple Differences

The triple differences approach is used to deal with the cycle slip, which occurs due to the loss of signal between the satellite and receiver (Hugentobler et al. 2001). As Figure 1.5 illustrates, three single differences are formed between two receivers, two satellites and two epochs, t_1 and t_2 , is shown by δ . Equation 1.5 presents the phase triple difference observations (Raquet & Lachapelle 2001):

$$\delta\Delta\nabla = [\{(\cdot)^{sat2} - (\cdot)^{sat1}\}^{re1} - \{(\cdot)^{sat2} - (\cdot)^{sat1}\}^{re2}]_{t1} - \\ [\{(\cdot)^{sat2} - (\cdot)^{sat1}\}^{re1} - \{(\cdot)^{sat2} - (\cdot)^{sat1}\}^{re2}]_{t2}$$

$$\delta\Delta\nabla\Phi = \delta\Delta\nabla\rho + \delta\Delta\nabla d\rho - \delta\Delta\nabla d_{ion} + \delta\Delta\nabla d_{trop} + \delta\Delta\nabla\varepsilon_{\Phi} \quad (1.5)$$

where, $\delta\Delta\nabla\Phi$ is the triple differences for phase observations. $\delta\Delta\nabla\rho$ is the triple differences for the geometric distance, $\delta\Delta\nabla d\rho$ is the triple differences for the orbital error, $\delta\Delta\nabla d_{ion}$ and $\delta\Delta\nabla d_{trop}$ are the triple differences for the ionospheric and tropospheric delays, $\delta\Delta\nabla\varepsilon_{\Phi}$ is the triple differences for the multipath error and the receiver code noise for the code observations, $\delta\Delta\nabla\varepsilon_{\Phi}$ is the triple difference for the multipath error and the receiver code noise for the phase observations.

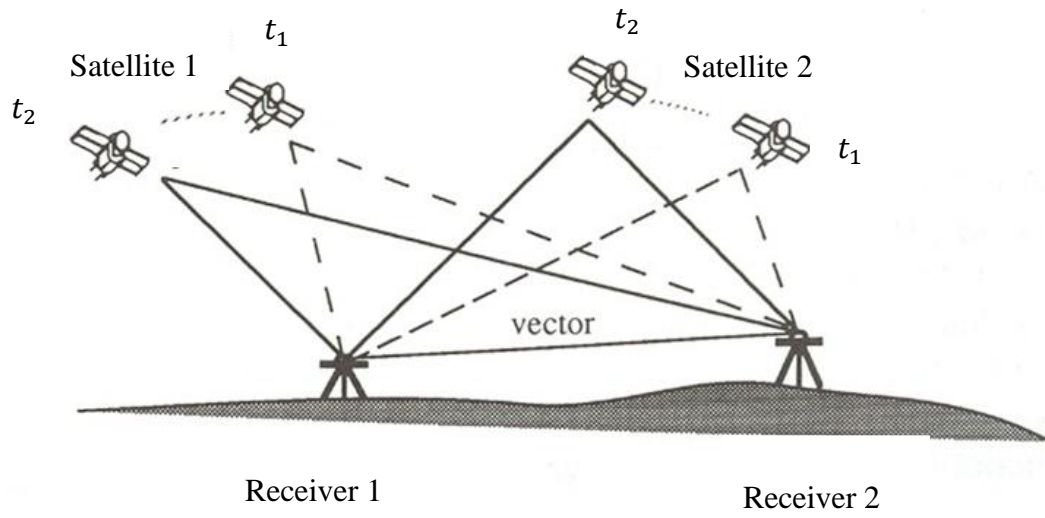


Figure 1.5. Triple Differences (Davidson 2016).

Because this approach can remove the initial ambiguity and estimates the approximate position of the receivers, it is used in pre-processing and before double differencing for the phase measurements (Davidson 2016). Similar to the double differencing method, this approach eliminates the satellite's and receiver's clock's errors and reduces the ionospheric and tropospheric errors.

1.5 Ionosphere Delay Modeling

To achieve a high precision GPS positioning, the ionospheric effect must be corrected from the GPS observables. For this purpose, currently, various linear combination of code and phase measurements including ionosphere-free (Odijk 2003), geometry-free (ionospheric) (Huang et al. 2012), wide-lane (Cocard & Geiger 1992), and Melbourne-Wübbena (Melbourne 1985; Wübbena 1985) are used in different applications. For example, Erenoglu (2015) used a geometry-free approach to compute the vertical TEC without reducing the number of code measurements. Liu (2010) used the Melbourne-Wübbena wide-lane (MWWL) linear combination to measure and fix the cycle slips. They employed dual-frequency carrier phase and pseudo-range data from only one single GPS receiver. Furthermore, Li et al. (2010) proposed to combine a triple-frequency

geometry-free and ionosphere-free (GFIF) approaches. In their methods, the narrow-lane (NL) ambiguity is solved free of the distance constraints.

The ionosphere-free linear combination is mostly used in PPP and double-differencing processing approaches to eliminate the ionospheric delay from the observables. In fact, the ionospheric effect depends on the inverse of squared frequency and therefore ionospheric-free combination which combines f_1 and f_2 from the dual-frequency receivers, can be used to eliminate this effect from the GPS signals (Hofmann-Wellenhof et al. 2001). According to Equations 1.6, the dual-frequency signals in the ionospheric-free linear combination method creates code and phase observations without the ionosphere error.

$$P_{ino-free} = \frac{1}{f_1^2 - f_2^2} (f_1^2 P_1 - f_2^2 P_2) = \rho + c(dt - dT) + d_{trop} + \varepsilon_p$$

$$\Phi_{ino-free} = \frac{1}{f_1^2 - f_2^2} (f_1^2 \Phi_1 - f_2^2 \Phi_2) = \rho + \frac{cf_1}{f_1^2 - f_2^2} N_1 - \frac{cf_2}{f_1^2 - f_2^2} N_2 + c(dt - dT) + d_{trop} + \lambda \varepsilon_\Phi \quad (1.6)$$

where, $P_{ino-free}$ and $\Phi_{ino-free}$ are the ionosphere-free code and carrier phase observables, P_1 and P_2 are the code observations, Φ_1 and Φ_2 are the phase observations, f_1 and f_2 are the frequency of the signals, N_1 and N_2 are the integer ambiguity of the signals.

1.6 Tropospheric delay Modeling

As discussed earlier in sections 1.3 to 1.5, unlike the various errors affecting the GPS observations, which can be reduced or eliminated by employing differencing approaches, the tropospheric error remains one of the significant accuracy limiting factors in precise GPS applications. The amplitude of the tropospheric delay is directly proportional to the changes of the refractivity in the path of the signal.

In this section, initially, I will discuss the calculation of the refractivity in the troposphere. Then, I will review the most recent models proposed to estimate the

tropospheric delay. Moreover, I will present the mapping functions currently employed for high precision GPS applications.

1.6.1 Refractivity

The amount of the refractivity of a signal, N , in the atmosphere can be expressed based on the refractive index, n , as follows:

$$n = \frac{c}{v}$$

$$N = 10^6(n - 1) \quad (1.7)$$

where, c is the speed of light in vacuum, v is the velocity of the propagation of the signal in the atmosphere.

The refractive index is greater than unity. Hence from Equation 1.7, the length of the path of the GPS signal in the troposphere is overestimated. The exceedance path delay of the signals at 5° elevation angle can be approximately 20 cm and for the signals at 15° elevation angle is approximately 1cm.

The total refractivity as a function of atmospheric parameters can be written as follows (Smith & Weintraub 1953):

$$N = k_1 \left(\frac{P_d}{T} \right) Z_d^{-1} + \left[k_2 \frac{e}{T} + k_3 \frac{e}{T^2} \right] Z_w^{-1} \quad (1.8)$$

where, P_d is the partial pressure of dry air (hPa), T is the absolute temperature (K), e is the partial pressure of water vapor (hPa), k_1 , k_2 and k_3 are the refractivities empirically constants, Z_d and Z_w are the compressibility factors for dry air and water vapor, respectively, and are very close to one (Ghoddousi-Fard 2009). Z_d and Z_w are usually determined empirically from pressure and temperature.

The refractivity coefficients are determined empirically in a laboratory (Boudouris 1963; Smith & Weintraub 1953; Thayer 1974; Bevis et al. 1994; Rieger 2002).

Nievinski (2009) studied the discrepancies in the estimates of the zenith delays using the

three different coefficients determined by Rieger (2002), Bevis et al. (1994) and Thayer (1974), with respect to International Union of Geodesy and Geophysics (IUGG, 1963), a simplification of Essen and Froome (1951), and determined the differences to be less than one millimeter. Also, negligible discrepancies in ZHD estimates from using different determinations of the refractivity coefficients were observed by Mendes (1999). In this dissertation, I have adopted the Rieger's (2002) refractivity constants k_1 , k_2 and k_3 as $77.69 \text{ K mbar}^{-1}$, $71.29 \text{ K mbar}^{-1}$, and $375463 \text{ K}^2 \text{ mbar}^{-1}$, respectively.

1.6.2 Tropospheric Path Delay

The tropospheric delay is directly proportional to the refractive index or refractivity and can be expressed as a function of atmospheric temperature and pressure. The tropospheric delay can be computed through the integration along the signal path as follow:

$$d_{trop} = \int_{path} (n - 1) ds$$

$$d_{trop} = 10^{-6} \int_{path} N ds \quad (1.9)$$

where, d_{trop} is the tropospheric delay in meter., N is refractivity, and n is the refractive index.

The tropospheric delay can be separated into two main components, the hydrostatic delay and the wet delay (Saastamoinen 1972). The hydrostatic is due to the dry gases and can be computed precisely from surface temperature and pressure measurements. However, the wet component is due primarily to the water vapor pressure, which is highly variable in space and time and cannot be accurately modeled from surface atmosphere measurements. This component of the delay can be estimated by subtracting the hydrostatic component from the total tropospheric delay.

For low-accuracy positioning, a simple prediction model to estimate the troposphere delay is sufficient. Models which accurately estimate the distribution of water vapor pressure is essential for precise positioning.

The other challenge in dealing with the tropospheric delay is that the magnitude of the effects of this delay depends on the elevation angle and azimuthal directions of the GPS signals, so that each received signal has a different amount of delay. Hence, its estimation on each received signal along with other unknown parameters, including the coordinates of the receiver, is impossible due to the lack of redundancy. Therefore, the delay on the received signals from different satellites, the slant tropospheric delay, must be mapped to the zenith direction. As a result, instead of solving several unknown delays, only one unknown is solved at each epoch. To achieve this, employing a mapping function with known coefficients is essential to map all the tropospheric delays from any direction and azimuth to the zenith direction. The total tropospheric path delay on the incoming signal from the satellite can be expressed as follow:

$$d_{trop}^s = ZHD \cdot m_h(\varepsilon) + ZWD \cdot m_w(\varepsilon) + mg_h(\varepsilon) \cdot (gh_{ns}(\varepsilon) \cos(a) + gh_{ew}(\varepsilon) \sin(a)) + mg_w(\varepsilon) \cdot (gw_{ns}(\varepsilon) \cos(a) + gw_{ew}(\varepsilon) \sin(a)) \quad (1.10)$$

where, d_{trop}^s is the slant troposphere path delay in the LOS of satellite-receiver, ZHD and ZWD are the hydrostatic and wet components of the tropospheric delay in the zenith direction, respectively, ε is the elevation angle, a is the azimuth, m_h and m_w are the hydrostatic and wet mapping functions, respectively, mg_h and mg_w are the hydrostatic and wet gradient mapping functions, respectively, gh_{ns} and gh_{ew} are the north-south and east-west hydrostatic horizontal gradients, gw_{ns} and gw_{ew} are the north-south and east-west wet horizontal gradients.

Some researchers proposed to estimate the tropospheric gradient parameters along with the ZTD when low elevation angle measurements are employed (e.g., Chen & Herring 1997; Bar-Sever et al. 1998; Hugentobler et al., 2001).

Several tropospheric delay models have been proposed for computing the a priori values for zenith hydrostatic delay (ZHD) and zenith wet delay (ZWD) and mapping functions based on the measurements of the surface atmospheric parameters (pressure, temperature, and water vapor pressure). However, those models computed based on the standard atmosphere conditions indicate a different behavior in abnormal climate regions. Some of the developed troposphere models are presented in the next sub-sections.

1.6.2.1 Zenith Hydrostatic (Dry) Delay (ZHD) Models

In the theoretical approaches, computation of the ZHD is straightforward. The developed models vary based on the employed refractivity constants and the acceleration of gravity modeling. Also, they are dependent on the latitude and altitude of stations (Mendes 1999).

Hopfield (1969) proposed a quartic model for the dry refractivity profile based on the temperature and the elevation of the site above mean sea level (msl) and employed the refractivity constants proposed by Smith & Weintraub (1953). Saastamoinen (1972; 1973) developed a model based on the measurements of the surface pressure and calculated the acceleration of gravity from the latitude and height of the station. In his model, the refractivity constants calculated by Essen & Froome (1951) were adopted. Davis et al. (1985) used the same approach as Saastamoinen (1972; 1973). However, they employed the refractivity constants proposed by Thayer (1974). Baby et al. (1988) considered the refractivity constant k_1 of Bean and Dutton (1966) and proposed computing the acceleration gravity based on the surface temperature and temperature lapse rate.

As noted by Mendes & Langley (1998), the models developed by Baby et al. (1988) and Hopfield (1969) overestimate the ZHD values in all regions, with the exception of the equatorial area. In the research studies of Mendes & Langley (1998) and Mendes (1999), a comparison between the *a priori* value of ZHD obtained from ray tracing approach and that calculated by employing other modeled was carried out. They showed that the *a priori* value of ZHD can be more accurately (sub-millimeter) estimated from Saastamoinen's (1972; 1973) model, assuming an accurate surface pressure incorporated into the model. Although, they concluded that other models results in ZHD with a millimeter level of agreement to those obtained from ray tracing approach.

1.6.2.2 Zenith Wet Delay (ZWD) Models

Due to the dependency of the ZWD on the water vapor pressure and because of variations in time and space, several theoretical and empirical models for modeling the *a priori* value of ZWD have been developed further than those for modeling ZHD. However, as determined by Mendes (1999), the accuracy of the ZWD computed based on the surface meteorological measurements is not better than a few centimeters.

Saastamoinen (1973) formulated a model for estimating ZWD assuming that temperature and water vapor pressure linearly decrease with height according to a power law function. In their model, the refractivity constants were the same as those they considered for computing ZHD. Their model has a good performance in mid-latitude regions. Hopfield (1969) proposed a model based on the profile of wet component of refractivity and assumed the refractivity constants from Smith & Weintraub (1953). Berman (1976) developed a model on the assumption that there is a strong correlation between the ratio of ZHD and ZWD and the corresponding refractivities. In their model, the ZWD is computed from its linear relationship with the surface meteorological parameters was proposed by Ifadis (1986). As shown by Mendes (1999), Saastamoinen's (1973) (Equation 1.11) and Ifadis' (1986) (Equation 1.12) models provide a better estimation for ZWD compared to the other estimates from other models.

$$ZWD = 0.002277 \left(\frac{1255}{T_s} + 0.05 \right) e_s \quad (1.11)$$

where, e_s is the water vapor pressure at the surface of Earth in mbar, T_s is the temperature at the surface of Earth in degrees Kelvin.

$$ZWD = 0.00554 - 0.880 \times 10^{-4} (P_s - 1000.0) + 0.272 \times 10^{-4} e_s + 2.771 \left(\frac{e_s}{T_s} \right) \quad (1.12)$$

where, e_s is the water vapor pressure at the surface of Earth in mbar, T_s is the surface temperature in degrees Kelvin, P_s is the surface pressure in mbar.

1.7 Mapping Functions for Zenith Hydrostatic and Wet Delays (ZHD and ZWD)

Because of the lower accuracy of the *a priori* ZWD compared to the *a priori* ZHD, as discussed earlier, the mapping functions usually are defined for hydrostatic and wet parts separately. According to Boehm et al. (2006), a total mapping function is less accurate, and therefore not many researchers have focused on that.

Over the last two decades, different mapping functions have been developed by many researchers (Hopfield 1969; Chao 1972; Black 1978; Baby et al. 1988; Herring 1992; Niell 1966; Niell 2000; Boehm & Schuh 2004; Boehm et al. 2006). The recent proposed hydrostatic and wet mapping functions are formed as a continued fraction (Marini 1972). In this section, in addition to reviewing the two most recent mapping functions, the Vienna Mapping Functions (VMF) and the Global Mapping Function (GMF), I review the Niell Mapping Function (NMF) (Niell 1996).

Although the NMF is older, it is still being used in many GPS processing software because it is independent of the atmospheric parameter measurements and its application is straightforward. This mapping function was employed for both hydrostatic and wet components in the first phase of this dissertation (see Section 2).

The modern mapping functions are based on the global numerical weather prediction (NWP) models or the empirical model of global pressure and temperature (GPT) developed by Boehm et al. (2007). This global model provides pressure and temperature at any location at or near the Earth's surface, in addition to providing the seasonal variability of global temperature. This model is based upon spherical harmonics up to degree and order nine, and was computed from three years of a $15^\circ \times 15^\circ$ global grid of monthly mean profiles for pressure and temperature from the European Centre for Medium-Range Weather Forecasts (ECMWF) 40-year re-analysis (ERA40) dataset (Kouba 2008).

1.7.1 Niell Mapping Function (NMF)

The NMF (Niell 1996) is independent of the atmospheric parameter measurements. This mapping function is widely used in GPS processing software including Bernese (Dach 2005; Dach et al. 2007), and we used it in the processing of the GPS data in the first part of this dissertation. The advantage of using this mapping function, in comparison to the other mapping functions proposed earlier, is that it provides accurate positions for the stations located in the latitude range 43° and 75°N for a minimum elevation angle of three degrees.

The NMF mapping function is:

$$m_i(\varepsilon) = \frac{1 + \frac{a_i}{b_i}}{1 + \frac{c_i}{\sin \varepsilon + \frac{a_i}{b_i}}} + \left[\frac{1}{\sin \varepsilon} - \frac{1 + \frac{a_{ht}}{b_{ht}}}{\sin \varepsilon + \frac{a_{ht}}{b_{ht}}} \right] \times \frac{H}{1000} \quad (1.13)$$

where, a_i , b_i and c_i coefficients are the parameters of the hydrostatic and wet mapping functions in which h or w is used instead of i to specify the hydrostatic and wet parts, respectively. a_{ht} , b_{ht} and c_{ht} are the constant values equal to 2.53×10^{-5} km, 5.49×10^{-3} km and 1.14×10^{-3} km, respectively. H is the orthometric height of the GPS station in meter above msl.

It must be noted that the second term in Equation 1.11 is the height correction term and is only applied to the hydrostatic mapping function. The a_i , b_i and c_i coefficients for the hydrostatic part are modeled based on the station's latitude and day of the year (DoY) (taken from January 0.0 in UT days) and they can be calculated by

$$a_h(\varphi, DoY) = a_{h_{avg}}(\varphi) + a_{h_{amp}}(\varphi) \cos\left(2\pi \frac{DoY - 28}{365.25}\right) \quad (1.14)$$

where, the values for $a_{h_{avg}}$ and $a_{h_{amp}}$ are the average value of a_h and its amplitude, respectively, and φ is the latitude of the station in degree. They are provided by Niell (1996) for five latitudes (Table 1.1). Linear interpolation is performed to calculate them for non-tabulated latitudes. The same procedure as computing a_h is performed for computing the b_h and c_h coefficients.

The a_i , b_i , and c_i coefficients in the wet mapping function are only dependent on latitude and are given as a_w , b_w , and c_w in Table 1.1

Table 1.1. Coefficients of the hydrostatic and wet mapping functions (Niell 1996)

| Coefficients | Latitude (degrees) | | | | |
|---------------|--------------------|---------------|--------------|--------------|--------------|
| | 15 | 30 | 45 | 60 | 75 |
| $a_{h_{avg}}$ | 1.2769934e-3 | 1.2683230e-3 | 1.2465397e-3 | 1.2196049e-3 | 1.2045996e-3 |
| $b_{h_{avg}}$ | 2.9153695e-3 | 2.9152299e-3 | 2.9288445e-3 | 2.9022565e-3 | 2.9024912e-3 |
| $c_{h_{avg}}$ | 62.610505e-3 | 62.837393e-3 | 63.721774e-3 | 63.824265e-3 | 64.258455e-3 |
| $a_{h_{amp}}$ | 0.0 | 1.27079626e-5 | 2.6523662e-5 | 3.4000452e-5 | 4.1202191e-5 |
| $b_{h_{amp}}$ | 0.0 | 2.1414979e-5 | 3.0160779e-5 | 7.2562722e-5 | 11.723375e-5 |
| $c_{h_{amp}}$ | 0.0 | 9.0128400e-5 | 4.3497037e-5 | 84.795348e-5 | 170.37206e-5 |
| a_w | 5.8021897e-4 | 5.6794847e-4 | 5.8118019e-4 | 5.9727542e-4 | 6.1641693e-4 |
| b_w | 1.4275268e-3 | 1.5138625e-3 | 1.457252e-3 | 1.5007428e-3 | 1.7599082e-3 |
| c_w | 4.3472961e-2 | 4.6729510e-2 | 4.3908931e-2 | 4.4526982e-2 | 5.4736038e-2 |

1.7.2 Vienna Mapping Function (VMF)

Boehm & Schuh (2004) proposed VMF in the same form of continued fraction used in the NMF (Niell 1996). In VMF, the coefficients b_h and c_h are equal to the coefficients $b = 0.002905$ and $c = 0.0634 + 0.0014 \cos(\varphi)$ of the Isobaric Mapping Function (IMF) proposed by Niell (2000). In addition, the coefficients b_w and c_w are the coefficients of the wet component at latitude of 45° given by Niell (1966) (Table 1.1). The a_h and a_w coefficients for hydrostatic and wet parts can be calculated as a function of b_h , c_h , b_w , c_w , and the vacuum elevation angle ε and the mapping function values obtained from raytracing at a 3.3° initial elevation angle.

1.7.3 Vienna Mapping Function 1 (VMF1)

Boehm et al. (2006) developed VMF1, an update of VMF, in which they removed the systematic errors in the estimation of coefficients by fitting the c coefficients to a function of the latitude of station and DoY. They also calculated $b_t = b_h$ equal to 0.0029 and proposed Equation 1.13 for calculating coefficient c for hydrostatic and total mapping function.

$$c = c_0 + \left[\left(\cos \left(\frac{\text{DoY} - 28}{365} \cdot 2\pi + \psi \right) + 1 \right) \frac{c_{11}}{2} + c_{10} \right] (1 - \cos \varphi) \quad (1.15)$$

where, ψ represents the hemisphere section in radian, φ is the latitude of a station in degree, c_0 , c_{10} , and c_{11} are constants.

Table 1.2 represents the values of c_0 , c_{10} , c_{11} , and ψ for hydrostatic and total mapping provided by Boehm et al. (2006).

Table 1.2. Constant parameters for hydrostatic and total VMF1 (Boehm et al. 2006)

| Hemisphere | Hydrostatic VMF1 | | | | total VMF1 | | | |
|------------|------------------|----------|----------|--------|------------|----------|----------|--------|
| | c_0 | c_{10} | c_{11} | ψ | c_0 | c_{10} | c_{11} | ψ |
| Northern | 0.062 | 0.001 | 0.005 | 0 | 0.063 | 0.000 | 0.004 | 0 |
| Southern | 0.062 | 0.002 | 0.007 | π | 0.063 | 0.001 | 0.006 | π |

The b_ω and c_ω coefficients in VMF1 are the coefficients of wet component at latitude of 45° given by Niell (1966) and from Table 1.1 are equal to 0.00146 and 0.04391, respectively.

1.7.4 Global Mapping Function (GMF)

The GMF is the latest mapping function developed by Boehm et al. (2006), and it is determined on the basis of the $15^\circ \times 15^\circ$ global grid of monthly mean profile of pressure, temperature and relative humidity data produced from the ECMWF numerical weather model data (Kouba 2008).

The coefficients b and c for hydrostatic and wet parts are computed with a similar strategy used in VMF1. The coefficient a is calculated from the spherical harmonic on a global grid:

$$a = a_0 + A \cos\left(\frac{\text{DoY} - 28}{365} \cdot 2\pi\right)$$

$$a_0 = \sum_{n=0}^9 \sum_{m=0}^n P_{nm}(\sin(\varphi)) \cdot [A_{nm} \cos(m\lambda) + B_{nm} \sin(m\lambda)] \quad (1.16)$$

where, a_0 is the mean value and is constant and A is the annual amplitude on the global grid of monthly mean between September 1999 and August 2002 in a least-square adjustment, $P_{nm}(\sin(\varphi))$ are the associated Legendre functions with n degree and m order, and A_{nm} and B_{nm} are the spherical harmonic coefficients.

The advantage of employing GMF compared to VMF1 is that GMF can compute the coefficients only based on the position of the station and DoY.

1.8 Modeling the meteorological parameters

As discussed earlier, the mapping functions employ meteorological parameters measured at the surface of Earth. Because of the lack of the surface meteorological data at any location on earth, several studies have been carried out to propose global models, such as GPT by Boehm et al. (2007), GPT 2 wet (GPT2w) developed by Boehm et al. (2015), and ERA-Interim produced by ECMEF (Dee et al., 2011) for modeling the meteorological parameters. As discussed above, the GPS processing can estimate the GPS signals' ZTD, which can be divided into hydrostatic and wet components. ZWD can be computed by subtracting ZHD, can be accurately computed from the surface meteorological data, from ZTD. The wet component of the delay is used to measure

PWV above a station by multiplying a conversion factor, which is a function of the weighted mean surface temperature above the station for implementing climate studies.

As mentioned earlier, the Saastamoinen (1973)'s model is adopted to estimate the ZHD at millimeter levels of accuracy, as a function of surface pressure. As discussed in Davis et al. (1985), the uncertainties in this model resulted from biases in the physical constants and the mean value of gravity which were employed and are approximately 0.5 mm. These uncertainties result in less than 0.1 kgm^{-2} uncertainties in PWV estimations and can be neglected (Davis et al. 1985). The weighted mean surface temperature can be estimated from the integration of water vapor pressure and temperature above the station at vertical levels as proposed by Davis et al. (1985).

To achieve the atmospheric parameters' profiles, the ERA-Interim model that provides atmospheric parameters for 60 vertical levels from the Earth's surface can be employed. This parameter can be accurately approximated from the surface temperature based on the formula proposed by Bavis et al. (1992). Alshawaf et al. (2017) compared the weighted mean surface temperature computed from surface temperature and from the ERA-Interim for two stations in Germany and found that the value of the later approach had a higher error and related this to the inaccuracy of the coarse grid of ERA-Interim modeled in the mountainous areas. Studies carried out by Pikridas et al. (2014) and Liu et al. (2005) indicate that uncertainties in the surface temperature do not significantly affect the PWV determinations.

For an accurate measurement of ZHD and PWV using GPS, less than 6.6 mm and 1 kgm^{-2} , respectively, accurate estimation of the surface pressure, less than 2.9 hpa, at the location of each GPS site is important (Wang et al. 2017). In their study (Wang et al. 2017) they employed surface pressure observed at 108 global GNSS stations between 2000 and 2013. They observed that ERA-Interim-derived pressure provides more accurate estimation of monthly PWV, with a relative error of approximately 1.6%.

The ZTD at the location of each site can be computed from the horizontal interpolation of the meteorological data observed at the adjacent weather stations (Gendt et al. 2004) and the vertical interpolating of those data for the height difference of the weather stations

and the station (Musa et al. 2011; Dousa & Elias 2014). Although, the interpolation may result in errors in ZTD and PWV, the exponential interpolation of the pressure for the height difference matches well with the vertical profile of pressure. The linear interpolation of the temperature is erroneous, particularly in cases with the large differences between the height of the GPS station and the weather station. However, because the effect of temperature errors in ZTD and PWV estimations are insignificant compared to the pressure errors, the resulted errors can be ignored (Ghoddousi-Fard 2009). Similar interpolation approaches can be performed on the surface values on the grid points of NWP global and regional models.

1.9 Noise analysis

The linear regression of the position time series of a station cannot accurately estimate the rate of the surface deformation because it is based on the assumption that the observations are not correlated with time. In traditional methods, it is assumed that the measurement errors are uncorrelated with time, or white noise, and they can be reduced by averaging of the measurements. Employing that method results in underestimation of the velocity uncertainties (Zhang et al. 1997; Mao et al., 1999). Many studies indicate that the measurements errors are correlated in time, or colored noise, and this should be accounted for in order to estimate more realistic uncertainties of the surface deformation rate (Agnew 1992; Williams et al. 2004; Hackl et al. 2011).

The noise in the GPS position time series can be defined as a power-law process which is mainly due to the instabilities of the geodetic monuments (Johnson and Agnew 1995).

This type of noise can be characterized in the time domain as follow:

$$P_x(f) = P_0 \left(\frac{f}{f_0}\right)^k \quad (1.17)$$

where, f is the temporal frequency, P_0 and f_0 are constants, and k is the spectral index (Mandelbrot and Van Ness, 1968).

The spectral index represents the type of noise, which can be divided into stationary and non-stationary processes. The non-stationary process is observed in many natural

processes and they have higher power at low frequencies. Their power spectrum shows that they have negative indices range between -3 and -1 (Williams et al. 2004). The three most common noise components, including white noise, flicker noise, and random walk noise, are analyzed in this dissertation in order to construct fixed noise combinations for the GPS position time series analysis.

White noise is a random signal and has an index of $k=0$. It is the special case of the stationary process in which the power spectral density is flat. The random walk noise is classical Brownian motion with spectral index of -2 and is commonly observed in strainmeter and tiltmeter data (Wyatt 1989). Flicker noise is identified in many dynamical processes and is in the main feature in GPS position time series (Mao et al. 1999; Williams et al. 2004).

Here, the power-law process refers to a non-stationary process or coloured noise other than classical white noise.

1.9.1 Maximum Likelihood Estimation (MLE)

The maximum likelihood approach is used to compute the amount of white noise and power law noise in the GPS time series. The best fit noise model to the GPS observations which maximize the probability function is defined as follow:

$$P(\hat{v}, C) = \frac{1}{(2\pi)^{\frac{N}{2}} (\det C)^{\frac{1}{2}}} \exp(-0.5 v^T C^{-1} v) \quad (1.18)$$

where, P is likelihood and \det is the determinant of matrix, C is the covariance matrix, N is the number of epochs and v is the postfit residuals resulted from the best fit linear functions with the same covariance matrix C .

To maximize the probability function, the logarithm of the likelihood function is maximized:

$$\ln[P(\hat{v}, C)] = -0.5[\ln(\det C) + v^T C^{-1} v + N \ln(2\pi)] \quad (1.19)$$

where, $\ln[P(\hat{v}, C)]$ is the natural logarithm, the other parameters are similar to those in Equation 1.18.

The covariance matrix C represents Gaussian stochastic noise modeled including white, power law noise, first order Gauss Markov, and their combinations. In the first phase of this dissertation, we assumed that C is the combination of a white and a power law noise. Therefore, the covariance matrix of the GPS position time series can be obtained as:

$$C = a_w^2 I + b_w^2 J_k \quad (1.20)$$

where, a and b are the amplitudes of the white and power-law noise, respectively. I is the identity matrix with the dimension of $N \times N$, J_k is the covariance matrix of the power law noise with spectral index k .

The power law covariance matrix can be written as follow (Johnson & Wyatt 1994):

$$J_k = T C_d T^T \quad (1.21)$$

where, J_k is the power law covariance matrix, T is the transformation matrix (Hosking 1981), C_d is the covariance of vector d of independent and identically distributed random variables with unit variance.

With $C_d = I$,

$$J_k = T T^T \quad (1.22)$$

where,

$$T = \Delta T^{-\frac{k}{4}} \begin{bmatrix} \phi_0 & 0 & 0 & 0 & \dots & 0 \\ \phi_1 & \phi_0 & 0 & 0 & \dots & 0 \\ \phi_2 & \phi_1 & \phi_0 & 0 & \dots & 0 \\ \dots & \dots & \dots & \dots & \dots & \dots \\ \phi_N & \phi_{N-1} & \phi_{N-2} & \phi_{N-3} & \dots & \phi_0 \end{bmatrix} \quad (1.23)$$

where, ΔT is the sampling interval, ϕ_N are the coefficient values and are calculated as follow:

$$\phi_N = \frac{\Gamma(N-\frac{k}{2})}{N!\Gamma(-\frac{k}{2})} \quad (1.24)$$

The power spectrum equation can be written as:

$$P = \frac{D_x b_k^2}{f_s^{\frac{k}{2}+1}} f^k \quad (1.25)$$

where, f_s is the sampling frequency in Hz and $D_x = 2(2\pi)^k (24.60.60.365.25)^{\frac{k}{2}}$.

From the above discussion, the white noise has $\phi_0=1$ and $\phi_N=0$ for all N greater than zero by substituting $k=0$. The transformation matrix, T , and power law covariance matrix, J_0 , are identity matrices and are time-independent. The random walk noise with $k=-2$ results in $\phi_N=1$ and the transformation matrix with lower triangular equal 1. The amplitude of the flicker noise. For the flicker noise, the constant in the covariance matrix proposed by Zhang et al. (1997) is selected such that the power spectrum of flicker noise and random walk noise have equal amplitudes. Therefore, the amplitude of the flicker noise covariance matrix is scaled by multiplying by 1.744.

1.10 Purpose of the work

The first objective of my dissertation is to identify the optimal solution with lower errors from a network of sparse GPS stations and with the significant changes in the local atmospheric conditions in eastern Ontario and western Québec to provide an accurate constraint for the prediction models of regional dynamics of lithosphere due to GIA. This goal was achieved by processing different subsets of the GPS stations using double-differencing approach and evaluating the accuracy of the vertical and horizontal deformation based on the results from global solutions and comparison with GIA models.

A second objective of the work is to propose a simple elevation-dependent model which can accurately estimate the seasonal amplitude of ZTD between each GPS station and a reference station for a local region. To obtain this model, the meteorological observations from the weather stations near the GPS stations are used and corrected for the height difference. Then the evaluation of the accuracy of the proposed model is assessed by

comparing the estimates of the seasonal amplitudes of ZTD from the proposed model to those observed in the ZTD times series derived from GPS processing techniques.

As noted above, many empirical and theoretical approaches have been proposed for computing ZTD affecting the GPS observations, which are based on the empirical low-resolution global models or NWP models. Using this model with or in lieu of the global weather prediction models in the GPS processing software can produce improved, sub-centimeter level positioning accuracy because tropospheric errors are estimated at smaller spatial scales for local or regional networks.

The third objective of this work incorporates the high density DInSAR data in a small region to propose a model which provides a best fit to the seasonal amplitude of ZTD in the vertical time series of DInSAR data. This model is obtained from radiosonde data and meteorological data from a weather station and is a function of elevation. This model not only eliminates the need to the meteorological observations at each GPS station, but it also can be used to accurately estimate the seasonal amplitude of local ZTD on GPS data at any altitude.

In this dissertation, I will show that the proposed model can produce more accurate positioning estimates.

I carried out the following studies to pursue these goals:

- New measurements of GPS data in eastern Ontario and western Québec, to provide a better constraint for the crustal motion predicted by the GIA prediction models in this region.
- Simplified one-dimensional methodology to retrieve the ZTD on GPS data to model the elevation-dependent seasonal amplitudes of ZTD in GPS stations in eastern Ontario and western Québec, despite the fact that the variation in topography in this regions is not significant.
- Modeling the elevation-dependent seasonal amplitude of local ZTD in GPS data based on meteorological data from a weather station and radiosonde data in the area

surrounding the Kilauea volcano in Hawaii, with significant changes of topography. This model is the best fit to the observed seasonal amplitude in the vertical time series of DInSAR data in this region and provides tropospheric corrections to the local GPS network on spatial scales much smaller than those of the global model.

1.11 Structure of the thesis

This thesis is composed of five main sections. Chapter 1 is an introduction and provides background information about GPS, its effective errors and the important recent models, and outlines the research objectives. Chapter 2 presents the measurements of the horizontal and vertical velocities of GPS stations in eastern Ontario and western Québec. Chapter 3 presents the detailed of the elevation-dependent model proposed to estimate the seasonal amplitude of ZTD in GPS data in eastern Ontario and western Québec and also presents a comparative study of local PWV time series estimated from the wet component of ZTD derived using PPP technique and meteorological data at each GPS station. Chapter 4 presents a detailed examination of the seasonal amplitude of ZTD derived from DInSAR data, GPS data and from the elevation-dependent model derived based on the radiosonde and meteorology data in the area surrounding Kilauea volcano, Hawaii. Chapter 5 presents the summation and conclusion of the results and suggestions for future studies.

1.12 References

- Adams, J. (1989), Postglacial faulting in eastern Canada: nature, origin and seismic hazard implications. *Tectonophysics* 163:323–331. doi:10.1016/0040-1951(89)90267-9
- Altamimi Z, Collilieux X, Métivier L. (2011), ITRF2008: an improved solution of the International Terrestrial Reference Frame. *J Geodesy* 85(8):457–473. doi:10.1007/s00190-011-0444-4
- Altamimi Z, Métivier L, Collilieux X. (2012), Itrf2008 plate motion model. *J Geophys Res* 1978–2012. doi:10.1029/2011JB008930

- Agnew, D.C. (1992), The time-domain behavior of power-law noises, *Geophys. Res. Lett.*, 19, 333-336.
- Baby, H.B., Golé, P., and Lavergnat, J. (1988), A model for the tropospheric excess path length of radio waves from surface meteorological measurements. *Radio Sci*, Vol. 23, No. 6, pp. 1023-1038.
- Bar-Sever Y.E., Kroger P.M., Borjesson J.A. (1998), Estimating horizontal gradients of tropospheric path delay with a single GPS receiver. *J Geophys Res* 103(B3):5019–5035
- Basham P.W., Forsyth D.A., Wetmiller R.J. (1977), The seismicity of northern Canada. *Can J Earth Sci* 14(7):1646–1667. doi:10.1139/e77-140
- Bauersima, I. (1983), NAVSTAR/Global Positioning Systems (GPS), II, *Mitteilungen der Satellitenbeobachtungsstation Zimmerwald*, Nr.10, Astronomical Institute, University of Berne, Switzerland.
- Bean, B. R., and Dutton, E. J. (1968), *Radar Meteorology*. Dover Publications, Inc., New York.
- Bent A.L. (1996), An improved source mechanism for the 1935 Timiskaming, Québec earthquake from regional waveforms. *Pure Appl Geophys* 146(1):5–20
- Berman, A.L. (1976), *The Prediction of Zenith Range Refraction From Surface Measurements of Meteorological Parameters*, Jet Propulsion Laboratory, California Institute of Technology, Pasadena, California, 15 July, National Aeronautics and Space Administration Technical Report 32–1602, pp. 40.
- Bevis M., Businger, S., Herring, T.A., Rocken, C., Anthes, R.A., and Ware, R.H. (1992), GPS meteorology: remote sensing of atmospheric water vapor using the Global Positioning System. *J Geophys Res* 97:15784–15801
- Bevis, M., Businger S., and Chiswell S. (1994), GPS meteorology: Mapping zenith wet delays on to Precipitable water, *J. Appl. Meteorol*, 33, 379 – 386.

- Bianchi, C. E., Mendoza, L. P. O., Fernández, L. I., Natali, M. P., Meza, A. M. and Moirano, J. F. (2016), Multiyear GNSS monitoring of atmospheric IWV over Central and South America for climate studies. *Annales Geophysicae*, 34, 623-639, doi: 10.5194/angeo-34-623-2016.
- Black, H. (1978), An easily implemented algorithm for the tropospheric range correction. *J. Geophys. Res.*, 83, 1825–1828.
- Bock, Y., and Williams, C.A. (1997), Integrated satellite interferometry in southern California, EOS, TRANSACTIONS, AGU, 78 (29), 299-300.
- Boehm J, Niell AE, Tregoning P, and Schuh H. (2006), Global mapping function (GMF): a new empirical mapping function based on data from numerical weather model data. *J Geophys Res.* 10.129/2005GL025546
- Boehm, J., and Schuh H. (2004), Vienna mapping functions in VLBI analyses. *Geophys. Res. Lett.*, Vol. 31, L01603, DOI: 10.1029/2003GL018984.
- Boehm, J., Heinkelmann, R. and Schuh, H. (2007), A global model of pressure and temperature for geodetic applications. *Journal of Geodesy*, 81(10), pp.679–83.
- Bonforte, A., Ferretti A., Prati C., Puglisi G., and Rocca F. (2001), Calibration of atmospheric effects on SAR interferograms by GPS and local atmospheric models: First results, *J. Atmos. Solar-Terrestrial Phys.*, 63, 1343 – 1357.
- Boudouris, G. (1963), On the index of refraction of air, the absorption and dispersion of centimeter waves in gas, *Radio Sci.*, 67, 631–684.
- Calais E, Han, J.Y., DeMets, C., and Nocquet, J.M. (2006), Deformation of the North American plate interior from a decade of continuous GPS measurements. *J Geophys Res* 111. doi:10.1029/2005JB004253
- Celestino C.C., Sousa C.T., Yamaguti W., and Kuga H.K. (2007), Evaluation of Tropospheric and Ionospheric Effects on the Geographic Localization of Data

Collection Platforms. MPE, volume 2007, Article ID 32514, 11 pages,
doi:10.1155/2007/32514.

Chao, C. (1972), A model for tropospheric calibration from daily surface and radiosonde balloon measurements. In Technical Memorandum; Jet Propulsion Laboratory: Pasadena, CA, USA; pp. 350–391.

Chen, G., and Herring, T.A. (1997), Effects of atmospheric azimuthal asymmetry on the analysis of space geodetic data, *J Geophys Res.* Vol. 102, No. B9, pp. 20489-20502.

Chen, Y.-H., Juang, J.C., Seo, J., Lo, S., Akos, D.M., de Lorenzo, D.S., and Enge, P. (2012), Design and implementation of real-time software radio for anti-interference GPS/WAAS sensors. *Sensors*, 12, 13417–13440.

Cocard, M., and Geiger, A. (1992), Systematic search for all possible widelanes. *Proceedings of The Sixth International Geodetic Symposium on Satellite Positioning*, Columbus, Ohio, 17-20 March, pp. 312-318.

Cong, L., Li, E., Qin, H., Ling, K.V., and Xue, R.A. (2015), Performance improvement method for low-cost land vehicle GPS/MEMS-INS attitude determination. *Sensors*, 15, 5722–5746.

Dach, R., Hugentobler, U., and Fridez, P. (2005), *Bernese GPS Software 5.0*. Astron. Institute University Of Berne, Berne

Dach, R., Hugentobler U, Fridez P, and Meindl M. (2007), *Bernese GPS Software Version 5.0*. Astron. Institute University Of Berne, Berne

Davidson P.I. (2016), Pseudoranges to four satellites.
<http://slideplayer.com/slide/9345082/>

Davis, J.L., Herring T.A., Shapiro I.I., Rogers A.E.E, and Elgered G. (1985), Geodesy by radio interferometry: effects of atmospheric modeling errors on estimates of baseline length. *Radio Sci*, Vol. 20, No. 6, 1593-1607.

- Dee, D., Uppala, S., Simmons, A., Berrisford, P., Poli, P., Kobayashi, S., Andrae, U.,
Balmaseda, M., Balsamo, G., and Bauer, P. (2011), The ERA-Interim reanalysis:
Configuration and performance of the data assimilation system, *Q. J. Roy.
Meteor. Soc.*, 137, 553–597.
- Dineva S, Eaton, D., Ma, S., and Mereu R.F. (2007), The October 2005 Georgian Bay,
Canada, earthquake sequence: Mafic Dykes and their role in the mechanical
heterogeneity of precambrian crust. *Bull Seism Soc Am* 97:457–473.
doi:10.1785/0120060176
- Dong, D., Fang, P., Bock, Y., Cheng, M.K., and Miyazaki, S. (2002), Anatomy of
apparent seasonal variations from GPS-derived site position time series. *J
Geophys Res* 107(B4). doi:10.1029/2001JB000573
- Duquenne, H., Everaerts, M., and Lambot, P. (2005), Merging a Gravimetric Model of
the Geoid with GPS/Levelling data: an Example in Belgium, Springer Berlin
Heidelberg, Berlin, Heidelberg, pp 131–136. DOI 10.1007/3-540-26932-0_23
- Eaton, D.W., Adams, J., Asudeh, I., Atkinson, G.M., Bostock, M.G., Cassidy, J.F.,
Ferguson, I.J., Samson, C., Snyder, D.B., Tiampo, K.F., Unsworth, M.J. (2005),
Investigating Canada's lithosphere and earthquake hazards with portable arrays.
Eos 86(17):169–176. doi:10.1029/2005EO170001
- Elizabeth, J. P., Matt A.K., Philip M., and David A.L. (2010), A first look at the effects
of ionospheric signal bending on a globally processed GPS network. *J Geod*, Vol.
84, pp. 491-499, DOI 10.1007/s00190-010-0386-2.
- Erenoglu R.C. (2015), A new approach to outlying data in estimation of vertical total
electron content. *Tehnički vjesnik* 22, 4, 971-979. doi: 10.17559/TV-
20141117201942
- Essen, L., and Froome, K. D. (1951), The Refractive Indices and Dielectric Constants of
Air and its Principal Constituents at 24 GHz. *Proc. of the Physical Society*
(London), Section B, 64:862-875.

- Gabriel, A. G., Goldstein, R. M., and Zebker, H. A. (1989), Mapping small elevation changes over large areas: Differential radar interferometry, *J Geophys Res*, 94, 9183-9191.
- Gao, G. X. (2008), Towards navigation based on 120 satellites: analyzing the new signals. Doctoral thesis, Department of Electrical Engineering, Stanford University.
- Ge, L. (2000), Development and testing of augmentations of continuously-operating GPS networks to improve their spatial and temporal resolution. UNISURV S-63, The University of New South Wales, Australia
- Ghoddousi-Fard R. (2009), Modeling troposphere gradients and parameters from NWP models: Effects on GPS estimates. PhD dissertation, Department of Geodesy and Geomatics Engineering Technical Report No. 264, University of New Brunswick, Fredericton, New Brunswick, Canada, 216 pp.
- Goad, C.C., and Goodman L. (1974), A modified Hopfield tropospheric refraction correction model. In: American Geophysical Union Annual Fall Meeting, 12-17 December 1974, San Francisco, California, USA (abstract EOS Trans. AGU 55, 1106).
- Hackl M., Malservisi R., Hugentobler U., Wonnacott R. (2011), Estimation of velocity uncertainties from GPS time series: examples from the analysis of the South African TrigNet network. *J Geophys Res* 116(B11):B11404.
doi:10.1029/2010jb008142
- Hanssen, R.F. (2001), Radar Interferometry. Data Interpretation and Error Analysis, Kluwer.
- Herring, T. (1992), Modeling atmospheric delays in the analysis of space geodetic data. In Proceedings of Refraction of Transatmospheric Signals in Geodesy; De Munck, J., Spoelstra, T., Eds.; Netherlands Geodetic Commission Publications on Geodesy: The Hague, The Netherlands; Volume 36, pp. 157–164.

- Hofmann-Wellenhof, B., Lichtenegger, H. and Collins, J. (2001), GPS Theory and practice 5th Edition. Springer, New York, ISBN 3-211-83534-2, 384 pp.
- Hopfield, H.S. (1969), Two-quadratic tropospheric refractivity profile for correcting satellite data. *J. Geophys. Res.*, Vol. 74, PP. 4487-4499.
- Hopfield, H.S., (1969), Two Quartic Tropospheric refractive profile for correcting satellite data, *J. Geophys. Res.*, 74(18), 4487-4499.
- Hoque, M.M., Jakowski, N. (2012), Ionospheric Propagation Effects on GNSS Signals and New Correction Approaches. In Tech. ISBN 978-953-307-843-4.
- Huang L., Song L., and Wang Y. (2012), Beidou Triple-frequency Geometry-Free Phase Combination for Cycle-slip Detection and Correction. *Acta Geodaetica et Cartographica Sinica*, 41 (5):763-768.
- Hudnut, K. W., Shen Z., Murray M., McClusky S., King R. W., Herring T., Hager B., Feng Y., Fang P., Donnellan A., and Bock Y. (1996), Coseismic displacements of the 1994 Northridge, California, earthquake, *Bull. Seism. Soc. Am.* 86, S19–S36
- Hugentobler, U., Schaer, S., and Fridez, P. (2001), Bernese GPS Software Version 4.2, Astronomical Institute, University of Berne.
- Ifadis, II (1986), The Atmospheric delay of radio waves: Modeling the elevation dependence on a global scale, Technical Report 38L. Chalmers University of Technology, Goteborg, Sweden.
- IUGG (International Union of Geodesy and Geophysics) (1963), Resolutions, 13th General Assembly, 19-31 August 1963, Berkeley, California, USA. *Bulletin Géodésique*, 70: 390
- James, T.S. (1991), Post-glacial deformation. Princeton University, Princeton, NJ, Ph.D. dissertation

- Jin, SG, Luo, O.F. (2009), Variability and climatology of PWV from global 13-year GPS observations. *IEEE Trans. Geosci. Remote Sens.* 47: 1918–1924. DOI: 10.1109/TGRS.2008.2010401.
- Johnson, H. O., and Wyatt F. K. (1994), Geodetic network design for fault mechanics studies, *Manuser. Geod.*, 19, 309-323.
- Kaplan, E. D. ed. (1996), *Understanding GPS: Principles and Applications*. Boston: Artech House Publishers.
- Katsougiannopoulos, S. (2008), Study of tropospheric effect on GNSS signals. Application to the European area. PhD thesis, Department of Geodesy and Surveying, Aristotle University of Thessaloniki, Greece
- Kim, B.C., and Tinin, M.V. (2011), Potentialities of multifrequency ionospheric correction in Global Navigation Satellite Systems, *J Geod.*, 85: 159. <https://doi.org/10.1007/s00190-010-0425-z>
- Kouba, J. (2008), Implementation and testing of the gridded Vienna Mapping Function 1 (VMF1). *J Geodesy* 82(4):193–205. doi:10.1007/s00190-007-0170-0
- Larson, K.M., Small, E.E., Gutmann, E., Bilich, A., and Axelrad, P. (2007), Using GPS multipath to measure soil moisture fluctuations: Initial results. *GPS Solutions*, doi:10.1007/s10291-007-0076-6.
- Li, B., Feng, Y., and Shen, Y. (2010), Three carrier ambiguity resolution: Distance-independent performance demonstrated using semi-generated triple frequency GPS signals. *GPS Solut.*, 14, 177–184.
- Li, X., Ge, M., Zhang, Y., Wang, R., Xu, P., Wickert, J., and Schuh, H. (2013), New approach for earthquake/tsunami monitoring using dense GPS networks, *Sci. Rep.*, 3, 2682, doi:10.1038/srep02682.
- Li, Z., Fielding E.J., Cross P., and Muller J.P. (2006a), Interferometric synthetic aperture radar (InSAR) atmospheric correction: MEdium Resolution Imaging

Spectrometer (MERIS) and Advanced Synthetic Aperture Radar (ASAR) integration, *Geophys. Res. Lett.*, doi: 10.1029/2005GL025299.

- Liu, J. Y., Chen, C.H., Sun, Y.Y., Tsai, H.F., Yen, H.Y., Chum, J., Lastovicka, J., Yang, Q.S., Chen, W.S., and Wen, S. (2016), The vertical propagation of disturbances triggered by seismic waves of the 11 March 2011M9.0 Tohoku earthquake over Taiwan, *Geophys. Res. Lett.*, 43(4), 1759–1765
- Liu, Z. (2010), A new automated cycle slip detection and repair method for a single dual-frequency GPS receiver. *J Geod.*, v. 85, n. 3, p. 171-183.
- Manconi, A., Walter, T.R., Manzo, M., Zeni, G., Tizzani, P., Sansosti, E., and Lanari, R. (2010), On the effects of 3-D mechanical heterogeneities at Campi Flegrei caldera, southern Italy. *J. Geophys. Res.*, 115, p. B08405, 10.1029/2009JB007099
- Marini, J.W. (1972), Correction of satellite tracking data for an arbitrary tropospheric profile. *Radio science*, Vol. 7, No. 2, pp. 223-231.
- Massonnet, D., and Feigl, K.L. (1998), Radar interferometry and its application to changes in the Earth's surface, *Rev. Geophys.*, 36 (4), 441-500.
- Melbourne, W.G. (1985), The case for ranging in GPS based geodetic systems, *Proceedings of 1st International Symposium on Precise Positioning with the Global Positioning System*, edited by Clyde Goad, U.S. Department of Commerce, Rockville, Maryland, 15-19 April, pp. 373-386.
- Mendes, V. B. (1999), Modeling the neutral-atmosphere propagation delay in radiometric space techniques. Ph.D. dissertation, Department of Geodesy and Geomatics Engineering Technical Report No. 199, University of New Brunswick, Fredericton, New Brunswick, Canada, 353 pp
- Mendes, V.B., and Langley, R.B. (1998), An Analysis of High-Accuracy Tropospheric Delay Mapping Functions. Viewgraphs presented at the European Geophysical Society XXIII General Assembly, Nice, France, 20-24 April 1998. Paper published in *Phys Chem Earth*, Vol. 25, No. 12, 2000, pp. 809-812.

- Misra, P. and Enge, P. (2006), *Global Positioning System: Signals, Measurements, and Performance*. 2nd Edition, Ganga-Jamuna Press, Lincoln.
- Montenbruck, O., and Gill, E. (2000), *Satellite Orbits Models, Methods, Applications*, Springer.
- Morland, J., Collaud Coen, M., Hocke, K., Jeannet, P., Mätzler, C., (2009), Tropospheric water vapour above Switzerland over the last 12 years. *Atmos. Chem. Phys.*, 9(16), pp. 5975–5988.
- Niell, A.E. (1996), Global mapping functions for the atmosphere delay at radio wavelengths. *J Geophys Res* 101:3227–3246
- Niell, A.E. (2000), Improved atmospheric mapping functions for VLBI and GPS Earth, Planets and Space, Vol. 52, No. 10, 699-702.
- Nievinski, F.G. (2009), Ray-tracing options to mitigate the neutral atmosphere delay in GPS, MSc thesis, 232 pp., Dep. of Geod. and Geomatics Eng., Univ. of N. B., Fredericton, N. B., Canada.
- Odiijk, D. (2003), Ionosphere-free phase combinations for modernized GPS. *J Surv Eng*, 129: 165–173
- Pikridas C., Katsougiannopoulos S., and Zinas N. (2014), A comparative study of zenith tropospheric delay and precipitable water vapor estimates using scientific GPS processing software and web based automated PPP service, *Acta Geodaetica et Geophysica*, June 2014, Volume 49, Issue 2, pp 177-188.
- Quinlan, G. (1984), Postglacial rebound and the focal mechanisms of eastern Canadian earthquakes. *Can J Earth Sci* 21:1018–1023. doi:10.1139/e84-106
- Raquet J., and Lachapelle, G. (2001), RTK positioning with multiple reference stations, *GPS World*, Apr 2001;12,4,48-53.

- Ray, J.K. (2000), Mitigation of GPS code and carrier phase multipath effects using a multi-antenna system. Ph.D. dissertation, University of Calgary
- Ray, J.K., and Cannon M.E. (2001), Synergy between Global Positioning System code, carrier, and signal-to-noise ratio multipath errors, *J.Guid. Control Dyn.*,24, 54–63.
- Rüeger, J. (2002), Refractive index formulae for electronic distance measurements with radio and millimetre waves, *Unisurv Rep. 109*, pp. 758–766, Univ. of N. S. W., Sydney, Australia.
- Saastamoinen, J. (1972), Atmospheric correction for the troposphere and stratosphere in radio ranging of satellites, in *The Use of Artificial Satellites for Geodesy, Geophys. Monogr.*, vol. 15, pp. 247–251, AGU, Washington, D. C.
- Saastamoinen, J. (1973), Contribution of the theory of atmospheric refraction, *Bulletin of Geodesique*, No. 105, pp. 279–298, No. 106, pp. 383–397, No. 107, pp. 13–34.
- Samsonov S., and d'Oreye N. (2012), Multidimensional time series analysis of ground deformation from multiple InSAR data sets applied to Virunga Volcanic Province. *Geophys. J. Int.*, 191(3):1095–1108. doi: 10.1111/j.1365-246X.2012.05669.x.
- Samsonov, S.V., Trishchenko, A.P., Tiampo K.F, González P.J., Zhang Y., and Fernández J. (2014), Removal of systematic seasonal atmospheric signal from interferometric synthetic aperture radar ground deformation time series, *Geophys. Res. Lett.*, 41, 6123–6130, doi:10.1002/2014GL061307.
- Sella, G.F., Stein, S., Dixon, T.H., Craymer, M., James, T.S., Mazzotti, S., and Dokka, R.K. (2007), Observations of glacial isostatic adjustment in the stable North America with GPS. *Geophys Res Lett* 34. doi:10.1029/2006GK027081
- Shrestha, S.M. (2003), Investigations into the Estimation of Tropospheric Delay and Wet Refractivity Using GPS Measurements (M.Sc. thesis), UCGE Report No. 20180.

- Smith, E.K., and Weintraub S. (1953), The constants in the equation for the atmospheric refractive index at radio frequencies, *Proc. IRE*, 41(8), 1035–1037.
- Sokolovskiy, S., Schreiner, W., Rocken, C., and Hunt, D. (2008), Optimal Noise Filtering for the Ionospheric Correction of GPS Radio Occultation Signals, *J. Atmos. Oceanic Tech.* 26 (7), 1398-1403.
- Sykes, L.R. (1978), Intraplate seismicity, reactivation of re-existing zones of weakness, alkaline magmatism and other tectonism post-dating continental fragmentation. *Rev Geophys* 16:621–688
- Thayer, G. (1974), An improved equation for the refractive index of air, *Radio Sci.*, 9(10), 803–807, doi:10.1029/RS009i010p00803.
- Tiampo K.F., Mazzotti, S., James, T.S. (2011), Analysis of GPS measurements in Eastern Canada using principal component analysis. *Pure Appl Geophys* 169(8):1483–1506. doi:10.1007/s00024-011-0420-1
- Tregoning, P., and van Dam T. (2005), Atmospheric pressure loading corrections applied to GPS data at the observation level, *Geophys. Res. Lett.*, 32, L22310, doi:10.1029/2005GL024104.
- van Dam, T., Collilieux, X., Wuite, J., Altamimi, Z, Ray, J. (2012), Nontidal ocean loading: amplitudes and potential effects in GPS height time series. *J Geodesy* 86:1043–1057
- van Dam, T., Wahr, J., Milly, P.C.D., Shmakin, A.B., Blewitt, G., Lavallée, D., and Larson, K.M. (2001), Crustal displacements due to continental water loading. *J Geophys Res* 28:651–654
- van Dam, T. M., Blewitt G., and Heflin M. (1994), Detection of atmospheric pressure loading using the Global Positioning System, *J. Geophys. Res.*, 99, 23,939–23,950, doi:10.1029/94JB02122.

- Vimal, V. (2013), GPS measurements, CSED Bahir Dar University.
(<https://www.slideshare.net/vrincevimal/gps-measurements>)
- Wang, H., Wu, P., van der Wal, W. (2008), Using postglacial sea level, crustal velocities and gravity-rate-of-change to constrain the influence of thermal effects on mantle heterogeneities. *J Geodyn* 46:104–117
- Williams S.D.P., Bock Y., Fang P., Jamason P., Nikolaidis R.M., Prawirodirdjo L., Miller M., Johnson D.J. (2004), Error analysis of continuous GPS position time series. *J Geophys Res* 109(B03412). doi:10.1029/2003JB002741
- Woodgold, C. (2010), Earthquakes Canada. Personal Communication, New York
- Wübbena, G. (1985), Software developments for geodetic positioning with GPS using TI 4100 code and carrier measurements, Proceedings of 1st International Symposium on Precise Positioning with the Global Positioning System, edited by Clyde Goad, U.S. Department of Commerce, Rockville, Maryland, 15-19 April, pp. 403-412.
- Wyatt, F. K. (1989), Displacements of surface monuments: Vertical motion, *J. Geophys. Res.*, 94, 1655 – 1664.
- Yuan, Y., Zhang, K., Rohm, W., Choy, S., Norman, R., Wang, C. (2014), Real-time retrieval of precipitable water vapor from GPS precise point positioning. *J Geophys Res Atmos* 119:10044–10057
- Zebker, H.A., and Goldstein, R.M. (1986), Topographic Mapping from Interferometric Synthetic Aperture Radar Observations, *J. Geophys. Res.*, vol.91, no.B5, pp.4993-4999.
- Zhang J, Bock Y, Johnson H, Fang P, Williams S, Genrich J, Wdowinski S, Behr J. (1997), Southern California permanent GPS geodetic array: error analysis of daily position estimates and site velocities. *J Geophys Res* 102(B8):18,035–18,055. doi:10.1029/97JB01380

Chapter 2

2 GPS coordinate time series measurements in Ontario and Québec, Canada¹

This chapter presents new precise network solutions for continuous GPS (cGPS) stations distributed in eastern Ontario and western Québec to provide constraints on the regional three-dimensional crustal velocity field. Five years of continuous observations at fourteen cGPS sites were analyzed using Bernese GPS processing software. Several different subnetworks were chosen from these stations, and the data were processed and compared in order to select the optimal configuration which can accurately estimate the three components of the velocities of the stations and can minimize the associated errors. Then, the coordinate time series are compared to the crustal motions from global solutions and the optimized solution is presented here. A noise analysis model with power-law and white noise, which best describes the noise characteristics of all three components, was employed for the GPS time series analysis. The linear trend, associated uncertainties, and the spectral index of the power-law noise were computed using a maximum likelihood estimation approach. The residual horizontal velocities, after removal of rigid plate motion, have a magnitude consistent with expected glacial isostatic adjustment (GIA). The vertical velocities increase from subsidence of almost 1.9 mm/year south of the Great Lakes to uplift near Hudson Bay, where the highest rate is approximately 10.9 mm/year. The residual horizontal velocities range from approximately 0.5mm/year, oriented south–southeastward, at the Great Lakes to nearly 1.5 mm/year directed toward the interior of Hudson Bay at stations adjacent to its shoreline. However, the pattern of horizontal deformation is not well explained in the north, along Hudson Bay, suggesting that revisions to the ice thickness history are needed to improve the fit to observations.

¹ A version of this chapter has been published in Geodesy journal. Samadi Alinia H., Tiampo, K.F., James, T.S. (2017) GPS coordinate time series measurements in Ontario and Québec, Canada, *J. Geodesy*. 91(6), pp. 653-683. DOI 10.1007/s00190-016-0987-5.

2.1 Introduction

Horizontal and vertical deformation of the Earth's crust is due to a variety of different geophysical processes that take place on various spatiotemporal scales. In eastern North America, from south of the Great Lakes to east of Hudson Bay, current deformation is primarily a result of the ongoing relaxation of the Earth's mantle from ice sheet retreat after the last glacial maximum, a process termed glacial isostatic adjustment (GIA). Observations from the Portable Observatories for Lithospheric Analysis and Research Investigating Seismicity (POLARIS) continuous Global Positioning System (cGPS) regional network (Eaton et al. 2005) in eastern Canada, combined with data from other high-quality sites, provide the means to define a more accurate crustal velocity field for the study of regional geophysical processes, particularly GIA.

POLARIS was a multi-institutional geophysical project focussing on seismology that began in 2002. More than thirty POLARIS stations were placed throughout southern Ontario and portions of western Québec. Most of the POLARIS stations were remote seismometer installations that used satellite communication technology, enabling the densification of the seismic network coverage in parts of eastern Canada, a region with significant but poorly understood seismicity. In addition, cGPS instruments were installed at a number of POLARIS stations with the goal of providing crustal deformation measurements in regions without pre-existing high-quality data. This will provide important insights into the structure of the Earth's lithosphere and regional crustal deformation (Eaton et al. 2005).

Early modeling investigations into North American crustal deformation indicated that intraplate horizontal deformation due to glacial isostatic adjustment (GIA) is expected to be a few millimeters per year in magnitude (James & Morgan 1990; James & Lambert 1993; Mitrovica et al. 1993, 1994), a result of the thinning and retreat of large ice sheets during deglaciation at the end of the last glaciation. Early comparisons to Very Long Baseline Interferometry (VLBI) observations suggested that the postglacial rebound signal was at the limit of detectability (James & Lambert 1993; Mitrovica et al. 1993, 1994). Crustal motion observations from cGPS stations have much greater spatial density and have shown that GIA is a strong, measurable signal. Calais et al. (2006) and Sella et

al. (2007) processed approximately 300 distributed GPS stations observations in Canada and United States and compared the station velocities to several different GIA models. Their results show significant discrepancies between the model predictions and the observed horizontal velocities and demonstrate the need for improved models of lithospheric deformation in central and eastern North America.

Tiampo et al. (2004, 2011) developed a technique to analyze cGPS time series using Karhunen–Loeve expansion (KLE) analysis to improve the local and regional time series results for a better understanding of the underlying physical sources. They decomposed available cGPS data from southeastern Canada and the eastern USA in order to characterize the significant deformation modes using spatial maps and their associated time series (Tiampo et al. 2011). In addition, they investigated the relationship between horizontal displacement and GIA models based on ICE-3G (Tushingham & Peltier 1991). They concluded that better estimates of horizontal GIA velocities provide important constraints on upper and lower mantle viscosity models, although the sparsity of stations north of the Great Lakes precluded differentiation between certain viscosities (Tiampo et al. 2011).

Here we present results for new time series spanning five years for cGPS stations from the POLARIS network combined with established continuous stations in eastern Ontario and western Québec. Given the large aperture of the network and the significant differences in local atmospheric conditions, an intensive study was undertaken in order to identify the optimal sub-networks for this analysis. We also studied several different subsets of reference stations that included at least one long-running IGS reference station (ALGO) operated by the Canadian Geodetic Survey (CGS) of Natural Resources Canada (NRCan). Subsequently, these improved time series were corrected with respect to the rigid plate motion proposed by Altamimi et al. (2011, 2012). The improved absolute velocities for each station are compared to the global solutions. We demonstrate the effectiveness of our double-differenced GPS sub-network processing to observe horizontal and vertical surface deformation in eastern Canada in a region with sparse coverage. In addition, we aggregate these results with those from additional stations provided by other agencies and compare them with current GIA models of horizontal and

vertical deformation in order to illustrate their potential to provide new insights into the broader regional dynamics (e.g., James & Morgan 1990; James & Lambert 1993; Mitrovica et al. 1994; Tiampo et al. 2013; Peltier et al. 2015).

The annual and semi-annual seasonal loading signals affect the GPS time series coordinates, particularly the up component (van Dam et al., 2001; Dong et al. 2002). Neglecting these affects in the velocity estimations will result in bias. Furthermore, many studies (Mao et al. 1999; Zhang et al 1997) demonstrate that mismodeled satellite orbits, multipath, antenna phase centre and atmospheric effects will produce rate uncertainties which must be estimated by using both white noise and time-correlated colored noise models (Williams et al. 2004). Analysis of the GPS time series in all three components using the combination of a white and power law noise model and estimating the associated spectral index of the power law noise indicates that all components at the GPS stations in our study area are subject to an identical type of noise, as they possess a very similar mean spectral index, approximately -1.01 ± 0.09 and -0.79 ± 0.07 for the velocities obtained from Bernese time series and NGL time series, respectively.

An overview of the study area is provided in Section 2. Section 3 presents details of the cGPS network and data analysis. Results for the most accurate reference frame solution and the associated five-year time series, as well as horizontal and vertical surface displacement rates and their associated uncertainties, are given in Section 4. We examine these results and compare them with GIA deformation models in Section 5. Interpretation and conclusions are presented in the final section.

2.2 Background

Plate tectonics theory provides an explanation for seismicity and deformation along plate boundaries and predicts that intraplate events located in continental interiors will generally occur with lower frequency and smaller magnitude (e.g., Adams & Basham 1989; Talwani 1999). The seismicity and tectonic setting of these intraplate regions, including the North American plate, have been extensively investigated (Basham et al. 1977; Sykes 1978; Quinlan 1984; Adams 1989; Bent 1996; Eaton et al. 2005; Wang et al. 2008; Woodgold 2010). One major source of stress perturbation in these regions is GIA

(James 1991; Wang et al. 2008; Wu et al. 2010; Dineva et al., 2007), potentially affecting regional spatiotemporal seismic activity along pre-existing, reactivated low friction faults (Wu & Hasegawa 1996; Mazzotti & Townend 2010). Some researchers also argue that the base of the lithosphere was warmed and weakened along the Great Meteor Hotspot Track in eastern North America and they relate that weakening to current seismicity along the hotspot track (Crough 1981; Heaman & Kjarsgaard 2000; Ma & Atkinson 2006; Ma & Eaton 2007).

2.2.1 Geological Structure and Recent Glaciations

The Superior Province, the largest Archean craton on the Earth, forms the oldest core of the North American plate and is one of the major geological units in northeastern Ontario. In addition, the Huronian supergroup of northeastern Ontario, with a thickness of 15 km, consists of ~2 Ga old rocks that form the passive edge along the southern margin of the Superior craton (Ludden & Hynes, 2000).

The Charlevoix region, 150 km northeast of Québec City, is the most active intraplate earthquake zone in eastern Canada. This region is affected by a large fault system which was formed as a result of four tectonic events that include the Grenvillian continental collision ~1100-900 Ma, the rifting and opening of the Iapetus Ocean ~700 Ma, reactivation of faults during closing of Iapetus Ocean (during mid- to late-Paleozoic), and Mesozoic extension opening of the Atlantic Ocean ~450 Ma (Buchbinder et al. 1988; Ma and Atkinson 2006).

The two most recent glacial periods in North America are the Wisconsinan (79-10 ka BP) and Illinoian (302-132 ka BP) (Lougheed & Morrill 2015). From 24-16 ka BP, during the Wisconsinan Ice Age, ice advanced such that glaciers extended over southwestern Ontario and totally covered the Great Lakes watershed (Terasmae 1981; Grimley 2000). The Great Lakes watershed itself is the result of several glaciations, currently covering 765,990 km² of Ontario and a large portion of the northcentral United States (Larson & Schaetzl 2001; Lougheed & Morrill 2015; Dyke et al., 2002).

2.2.2 Regional Seismicity

Seismicity between 1985 and 2013 is shown in Figure 2.1 for a region encompassing much of Ontario and Québec and adjacent regions of the United States to the south. There are four regions of higher seismic activity in the southeast and another region with lower rates near Hudson Bay: Southern Ontario Seismic Zone (SOSZ); Western Québec Seismic Zone (WQSZ); Charlevoix Seismic Zone (CSZ); Lower St. Lawrence Zone (LSZ) and the Boothia Ungava Zone (BUZ) (Figure 2.1) (Adam & Basham 1989; Ma & Atkinson 2006; Ma & Eaton 2007). The bulk of eastern Canadian seismicity is concentrated in the CSZ and LSZ, downriver from Québec City (Thomas 2006). Earthquakes in the southern region of Canada have been attributed to a reactivated 500 Ma old rift structure and represented by reverse faulting (Fenton 1994; Dyke et al. 1991; Mazzotti & Townend 2010).

As seen in Figure 2.1, the CSZ has experienced five earthquakes with magnitude (M) greater than 6 since 1663 and approximately ten events of $5 \leq M \leq 6$ since the mid-19th century (Adams & Halchuk 2003). Approximately 450 earthquakes of magnitude greater than 2 occur in the eastern Ontario region each year (Canadian National Earthquake Database (NEDB), Earthquake Canada Online Bulletin, GSC, <http://www.earthquakescanada.nrcan.gc.ca/>). Because of the general tectonic stability of the craton and the fact that the higher seismic activity in these regions occurred at the end of deglaciation, these earthquakes generally are attributed to GIA (Shilts et al. 1992).

2.3 Observations and Method

Here we focus on POLARIS cGPS stations and a selected subset of NRCan stations encompassing a region of eastern Ontario and western Québec that includes the SOSZ, the WQSZ, and the BUZ seismic zones (Figures 2.1 and 2.2).

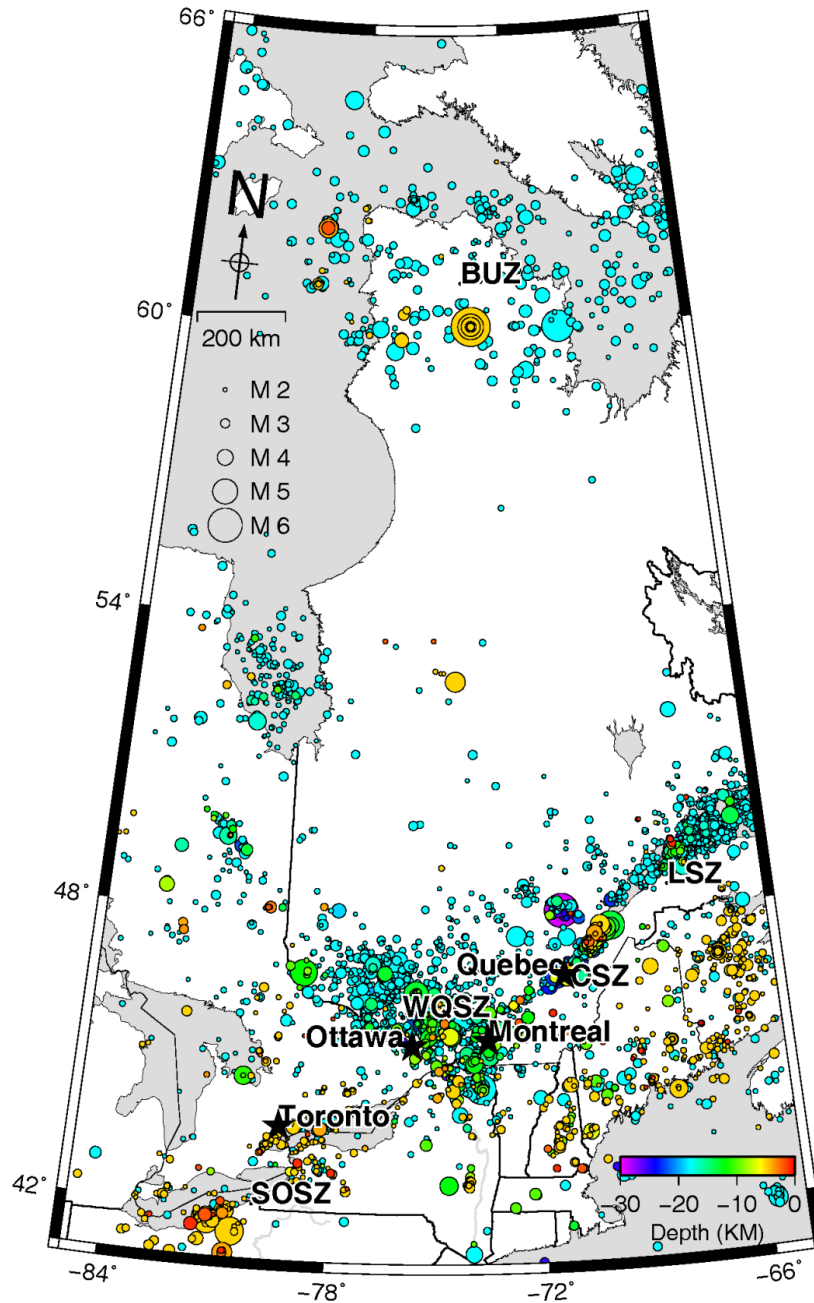


Figure 2.1. Earthquake distribution with magnitudes between 2 and 6 (1985 to 2013) for a portion of eastern North America. Events of magnitude greater than 2, and shallower than 30 km depth, were plotted. The seismic regions are: Southern Ontario Seismic Zone (SOSZ), Western Québec Seismic Zone (WQSZ), Charlevoix Seismic Zone (CSZ), Lower St. Lawrence Zone (LSZ) and Boothia Ungava Zone (BUZ) (GSC 2015).

2.3.1 GPS Data and Analysis

2.3.1.1 Double-Difference Bernese Analysis

Continuous GPS RINEX (Receiver Independent Exchange Format) data from seven stations of the POLARIS network (Eaton et al. 2005) and seven continuous cGPS stations from the NRCan network were acquired, respectively, from the POLARIS GPS database (<ftp://polaris4.es.uwo.ca>) and the Canadian Active Control System (CACS; accessible from <http://www.nrcan.gc.ca/earth-sciences/geomatics/geodetic-reference-systems/data>) (Table 2.1). Stations ALGO, CAGS, VALD, NRC1 and KUUI are IGS reference stations operated by CGS. Figure 2.2 shows the distribution of GPS stations from the two regional networks. Data were downloaded for a maximum five year period starting from 1st January 2008 to 31st December 2012 at a 30-second sampling interval (Table 2.1). This is the five year time period was chosen because the GPS stations INUQ, IVKQ and MATQ from POLARIS network began their positioning in 2008. Decommissioning of the POLARIS stations begin in late 2012. Therefore, in order to ensure consistency in the selection and analysis of the various sub-networks, we included data from 2008 to 2012 (for more detailed of the GPS data see Table A-1 in Appendix A)

The GPS stations use dual-frequency receivers, although their antennas, monuments and receiver types differ among stations (Table A-1). Stations ACTO, TYNO and STCO are continuously operating reference stations (CORS) consisting of reinforced concrete piers approximately three meters deep. All other stations have stainless steel pedestals anchored to bedrock. Data and meta-data collected for processing included precise orbits, clock corrections, and ocean tidal loading effects for each station, station information files, CODE ionosphere models, and a list of fiducial stations to be used as reference stations.

Daily coordinates in ITRF2008 for the GPS sites were computed for various sub-networks (see section 3.1.2) using Bernese 5.0 (Dach 2005; Dach et al. 2007). In this way, we also acquired the information files for additional stations which are not provided in the IGS08 and ITRF2008. A priori coordinates text files were produced at centimeter-

level accuracy using precise point positioning (PPP) for new stations not listed in the original ITRF solutions (<ftp://ftp.unibe.ch/aiub/BSWUSER50/STA>).

Table 2.1. GPS station information for stations from the POLARIS network and those operated by Canadian Geodetic Survey (CGS), Natural Resources Canada. All coordinates are based on WGS84.

| Site | Monument | Latitude | Longitude | Start Date | Location | Receiver Type |
|-------|-------------------------|---------------|---------------|------------|--------------------------------------|-------------------|
| ALGO* | Stainless steel pillars | N45°57'20.85" | W78°04'16.91" | 2001 Jun. | Algonquin Park, ON, Canada | AOA BENCHMARK ACT |
| ACTO | Concrete pier | N43°36'31.32" | W80°03'44.64" | 2004 Nov. | Acton, ON, Canada | NOVATEL1 |
| TYNO | Concrete pier | N43°05'42" | W79°52'12.72" | 2004 Nov. | Tyneside, ON, Canada | NOVATEL2 |
| STCO | Concrete pier | N43°12'34.56" | W79°10'13.8" | 2005 Apr. | Saint Catharines, ON, Canada | NOVATEL3 |
| KLBO | Stainless steel pillars | N45°21'23.76" | W80°12'47.52" | 2009 May | Killbear Provincial Park, ON, Canada | NOVATEL4 |
| MATQ | Stainless steel pillars | N49°45'32.25" | W77°38'15.16" | 2008 Jul. | Matagami La Palce, QC, Canada | TRIMBLE NETRS |
| IVKQ | Stainless steel pillars | N62°25'52.35" | W77°54'39.37" | 2008 Jul. | Ivujivik, QC, Canada | TRIMBLE NETRS |
| INUQ | Stainless steel pillars | N58°27'3.76" | W78°7'6.11" | 2008 Jul. | Inukjuak, QC, Canada | TRIMBLE NETRS |
| KUJ* | Concrete pier | N55°16'42.10" | W77°44'43.56" | 2002 Jul. | Kuujuarapik, QC, Canada | TPS NETG3 |
| VALD* | Concrete pillar | N48°05'49.41" | W77°33'51" | 2001 Nov. | Val D'Or, QC, Canada | TPS NETG3 |
| CAGS* | Pillar | N45°35'06" | W75°48'26.28" | 2000 Feb. | Gatineau, QC, Canada | TRIMBLE NETR8 |
| NRC1* | Steel I Beam | N45°27'15.12" | W75°37'25.68" | 1994 Apr. | Ottawa, Canada | AOA SNR-12 ACT |
| PWEL* | Stainless steel pillars | N43°14'12.23" | W79°13'10.79" | 2002 May | Port Weller, ON, Canada | TRIMBLE NETRS |
| PARY* | Stainless steel pillars | N45°20'18.79" | W80°02'9.2" | 2002 May | Parry Sound, ON, Canada | TRIMBLE NETRS |

* Stations operated by Canadian Geodetic Survey (CGS), Natural Resources Canada

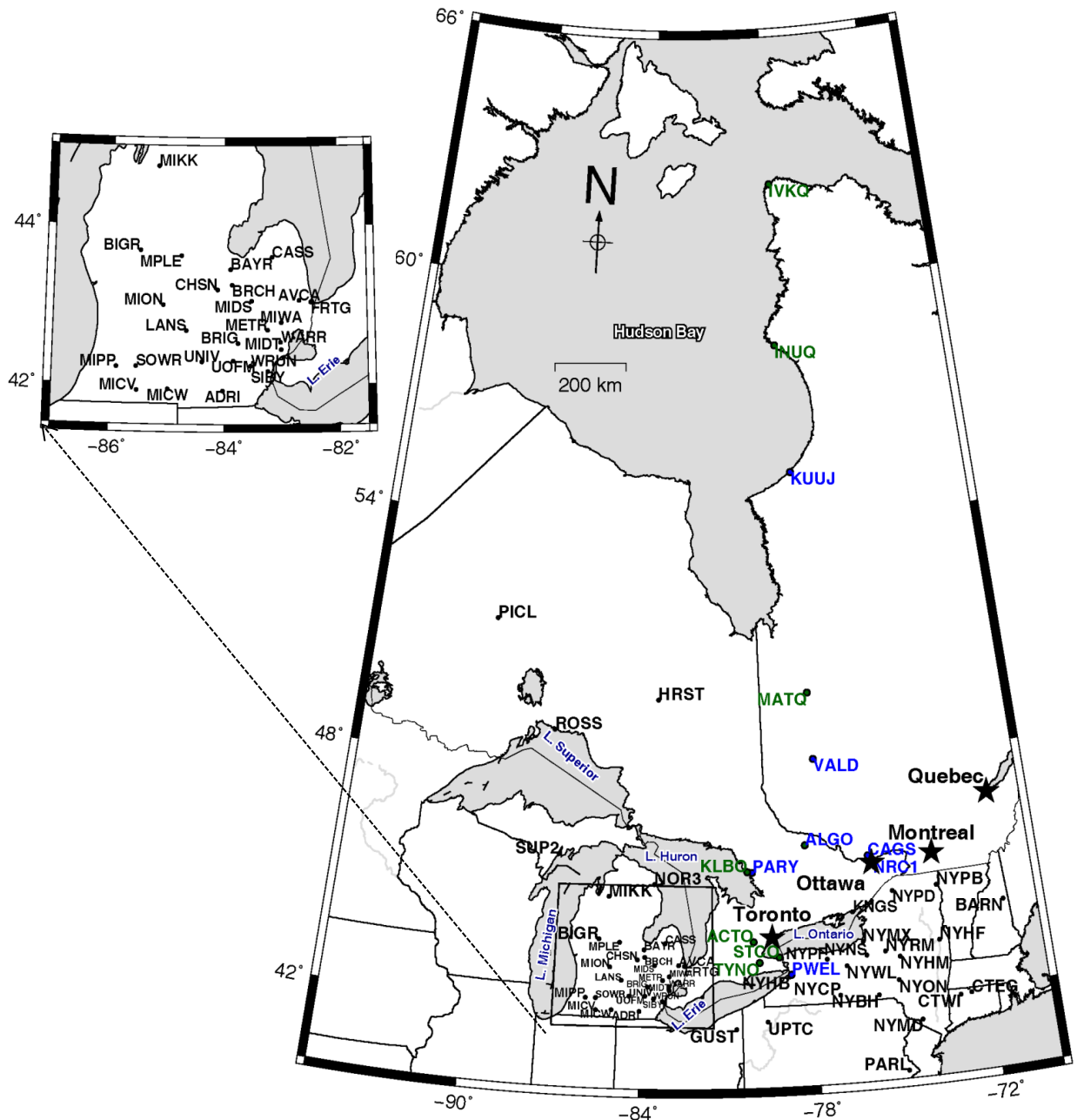


Figure 2.2. Location of continuous GPS stations. Stations used in the Bernese processing and sub-network analysis are shown in green (POLARIS) and blue (permanent NRCan). GPS station motions were also estimated from information downloaded from NGL, as discussed in the text, for these sites and for other stations (black circles). See Tables 2.1 through 2.3 for GPS station details. Inset shows enlargement of stations in the Michigan area.

The Bernese Processing Engine (BPE) (Beutler et al. 2007) was used to compute daily solutions automatically after manual data and supplemental information preparation. In addition, double-difference network solutions were generated and aligned to the ITRF2008 reference frame (Altamimi et al. 2011, 2012). These network solutions are dependent on the baselines of the stations used in the processing. Here we also corrected for the effect of ocean tidal loading on the crustal deformation. The ocean tide loading amplitudes and phase offsets for each station were calculated by considering the GOT00.2 model of Bos & Scherneck (2011) (see Appendix A for more detail).

The final estimated daily coordinates at each station were transformed into the WGS84 system and ITRF2008 for further analysis and the mean and root mean square (RMS) errors of the output coordinates for every epoch of the network solution were estimated. In addition, velocities at each station were estimated and are given in millimeters per year.

2.3.1.2 Bernese Sub-Network Analyses

Given the large aperture of the POLARIS cGPS network and the significant differences in local atmospheric conditions, an intensive study was performed in order to identify the optimal sub-networks for a regional analysis. To achieve this goal, twenty-four possible cGPS sub-network configurations were initially processed and evaluated for a time interval of one year (2012).

Table 2.2 shows a selected set of the sub-networks (campaigns) processed for 2012. In general, the sub-network stations, or campaigns, were separated based on their general location – north versus south - over various region sizes that are reflected in the total number and location of the included stations. In addition to the sub-network analysis, a network which contained all 14 GPS stations also was taken into account. The cGPS station at Algonquin Park (ALGO) was employed as the common reference station between different solutions.

The resulting discrepancy between the estimated coordinates from the published ITRF2008 positions (Altamimi et al. 2011, 2012) and the repeatability RMS errors (standard deviation) of the daily solutions with respect to the combined yearly solution was used to select the two most reliable northern and southern sub-networks for subsequent analysis over the complete time span of five years (See Appendix A). Mean coordinate differences (estimated coordinates minus expected primary coordinates) in the east, north and up components for the GPS stations in each individual solution are given for nine of the twenty-four network solutions (Table 2.2).

The average of the RMS scatter of the residuals also is presented in Table 2.2. Individual solutions with mean RMS repeatabilities of almost 1 mm in the horizontal and 3 mm in the vertical component are at the level of present-day precise measurements (Steigenberger et al. 2012). Sub-network solutions with higher RMS values and large differences from the anticipated coordinates are not considered further (i.e. CAMST4, CAMST8, and CAMST9). From Table 2.2, results for the sub-networks in southern Ontario show small differences from the expected values (CAMST1, CAMST2, CAMST3, CAMST5) and higher differences for sub-networks in northern Ontario and Québec (CAMST4, CAMST6, CAMST7). This is a consequence of the lower density of GPS stations and longer baselines in northern Ontario and Québec. The mean coordinate differences for Campaign 3 (CAMST3 in Table 2.2; southern stations) show good agreement with the expected values: -0.00 mm in east, 0.03 mm in north and 0.01 mm in the up direction.

It should be noted that the differences for the estimated coordinates in northern Ontario are large for most configurations that include INUQ and IVKQ stations. Here, Campaign 7 (northern stations) (CAMST7 in Table 2.2) gives the best agreement with previously reported values with 0.02 mm, 0.01 mm and 0.10 mm mean differences for east, north and up components, respectively. As a result of this detailed investigation, CAMST3 and CAMST7 were considered for further analysis.

Table 2.2. Mean coordinate differences (relative to ITRF2008 values; Altamimi et al., 2012) and RMS repeatabilities for a selection of the 24 sub-networks for 2012. All values are in millimeters.

| Sub-network | Stations | Mean Coordinate Differences | | | RMS repeatability | | |
|---------------|--|-----------------------------|-------|-------|-------------------|-------|------|
| | | East | North | Up | East | North | Up |
| CAMST1 | ACTO, ALGO, KLBO, NRC1, STCO, TYNO | 0.04 | 0.10 | 0.07 | 1.49 | 1.34 | 2.28 |
| CAMST2 | ACTO, ALGO, KLBO, STCO, TYNO | -0.03 | 0.03 | 0.02 | 1.20 | 1.04 | 1.84 |
| CAMST3 | ACTO, STCO, TYNO, ALGO, KLBO, PARY | -0.00 | 0.03 | 0.01 | 1.44 | 1.13 | 2.49 |
| CAMST4 | INUQ, IVKQ, KUUI, MATQ, VALD, ALGO | 0.80 | -2.63 | -1.73 | 1.08 | 2.22 | 4.97 |
| CAMST5 | ACTO, STCO, TYNO, ALGO, MATQ, KLBO | -0.04 | 0.10 | 0.07 | 1.38 | 1.28 | 2.70 |
| CAMST6 | IVKQ, INUQ, MATQ, ALGO, KUUI | 0.14 | 0.01 | 0.18 | 1.19 | 1.05 | 2.83 |
| CAMST7 | IVKQ, INUQ, MATQ, ALGO | 0.02 | 0.01 | 0.10 | 1.18 | 1.35 | 2.94 |
| CAMST8 | ACTO, STCO, TYNO, ALGO, KLBO, PARY, IVKQ, INUQ, MATQ | -1.00 | -0.29 | 1.50 | 1.26 | 1.68 | 2.89 |
| CAMST9 | ACTO, STCO, TYNO, ALGO, KLBO, PARY, IVKQ, INUQ, MATQ, VALD, KUUI, NRC1, CAGS, PWEL | -1.10 | 0.67 | -1.55 | 1.34 | 1.43 | 3.50 |

2.3.1.3 Bernese Time Series Analyses

Figures 2.3 and 2.4 present the time series results in the eastward and northward components for the optimized sub-network analysis. The discontinuities or jumps that occur in the GPS coordinate time series are due to either antenna changes or the changes in the antenna reference point (ARP) value, requiring their detection and removal (Williams 2003). Initial outlier filtering is implemented such that coordinates with jumps of more than 300 mm were removed manually. Subsequently, daily coordinate outliers were removed with an adaptive threshold parameter equal to 0.1, which controls the size of the acceptance region for the outlier filter, based on the median absolute deviation (Hampel 1974; Leys et al. 2013). This parameter corresponds to a maximum acceptable change of 10% in the local scaled median absolute deviation. Finally, we employed a sigma averaging (SIGAVG) method (Goudarzi et al. 2012) for GPS interactive time series analysis (GITSA) in order to remove offsets or discontinuities that exceed 3 mm threshold and result in velocity uncertainty. This approach divides the time series into different segments based on the introduced threshold and detects discontinuities at the border of adjacent segments without jumps.

In order to estimate the station velocities more accurately, the effects of surface loading signals including hydrological, atmosphere and ocean which are significant in the north and up components of GPS time series must be detected and removed (van Dam et al. 2001). Therefore, the station velocities and annual and semi-annual sinusoidal signal, together with their corresponding uncertainties, were computed in the two optimal sub-networks by employing Hector software (Bos et al., 2013) and a complex time correlated-noise model. The complex noise model considered here is a combination of white noise (not time correlated) and power law noise (time correlated), either flicker or random walk noise (Mao et al., 1999). In general, this model is the preferred model (Williams 2008; Mao et al., 1999) (see Appendix A for more details).

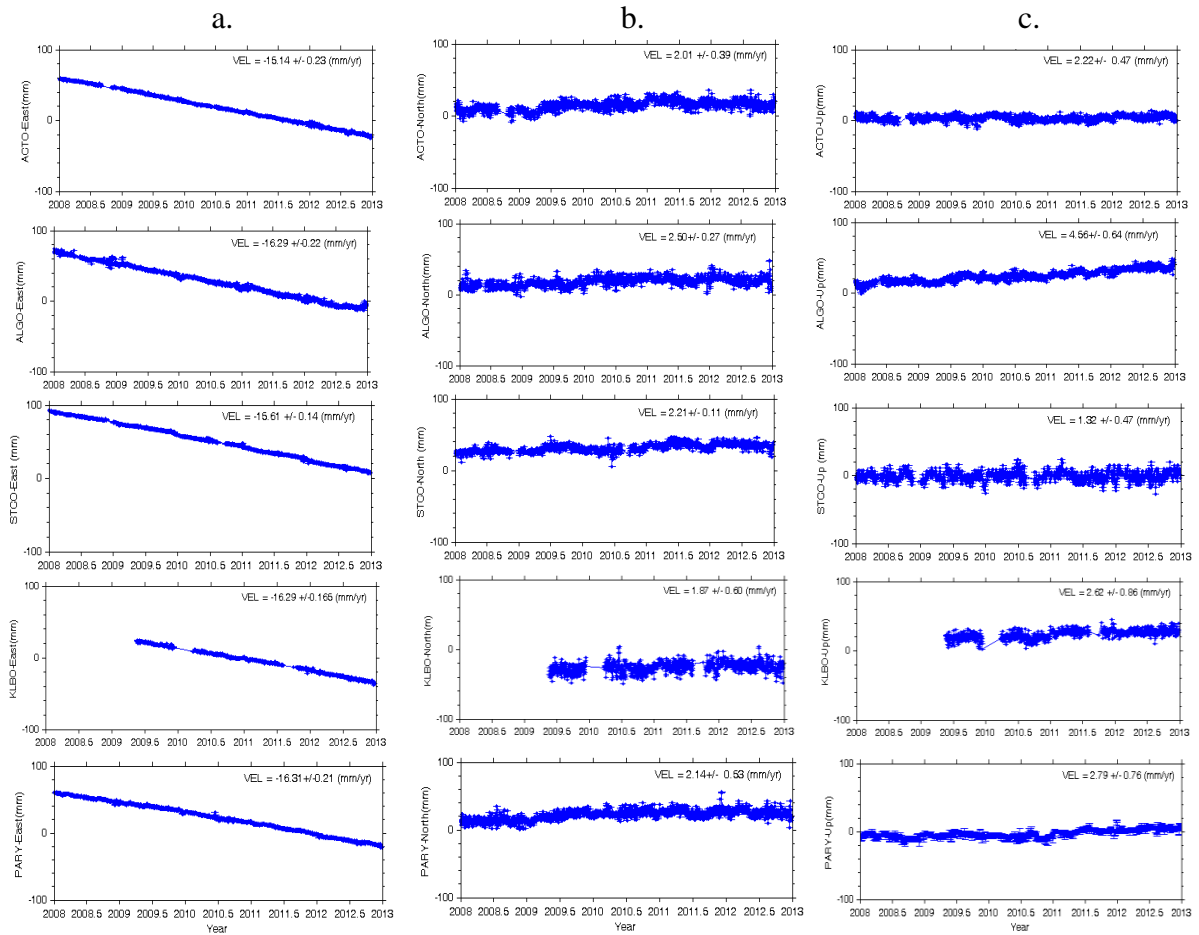


Figure 2.3. Daily position time series plots of five selected sites from the CAMST3 sub-network analysis (Table 2.2). Shown are component time series for three POLARIS sites (ACTO, STCO, and KLBO) and two NRCan sites (ALGO and PARY) (locations in Figure 2.2) for (a) east (positive eastward); b) north (positive northward); and (c) vertical component (positive up). Errors bars for the daily solutions are the standard uncertainties calculated by the Bernese software. The velocities and their corresponding uncertainties calculated from Hector software and employing a complex noise model.

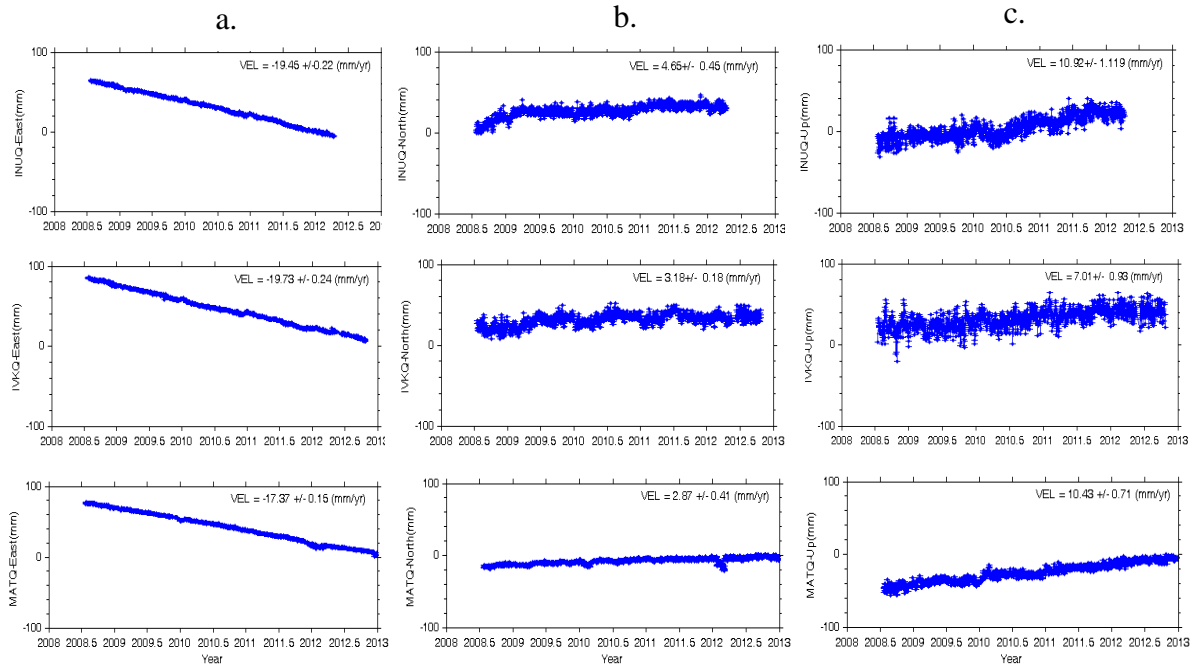


Figure 2.4. Daily position time series plots of selected POLARIS sites from a northern sub-network analysis (CAMST7, Table 2.2) for the (a) east, (b) north, and (c) up components. Symbols and labeling are as in Figure 2.3. The velocities and their corresponding uncertainties calculated from Hector software and employing a complex noise model.

In order to remove the remaining offsets before computing the GPS station velocities, those times at which major offsets (larger than 0.5 mm) occurred and were not eliminated in the previous steps were introduced into the Hector program. This software calculates the offsets and computes the velocities based on their elimination. These discontinuities primarily are observed at the end of each year and are likely caused by servicing of the GPS equipment. Table 2.3 presents the computed velocities and their corresponding uncertainties together with the estimated sinusoidal term for an annual signal. The estimated spectral index is one of the power-law noise parameters and is provided for all three components and stations in Table 2.3. Based on the similarity in the estimated

values for the spectral indices of the three components, the GPS stations in the two optimal networks are affected by a similar source of noise. From the computed mean spectral index value for the Bernese time series, approximately -1.01 ± 0.09 , it can be concluded that the GPS stations are mainly affected by flicker noise.

2.3.1.4 GIPSY Analysis, Nevada Geodetic Laboratory

A wider aperture of stations, located in eastern Ontario and the northern US between longitudes 95° to 70° W and latitudes 40° to 67° N, was chosen in order to provide a broader spatial aperture than the GPS stations considered in the detailed Bernese analysis alone. Fifty-five additional GPS stations are operated by various national and regional agencies including Pennsylvania Department of Transportation (PENNDOT), New York State Department of Transportation (NYSDOT), Ohio Department of Transportation (ODOT), Precision Laser & Instrument (PLI), Connecticut Department of Transportation (CONNDOT), Michigan Department of Transportation (MDOT), Natural Resources Canada, Geodetic Survey Division (NRCan GSD), NOAA Earth System Research Laboratory (NOAA ESRL), and POLARIS. The stations were selected with apparently stable monuments and time periods that were similar to the stations in our smaller network in order to compare GPS-constrained crustal motion to GIA model predictions.

Table 2.4 presents a list of the GPS stations in our study area (Figure 2.2, black circles) with their associated positions and the velocities estimated from the three components time series were processed using GIPSY/OASIS-II software (Webb & Zumberge 1997) available and downloaded from the Nevada Geodetic Laboratory (NGL; <http://geodesy.unr.edu/>) (Blewitt 2014).

Table 2.3. Estimated and predicted velocity of POLARIS stations and the NRCan PARY and ALGO sites from the time series obtained from the two optimal sub-networks. The velocities and their corresponding uncertainties for the three components were calculated from Hector and employing a complex noise model. The seasonal sinusoidal parameters for all three components time series and the spectral indices associated with the power-law noise model are presented below. Predicted velocities are derived from the ITRF2008 angular velocity of the North American (NOAM) plate (Altamimi et al. 2011, 2012).

| SITES | V_{east} | V_{north} | V_{up} | East | | North | | Up | | K_{east} | K_{north} | K_{up} | V_{east}^{NOAM} | V_{north}^{NOAM} |
|-------|-----------------|---------------|----------------|----------------|----------------|----------------|----------------|----------------|----------------|----------------|----------------|----------------|-------------------|--------------------|
| | | | | Cos (mm) | Sin (mm) | Cos (mm) | Sin (mm) | Cos (mm) | Sin (mm) | | | | | |
| ALGO | -16.29 +/- 0.22 | 2.50 +/- 0.27 | 4.56 +/- 0.64 | 0.76 +/- 0.21 | 0.49 +/- 0.22 | 0.94 +/- 0.52 | 1.75 +/- 0.53 | -0.99 +/- 0.50 | -0.61 +/- 0.51 | -0.77 +/- 0.11 | -0.65 +/- 0.10 | -0.96 +/- 0.10 | -16.32 | 3.50 |
| ACTO | -15.14 +/- 0.23 | 2.01 +/- 0.39 | 2.22 +/- 0.47 | 0.01 +/- 0.11 | -0.09 +/- 0.12 | -0.51 +/- 0.74 | 0.27 +/- 0.77 | 0.94 +/- 0.52 | 1.75 +/- 0.53 | -0.88 +/- 0.09 | -1.26 +/- 0.12 | -1.12 +/- 0.13 | -15.90 | 2.80 |
| TYNO | -15.81 +/- 0.11 | 1.75 +/- 0.24 | -1.93 +/- 0.46 | 0.02 +/- 0.18 | 0.24 +/- 0.19 | -0.09 +/- 0.24 | 0.31 +/- 0.24 | 0.12 +/- 0.42 | 0.70 +/- 0.43 | -1.40 +/- 0.08 | -1.53 +/- 0.10 | -0.83 +/- 0.10 | -15.78 | 2.87 |
| STCO | -15.61 +/- 0.14 | 2.21 +/- 0.11 | 1.32 +/- 0.47 | 0.04 +/- 0.14 | -0.93 +/- 0.14 | -1.47 +/- 0.60 | -0.08 +/- 0.62 | 0.94 +/- 0.52 | 1.75 +/- 0.53 | -1.19 +/- 0.09 | -1.30 +/- 0.12 | -1.11 +/- 0.11 | -15.78 | 3.11 |
| KLBO | -16.29 +/- 0.17 | 1.87 +/- 0.60 | 2.62 +/- 0.86 | -0.17 +/- 0.18 | 0.04 +/- 0.18 | 0.46 +/- 0.64 | 2.19 +/- 0.65 | -0.63 +/- 0.68 | 0.62 +/- 0.68 | -0.97 +/- 0.11 | -0.68 +/- 0.22 | -0.85 +/- 0.14 | -16.27 | 2.81 |
| MATQ | -17.37 +/- 0.15 | 2.87 +/- 0.41 | 10.43 +/- 0.71 | -0.45 +/- 0.19 | -0.50 +/- 0.19 | -0.26 +/- 0.34 | -0.35 +/- 0.35 | -0.85 +/- 0.58 | 1.86 +/- 0.60 | -1.23 +/- 0.09 | -1.19 +/- 0.12 | -0.87 +/- 0.10 | -17.05 | 3.65 |
| IVKQ | -19.73 +/- 0.24 | 3.18 +/- 0.18 | 7.01 +/- 0.93 | -0.16 +/- 0.31 | 0.28 +/- 0.32 | -2.61 +/- 0.93 | -1.37 +/- 0.93 | 2.11 +/- 1.10 | -0.19 +/- 1.09 | -1.19 +/- 0.11 | -0.97 +/- 0.10 | -0.67 +/- 0.00 | -19.00 | 3.55 |
| INUQ | -19.45 +/- 0.22 | 4.65 +/- 0.45 | 10.92 +/- 1.12 | -0.09 +/- 0.21 | 0.47 +/- 0.21 | 0.06 +/- 0.82 | 1.45 +/- 0.83 | 1.80 +/- 0.99 | -1.63 +/- 0.98 | -1.00 +/- 0.00 | -0.90 +/- 0.00 | -0.69 +/- 0.00 | -18.51 | 3.48 |
| PARY | -16.31 +/- 0.21 | 2.14 +/- 0.53 | 2.79 +/- 0.76 | -0.00 +/- 0.22 | -0.23 +/- 0.23 | -0.08 +/- 0.62 | 0.22 +/- 0.64 | -0.59 +/- 0.58 | 0.67 +/- 0.60 | -1.25 +/- 0.08 | -0.89 +/- 0.09 | -0.97 +/- 0.09 | -16.27 | 2.81 |

GIPSY/OASIS-II software processes GPS observations in undifferenced mode, unlike the Bernese GPS processing software that uses a double-differencing approach and Quasi Ionosphere Free (QIF) to resolve the ambiguities. Also, in contrast to Bernese, GIPSY models the satellite and receiver clock biases as white noise, and the clock offsets are introduced as known parameters (Kaniuth & Völksen 2003) (See Appendices A and B for more detail).

The Hector program also was used to analyze the time series of these additional stations, and the corresponding velocities and uncertainties were computed. According to Table 2.4, almost all the stations included in this study are affected by similar noise sources, as they have similar spectral indices values that are associated with the power-law noise model. The estimated mean spectral index of the time series of the stations in the three components is approximately -0.79 ± 0.07 .

The estimated station velocities and uncertainties are shown in Figure 2.5 and are compared to the values obtained for the station time series processed in Bernese in the following section.

2.3.2 Comparison of Bernese and NGL Time Series

Comparison of the velocities of the two solutions at each station in Figure 2.5 shows general agreement in the horizontal component, with a disagreement of ± 0.03 mm/year in the east and -0.10 to 0.19 mm/year in the north components. The horizontal velocities presented here are the velocity rates in ITRF2008 (IGS08) reference frame.

Figure 2.6 indicates that the general pattern of the observed velocities in this study (Figure 2.6, red vectors) are consistent with the vertical velocities of the NGL time series for the GPS stations located in eastern Ontario and northern US (Figure 2.6-black vectors), with uplift and subsidence in the north and south of Great Lakes, respectively. The differences between these two solutions at the common stations are in the range of -0.52 to 0.20 mm/yr.

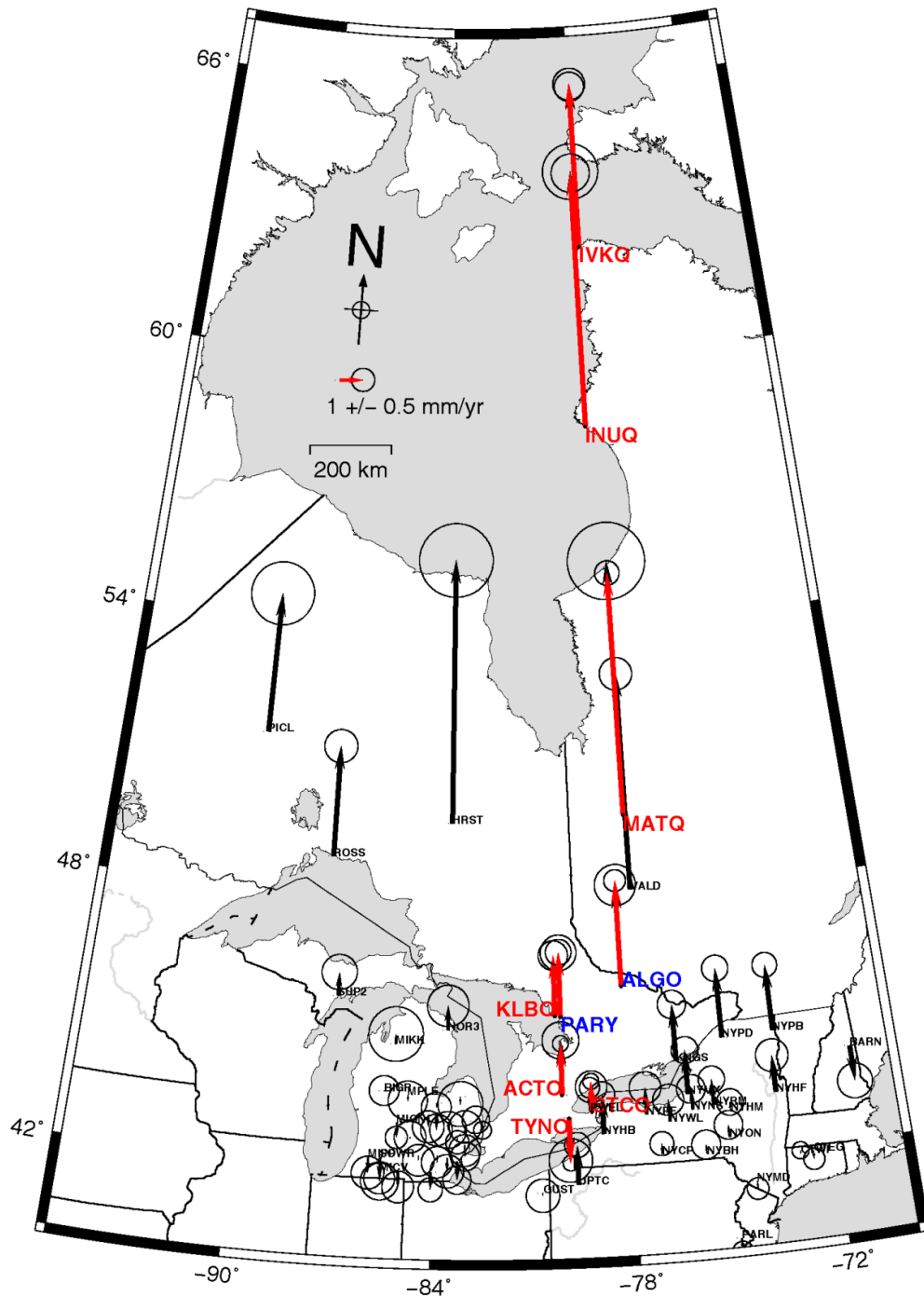


Figure 2.6. Observed vertical velocities (in millimeters per year) for the Bernese (red arrows) and NGL (black arrows) analyses derived from observations spanning January 2008 through December 2012. Error ellipses show 95% confidence interval corresponding to the uncertainties calculated with Hector.

Figure 2.7 presents the scatter plot comparing the GPS station velocities for the two solution and their corresponding uncertainties estimated from combination of white and power-law noise in the three components (east, north and up). It is worthwhile to mention that the average estimated horizontal velocity uncertainties of stations in our study area for 5 years of daily data are approximately 0.3 mm/yr, which are consistent with the computed velocity uncertainties by Dmitriev & Segall (2013). The results show that the computed vertical velocities of the NGL time series vary between -1.83 mm/yr and 11.31 mm/yr, increasing from south to north, with the uncertainties smaller than approximately 2 mm/yr (Table 4). Among of the eight common GPS stations in the two solutions, the vertical velocities show a significant and generally steady rate of uplift near Hudson Bay that decreases southward to the Great Lakes, as expected. The estimated vertical velocity from the Bernese solution ranges from -1.93 ± 0.46 mm/yr at TYNO to 10.92 ± 1.12 mm/yr at INUQ. Results from both solutions are comparable with results of earlier studies (Calais et al. 2006; Sella et al. 2007; Tiampo et al. 2011).

A comparison of the time series for TYNO illustrates the differences in the two results for the longest running continuously operated station with measurable subsidence in the southern Great Lakes region (Figure 2.8). In addition, the average velocity uncertainty reduction under our analysis for all stations in our solution is 0.04 mm/year in the east component, 0.06 mm/year in the north component and 0.59 mm/year in the up component.

In order to compare the GPS station velocities to the GIA predictions, the observed horizontal velocities are corrected for North American plate motions and discussed in the next sections.

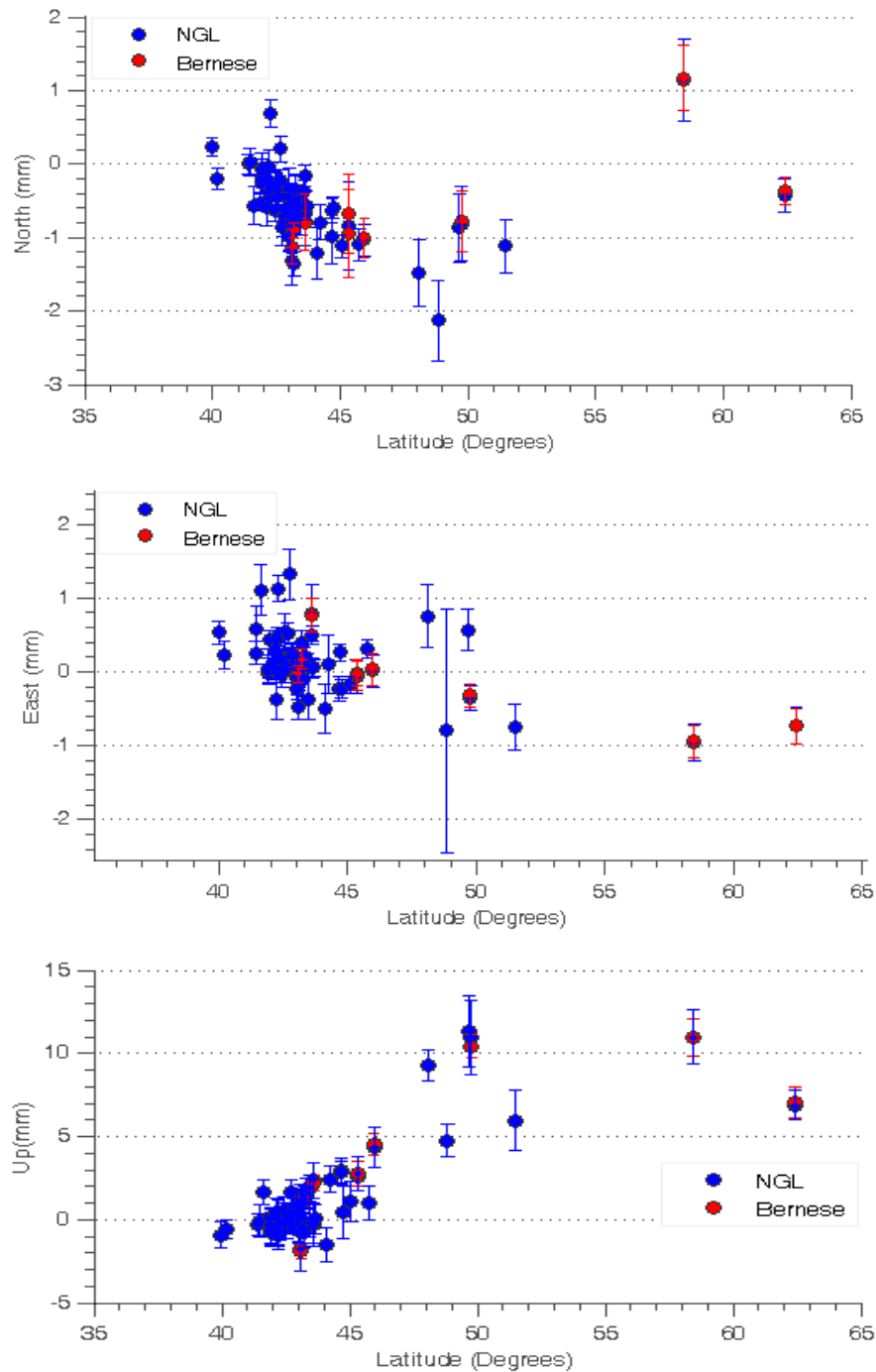


Figure 2.7. Scatter plot of the computed velocities and their uncertainties in the three components, north, east, and up for the GPS stations in both Bernese and NGL solutions. The velocities and their corresponding uncertainties calculated from Hector software and employing a complex noise model. The horizontal axis shows latitude of GPS stations.

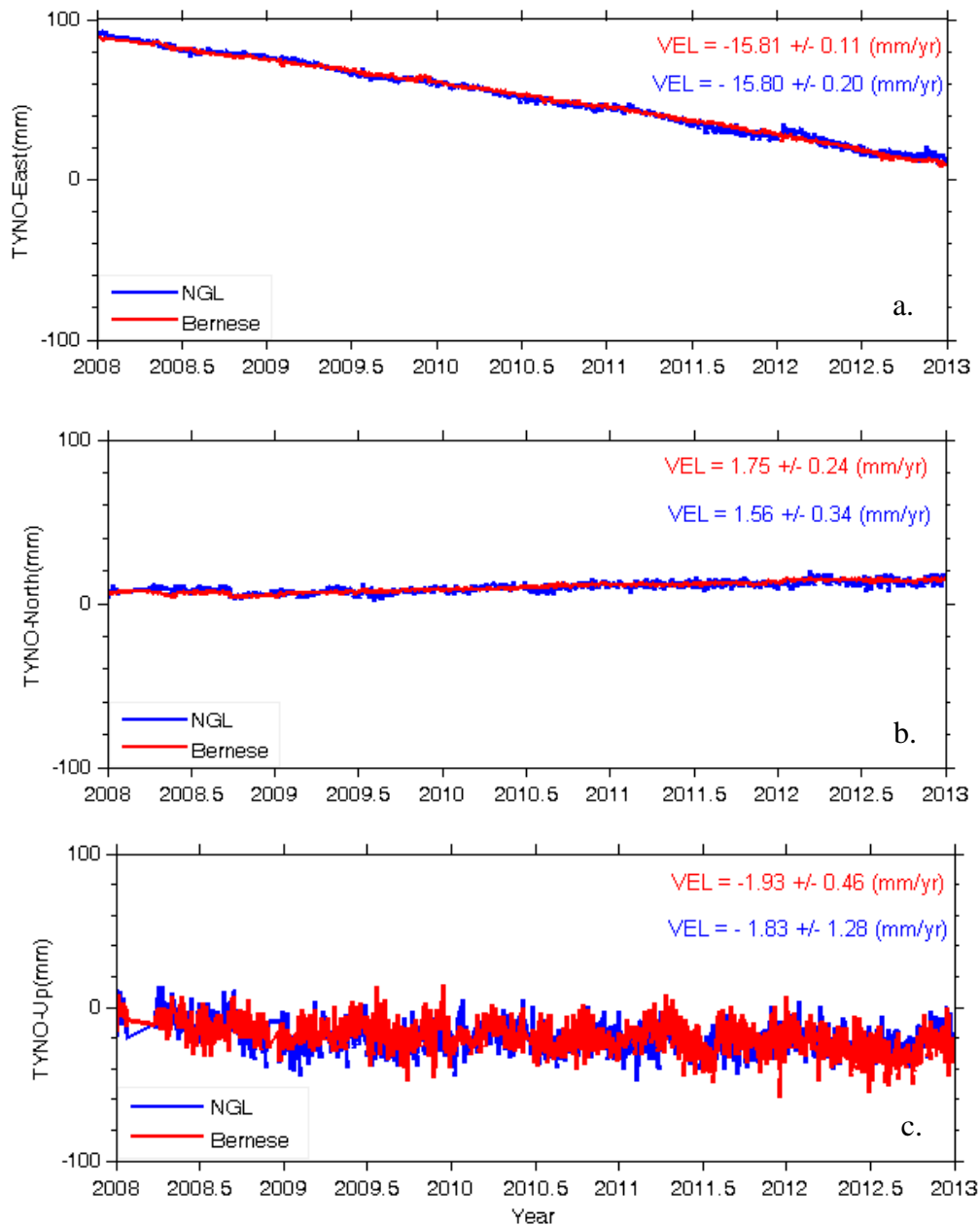


Figure 2.8. Comparison of the (a) east, (b) north, and (c) up position time series for TYNO for the CAMST3 sub-network Bernese analysis to the time series obtained from NGL (<http://geodesy.unr.edu/>). TYNO is a POLARIS station. The velocities and their corresponding uncertainties calculated from Hector software and employing a complex noise model. See Figure 2.2 for location.

2.3.3 ITRF2008 Angular Velocity

The velocities of the North American (NOAM) plate at each site are calculated based on the rotational parameters given by Altamimi et al. (2011, 2012).

Rigid plate motion is given by:

$$\vec{R} \times \vec{X} = \vec{V} \quad (2.1)$$

where, \vec{X} is the vector of site positions and \vec{V} is the site velocity vector. The rotation vector \vec{R} was determined for NOAM on the basis of 44 selected ITRF core stations and without correcting the stations velocities for any GIA models (Altamimi et al. 2011, 2012). In Cartesian coordinates,

$$\Omega \vec{X} = \vec{V} \quad (2.2)$$

The quantity Ω is the Euler matrix containing the rotation parameters, obtained by a least squares adjustment.

$$\Omega = \begin{bmatrix} 0 & -\omega_z & \omega_y \\ \omega_z & 0 & -\omega_x \\ -\omega_y & \omega_x & 0 \end{bmatrix} \quad (2.3)$$

Here, the rotation parameters are $(\omega_x, \omega_y, \omega_z) = (0.035 \pm 0.008, -0.662 \pm 0.009, -0.1 \pm 0.008 \text{ mas/year})$ (1 mas = 10^{-3} seconds of an arc or 1/3,600,000 of a degree) (Altamimi et al. 2011, 2012). The weighted root mean scatter (WRMS) of the pole is 0.21 (mm/yr) E and 0.34 (mm/yr) N. This estimate corresponds to an Euler pole at $-88.0 \pm 0.7^\circ$ longitude, $-7.9 \pm 0.8^\circ$ latitude and rotation rate of $0.184 \pm 0.003^\circ/My$. Therefore, the plate motion rates at the GPS locations are calculated by using Equation 2.2.

The estimated values for the GPS stations in the optimal sub-networks are presented in Table 2.3. As shown by King et al. (2015) and Klemann et al. (2008), the plate rotation estimations contain biases due to unmodeled or mismodeled GIA signals in the velocities of the GPS sites used in the plate rotation estimate. King et al. (2015) have shown that the

maximum biases caused by different GIA models vary from 0.11 and 0.84 mm/yr taking into account the two strategies of subtracting or not subtracting a GIA model of unknown accuracy from the GPS velocities during estimation of the rotation pole. They have also computed the mean maximum biases across all the GIA models for the two strategies, which are equal 0.46 and 0.36 mm/yr.

The critical point is that while this bias is small relative to the plate rotation signal, it can be large when compared to the horizontal GIA velocities. These biases inevitably can be introduced into the GPS horizontal velocities in both magnitude and directional components, particularly in Antarctica and North America regions where the GIA signals are significant (King et al. 2015), and should be taken into account when interpreting the estimated motions.

2.4 GPS Analysis Results

In order to estimate the horizontal velocities at each station with respect to the North American fixed plate, the computed ITRF2008 plate motion (Equation 2.1) is subtracted site-by-site from the estimated horizontal velocities from the two solutions. This difference vector is designated the residual velocity.

The horizontal residual velocity of the Bernese solution in the east direction is approximately 0.8 mm/yr for station ACTO, is nearly zero mm/yr for stations ALGO, TYNO, KLBO and PARY and is about 0.2 mm/yr at station STCO. For the remaining stations, it ranges from -0.32 mm/yr to -0.94 mm/yr. The residual velocity in the north direction for all stations in our solution is approximately -1 mm/yr, with the exception of the two northern stations close to Hudson Bay (IVKQ and INUQ), which are at the level of -0.37 mm/yr and 1.17 mm/yr, respectively. In general, estimates of residual horizontal motion of GPS stations, excluding those stations close to Hudson Bay, show an average rate of approximately 1 mm/year and an azimuth of 167.3 degrees.

In addition to the stations analyzed here, the residual horizontal velocities also were computed for those stations in eastern Ontario and northern US compiled from the NGL website (Table 4). The average of these residual velocities is approximately 0.6 ± 0.3

mm/yr within the considered five year period. The magnitude of these residual velocity values are all within the upper limit of 1.7 mm/yr for non-rigid plate rotation estimated by Sella et al. (2002), and which generally has been considered to be a function of the horizontal GIA.

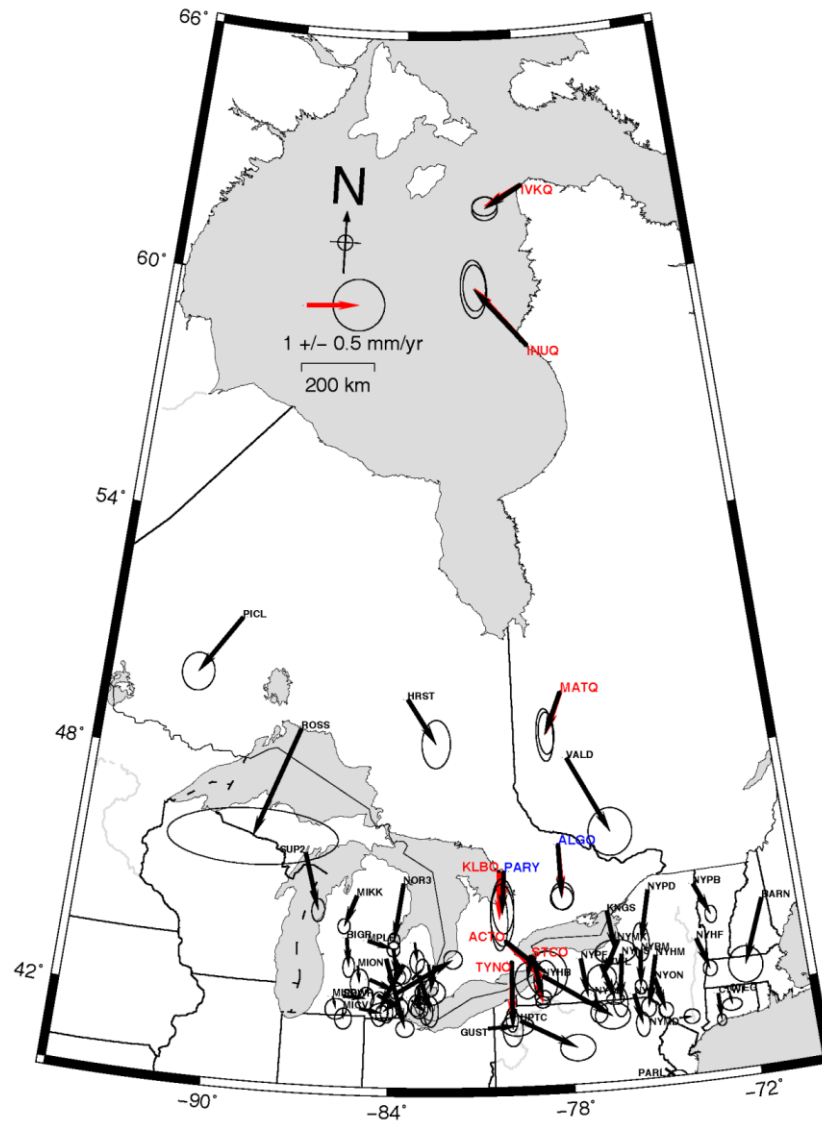


Figure 2.9. Comparison of residual horizontal velocities for the Bernese (red arrows) and NGL (black arrows) analysis after removal of plate motions assuming the ITRF2008 North American pole of rotation (Altamimi et al. 2011, 2012). Error ellipses show 95% confidence interval corresponding to the uncertainties calculated with Hector.

Figure 2.9 shows the observed horizontal motions for the GPS stations after removal of plate motions calculated from the ITRF2008 North American pole of rotation (Section 3.3) for this study (red vectors), which rotate counterclockwise from north to south with amplitudes between 0.67 mm/yr and 1.50 mm/yr. This again is consistent with the given horizontal velocities by NGL (Figure 2.9, black vectors).

2.4.1 Reliability Assessment

Although it is generally assumed that the GPS station velocities estimated from data spanning a period of at least three years are reliable (Blewitt & Lavallee 2002; Bos et al. 2010), modeling of the non-tidal surface loading deformation including variations due to atmosphere, oceanic mass and continental water (soil moisture and snow) mass are important because they increase the uncertainties associated with the velocities in relation to the length of the GPS time series (van Dam et al. 2012). Here, to evaluate the reliability of our results, we compare the uncertainty of the velocities in this study to the velocity errors obtained from power-law noise parameters derived by Santamaria-Gomez & Memin (2015) from the combination of all three loading contributions at the inter-annual band. In their study, the vertical velocity errors from the total mass loading series for the period 2009-2014 in southern Ontario and portions of western Québec, a uniform error of between approximately -0.2 to 0.2 mm/yr was estimated, which is nearly seven times greater than that of the horizontal velocity uncertainties (Santamaria-Gomez & Memin 2015, Figure 3). From the comparison between our velocity uncertainties and their velocity uncertainties results given in their paper, we can conclude that less than 23% of our estimated errors for the vertical velocities are due to the surface loading and this ratio is not larger than 10% for the horizontal velocity errors (Santamaria-Gomez & Memin 2015).

In addition, by considering the vertical velocity errors for the total surface loading from 0.3 to 0.4 mm/yr deduced from Santamaria-Gomez & Memin (2015, Figure 1), we conclude that a maximum of 34 to 45% of our estimated vertical velocity uncertainty is due to the total surface mass loading signal. As stated above, the horizontal velocity error is seven times smaller than that of the vertical velocity errors and the maximum percentage of the error in our calculated horizontal velocity error ranges from 16 to 21%.

2.5 GIA Models

The estimated horizontal and vertical velocities at each station were compared to the predictions of the ICE-5G (Peltier 2004; Peltier & Drummond 2008) and ICE-6G-C (Peltier et al. 2015) GIA models. The different mantle viscosity profiles and lithospheric thicknesses of the ICE-5G and ICE-6G-C loading models considered in this paper are presented in Table 2.5. The models give predictions of vertical and horizontal crustal motions based on a global ice thickness history and a viscoelastic Earth model. Unless otherwise specified, the calculations described here assume a lithospheric thickness of 120 km. The ICE-5G ice load history has an uncertainty of nearly $\pm 20\%$ for ice mass load trend (Geruo et al. 2013; Peltier 2004).

As shown in Figure 2.10, we adapted five different mantle viscosity profiles in which the viscosities vary as a function of radius for the purposes of assessing the sensitivity of the fit of the predictions to the GPS rates. The four mantle viscosity profiles of the ICE-5G loading model includes 10^{21} Pa s, 4×10^{20} and 5×10^{20} for the upper mantle viscosity (UMV), and 2×10^{21} Pa s, 3.2×10^{21} Pa s and 4.5×10^{21} Pa s for the lower mantle viscosity (LMV). The viscosity profile with LMV of 4.5×10^{21} Pa s and UMV of 10^{21} Pa s is designated profile A (Figure 2.10a). The viscosity structure associated with a UMV of 10^{21} Pa s and LMV of 2×10^{21} Pa s which is known as VM1 (Peltier 2004; Sella et al. 2007) is designated profile B in this paper (Figure 2.10b). The viscosity model with UMV of 5×10^{20} Pa s (radius between 5700 and 6281 km), a lower LMV of 3.2×10^{21} Pa s (radius between 3485.5 and 5211 km) and an upper LMV of 1.6×10^{21} Pa s (radius between 5211 and 5700 km), profile C in Figure 2.10a, is known as depth-averaged VM2. VM2 has a lithospheric thickness of 90 km with radius between 6281 km and 6371 km. Profile D in Figure 2.10b refers to the viscosity profile with LMV of 2×10^{21} Pa s and UMV of 4×10^{20} Pa s.

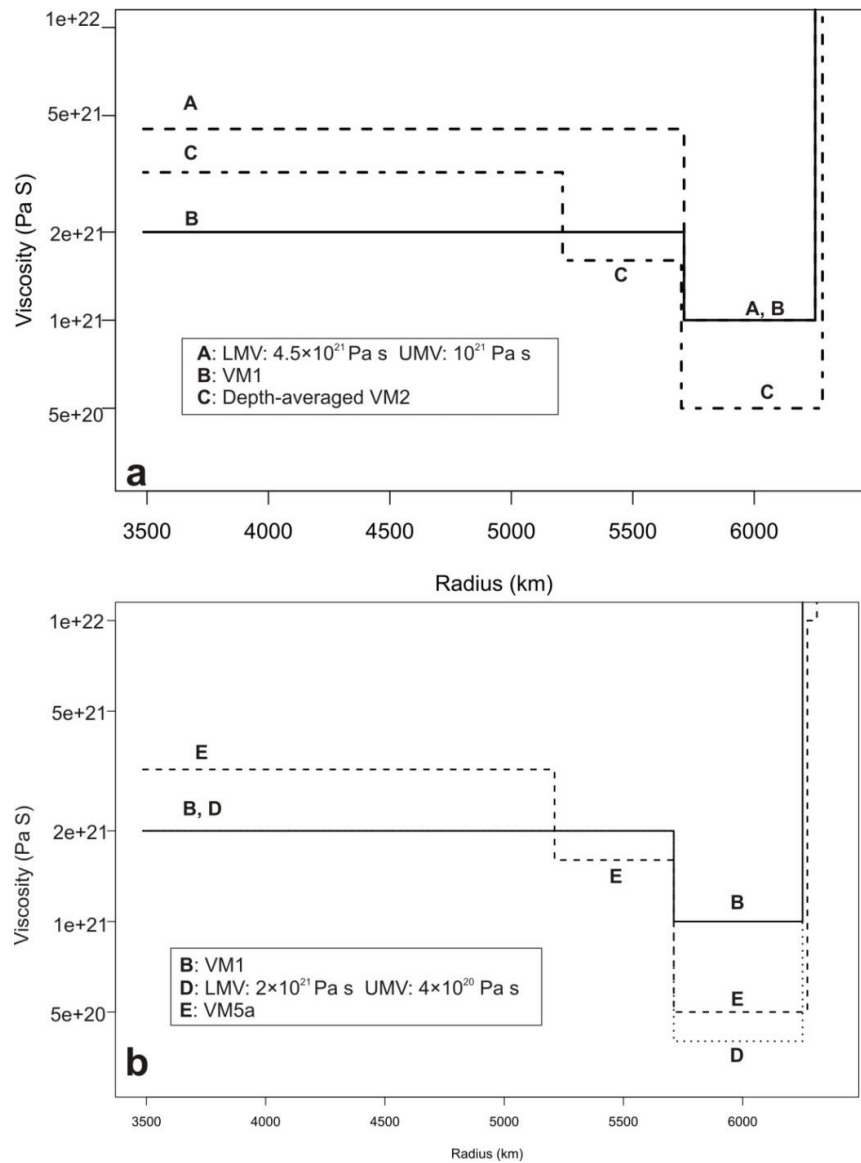


Figure 2.10. Viscosity profiles for the five Earth models considered in this study. Profile B (VM1) has a lower mantle viscosity of 2×10^{21} Pa s and upper mantle viscosity of 10^{21} Pa s and is common to both panels. (a) Profiles A, B, and C, as indicated. (b) Profiles B, D, and E, as indicated. Lithospheric thickness is 120 km, except for Profile C (depth-averaged VM2), which has a thickness of 90 km, and Profile E (VM5a), which has a 40-km thick high-viscosity layer (10^{22} Pa s) beneath the 60-km elastic lithosphere. The ICE-5G (Peltier 2004) loading history was employed to load all of the Earth models except profile E (VM5a), for which ICE-6G (Peltier et al. 2015) was employed.

Calculations were carried out using the methods described by Simon et al. (2016) and references therein. They assume a laterally homogeneous, compressible Maxwell Earth model based on PREM and fully gravitationally self-consistent ocean loading with changing coastlines and incorporation of marine-based ice sheets. ICE-5G was developed assuming the VM2 rheological model (later modified to VM5a) and the fit to other constraints, such as relative sea-level curves, will change for different rheological models. Thus, the comparison carried out here is only indicative. A full analysis would require iterative changes to the ice loading model to optimize the fit to both crustal velocity and relative sea-level measurements and is beyond the scope of this paper.

In addition to the ICE-5G loading models, the most recent update to GIA models, denoted by ICE-6G_C (VM5a) (Peltier et al. 2015), profile E in Figure 2.10b, also is evaluated here. This model uses GPS vertical crustal motion as a constraint (Argus and Heflin 1995; Peltier et al. 2015) and it employs a different ice history model and a different Earth structure to those considered above. The 1×1 grid dataset of this model is available at <http://www.atmos.physics.utoronto.ca/~peltier/data.php>. In addition, this model uses VM5a, a three-layer approximation of the VM2 mantle viscosity profile with an elastic lithosphere of 60 km thickness that is underlain by a 40-km thick high viscosity layer in order to improve the fit of the model on the horizontal observations in North America (Peltier & Drummond 2008) (Figure 2.10b).

2.5.1 Horizontal Component

Figure 2.11 shows the horizontal GIA motion computed for the four mantle viscosity profiles from ICE-5G loading model at the locations of the cGPS stations shown in Figure 2.2.

Comparison of the cGPS horizontal velocities shown in Figure 2.9 with the predicted horizontal velocities computed from ICE-5G in Figure 2.11a-d suggests that the velocity of stations distributed in eastern Ontario and western Québec are directed consistently outward from the Hudson Bay, as expected from the models.

Table 2.4. GPS sites positions and velocities from the position time series at the NGL website (<http://geodesy.unr.edu/>). The spectral index of the power law noise for the three components (K_{east} , K_{north} and K_{up}) and the horizontal velocities (in millimeters per year) are corrected for the North American rigid plate motion given by ITRF2008 (Altamimi et al. 2011, 2012). Pennsylvania Department of Transportation (PENNDOT), New York State Department of Transportation (NYSDOT), Ohio Department of Transportation (ODOT), Precision Laser & Instrument (PLI), Connecticut Department of Transportation (CONNDOT), Michigan Department of Transportation (MDOT), Natural Resources Canada, Geodetic Survey Division (NRCan GSD), NOAA Earth System Research Laboratory (NOAA ESRL), and POLARIS.

| Station | Lon. (degree) | Lat. (degree) | Up (meter) | V_{east} (mm/yr) | V_{north} (mm/yr) | V_{up} (mm/yr) | K_{east} | K_{north} | K_{up} | Agency | Monument |
|-------------|---------------|---------------|------------|--------------------|---------------------|-------------------|-------------------|-------------------|-------------------|---------|--------------------------|
| YORK | -76.74 | 39.99 | 98.41 | 0.54+/- 0.16 | 0.23+/- 0.12 | -0.94+/- 0.79 | -0.61 +/- 0.15 | -0.62 +/- 0.16 | -0.68 +/- 0.00 | PENNDOT | Concrete |
| PARL | -75.06 | 40.20 | 75.29 | 0.23+/- 0.19 | -0.2+/- 0.15 | -0.58 +/- 0.60 | -0.80 +/- 0.11 | -0.73 +/- 0.13 | -0.62 +/- 0.00 | PENNDOT | Concrete |
| NYMD | -74.44 | 41.41 | 126.97 | 0.25+/- 0.16 | 0.0+/- 0.14 | -0.33+/- 0.64 | -0.77 +/- 0.13 | -0.64 +/- 0.12 | -0.66 +/- 0.00 | NYSDOT | ALLUMINUM MAST |
| GUST | -80.72 | 41.46 | 282.02 | 0.57+/- 0.31 | 0.03+/- 0.19 | -0.11+/- 0.98 | -1.01 +/- 0.10 | -0.83 +/- 0.12 | -0.79 +/- 0.00 | ODOT | Concrete |
| UPTC | -79.66 | 41.63 | 342.07 | 1.1+/- 0.34 | -0.57+/- 0.26 | 1.69+/- 0.74 | -1.0 +/- 0.11 | -0.87 +/- 0.13 | -0.69 +/- 0.00 | PLI | Steel |
| CTWI | -73.07 | 41.90 | 190.90 | 0.01+/- 0.09 | -0.52+/- 0.11 | 0.13 +/- 0.50 | -0.43 +/- 0.00 | -0.47 +/- 0.00 | -0.58 +/- 0.00 | CONNDOT | Galvanized Steel Pole |

Table 2.4. Continued

| Station | Lon. (degree) | Lat. (degree) | Up (meter) | V _{east} (mm/yr) | V _{north} (mm/yr) | V _{up} (mm/yr) | K _{east} | K _{north} | K _{up} | Agency | Monument |
|---------|------------------|------------------|---------------|------------------------------|-------------------------------|----------------------------|-------------------|--------------------|-------------------|---------|--------------------------|
| ADRI | -84.02 | 41.92 | 205.96 | -0.03+/- 0.12 | -0.05+/- 0.2 | -0.74 +/- 0.71 | -0.63 +/- 0.12 | -0.80 +/- 0.12 | -0.72 +/- 0.00 | MDOT | PILLAR |
| CTEG | -72.70 | 41.92 | 29.06 | 0.03+/- 0.19 | -0.26+/- 0.12 | -0.36+/- 0.62 | -0.66 +/- 0.00 | -0.62 +/- 0.14 | -0.63 +/- 0.00 | CONNDOT | Galvanized Steel Pole |
| MICV | -85.52 | 41.92 | 233.44 | 0.01+/- 0.16 | -0.19+/- 0.2 | -0.43 +/- 1.11 | -0.78 +/- 0.12 | -0.77 +/- 0.11 | -0.86 +/- 0.00 | MDOT | concrete monument |
| MICW | -84.98 | 41.94 | 266.39 | 0.44+/- 0.12 | -0.08+/- 0.15 | -0.70 +/- 0.93 | -0.59 +/- 0.00 | -0.64 +/- 0.00 | -0.79 +/- 0.00 | MDOT | PILLAR |
| NYBH | -75.83 | 42.11 | 311.88 | 0.12+/- 0.13 | -0.6+/- 0.24 | 0.41+/- 0.85 | -0.61 +/- 0.00 | -0.95 +/- 0.13 | -0.76 +/- 0.00 | NYSDOT | Aluminum Mast |
| SIBY | -83.24 | 42.17 | 152.51 | 0.28+/- 0.13 | -0.23+/- 0.24 | -0.8+/- 0.83 | -0.62 +/- 0.11 | -0.93 +/- 0.12 | -0.76 +/- 0.00 | MDOT | PILLAR |
| NYCP | -77.14 | 42.19 | 276.44 | 0.06+/- 0.16 | -0.37+/- 0.2 | 0.45+/- 0.70 | -0.71 +/- 0.12 | -0.81 +/- 0.13 | -0.69 +/- 0.00 | NYSDOT | Aluminum Mast |
| MIPP | -85.88 | 42.22 | 199.02 | 0.07+/- 0.21 | -0.24+/- 0.2 | -0.68+/- 0.96 | -0.90 +/- 0.12 | -0.81 +/- 0.11 | -0.80 +/- 0.00 | MDOT | concrete |
| SOWR | -85.53 | 42.23 | 231.47 | 0.44+/- 0.15 | -0.03+/- 0.22 | -0.93 +/- 0.90 | -0.73+/- 0.12 | -0.84 +/- 0.10 | -0.79 +/- 0.00 | MDOT | CORS |
| WRUN | -83.54 | 42.24 | 186.59 | -0.38+/- 0.27 | -0.28+/- 0.17 | -0.56 +/- 0.98 | -0.95 +/- 0.11 | -0.76 +/- 0.13 | -0.81 +/- 0.00 | MDOT | PILLAR |
| UNIV | -84.39 | 42.29 | 264.53 | 0.48+/- 0.12 | -0.25+/- 0.17 | -0.21 +/- 0.93 | -0.63 +/- 0.13 | -0.73 +/- 0.11 | -0.79 +/- 0.00 | MDOT | PILLAR |

Table 2.4. Continued

| Station | Lon. (degree) | Lat. (degree) | Up (meter) | V _{east} (mm/yr) | V _{north} (mm/yr) | V _{up} (mm/yr) | K _{east} | K _{north} | K _{up} | Agency | Monument |
|-------------|------------------|------------------|---------------|------------------------------|-------------------------------|----------------------------|-------------------|--------------------|-------------------|--------|------------------|
| UOFM | -83.84 | 42.30 | 242.63 | 1.12+/- 0.18 | 0.69+/- 0.18 | -0.29 +/- 0.92 | -0.83 +/- 0.12 | -0.75 +/- 0.12 | -0.79 +/- 0.00 | MDOT | PILLAR |
| NYON | -75.11 | 42.44 | 305.86 | 0.15+/- 0.14 | -0.63+/- 0.15 | 0.52 +/- 0.84 | -0.66 +/- 0.12 | -0.68 +/- 0.12 | -0.75 +/- 0.00 | NYSDOT | Aluminum Mast |
| MIDT | -83.01 | 42.44 | 161.17 | -0.04+/- 0.16 | -0.31+/- 0.21 | -0.31 +/- 0.84 | -0.74 +/- 0.12 | -0.80 +/- 0.11 | -0.77 +/- 0.00 | MDOT | PILLAR |
| BRIG | -83.76 | 42.52 | 261.34 | 0.54+/- 0.24 | -0.33+/- 0.21 | 0.11 +/- 0.85 | -0.91 +/- 0.11 | -0.82 +/- 0.12 | -0.75 +/- 0.00 | MDOT | PILLAR |
| WARR | -83.02 | 42.53 | 157.16 | 0.02+/- 0.17 | -0.45+/- 0.18 | -0.22+/- 0.93 | -0.78 +/- 0.13 | -0.82 +/- 0.13 | -0.80 +/- 0.00 | MDOT | PILLAR |
| LANS | -84.66 | 42.67 | 241.12 | 0.52+/- 0.14 | -0.22+/- 0.15 | 0.04 +/- 0.93 | -0.68 +/- 0.12 | -0.67 +/- 0.12 | -0.81 +/- 0.00 | MDOT | PILLAR |
| METR | -83.24 | 42.69 | 260.52 | 0.2+/- 0.12 | 0.21+/- 0.18 | -0.18 +/- 0.68 | -0.59 +/- 0.00 | -0.77 +/- 0.12 | -0.69 +/- 0.00 | MDOT | PILLAR |
| NYHB | -78.85 | 42.72 | 211.32 | 1.32+/- 0.34 | -0.85+/- 0.26 | 1.69+/- 0.74 | -1.01 +/- 0.11 | -0.87 +/- 0.13 | -0.69 +/- 0.00 | NYSDOT | Aluminum Mast |
| MIWA | -83.01 | 42.78 | 203.47 | 0.24+/- 0.14 | -0.7+/- 0.3 | 0.31 +/- 0.94 | -0.72 +/- 0.13 | -0.98 +/- 0.11 | -0.80 +/- 0.00 | MDOT | PILLAR |
| NYWL | -76.85 | 42.90 | 108.79 | 0.22+/- 0.17 | -0.68+/- 0.11 | 0.92+/- 0.91 | -0.82 +/- 0.13 | -0.54 +/- 0.00 | -0.77 +/- 0.00 | NYSDOT | Aluminum Mast |
| MION | -85.07 | 43.00 | 222.59 | 0.04+/- 0.18 | -0.34+/- 0.28 | -0.64 +/- 0.65 | -0.76 +/- 0.13 | -0.92 +/- 0.13 | -0.62 +/- 0.00 | MDOT | PILLAR |
| NYHM | -75.00 | 43.02 | 94.10 | -0.23+/- 0.14 | -0.99+/- 0.18 | 0.36 +/- 0.77 | -0.71 +/- 0.14 | -0.67 +/- 0.12 | -0.71 +/- 0.00 | NYSDOT | Aluminum Mast |

Table 2.4. Continued

| Station | Lon. (degree) | Lat. (degree) | Up (meter) | V _{east} (mm/yr) | V _{north} (mm/yr) | V _{up} (mm/yr) | K _{east} | K _{north} | K _{up} | Agency | Monument |
|---------|------------------|------------------|---------------|------------------------------|-------------------------------|----------------------------|-------------------|--------------------|-------------------|--------------|----------------------------|
| FRTG | -82.49 | 43.04 | 156.47 | -0.08+/- 0.29 | -0.53+/- 0.24 | -0.34 +/- 0.52 | -1.03 +/- 0.13 | -0.89 +/- 0.11 | -0.59 +/- 0.00 | MDOT | PILLAR |
| MIDS | -83.52 | 43.05 | 212.91 | -0.47+/- 0.17 | -0.86+/- 0.33 | -0.36 +/- 1.08 | -0.79 +/- 0.12 | -1.06 +/- 0.10 | -0.83 +/- 0.00 | MDOT | PILLAR |
| AVCA | -82.69 | 43.06 | 200.48 | 0.06+/- 0.13 | -0.44+/- 0.18 | 0.07+/- 0.80 | -0.63 +/- 0.00 | -0.76 +/- 0.11 | -0.74 +/- 0.00 | MDOT | PILLAR |
| NYPF | -77.53 | 43.09 | 112.32 | 0.1+/- 0.15 | -0.75+/- 0.14 | 1.15 +/- 0.93 | -0.74 +/- 0.12 | -0.69 +/- 0.12 | -0.79 +/- 0.00 | NYSDOT | Aluminum Mast |
| TYNO | -79.87 | 43.10 | 168.30 | -0.02+/- 0.2 | -1.31+/- 0.34 | -1.83 +/- 1.28 | -0.82 +/- 0.11 | -1.00 +/- 0.10 | -0.86 +/- 0.00 | Polaris | Concrete pier |
| NYNS | -76.14 | 43.12 | 97.41 | -0.1+/- 0.14 | -0.92+/- 0.29 | 0.89 +/- 0.84 | -0.73 +/- 0.12 | -0.95 +/- 0.11 | -0.74 +/- 0.00 | NYSDOT | Aluminum Mast |
| NYRM | -75.49 | 43.18 | 127.36 | -0.06+/- 0.12 | -0.71+/- 0.14 | 1.10 +/- 0.77 | -0.60 +/- 0.12 | -0.71 +/- 0.12 | -0.72 +/- 0.00 | NYSDOT | Aluminum Mast |
| CHSN | -84.12 | 43.19 | 165.12 | 0.39+/- 0.18 | -1.35+/- 0.16 | -0.51 +/- 0.93 | -0.80 +/- 0.11 | -0.68 +/- 0.11 | -0.79 +/- 0.00 | MDOT | PILLAR |
| STCO | -79.17 | 43.21 | 57.32 | 0.18+/- 0.16 | -0.8+/- 0.13 | 1.09 +/- 0.93 | -0.78 +/- 0.13 | -0.59 +/- 0.12 | -0.75 +/- 0.00 | Polaris | Concrete pier |
| PWEL | -79.22 | 43.24 | 43.90 | -0.09+/- 0.24 | -0.49+/- 0.35 | 0.99+/- 0.59 | -0.93 +/- 0.13 | -1.08 +/- 0.12 | -0.62 +/- 0.00 | NRCan GSD | Stainless steel pillars |

Table 2.4. Continued

| Station | Lon. (degree) | Lat. (degree) | Up (meter) | V _{east} (mm/yr) | V _{north} (mm/yr) | V _{up} (mm/yr) | K _{east} | K _{north} | K _{up} | Agency | Monument |
|---------|------------------|------------------|---------------|------------------------------|-------------------------------|----------------------------|-------------------|--------------------|-------------------|-----------|----------------------------|
| BRCH | -83.87 | 43.25 | 160.00 | 0.18+/- 0.16 | -0.35+/- 0.18 | -0.76 +/- 0.93 | -0.68 +/- 0.00 | -0.75 +/- 0.11 | -0.78 +/- 0.00 | MDOT | PILLAR |
| NYHF | -73.57 | 43.32 | 63.34 | 0.2+/- 0.14 | -0.61+/- 0.15 | 1.57 +/- 0.96 | -0.66 +/- 0.15 | -0.63 +/- 0.12 | -0.73 +/- 0.00 | NYSDOT | Aluminum Mast |
| BAYR | -83.89 | 43.45 | 148.89 | 0.08+/- 0.17 | -0.56+/- 0.16 | -0.18 +/- 0.88 | -0.80 +/- 0.12 | -0.72 +/- 0.12 | -0.79 +/- 0.00 | MDOT | PILLAR |
| NYMX | -76.23 | 43.47 | 89.98 | -0.37+/- 0.28 | -0.7+/- 0.26 | 1.89+/- 0.78 | -1.00 +/- 0.10 | -0.90 +/- 0.11 | -0.73 +/- 0.00 | NYSDOT | Aluminum Mast |
| CASS | -83.16 | 43.60 | 196.84 | 0.05+/- 0.14 | -0.37+/- 0.23 | -0.31 +/- 1.32 | -0.58 +/- 0.00 | -0.84 +/- 0.13 | -0.83 +/- 0.00 | MDOT | PILLAR |
| ACTO | -80.06 | 43.61 | 330.38 | 0.79+/- 0.38 | -0.67+/- 0.45 | 2.35 +/- 1.08 | -1.10 +/- 0.10 | -1.15 +/- 0.12 | -0.79 +/- 0.00 | Polaris | Concrete pier |
| MPLP | -84.76 | 43.62 | 200.64 | 0.5+/- 0.12 | -0.15+/- 0.15 | -0.25+/- 1.14 | -0.61 +/- 0.00 | -0.67 +/- 0.12 | -0.85 +/- 0.00 | MDOT | PILLAR |
| BIGR | -85.49 | 43.68 | 284.49 | 0.06+/- 0.11 | -0.56+/- 0.2 | 0.03+/- 0.88 | -0.55 +/- 0.00 | -0.82 +/- 0.11 | -0.79 +/- 0.00 | MDOT | PILLAR |
| BARN | -71.16 | 44.10 | 139.66 | -0.5+/- 0.33 | -1.22+/- 0.35 | -1.52 +/- 1.02 | -0.84 +/- 0.13 | -0.84 +/- 0.14 | -0.74 +/- 0.12 | NOAA ESRL | Geodetic |
| KNGS | -76.52 | 44.22 | 48.85 | 0.1 +/- 0.4 | -0.79+/- 0.24 | 2.44+/- 0.83 | -1.16 +/- 0.12 | -0.92 +/- 0.11 | -0.74 +/- 0.00 | NRCan GSD | Stainless steel pillars |

Table 2.4. Continued

| Station | Lon. (degree) | Lat. (degree) | Up (meter) | V _{east} (mm/yr) | V _{north} (mm/yr) | V _{up} (mm/yr) | K _{east} | K _{north} | K _{up} | Agency | Monument |
|-------------|------------------|------------------|---------------|------------------------------|-------------------------------|----------------------------|-------------------|--------------------|-------------------|--------------|----------------------------|
| NYPD | -75.04 | 44.65 | 108.69 | -0.23+/- 0.16 | -0.99+/- 0.37 | 2.97+/- 0.77 | -0.81 +/- 0.13 | -1.02 +/- 0.10 | -0.73 +/- 0.00 | NYSDOT | Aluminum Mast |
| NYPB | -73.45 | 44.68 | 29.01 | 0.27+/- 0.11 | -0.63+/- 0.17 | 2.82 +/- 0.73 | -0.61 +/- 0.13 | -0.82 +/- 0.13 | -0.69 +/- 0.00 | NYSDOT | Aluminum Mast |
| MIKK | -85.19 | 44.74 | 288.36 | -0.23+/- 0.12 | -0.6+/- 0.14 | 0.42 +/- 1.60 | -0.58 +/- 0.00 | -0.60 +/- 0.00 | -0.94 +/- 0.00 | MDOT | PILLAR |
| NOR3 | -83.57 | 45.07 | 174.47 | -0.17+/- 0.12 | -1.11+/- 0.16 | 1.05+/- 1.21 | -0.60 +/- 0.12 | -0.71 +/- 0.11 | -0.88 +/- 0.00 | MDOT | PILLAR |
| PARY | -80.04 | 45.34 | 145.02 | -0.06+/- 0.23 | -0.84+/- 0.6 | 2.76 +/- 1.05 | -0.87 +/- 0.11 | -1.23 +/- 0.12 | -0.83 +/- 0.00 | NRCan GSD | Stainless steel pillars |
| SUP2 | -87.07 | 45.75 | 153.84 | 0.31+/- 0.12 | -1.09+/- 0.22 | 1.01+/- 1.03 | -0.59 +/- 0.00 | -0.84 +/- 0.11 | -0.83 +/- 0.00 | MDOT | PILLAR |
| ALGO | -78.07 | 45.96 | 200.90 | 0.01+/- 0.22 | -1.04+/- 0.22 | 4.36 +/- 1.21 | -0.76 +/- 0.00 | -0.77 +/- 0.11 | -0.90 +/- 0.00 | NRCan GSD | Stainless steel pillars |

Table 2.4. Continued

| Station | Lon. (degree) | Lat. (degree) | Up (meter) | V _{east} (mm/yr) | V _{north} (mm/yr) | V _{up} (mm/yr) | K _{east} | K _{north} | K _{up} | Agency | Monument |
|-------------|------------------|------------------|---------------|------------------------------|-------------------------------|----------------------------|-------------------|--------------------|-------------------|--------------|----------------------------|
| VALD | -77.57 | 48.10 | 312.80 | 0.75+/- 0.42 | -1.48+/- 0.46 | 9.28 +/- 0.95 | -0.90 +/- 0.00 | -0.95 +/- 0.10 | -0.80 +/- 0.00 | NRCan GSD | concrete pillar |
| ROSS | -87.52 | 48.83 | 149.84 | -0.8+/- 1.66 | -2.13+/- 0.54 | 4.75 +/- 0.97 | -1.52 +/- 0.12 | -1.15 +/- 0.11 | -0.76 +/- 0.00 | NRCan GSD | CORS |
| HRST | -83.51 | 49.67 | 228.41 | 0.56+/- 0.27 | -0.87+/- 0.47 | 11.31+/- 2.16 | -0.82 +/- 0.10 | -1.00 +/- 0.09 | -1.03 +/- 0.00 | NRCan GSD | Concrete |
| MATQ | -77.64 | 49.76 | 239.95 | -0.35+/- 0.16 | -0.81+/- 0.51 | 10.95 +/- 2.27 | -0.65 +/- 0.00 | -1.09 +/- 0.11 | -1.01 +/- 0.00 | Polaris | Stainless steel pillars |
| PICL | -90.16 | 51.48 | 315.10 | -0.75+/- 0.31 | -1.12+/- 0.37 | 5.97+/- 1.85 | -0.89 +/- 0.10 | -0.90 +/- 0.00 | -1.03 +/- 0.00 | NRCan GSD | Concrete |
| INUQ | -78.12 | 58.45 | -23.77 | -0.96+/- 0.25 | 1.14+/- 0.56 | 10.99+/- 1.62 | -0.71 +/- 0.00 | -1.07 +/- 0.11 | -0.85 +/- 0.00 | Polaris | Stainless steel pillars |
| IVKQ | -77.91 | 62.42 | -20.36 | -0.73+/- 0.25 | -0.42+/- 0.23 | 6.89+/- 0.85 | -0.80 +/- 0.11 | -0.70 +/- 0.12 | -0.69 +/- 0.00 | Polaris | Stainless steel pillars |
| MATQ | -77.64 | 49.76 | 239.95 | -0.35+/- 0.16 | -0.81+/- 0.51 | 10.95 +/- 2.27 | -0.65 +/- 0.00 | -1.09 +/- 0.11 | -1.01 +/- 0.00 | Polaris | Stainless steel pillars |

Note that although the additional stations (see Table 2.4) included here in order to provide a spatially denser comparison with the GIA models are somewhat noisy, they agree with the same general direction of motion. The amplitudes of the observed horizontal motion for the stations are much smaller than those of the GIA models with high UMV 4×10^{20} Pa s and 5×10^{20} Pa s (Figure 2.11c, d). Comparison of profiles A and B of the GIA models with our observed horizontal velocities shows small discrepancy for the stations in the southern region. For profile A, the differences range from -1.25 mm/yr. to 0.52 mm/yr (Figure 2.11a). For GIA model VM1 (Figure 2.11b), profile B, the differences range from -0.47 mm/yr. to 0.22 mm/yr. Comparison of the horizontal velocities in the predicted ICE-5G models with the observed rates at INUQ and IVKQ (Figure 2.11) shows a large misfit in direction with all of the ICE-5G viscosity profiles (Figure 2.11).

The goodness of the fit of the GIA models with different mantle viscosity structures and lithospheric thicknesses to the estimated horizontal and vertical velocities can be assessed by computing the reduced chi-square (χ^2) value. In this way, we considered the data from three different set of GPS stations; the nine GPS stations processed in our detailed analysis using Bernese software (χ^2_{9} stations), the nine processed stations plus 55 stations obtained from NGL are listed in Table 2.4 (χ^2_{64} stations) and the GPS stations in the southern region (all GPS stations except VALD, PICL, IVKQ, MATQ, HRST, INUQ and INUQ) (χ^2_{57}) (Table 2.5).

The values show that large discrepancies between the observed and predicted velocity directions for stations located in northern region result in reduced chi-square values of much greater than one. As a result, we must conclude that none of the models accurately predicts the horizontal directions for stations in the northern region, which are significantly affected by GIA.

The calculated reduced χ^2 values indicate that the observed residual horizontal velocities of GPS stations in the southern region are in good agreement with the predicted models ICE-5G with profile A and profile B (Figure 2.11a, b), which has a reduced chi-square value close to 1 (Table 2.5).

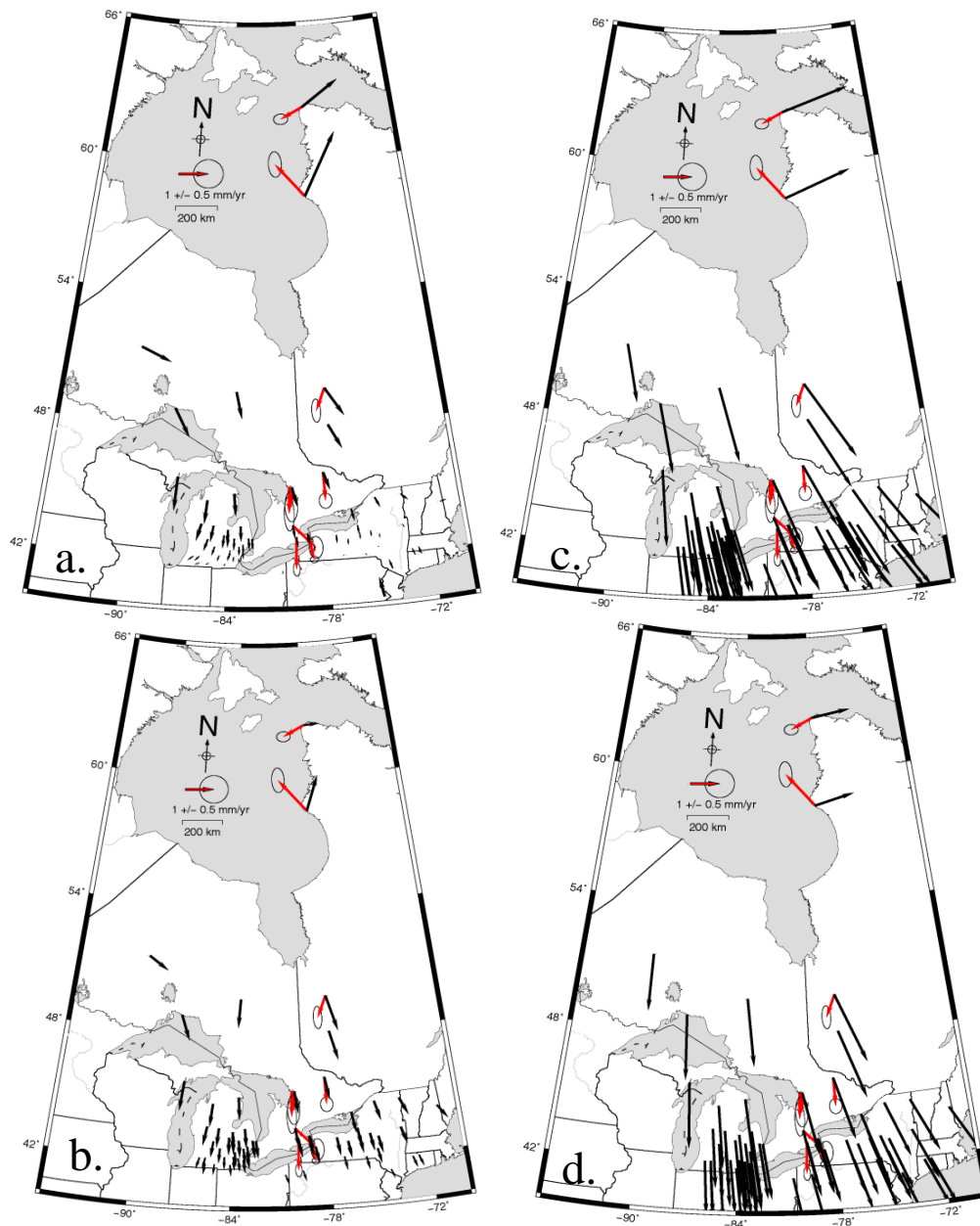


Figure 2.11. Horizontal crustal velocities predicted for ICE-5G (Peltier 2004) (black arrows) for four different viscosity structures, a) profile A b) profile B (VM1) c) profile C (depth-averaged VM2) d) profile D. The lithospheric thickness is 120 km except for c) depth averaged VM2, where the thickness is 90 km. Residual horizontal velocities for the Bernese (red arrows) analysis after removal of plate motions assuming the ITRF2008 North American pole of rotation (Altamimi et al. 2011, 2012). Error ellipses show 95% confidence interval corresponding to the uncertainties calculated with Hector.

Table 2.5. Reduced chi-square values for a comparison with the different GIA models considered in this study. The fit of the horizontal and vertical velocities to the GIA models is calculated for three different subsets of GPS stations, as noted in the text.

| | ICE-5G (Figures 11a/13a) | | ICE-5G (Figures 11b/13b) | | ICE-5G (Figures 11c/13c) | | ICE-5G (Figures 11d/13d) | | ICE-6G_C (VM5a) (Figures 12/14) | |
|---------------------------|-----------------------------|----------|-----------------------------|----------|-----------------------------|----------|-----------------------------|----------|--|----------|
| | Horizontal | Vertical | Horizontal | Vertical | Horizontal | Vertical | Horizontal | Vertical | Horizontal | Vertical |
| UMV | 10^{21} Pa s | | 10^{21} Pa s | | 5×10^{20} Pa s | | 4×10^{20} Pa s | | 5×10^{20} Pa s | |
| LMV | 4.5×10^{21} Pa s | | 2×10^{21} Pa s | | 3.2×10^{21} Pa s | | 2×10^{21} Pa s | | 3.2×10^{21} Pa s | |
| Lithospheric Thickness | 120 km | | 120 km | | 90 km | | 120 km | | 40 km thick high viscosity beneath the 60 km lithosphere | |
| χ^2_{-9} stations | 28.29 | 5.73 | 12.48 | 23.51 | 96.08 | 13.86 | 46.81 | 23.76 | 21.52 | 12.83 |
| χ^2_{-64} stations | 4.29 | 1.43 | 2.11 | 4.05 | 16.41 | 2.11 | 9.64 | 3.57 | 3.52 | 2.37 |
| χ^2_{-57} stations | 1.23 | 1.04 | 0.65 | 3.28 | 11.33 | 1.61 | 8.45 | 2.40 | 2.66 | 2.24 |

The comparison between observed horizontal velocities rates and the predicted GIA model computed for profile E (Figure 2.12) shows that there is generally good agreement to the average azimuth of velocity vectors for stations in eastern Ontario and western Québec, again excluding INUQ and IVKQ. However the magnitude of the differences for GPS stations ranges approximately from -0.2 mm/yr to 1.0 mm/yr. In addition, the “hinge line”, the zero velocity line separating rebounding from subsiding regions (Sella et al. 2007), in ICE-6G_C is much further to the north than that seen in the cGPS observations. Again, neither model accurately reproduces the horizontal directions at the Hudson Bay stations INUQ and IVKQ. It should be noted that the horizontal velocities are corrected for the plate rigid body rotation and this may inadvertently remove some components of the GIA motion and result in a bias in the produced horizontal residual velocities, as noted above.

2.5.2 Vertical Component

The cGPS estimates of vertical velocity (Figure 2.6) show a good agreement with the vertical motions predicted by ICE-5G (Figure 2.13), particularly with the lowest upper mantle viscosity and the highest lower mantle viscosity (Figure 2.13a) for stations located north of the Great Lakes. The observed vertical velocities in this paper shows that the areas north and south of the hinge lines presented in the maps of vertical crustal motion in eastern Ontario by Sella et al. (2007, Figure 1-left) and Koohzare et al. (2008, Figure 4), which are consistent with water level gauge records along the Great Lakes, are rebounding and subsiding respectively (Mainville & Craymer 2005; Tiampo et al. 2011). Comparing our results for stations from the POLARIS network close to the hinge line shows that station TYNO, which is located below the hinge line, subsides over the studied time period at rates of -1.93 ± 0.46 mm/year, while stations ACTO and STCO are above the hinge line and uplift at rates of 2.22 mm/year and 1.32 mm/year, respectively.

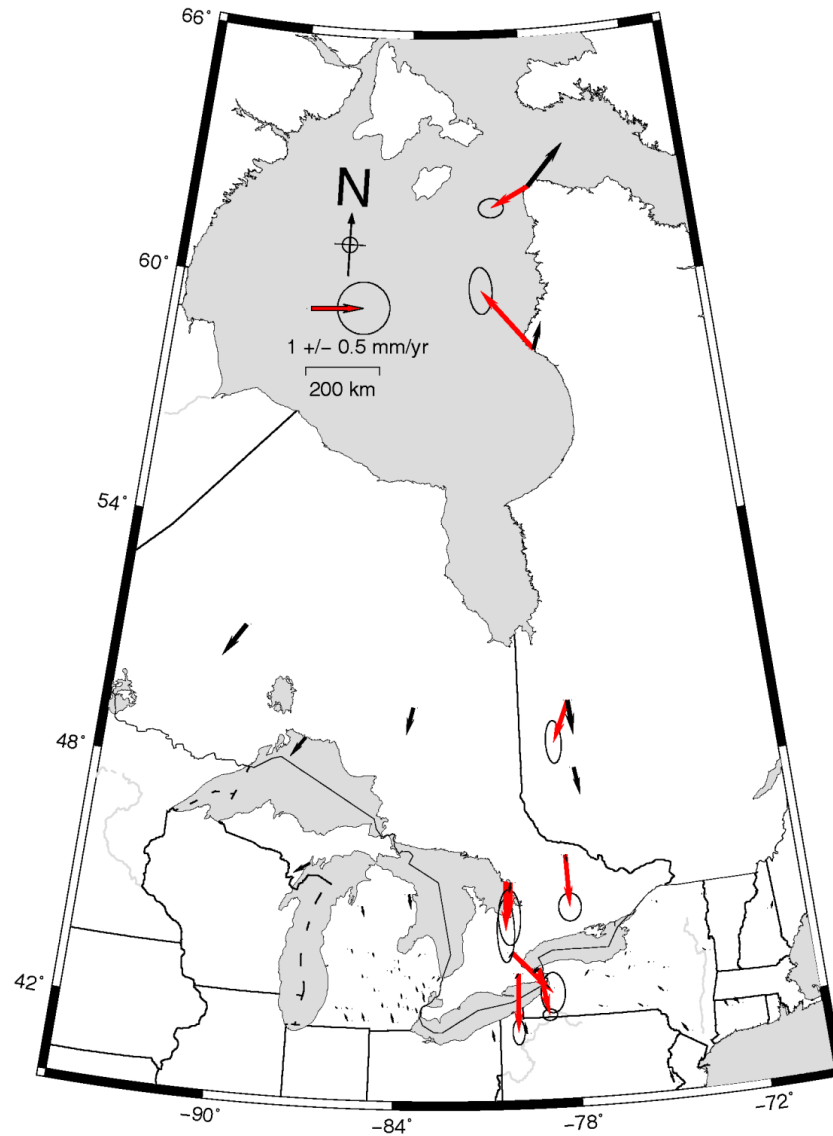


Figure 2.12. Horizontal crustal velocities computed by the ICE_6G_C (VM5a) (Viscosity profile E) GIA model (Peltier 2015) (black arrows). VM5a is a three-layer approximation of the VM2 mantle viscosity profile and features a 60 km thick elastic lithosphere underlain by a 40-km thick high-viscosity layer of 10^{22} Pa s. Residual horizontal velocities for the Bernese (red arrows) analysis after removal of plate motions assuming the ITRF2008 North American pole of rotation (Altamimi et al. 2011, 2012).

Error ellipses show 95% confidence interval corresponding to the uncertainties calculated with Hector

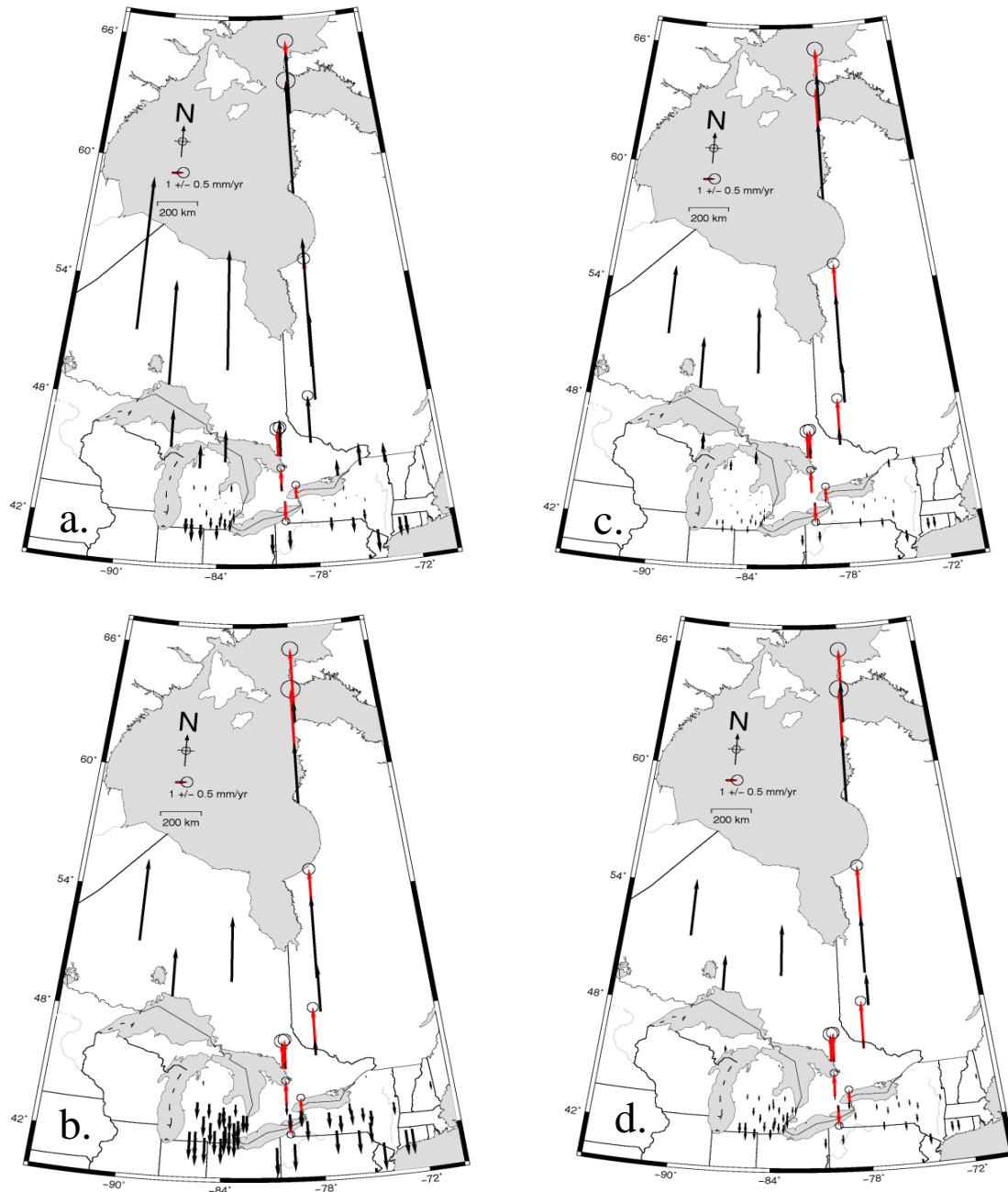


Figure 2.13. Predicted vertical velocities computed using ICE-5G (Peltier 2004) (black arrows) for four different viscosity structures. a) profile A b) profile B (VM1) c) profile C (VM2) d) profile D. The lithospheric thickness is 120 km except for c) depth averaged VM2, where the thickness is 90 km. Observed vertical velocities (in millimeters per year) for the Bernese (red arrows) analyses derived from observations spanning January 2008 through December 2012. Error ellipses show 95% confidence interval corresponding to the uncertainties calculated with Hector.

These results better constrain the subsidence south of the hinge line given by Sella et al. (2007; Figure 1, left) and Koohzare et al. (2008; Figure 4), which passes through the Great Lakes. The subsidence shows disagreement with the predicted vertical motion from ICE-5G and ICE6G_C, with the exception of ICE-5G with a lower mantle viscosity of 4.5×10^{21} and an upper mantle viscosity of 10^{21} , profile A, (Figure 2.13a) (Peltier 2004). This can be confirmed by the variance in the data of the GPS sites in the southern region, such that the reduced chi-square value is approximately 1 (Table 2.5). Here the two stations in the north, close to Hudson Bay, show the smallest discrepancy with profile A.

Comparison of the observed vertical velocities (Figure 2.6, red vectors) with the predicted velocities based on ICE-6G_C (Figure 2.14) (Peltier et al. 2015) shows a discrepancy of -0.91 mm/yr to 3.24 mm/yr. The relatively low level of disagreement between our observed velocities and predicted velocities from this model can be seen at stations TYNO, IVKQ and INUQ which are approximately -0.9 mm/yr, -0.7 mm/yr and 0.1 mm/yr, respectively.

The misfit of the observed vertical velocities with the ICE-5G models may be explained by the anomalously large uplift signals in unexpected regions, as pointed out by Purcell et al. (2016). They found misfit between their modelled vertical velocities with the published uplift rates of Peltier et al. (2015) for the regions where paleo-topography has moved from below sea level to above, and vice versa (e.g., Hudson Bay). They conclude that the main reason for this discrepancy is that the algorithms employed by Peltier et al. (2015) to derive the ice history model do not properly represent the transition from ice loading to water loading in the near-field (Purcell et al. 2016). This results in a significant error in the predicted uplift rates in areas where an ice/water loads transition has occurred, such as in Hudson Bay, Baffin Bay and the Baltic Sea.

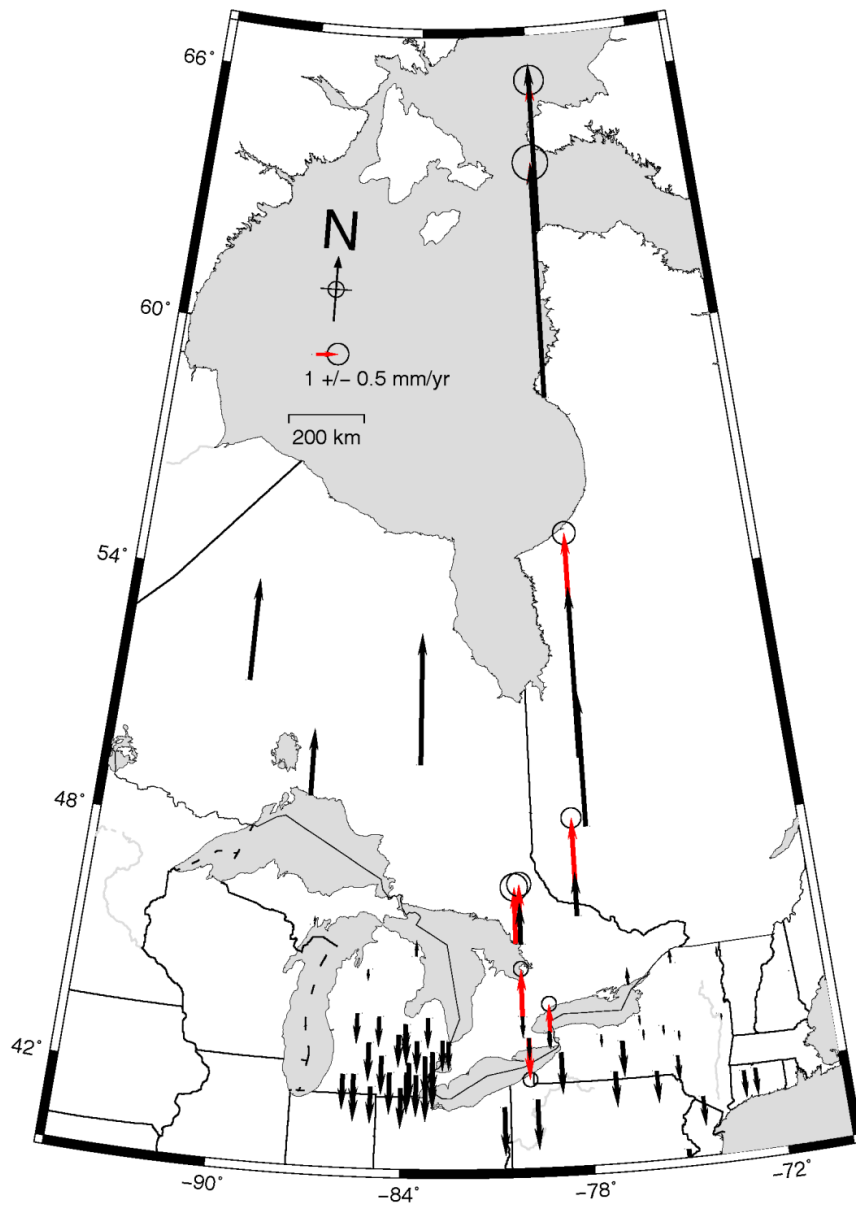


Figure 2.14. Vertical crustal velocities computed for ICE_6G_C (VM5a) (viscosity profile E) (Peltier et al. 2015). The Earth model VM5a features a three-layer approximation of the VM2 mantle viscosity profile and a 60 km thick elastic lithosphere underlain by a 40-km thick high-viscosity layer of 10^{22} Pa s. Observed vertical velocities (in millimeters per year) for the Bernese (red arrows) analyses derived from observations

spanning January 2008 through December 2012. Error ellipses show 95% confidence interval corresponding to the uncertainties calculated with Hector.

2.6 Conclusions

The most reliable combination of reference stations from seven permanent cGPS stations operated by NRCan plus seven stations from the POLARIS network was identified in this work in order to better constrain the lithospheric dynamics in eastern Ontario and western Québec. Time series of the two optimal sub-networks over a time period of five years were analyzed and a detailed comparison with various GIA models was carried out. The time series of fifty-five additional GPS stations spanning a similar period from a global solution shows that the residual horizontal velocities range from 0.67 mm/year in the south near the Great Lakes, to 1.50 mm/year in northwestern Québec, near Hudson Bay, with significant variation in direction between the northern and southern stations velocities. The estimated vertical velocities derived from our analysis reveals a subsidence of about 1.93 ± 0.46 mm/yr in the south and a large uplift in the north, near Hudson Bay, of 10.92 ± 1.12 mm/yr as expected from relative sea-level measurements. In addition to the consistency of observed velocities in the study region to the global solution, we obtained more accurate solutions with lower errors when compared to the regional network solutions. The differences between the velocities of the common stations in two solutions in the three components are -0.03 to 0.03 mm/year in the east, -0.10 to 0.19 mm/year in the north, and -0.52 to 0.20 mm/yr in the vertical component.

Although the GIA models used here for comparison with our analysis have uncertainties in ice load history and Earth rheology, our results can be employed to study GIA motions since the last glacial maximum. The strategies employed here using Bernese software and noise analysis provide the best fit of the vertical velocities in the southern region to that GIA model with the lowest upper mantle viscosity and highest lower mantle viscosity profile, profile A (Figure 2.10a). While estimation of reduced χ^2 values for the fit between the data and several GIA models suggests none of them fit the data over the entire region, several of them reproduce features of both the horizontal and vertical velocities at smaller spatial scales. In addition, eliminating the stations in the north results

in a better estimation of the fit between the GIA model and observed residual horizontal velocities for viscosity profiles A and B (Figure 2.10a). These misfit results suggest that improved ice loading histories with higher spatial resolution and the incorporation of three-dimensional rheologies (see, e.g., Van der Wal et al. 2013) are important for realistic modeling of the current pattern of crustal GIA signal and that cGPS is an important tool for constraining those more complicated models.

The time series analysis of GPS stations using a complex noise model is important because of the existence of time-correlated noises in the time series and seasonal variations from the surface loading signal, particularly in the north and up components. The model combining white noise with power-law noise was employed in the analysis and the estimated spectral index associated with the power-law noise suggests that most GPS stations in our study area are dominantly affected by flicker noise.

In order to evaluate the sensitivity of our velocity estimates to the non-tidal surface loading deformation models, we compared the velocity uncertainties in the horizontal and vertical components to the velocity uncertainties calculated by Santamaria-Gomez & Memin (2015) using a power-law noise model. The results show that the vertical velocity errors associated with the surface mass loading range between approximately -0.2 to 0.2 mm/yr and that no more than 40% of the estimated vertical velocity error in our GPS time series is due to that error source and that the surface loading mass contributes less than 17% to the horizontal velocities uncertainties.

In this research, we employed cGPS observations over nearly five years. Longer time series will contribute significantly to better estimates of the vertical and horizontal deformation in the region. In particular, the horizontal time series provide important insights into the spatial pattern and timing of the ice loading. Further analysis is required to determine the optimal combinations of ice loading history and Earth rheology that provide a simultaneous best fit to both vertical and horizontal velocities of all data in the region. Improved cGPS estimates, over longer time periods will contribute to advancements in GIA models.

2.7 References

- Adams J (1989), Postglacial faulting in eastern Canada: nature, origin and seismic hazard implications. *Tectonophysics* 163:323–331. doi:10.1016/0040-1951(89)90267-9
- Adams J, Basham P (1989), The seismicity and seismotectonics of Canada east of the Cordillera. *Geosci Can* 16(1):3–16
- Adams J, Halchuk S (2003), Fourth generation seismic hazard maps of Canada: values for over 650 Canadian localities intended for the 2005 National Building code of Canada. *Geolog Surv Can Open File* 4459:1–155. doi:10.4095/214223
- Altamimi Z, Collilieux X, Métivier L (2011), ITRF2008: an improved solution of the International Terrestrial Reference Frame. *J Geodesy* 85(8):457–473. doi:10.1007/s00190-011-0444-4
- Altamimi Z, Métivier L, Collilieux X (2012), Itrf2008 plate motion model. *J Geophys Res* 117:1978–2012. doi:10.1029/2011JB008930
- Argus DF, and Heflin MB (1995), Plate motion and crustal deformation estimated with geodetic data from the global positioning system. *Geophys Res Lett* 22:1973–1976. doi:10.1029/95GL02006
- Basham PW, Forsyth DA, Wetmiller RJ (1977), The seismicity of northern Canada. *Can J Earth Sci* 14(7):1646–1667. doi:10.1139/e77-140
- Bent AL (1996), An improved source mechanism for the 1935 Timiskaming, Québec earthquake from regional waveforms. *Pure Appl Geophys* 146(1):5–20
- Beutler G, Bock H, Dach R, Fridez P, Gade A, Hugentobler U, Jaggi A, Meindl M, Mervart L, Prange L, Schaer S, Springer T, Urschl C, Walser P (2007), Bernese GPS Software Version 5.0. In: Dach R, Hugentobler U, Fridez P, Meindl M (eds) *Astronomical Institute University of Bern, Bern*

- Blewitt G (2003), Self-consistency in reference frames, geocenter definition, and surface loading of the solid Earth. *J Geophys Res* 108(B2). doi:10.1029/2002JB002082
- Blewitt G (2014), Nevada Geodetic Laboratory (NGL), Position time series. Nevada Geodetic Laboratory, Reno, NV. <http://geodesy.unr.edu/index.php>. Accessed 1 July 2014
- Blewitt G, and Lavallée D (2002), Effect of annual signals on geodetic velocity. *J Geophys Res* 107:9–11 ETG 9-1-ETG 9-11
- Boehm J, Niell AE, Tregoning P, and Schuh H (2006), The global mapping function (GMF): a new empirical mapping function based on data from numerical weather model data. *J Geophys Res*. 10.129/2005GL025546
- Bos MS, Scherneck HG (2011), Free ocean tide loading provider. <http://holt.oso.chalmers.se/~loading>
- Bos MS, Bastos L, Fernandes RMS (2010), The influence of seasonal signals on the estimation of the tectonic motion in short continuous GPS time-series. *J Geodyn* 49:205–209
- Bos MS, Fernandes RMS, Williams SDP, Bastos L (2013), Fast error analysis of continuous GNSS observations with missing data. *J Geodesy* 87(4):351–360. doi:10.1007/s00190-012-0605-0
- Buchbinder GGR, Lambert A, Kurtz RD, Bower DR, Anglin FM, Peters J (1988), Twelve years of geophysical research in the Charlevoix seismic zone. *Tectonophysics* 156:193–224
- Calais E, Han JY, DeMets C, Nocquet JM (2006), Deformation of the North American plate interior from a decade of continuous GPS measurements. *J Geophys Res* 111. doi:10.1029/2005JB004253
- Crough ST (1981), Mesozoic hotspot epeirogeny in eastern North America. *J Geology* 9:2–6

- Dach R, Hugentobler U, Fridez P (2005), Bernese GPS Software 5.0. Astron. Institute University Of Berne, Berne
- Dach R, Hugentobler U, Fridez P, Meindl M (2007), Bernese GPS Software Version 5.0. Astron. Institute University Of Berne, Berne
- Dineva S, Eaton D, Ma S, Mereu RF (2007), The October 2005 Georgian Bay, Canada, earthquake sequence: Mafic Dykes and their role in the mechanical heterogeneity of precambrian crust. *Bull Seism Soc Am* 97:457–473. doi:10.1785/0120060176
- Dmitrieva K, Segall P (2013), A network approach to estimation of GPS velocity uncertainties. In: Abstract G21A-0737 presented at 2013 fall meeting, AGU, San Francisco, Calif., 9–13 Dec
- Dong D, Fang P, Bock Y, Cheng MK, Miyazaki S (2002), Anatomy of apparent seasonal variations from GPS-derived site position time series. *J Geophys Res* 107(B4). doi:10.1029/2001JB000573
- Dyke AS, Morris TF, Green DEC (1991), Postglacial tectonic and sea level history of the central Canadian Arctic. *J Geol Surv Can Bull* 397:56
- Dyke AS, Andrews JT, Clark PU, England JH, Miller GH, Shaw J, Veillette JJ (2002), The Laurentide and Innuitian ice sheets during the last glacial maximum. *J Quat Sci Rev* 21(1):9–31
- Eaton DW, Adams J, Asudeh I, Atkinson GM, Bostock MG, Cassidy JF, Ferguson IJ, Samson C, Snyder DB, Tiampo KF, Unsworth MJ (2005) Investigating Canada's lithosphere and earthquake hazards with portable arrays. *Eos* 86(17):169–176. doi:10.1029/2005EO170001
- Fenton CH (1994), Postglacial faulting in Canada: an annotated bibliography. *Geol Surv Can Open File* 2774:1–98
- Geruo A, Wahr J, Zhong S (2013), Computations of the viscoelastic response of a 3-D compressible Earth to surface loading: an application to glacial isostatic

adjustment in Antarctica and Canada. *Geophys J Int* 192(2):557–572.
doi:10.1093/gji/ggs030

Goudarzi MA, Cocard M, Santerre R, Woldai T (2013), GPS interactive time series analysis software. *GPS Solut* 17:595–603. doi:10.1007/s10291-012-0296-2

Grimley DA (2000), Glacial and non-glacial sediment contributions to Wisconsin episode loess in the Central United States. *Geol Soc Am Bull* 112:1475–1495

GSC (2015), Historic earthquakes in Canada. Tech. report.
<http://www.earthquakescanada.nrcan.gc.ca>. Accessed 2 June 2015

Hampel FR (1974), The influence curve and its role in robust estimation. *J Am Stat Assoc* 69(346):383–393

Heaman LM, Kjarsgaard BA (2000), Timing of eastern North American kimberlite magmatism: continental extension of the Great Meteor hotspot track? *Earth Planet Sci Lett* 178:253–268

James TS (1991), Post-glacial deformation. Princeton University, Princeton, NJ, Ph.D. dissertation

James TS, Lambert A (1993) A comparison of VLBI data with the ICE-3G glacial rebound model. *Geophys Res Lett* 20:871–874

James TS, and Morgan WJ (1990) Horizontal motions due to postglacial rebound. *Geophys Res Lett* 17:957–960

Kaniuth K, and Völksen C (2003) Comparison of the BERNESE and GIPSY/OASIS II software systems using EUREF data. *J Mitt Bundesamtes Kartographie Geodasie* 29:314–319

King MA, Whitehouse PL, and Van der Wal W (2016) Incomplete separability of Antarctic plate rotation from glacial isostatic adjustment deformation within geodetic observations. *Geophys J Int* 204(1):324–330

- Klemann V, Martinec Z, Ivins ER (2008) Glacial isostasy and plate motion. *J Geodyn* 46(3–5):95–103
- Koohzare A, Vanicek P, Santos M (2008) Pattern of recent vertical crustal movements in Canada. *J Geodyn* 45:133–145
- Larson G, Schaetzl R (2001) Origin and evolution of the Great Lakes. *J Great Lakes Res* 27:518–546
- Leys C, Ley C, Klein O, Bernard P, Licata L (2013) Detecting outliers: Do not use standard deviation around the mean, use absolute deviation around the median. *J Exp Soc Psychol* 49(4):764–766
- Lougheed SC, Morrill N (2015) Quaternary history of western Ontario: impacts on physical landscape and Biota. <http://opinicon.wordpress.com/physical-environment/quaternary>
- Ludden J, Hynes A (2000) The Abitibi–Grenville Lithoprobe project: two billion years of crust formation and recycling in the Precambrian Shield of Canada. *Can J Earth Sci* 37:459–476
- Ma S, Atkinson GM (2006) Focal depths for small to moderate earthquakes (mN_{2.8}) in Western Québec, Southern Ontario, and Northern New York. *Bull Seism Soc Am* 96:609–623
- Ma S, Eaton DW (2007) Western Québec seismic zone (Canada): clustered, midcrustal seismicity along a mesozoic hot spot track. *J Geophys Res* 112. doi:10.1029/2006JB004827
- Mainville A, Craymer M (2005) Present-day tilting of the Great Lakes region based on water level gauges. *Geol Soc Am Bull* 117:1070–1080
- Mao A, Harrison CGA, Dixon TH (1999) Noise in GPS coordinate time series. *J Geophys Res* 104:2797–2816

- Mazzotti S, and Townend J (2010) State of stress in central and eastern North American seismic zones. *Lithosphere* 2:76–83
- Mitrovica JX, Davis JL, Shapiro II (1993) Constraining proposed combinations of ice history and earth rheology using VLBI-determined baseline length rates in North America. *Geophys Res Lett* 20:2387–2390
- Mitrovica JX, Davis JL, Shapiro II (1994) A spectral formalism for computing three dimensional deformations due to surface loads: II. Present-day glacial isostatic adjustment. *J Geophys Res* 99:7075–7101
- Niell AE (1996) Global mapping functions for the atmosphere delay at radio wavelengths. *J Geophys Res* 101:3227–3246
- Peltier WR, Drummond R (2008) Rheological stratification of the lithosphere: a direct inference based upon the geodetically observed pattern of the glacial isostatic adjustment of the North American continent. *Geophys Res Lett* 35.
doi:10.1029/2008GL034586
- Peltier WR (2004) Global glacial isostasy and the surface of the ice-age Earth: the ICE-5G (VM2) Model and GRACE. *Ann Rev Earth Planet Sc* 32:111–149.
doi:10.1146/annurev.earth.32.082503.144359
- Peltier WR, Argus DF, Drummond R (2015) Space geodesy constrains ice-age terminal deglaciation: the global ICE-6G_C (VM5a) model. *J Geophys Res* 120:450–487.
doi:10.1002/2014JB011176
- Petrie EJ, King MA, Moore P, Lavallée DA (2010) A first look at the effects of ionospheric signal bending on a globally processed GPS network. *GPS Solut* 14:491–499. doi:10.1007/s00190-010-0386-2
- Purcell A, Tregoning P, Dehecq A (2016) An assessment of the ICE6G_C(VM5A) glacial isostatic adjustment model. *J Geophys Res Solid Earth* 121(5):3939–3950.
doi:10.1002/2015JB012742

- Quinlan G (1984) Postglacial rebound and the focal mechanisms of eastern Canadian earthquakes. *Can J Earth Sci* 21:1018–1023. doi:10.1139/e84-106
- Santamaría-Gómez A, Mémin A (2015) Geodetic secular velocity errors due to interannual surface loading deformation. *J Geophys Int* 202, doi:10.1093/gji/ggv190
- Sella GF, Dixon TH, Mao A (2002) Revel: a model for recent plate velocities from space geodesy. *J Geophys Res* 107. doi:10.1029/2000JB000033
- Sella GF, Stein S, Dixon TH, Craymer M, James TS, Mazzotti S, Dokka RK (2007) Observations of glacial isostatic adjustment in the stable North America with GPS. *Geophys Res Lett* 34. doi:10.1029/2006GK027081
- Shilts WW, Rappol M, Blais A (1992) Evidence of late and postglacial seismic activity in the Témiscouata-Madawaska Valley, Québec-New Brunswick, Canada. *Can J Earth Sci* 29:1043–1059. doi:10.1139/e92-085
- Simon KM, James TS, Henton JA, Dyke AS (2016) A glacial isostatic adjustment model for the Central and Northern Laurentide ice sheet based on relative sea level and GPS measurements. *Geophys J Int* 205(3):1618–1636
- Steigenberger P, Seitz M, Böckmann S, Tesmer V, Hugentobler U (2012) Precision and accuracy of GPS-derived station displacements. *J Phys Chem Earth* 53–54:72–79. doi:10.1016/j.pce.2010.07.035
- Sykes LR (1978) Intraplate seismicity, reactivation of re-existing zones of weakness, alkaline magmatism and other tectonism post-dating continental fragmentation. *Rev Geophys* 16:621–688
- Talwani P (1999) Fault geometry and earthquakes in continental interiors. *Tectonophysics* 305:371–379
- Terasmae J (1981) Some problems of late Wisconsin history and geochronology in southeastern Ontario. *Can J Earth Sci* 17:361–381

- Thomas WA (2006) Tectonic inheritance at a continental margin. *GSA Today* 16(2):4–11
- Tiampo KF, Fernández J, Jentzsch G, Charco M, Rundle JB (2004) New results at Mayon, Philippines, from a joint inversion of gravity and deformation measurements. *Pure Appl Geophys* 161:1433–1452
- Tiampo KF, Mazzotti S, James TS (2011) Analysis of GPS measurements in Eastern Canada using principal component analysis. *Pure Appl Geophys* 169(8):1483–1506. doi:10.1007/s00024-011-0420-1
- Tiampo KF, González PJ, Samsonov SV (2013) Results for a seismic creep on the Hayward fault using polarization persistent scatterer InSAR. *Earth Planet Sci Lett* 367:157–165
- Tushingham A.M., and Peltier, W.R. (1991), Ice-3G: A new global model of late Pleistocene deglaciation based upon geophysical predictions of post-glacial relative sea level change. *J Geophys Res* 96:4497–4523
- Van der Wal W, Barnhoorn A, Stocchi P, Gradmann S, Wu P, Drury M, Vermeersen B (2013) Glacial isostatic adjustment model with composite 3D earth rheology for Fennoscandia. *Geophys J Int* 192(3):1109–1115. doi:10.1093/gji/ggt099
- Van Dam T, Wahr J, Milly PCD, Shmakin AB, Blewitt G, Lavallée D, Larson KM (2001) Crustal displacements due to continental water loading. *J Geophys Res* 28:651–654
- Van Dam T, Collilieux X, Wuite J, Altamimi Z, Ray J (2012) Nontidal ocean loading: amplitudes and potential effects in GPS height time series. *J Geodesy* 86:1043–1057
- Wang H, Wu P, van der Wal W (2008) Using postglacial sea level, crustal velocities and gravity-rate-of-change to constrain the influence of thermal effects on mantle heterogeneities. *J Geodyn* 46:104–117

- Webb FH, Zumberge JF (1997) An introduction to GIPSY/OASIS II. JPL Publication D-11088
- Williams SDP, Bock Y, Fang P, Jamason P, Nikolaidis RM, Prawirodirdjo L, Miller M, Johnson DJ (2004) Error analysis of continuous GPS position time series. *J Geophys Res* 109(B03412). doi:10.1029/2003JB002741
- Williams SDP (2003) The effect of coloured noise on the uncertainties of rates estimated from geodetic time series. *J Geodesy* 76:483–494. doi:10.1007/s00190-002-0
- Williams SDP (2008) Cats: GPS coordinate time series analysis software. *GPS Solut* 12(2):147–153. doi:10.1007/s10291-007-0086-4
- Woodgold C (2010) Earthquakes Canada. Personal Communication, New York
- Wu P, Hasegawa HS (1996) Induced stresses and fault potential in eastern Canada due to a disc load: a preliminary analysis. *Geophys J Int* 125:415–430
- Zhang J, Bock Y, Johnson H, Fang P, Williams S, Genrich J, Wdowinski S, Behr J (1997) Southern California permanent GPS geodetic array: error analysis of daily position estimates and site velocities. *J Geophys Res* 102(B8):18,035–18,055. doi:10.1029/97JB01380
- Zumberge JF, Heflin MB, Jefferson DC, Watkins MM, Webb FH (1997) Precise point positioning for the efficient and robust analysis of GPS data from large networks. *J Geophys Res* 102:5005–5017

Chapter 3

3 Simplified one-dimensional methodology to retrieve the seasonal amplitude of zenith tropospheric delay on GPS data²

In this chapter, I propose an elevation-dependent model to estimate the seasonal amplitude of ZTD in GPS data on local spatial scales. To achieve this model, I estimate the decay parameter of refractivity with altitude and the seasonal amplitude of refractivity computed from atmospheric data (pressure, temperature, and water vapor pressure) at a reference station. This model estimates the seasonal amplitudes of ZTD between each GPS station and a reference. In order to assess the accuracy of the proposed model, I process five years of data for the period 2008 through 2012 from eight GPS stations by using a precise point positioning (PPP) online application from Natural Resource Canada (NRCAN) (<https://webapp.geod.nrcan.gc.ca/geod/tools-outils/ppp.php>) which computes the ZTD errors based on the atmospheric parameters from a numerical weather prediction model at each stations' location. Because this model estimates the seasonal amplitudes of ZTD between each GPS station and a reference station, taking advantage of the topographic dependency of seasonal amplitude of differenced ZTD, I formed the difference between ZTD derived from PPP at each station and ZTD at the reference station. I demonstrate that the model can accurately estimate the seasonal amplitude of ZTD signals for the GPS stations at any altitude relative to the reference station, comparable with the estimates from global numerical weather prediction models such as ECMWF. Moreover, I use hourly meteorological data from the weather station nearest to each GPS station for the same period and convert them to the height of GPS sites, to compute the ZTD at each GPS station, so called MET-ZTD. The daily averaged MET-ZTD is compared to the ZTD obtained from PPP processing at every station. I also

² A version of this chapter has been submitted to Radio Science journal. Samadi Alinia H., Tiampo, K.F., and Samsonov, S.V. (2017) Simplified one-dimensional methodology to retrieve the seasonal amplitude of zenith tropospheric delay on GPS data, *Radio Sci.* (under 2nd review)

calculate the PWV from the ZWD estimates at each station. These results provide an accurate platform to monitor long-term climate changes and inform future weather predictions.

3.1 Introduction

As radio signals propagate in the atmosphere, they experience an increase or decrease in their speed in ionosphere and troposphere layers, respectively. The induced delay, called the atmospheric path delay (APD), results from the fact that the refractivity index of the constituent gases in the ionospheric and tropospheric layers of the atmosphere is greater than unity. This delay is the dominant source of error in GPS measurements and can produce up to 600 meters position error (Celestino et al. 2007). Therefore, it must be taken into account in precise Global Positioning System (GPS) positioning estimates.

The delay resulting from signal propagation in the ionospheric layer, a region of electrically charged particles, is dispersive in nature. Therefore the magnitude of the ionospheric error, which can be as much as tens of meters (Hoque & Jakowski 2012), is dependent on the frequency of the radio signal. Eliminating this effect from GPS data can be achieved through a combination of two or three separate frequency signals (Shrestha 2003; Kim & Tinin 2011; Elizabeth et al. 2010), taking advantage of the dispersive properties of the ionospheric layer, or utilizing other data sources (Bernhardt et al. 2000; Katsougiannopoulos 2008; Sokolovskiy et al. 2008; Liu et al. 2016).

However, the effect of the troposphere on the GPS signals is not related to the frequency of the signals (Klobuchar 1996) and therefore the methods employed to remove ionosphere effects are not useful for eliminating this error. The magnitude of tropospheric error on the GPS data can be from 2 to 3 m. The tropospheric path delay can be separated into the two main components: the hydrostatic (dry) and the wet delay (Saastamoinen 1973). The hydrostatic component depends on the dry gases in the atmosphere and can be determined with sub millimeter of accuracy from surface pressure measurements (Saastamoinen 1973; Mendes et al. 1995). The wet delay changes with the variation of time and space and is dependent on the amount of water vapor in the atmosphere (Bevis et al. 1994; Fotiou & Pikridas 2012). In this paper, we focus on the tropospheric effects.

Knowledge of the zenith troposphere delay (ZTD) is important for providing information for accurate positioning and monitoring of the spatial and temporal weather and climate variations. ZTD can be estimated by using different GPS processing strategies and techniques including GPS network processing (Flouzat et al. 2009; Musa et al. 2011; Li et al. 2014), precise point positioning (PPP) technique (Bar-Sever et al. 1998; Dousa 2010) and atmospheric studies that use parameters such as air pressure, air temperature and water vapor pressure (Schuler 2001; Pikridas et al. 2014). Differencing of the dry component of this delay, which can be easily computed from the relationship with the surface pressure (Saastamoinen 1973), from ZTD results in the zenith wet delay (ZWD), which is used directly to compute the precipitable water vapor (PWV), applicable in weather prediction (Morland et al. 2009; Bianchi et al. 2016; Jin & Luo 2009; Pikridas et al. 2014).

Tregoning & Herring (2006) investigate the importance of using the actual surface pressure, including global pressure data such as those from European Center for Medium Range Weather Forecasts (ECMWF) or from global pressure and temperature model (GPT), rather than using a constant pressure value at sea level to estimate the a priori zenith hydrostatic delay (ZHD). They observed that not using the actual surface pressure produces a bias in GPS height estimation up to -0.2 mm/hpa and as much as 2 mm in amplitude of annual variations (Tregoning & Herring 2006).

Employing meteorological data collected at the sensors installed at the GPS station's locations is another approach to achieve the local atmospheric parameters. The problem is that in addition to the differences between the heights of weather station and GPS station, many weather stations are not collocated with the GPS receivers. Many studies have been carried out to correct the *in situ* pressure and temperature measured at the nearest meteorological station for the height of the local GPS station (e.g. Bai & Feng 2003; Gendt et al. 2004; Musa et al. 2011; Dousa & Elias 2014; Alshawaf et al. 2017).

Alshawaf et al. (2017) employed the vertically and horizontally interpolated surface pressure and temperature from the three meteorological stations nearest to each GPS station to compute ZHD and then calculate PWV at each station. In addition, they found a

good agreement between the PWV obtained from Global Navigation Satellite System (GNSS) observations and from European Center for Medium-Range Weather Forecasts Reanalysis (ERA-Interim) data in Germany in the lower altitude areas and a difference of approximately 0.6 mm in mountainous areas. They suggest that where there is an absence of the surface weather data, ERA-Interim is a good replacement for computing PWV from the ZTD derived from GNSS, particularly in flat regions, because of the coarse spatial grids for global surface pressure and temperature and the altitude difference with the GPS stations in areas with significant topography changes.

Dousa & Elias (2014) proposed a novel approach for modeling ZWD and its vertical approximation by motivating the concept presented in Askne & Nordius (1987). They used a combination of the exponential decay parameters obtained from the fitting of the exponential function to the vertical profile of ZWD and partial water vapor pressure. Their approach reduces the low resolution numerical model to an accurate grid at a reference level.

Emardson et al. (2003) used the computed neutral delay obtained from GPS data to understand the noise level in differential interferometric synthetic aperture radar (DInSAR) images by monitoring the differential ZTD at different times between two GPS stations. They showed that the spatio-temporally averaged variance resulting from water vapor, σ , in mm, is dependent on the differential distance and height between continuous GPS (CGPS) observations. They proposed a function of the form $\sigma = cL^\alpha + kH$, where σ is in mm, and L and H are in kilometers and estimated the values of c , α , and k for different time periods. For example, using zenith neutral atmospheric delays computed from daily GPS data from 126 stations in the Southern California Integrated GPS Network (SCIGN) network, they obtained values of 2.8 ± 0.1 , 0.44 ± 0.004 and 0.5 ± 0.1 for c , α , and k , respectively. Note that the value of α is generally site-independent. They also showed that the mean vertical stratification of the troposphere is correlated with observations between one and three days. This model is valid for lengths with a range of 10 to 800 km and height differences between 0 and 3 km. These ideas led to a topography-dependent turbulence model for DInSAR tropospheric corrections using values of the wet part of the zenith delay estimated from GPS data (Li et al., 2005).

In other work, Li et al. (2005, 2006a) used a water vapor correction model derived from the integration of GPS and either NASA Moderate Resolution Imaging Spectroradiometer (MODIS) data and ESA's MEdium Resolution Imaging Spectrometer (MERIS) data. They showed that atmospheric water vapor is a significant error source for repeat-pass DInSAR measurements and is particularly important when studying small amplitude geophysical signals with long wavelengths, including interseismic deformation and some anthropogenic processes. In their approach, a linear correction model was produced based on the comparison between MODIS- Precipitable Water Vapor (MODIS-PWV) and GPS-PWV values in cloudy areas and $1 \text{ km} \times 1 \text{ km}$ water vapor fields for DInSAR atmospheric correction.

Li et al. (2006b) proposed a MODIS/MERIS combination water vapor correction model to take advantage of the properties of both types of data that can be used when one or the other data is not available. MERIS has better spatial resolution than MODIS. Also, its near-IR water vapor products are closer to GPS than MODIS (Li et al., 2006b). Unlike MODIS, MERIS is available for the same times as the Advanced Synthetic Aperture Radar (ASAR) image product. In addition, employing MODIS with the MERIS near-IR water vapor product enables the detection of cloud pixels, while MERIS data are usable only under cloud-free conditions.

Samsonov et al. (2014) proposed an elevation-dependent exponential model to compute the systematic seasonal troposphere signal in DInSAR height time series. They calculated the ground deformation time series from ENVISAT and RADARSAT-2 interferograms over Naples Bay in Italy for a period of ten years. In their approach, they employed multiyear refractivity obtained from the surface weather station and radiosonde station located near the location of a DInSAR reference point, at mean sea level (msl). They computed the exponential decay parameter by fitting an exponential function to the vertical profile of refractivity computed from the radiosonde data. Their results indicate that removing the troposphere seasonal sinusoidal signal, computed based on the estimated seasonal amplitudes of ZTD, from DInSAR height times series could calculate the deformation rate of signals with 50% better precision than those estimated before correction (Samsonov et al., 2014).

In this paper, initially, we process the RINEX data for the time period spanning January 2008 to December 2012 for eight GPS stations distributed sparsely in southeastern Ontario through northwestern Québec by using PPP processing online service available from Natural Resource Canada (NRCAN) (<https://webapp.geod.nrcan.gc.ca/geod/tools-outils/ppp.php>). Employing this application results in absolute estimates of ZTD and position, with a time step of 30 seconds, for every GPS station. Next, we calculate the ZTD at each GPS station by using hourly meteorological data from weather stations close to the GPS stations over the same time period as the original data. For more accurate results, the meteorological data, including temperature, pressure and water vapor pressure, are corrected for the height difference between GPS stations and weather stations based on the approaches proposed by Musa et al. (2011) and Dousa & Elias (2014). Then, the ZTD results from the GPS processing, so called GPS-ZTD, and the ZTD estimated from the meteorological data, so called MET-ZTD, are averaged on a daily basis and for comparison with each other.

As mentioned above, in addition to the importance of proper estimation of the tropospheric path delay in precise positioning, it is widely used in determining the amount of water vapor pressure in the atmosphere. A better understanding of this relationship can help to estimate the precipitable water, which is the most important greenhouse gas, long-term monitoring of which can help to estimate climate change. Many studies employed GPS observations to compute PWV (e.g., Bevis et al. 1992; Duan et al. 1996; Tregoning et al. 1998; Steigenberger et al. 2007; Tregoning & Watson, 2009). Bevis et al. (1992) employed the GPS meteorology (GPS-MET) approach to measure atmospheric water vapor both in time and space in near real-time from GPS data analysis and ZWD. In this work, we use their proposed approach and input the corrected atmospheric parameters for the height difference between each GPS station and the nearby weather station to retrieve the PWV from the ZWD at each GPS station.

Based on the work of Samsonov et al. (2014), we propose an elevation-dependent model based on the exponential decay parameter of refractivity computed from the fit to the vertical profile of the mean refractivity at the GPS stations. This model computes the seasonal amplitude of ZTD in GPS data referenced to a station at higher altitude, ACTO

at 367.22 m above msl. We then compare the results to the seasonal amplitudes of the differenced GPS-ZTD at each station relative to the GPS-ZTD at station ACTO. The differenced ZTD will increase the dependency of the seasonal amplitude of ZTD with altitude and the estimated seasonal amplitudes from the model are comparable to the observed seasonal amplitude from differenced ZTD.

Before addressing the tropospheric modeling errors, we discuss the GPS and weather station data in Section 2. In Section 3, we focus on the methods used to model the ZTD at GPS stations by using meteorological data and processing of GPS stations. In this section, we also present the model for computing the elevation-dependent seasonal amplitude of ZTD at each GPS site. In addition, we also elaborate on how we calculated PWV using the ZWD at each site. In the following section, the results are discussed in detail. Interpretation and conclusions are presented in the final section.

3.2 Data Preparation

As this paper follows upon our earlier work on processing GPS data in eastern Ontario and western Québec using Bernese GPS Software version 5.0 (Samadi Alinia et al., 2017), here we use the RINEX data from eight common GPS stations, seven GPS stations of the POLARIS network (<ftp://polaris4.es.uwo.ca>) (Eaton et al., 2005) and one long-running IGS reference station (ALGO) operated by the Canadian Geodetic Survey (CGS) of Natural Resources Canada (NRCan) in the same time period as the previous study, for a period of five years from the beginning of 2008 to end of December 2012, at a 30 second sampling rate. Note that here we employed a PPP analysis from the Canadian Spatial Reference System (CSRS) online service provided by NRCan (<https://webapp.geod.nrcan.gc.ca/geod/tools-outils/ppp.php>)

These GPS sites were equipped with dual-frequency receivers, although the antennas, monuments and receiver types differed between stations. GPS stations ACTO, TYNO and, STCO are continuously operating reference stations (CORS) with monuments consisting of reinforced concrete pillars approximately three meters deep. All other stations have stainless steel pedestals anchored to bedrock. The manufacturers of the receivers and antennas include Trimble, Novatel, Topcon Positioning System (TPS) and

Allen Osborne Associates, Inc. (AOA). Figure 3.1 depicts the geographical location of the selected GPS stations (black circles) in our study area.

In order to perform a comparative study of ZTD, we also employ the local surface atmospheric parameters spanning from 2008 to the end of 2012 measured at weather stations near the GPS stations (Figure 3.1, green triangles). The hourly historical climate data provided by Environmental Canada (<http://climate.weather.gc.ca/>) was retrieved for the weather stations within 10 km of TYNO (Hamilton), within 5.9 km of STCO (Port Weller, AUT), within 29 km of ACTO (Elora, RCS), within 13 km of KLBO (Parry Sound, CCG), within 49 km of ALGO (Algonquin Park East Gate), within 11 km of MATQ (Matagami), and within 4 km of INUQ (Inukjuak). Because the closest weather station to the northernmost station, IVKQ, with valid weather data is Cape Dorset, across Hudson Bay, we consider this in our analysis of this station. Note that this station is 213 km from IVKQ. In addition, Guelph Turfgrass weather station, the closest weather station to ACTO, does not record surface pressure data. As a result, we included data from the second closest weather station, Elora RCS. Finally, because of missing hourly climate data for the period October 2011 to the end of 2012, due to the loss of connection at the Matagami weather station, we employed data from another nearby weather station, Matagami A, for that missing time interval. The elevations of Matagami and Matagami A stations are very similar, 281 and 280 m respectively.

Table 3.1 presents the altitude of the GPS stations and the nearby weather stations above msl. As the atmospheric parameters are sensitive to the height of a station (Emardson et al. 2003; Musa et al. 2011), the height difference between the weather stations and the GPS stations must be taken into account for an accurate estimation of ZTD at the GPS stations. In our study area, the difference between the heights of GPS stations and the nearby weather stations range between -15.2 and 159.8 m above msl. Therefore, in order to correct pressure, temperature and water vapor pressure for the height difference, we use the relationships proposed by Dousa & Elias (2014) and Musa et al. (2011).

Initially, we convert the atmospheric parameters observed at the weather stations' height to a common reference level at msl and then transfer that to the GPS stations' height (Bai & Feng, 2003).

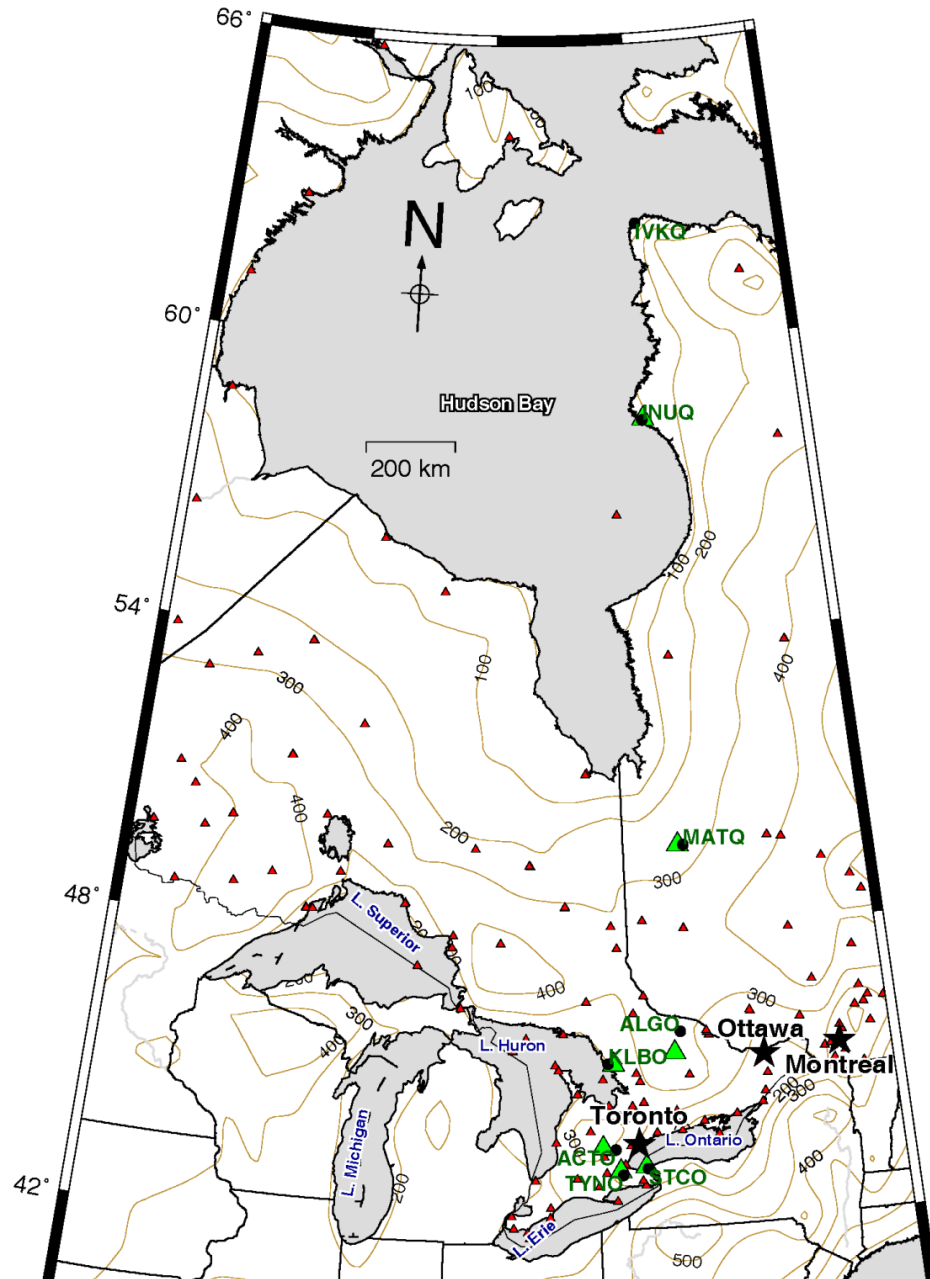


Figure 3.1. Location of the weather stations in eastern Ontario and western Québec (red triangles), GPS stations (black circles) and weather stations considered in this study (green triangles). Contour lines illustrating elevations are shown in brown and are spaced at 100-meter intervals.

Table 3.1. GPS and weather station details, including elevations above mean sea level (msl) and the mean of the atmospheric parameters observed at the meteorological station between 2008 and 2012 together with their rms errors after corrected for the height difference between the weather station and GPS station. The refractivity at each GPS station is computed using Equation 3.8. GPS stations are sorted based on their latitudes.

| GPS stations | Weather stations | GPS Height meter above (msl) | weather station Height meter above (msl) | Pressure (mbar) | Water Vapor Pressure (mbar) | Air Temperature ($^{\circ}\text{C}$) | Dew point Temperature ($^{\circ}\text{C}$) | Refractivity (N-unit) |
|--------------|--------------------------|------------------------------|--|-------------------|-----------------------------|--|--|-----------------------|
| TYNO | Hamilton | 205.10 | 237.70 | 995.3 \pm 0.04 | 10.39 \pm 0.03 | 8.99 \pm 0.05 | 4.34 \pm 0.05 | 323.83 \pm 0.09 |
| STCO | Port Weller (AUT) | 94.17 | 79.00 | 1008.4 \pm 0.04 | 10.20 \pm 0.03 | 9.68 \pm 0.04 | 4.83 \pm 0.05 | 325.83 \pm 0.08 |
| ACTO | Elora RCS | 367.22 | 376.40 | 975.1 \pm 0.06 | 9.86 \pm 0.03 | 7.59 \pm 0.05 | 3.73 \pm 0.06 | 317.68 \pm 0.08 |
| KLBO | Parry Sound CCG | 185.57 | 176.30 | 992.4 \pm 0.04 | 9.34 \pm 0.03 | 7.09 \pm 0.05 | 2.77 \pm 0.05 | 320.34 \pm 0.09 |
| ALGO | Algonquin Park East Gate | 237.18 | 397.00 | 989.8 \pm 0.04 | 8.74 \pm 0.03 | 5.86 \pm 0.06 | 0.35 \pm 0.05 | 318.74 \pm 0.08 |
| MATQ | Matagami | 279.70 | 281.00 | 984.6 \pm 0.04 | 6.96 \pm 0.02 | 1.86 \pm 0.06 | -2.92 \pm 0.06 | 312.83 \pm 0.06 |
| INUQ | Inukjuak | 16.53 | 25.75 | 1014.4 \pm 0.05 | 5.34 \pm 0.02 | -3.40 \pm 0.06 | -6.72 \pm 0.06 | 319.83 \pm 0.04 |
| IVKQ | Cape Dorset | 12.23 | 49.10 | 1012.5 \pm 0.05 | 4.13 \pm 0.01 | -6.47 \pm 0.05 | -9.56 \pm 0.05 | 316.80 \pm 0.02 |

Temperature observed at the meteorological station can be corrected for the height difference with the GPS station as follows:

$$\begin{aligned} T_{MSL} &= T_{MET} + \beta H_{MET} \\ T_{GPS} &= T_{MSL} - \beta H_{GPS} \end{aligned} \quad (3.1)$$

where, T_{GPS} and T_{MET} are the temperatures at GPS station and at meteorological station in Kelvin, T_{MSL} is the temperature at mean sea level in degrees Kelvin, H_{GPS} and H_{MET} are, respectively, the altitudes of the GPS station and meteorological station above mean sea level in meters, and β is the temperature lapse rate, estimated at 6.5 K/km (Dousa & Elias 2014).

The air pressure at a GPS station can be obtained by employing Equation 3.2 (Dousa & Elias 2014):

$$\begin{aligned} P_{MSL} &= P_{Met} * \left(\frac{T_{MSL} - \beta H_{MET}}{T_{MSL}} \right)^{\frac{-g}{R\beta}} \\ P_{GPS} &= P_{MSL} * \left(\frac{T_{MSL} - \beta H_{GPS}}{T_{MSL}} \right)^{\frac{g}{R\beta}} \end{aligned} \quad (3.2)$$

where, P_{MSL} , P_{Met} and P_{GPS} are the air pressure at mean sea level, meteorological station and GPS station, respectively, $g = 9.80665$ is the gravitational acceleration in (m/s^2), R is the specific gas constant for dry air estimated as 287.058 (J/kg/K).

Partial water vapor pressure can be computed from the hourly dew point temperature observed at the meteorological station for the time period 2008 to 2012. This temperature is a value that describes the amount of moisture content in the air at a particular temperature (Elliott & Gaffen, 1993). To achieve this temperature, we use equation AEGR developed by Alduchov & Eskridge (1996) because the temperature for every weather station in our study area is less than 50⁰ Celsius. This formulation is exponentially dependent on the temperature.

Utilizing the relationships between the partial water vapor pressure and pressure presented by Dousa & Elias (2014) and an exponential decay parameter of partial water vapor pressure from Smith (1966), the computed partial water vapor pressure at the meteorological station can be transferred to the GPS station as follows:

$$E_{MSL} = E_{Met} * \left(\frac{P_{Met}}{P_{MSL}}\right)^{-(\lambda+1)}$$

$$E_{GPS} = E_{MSL} * \left(\frac{P_{GPS}}{P_{MSL}}\right)^{(\lambda+1)} \quad (3.3)$$

where, E_{MSL} , E_{Met} and E_{GPS} are the partial water vapor pressure at mean sea level, meteorological station and GPS station, respectively. λ is the exponential decay parameter of partial water vapor pressure given by Smith (1966) and is dependent on the season of year and the latitude of the site.

In this paper, we employed the annual average values of λ corresponding to the latitude bands presented by Smith (1966). According to Alshawaf et al. (2017), this parameter is not highly variable at sites below 700 m. Table 3.2 represents the values of λ for each station.

Figure 3.2 indicates the relation between air temperature, dew point and partial pressure of water vapor variations as a function of height. As shown in this figure, INUQ and IVKQ have very low dew point temperature and water vapor pressure, despite their relatively low altitude. This is because they are located east of Hudson Bay, a region that is abnormally cold and dry when compared to other areas with the same altitude (Danielson 1969; Maxwell 1986). In contrast, the temperature and water vapor pressure at station ACTO are as high as those at stations STCO and TYNO but higher than station MATQ. This is in spite of its higher altitude relative to MATQ. This may be because it is situated further south and is warmer and moister than station MATQ, which is located further to the north.

Table 3.2. The partial water vapor decay parameter (λ) obtained from Smith (1966) based on the latitude of the GPS stations. The mean of the ZTDs obtained from MET and GPS data for the time period between 2008 and 2012 for every GPS station. The rms differences between MET-ZTD and GPS-ZTD. The observed seasonal amplitude of the ΔZTD_{GPS} for every GPS station is referenced to station ACTO. The seasonal amplitudes of ZTD are derived from the proposed elevation-dependent model (Equation 12). Correlation coefficients between MET-ZTD and GPS-ZTD time series are computed using Pearson's approach. GPS stations in this table are sorted based on their latitudes.

| Stations | Annual average of λ (smith 1966) | Mean MET-ZTD (m) | Mean GPS-ZTD (m) | RMS difference (cm) | Amplitude derived from ΔZTD_{GPS} (cm) | Amplitude derived from the proposed model (Equation 3.12) (cm) | Correlation between MET-ZTD and GPS-ZTD (%) | MET-PWV (cm) | GPS-PWV (cm) |
|----------|--|------------------|------------------|---------------------|--|--|---|--------------|--------------|
| TYNO | 2.78 | 2.40±0.00 | 2.35±0.00 | 9.25 | 0.15 | 0.30 | 92 | 2.13±0.05 | 1.38±0.02 |
| STCO | 2.78 | 2.41±0.00 | 2.38±0.00 | 7.27 | 0.22 | 0.50 | 90 | 1.86±0.05 | 1.36±0.02 |
| ACTO | 2.78 | 2.35±0.00 | 2.30±0.00 | 7.25 | 0.00 | 0.00 | 91 | 2.05±0.05 | 1.16±0.02 |
| KLBO | 2.78 | 2.37±0.00 | 2.36±0.00 | 11.01 | 0.30 | 0.33 | 90 | 1.88±0.05 | 1.67±0.02 |
| ALGO | 2.78 | 2.36±0.00 | 2.34±0.00 | 6.78 | 0.19 | 0.24 | 93 | 1.70±0.05 | 1.42±0.02 |
| MATQ | 2.78 | 2.32±0.00 | 2.31±0.00 | 5.24 | 0.63 | 0.16 | 86 | 1.19±0.05 | 0.98±0.02 |
| INUQ | 2.79 | 2.37±0.00 | 2.36±0.00 | 4.13 | 1.90 | 0.65 | 75 | 0.95±0.02 | 0.83±0.02 |
| IVKQ | 2.41 | 2.35±0.00 | 2.35±0.00 | 3.78 | 1.95 | 0.66 | 60 | 0.66±0.01 | 0.61±0.01 |

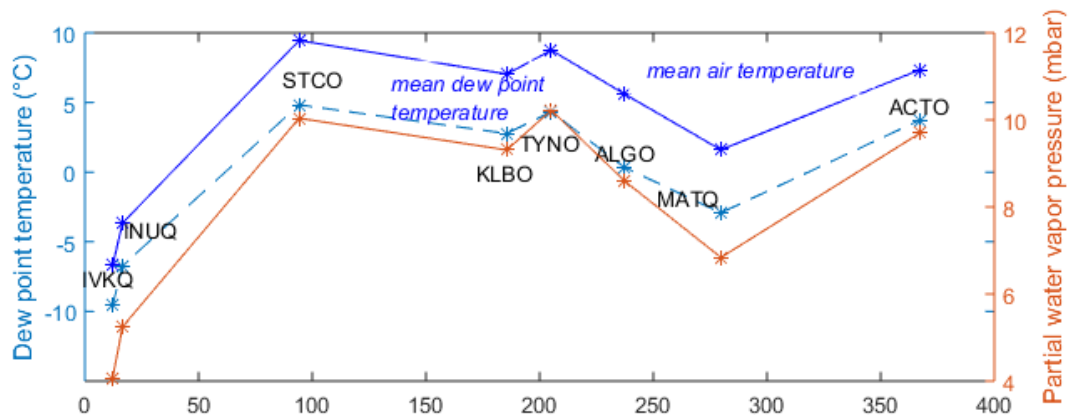


Figure 3.2. Vertical profile of the mean partial water vapor pressures (solid red), the mean dew point temperature (dashed blue) and the mean air temperature (solid blue) at the GPS stations.

3.3 Methods

3.3.1 GPS Processing

The first step of the ZTD computation relates to the use of PPP technique from the CSRS online service provided by NRCan (<https://webapp.geod.nrcan.gc.ca/geod/tools-outils/ppp.php>) (Lahaye et al. 2008). This application estimates a high-accuracy absolute position for a single receiver. The accuracy of the positions derived from PPP coordinates is mostly dependent on the length of observation session for resolving the carrier phase ambiguities (CSRS-PPP guide 2004; Geng et al. 2012). In addition, the quality of the equipment and employing dual-frequency receivers are important factors in obtaining very accurate positioning results (CSRS-PPP guide 2004; Berg & Holliday 2011).

This technique takes into account ZTD as an unknown during processing and estimates it every 15 seconds along with the position estimates. We employed the international terrestrial reference frame (ITRF) as the reference system and static mode for post-processing of the GPS data. This application uses precise satellite orbits and clock

corrections at the epoch of the observation data. In addition, it uses the final satellite products available by International GNSS Service (IGS) and by the National Geodetic Survey (NGS) available at <http://www.ngs.noaa.gov/ANTCAL>. The CSRS-PPP online service includes cycle-slip filtering and antenna phase center calibration values, along with applying the ocean loading corrections computed with the Onsala Space Observatory (OSO) Chalmers grid model (Bos & Scherneck 2011). The first-order ionospheric error is removed using the linear combination of the dual frequency L1 and L2 of the code and phase observations. The higher order of delay, which is less than 1% of the first order delay, is not taken into account.

As mentioned earlier, the troposphere error in the radio signals causes a delay in the arrival of signal to the receiver and can be divided into the wet and dry components (Saastamoinen 1973). In order to reduce this to only one unknown tropospheric delay for all satellites in view, this application uses global mapping function (GMF), a high accuracy mapping function, to project the zenith troposphere to the satellite-receiver direction (El-Mowafy 2011).

The GMF in the current version of CSRS-PPP application (CSRS-PPP 2017), uses a $15^\circ \times 15^\circ$ global grid from the monthly mean profile of pressure, temperature and relative humidity data produced from the ECMWF numerical weather model data, a 40-year reanalysis (ERA40) data (Kouba 2008). This mapping function for both hydrostatic and wet components is defined as follow (Boehm et al. 2006a):

$$m(\varepsilon) = \frac{1 + \frac{a}{b}}{1 + \frac{1+c}{a}} \frac{\sin \varepsilon + \frac{b}{\sin \varepsilon + c}}{\sin \varepsilon + \frac{a}{\sin \varepsilon + c}} \quad (3.4)$$

where, a , b and c are constant coefficients. ε is the elevation cut-off angle, and a value of 10° is applied in CSRS-PPP by default.

This function is the spherical harmonic expansion of the Vienna Mapping Function 1 (VMF1) parameters (Boehm et al. 2006b) and requires the station coordinates and day of the year as input parameters. The coefficient a for both hydrostatic and wet components is estimated from the spherical harmonics and computed based on the same process as

used in VMF1 (Boehm et al. 2006b). This parameter, at any latitude at the day of year t (referred to January 28), can be calculated as:

$$a = a_0 + A \cos\left(\frac{t-T_0}{365} \cdot 2\pi\right)$$

$$a_0 = \sum_{n=0}^9 \sum_{m=0}^n P_{nm}(\sin(\varphi)) \cdot [A_{nm} \cos(m\lambda) + B_{nm} \sin(m\lambda)] \quad (3.5)$$

where, constant a_0 and the annual amplitude A , on a global grid of monthly mean between September 1999 and August 2002 in a least-square adjustment. The coefficients b and c are estimated based on the empirical equations with the same strategy used in VMF1.

3.3.2 Employing Meteorological Data

In this approach, we use the meteorological data observed at the weather stations, converted to the nearby GPS station as discussed in detail in Section 3.2, in order to compute the refractivity and to estimate the absolute ZTD time series at each site.

3.3.2.1 Refractivity

The refractive index of a medium, n , is expressed as the ratio of the speed of propagation of a radio wave in a vacuum, c , to the speed of propagation in the medium, v :

$$n = \frac{c}{v} \quad (3.6)$$

As the electromagnetic waves in the atmosphere propagate just slightly slower than in a vacuum, the refractive index is more conveniently expressed in terms of the refractivity, N :

$$N = 10^6(n - 1) \quad (3.7)$$

The radio refractivity (N) can be computed based on the meteorological parameters of atmospheric pressure, water vapor, and temperature. The following expression (Equation 3.8) from Smith & Weintraub (1953) represents the relationship between the meteorological parameters and refractivity:

$$N = K_1 \frac{P_d}{T} + K_2 \frac{e}{T} + K_3 \frac{e}{T^2} \quad (3.8)$$

Here P_d is the partial pressure of dry air (hPa), K_i are the refractivity constants, e is the partial pressure of water vapor (hPa), and T is the absolute temperature (degrees Kelvin) at the GPS stations' height. The refractivity constants K_i are determined empirically in a laboratory. We use the values determined by Rueger (2002) of $77.69 \text{ K mbar}^{-1}$, $71.29 \text{ K mbar}^{-1}$, and $375463 \text{ K}^2 \text{ mbar}^{-1}$ for the refractivity constants K_1 , K_2 , and K_3 , respectively.

By substituting meteorological observations for partial pressure, partial water vapor pressure and temperature parameters at each GPS station into Equation 3.8, we calculate the refractivity time series for every GPS station in our study (Figure 3.3). According to Figure 3.3, a minimum occurs during summer and a maximum occurs in the winter in every year. Note that there are a number of gaps, ranging from 2% to 5%, in the time series at STCO, INUQ, ALGO, and IVKQ that occur due to the lack of some of the weather parameters required for the refractivity calculation (water vapor pressure, temperature or pressure) and that are not provided by other nearby weather stations. Table 3.1 represents the mean of refractivity at each station.

3.3.2.2 Computing ZTD from Meteorological Data

The ZTD of the signal can be computed in terms of refractivity N integrated over the path with a given altitude as (Jin 2012; Solheim et al. 1999):

$$d_{trop} = 10^{-6} \int_{path} N ds \quad (3.9)$$

The ZTD can be calculated by employing an exponential decay model as proposed by Martin & Waldron (1961). This model is expressed by the integration of refractivity along a vertical path above msl according to the following equation:

$$d_{trop}(t, z_i) = 10^{-6} N_i(t) \int_0^\infty e^{-cz} dz \quad (3.10)$$

In this equation, $N_i(t)$ is the refractivity time series at a station, z_i is the elevation of the station above msl and c is the refractivity decay parameter.

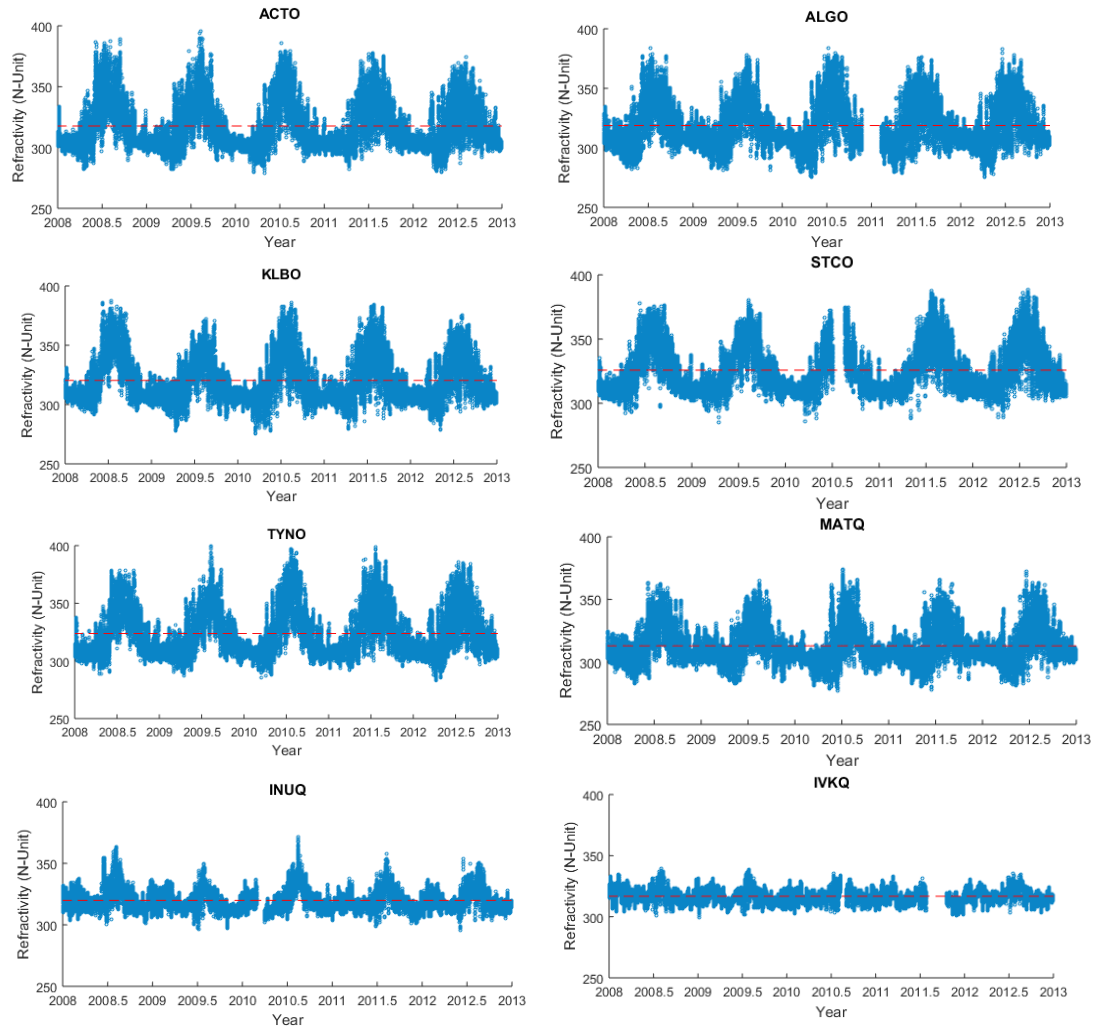


Figure 3.3. Refractivity time series computed from meteorological data such as temperature, air and water vapor pressure (Equation 3.3) observed at the weather stations near the GPS stations and corrected for the height differences with the GPS stations, distributed from southeastern Ontario to northwestern Québec, using Equations 3.1 to 3.3 (Dousa & Elias 2014) (Figure 3.1).

Figure 3.4 indicates the vertical profile of the mean refractivity at all GPS stations. The dependency of mean refractivity with elevation is strongly proportional to the ratio of partial water vapor pressure and surface temperature variations with height at GPS stations (see Equation 3.8). This fact is demonstrated by the similarity between the vertical profiles of the mean refractivity in Figure 3.4 to the vertical profile of partial water vapor pressure and temperature in Figure 3.2. By increasing the humidity, which is related to an increase in water vapor and temperature, refractivity also increases, while the refractivity decreases with a decrease in these two effective atmospheric parameters (Lawrence 2005).

Although the refractivity theoretically should decrease with higher elevation, the mean refractivity calculated at INUQ and IVKQ GPS sites shows some inconsistencies. The refractivity values at these sites are smaller than expected due to the very low local temperatures and partial water vapor pressure for the time period of five years between 2008 and 2012, when compared to the other stations in southern region. The mean temperature of these sites in the considered time span is approximately, $-3.40 \pm 0.06^\circ$ and $-6.47 \pm 0.05^\circ$ Celsius, respectively. Moreover, as presented in Table 3.1 and Figure 3.2, they have the lowest dew point temperatures and therefore the lowest water vapor pressure (Alduchov & Eskridge 1996). The dew point temperature at INUQ is $-6.72 \pm 0.06^\circ$ Celsius and $-9.56 \pm 0.05^\circ$ Celsius at IVKQ (Table 3.1). Also as presented in Table 3.1, the water vapor pressure computed for these sites is approximately 5.34 ± 0.02 and 4.13 ± 0.01 mbar, respectively.

The plot of mean refractivity with elevation at each GPS station ranges from 0 to 400 m above msl. In this paper, we calculate the decay parameter by fitting the exponential models to the vertical profile of computed mean refractivity at eight stations for four different scenarios in order to estimate a value very close to the given global empirical values. The exponential models and the associated 95% confidence interval for the four scenarios are shown in Figure 3.4. As this figure illustrates, the fitted exponential model for all scenarios is almost linear within the ranges of considered elevations. This matches well to the linear relationship of refractivity at heights below one km found by Samsonov et al. (2014) using radiosonde data.

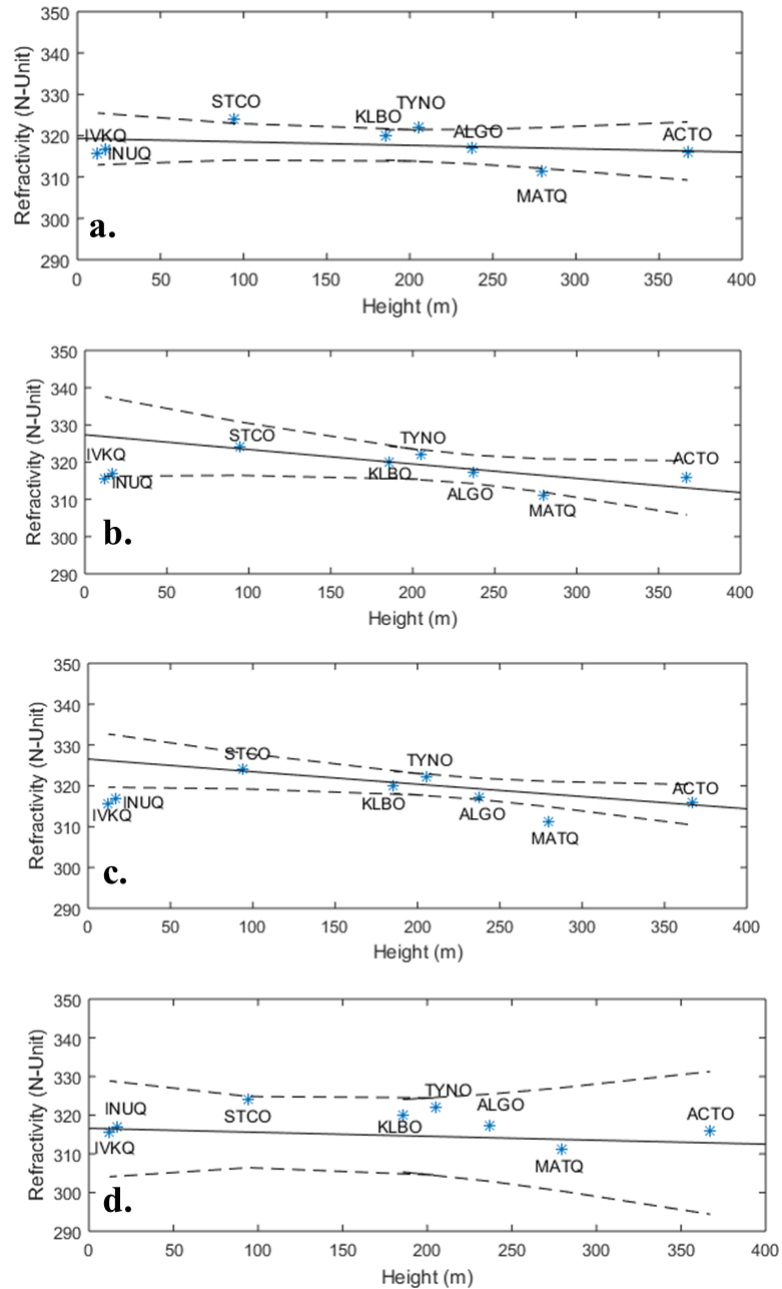


Figure 3.4. Vertical profile of the mean refractivity at GPS stations (blue stars). Comparison of the fitted exponential model a) to the values of all eight stations b) to the values of all stations except for that at INUQ and IVKQ c) to the values of all weather stations except MATQ, INUQ and IVKQ; d) to the values of stations INUQ, IVKQ, MATQ and ALGO. The 95% confidence intervals for the calculated exponential fit to the data in each scenario is presented with dashed lines.

In the first scenario, we fitted an exponential model to the values of refractivity at all eight stations (Figure 3.4a). INUQ and the IVKQ stations are excluded in the second scenario as they have the lowest temperature and inconsistent refractivity (Figure 3.4b). Because MATQ has the lowest temperature after INUQ and IVKQ, in scenario 3 an exponential model was fitted to the refractivity values at all stations except to those refractivity values computed for MATQ, INUQ, and IVKQ (Figure 3.4c). In scenario 4 we model an exponential fit to the values of IVKQ, INUQ, MATQ, and ALGO in order to calculate the decay parameter for stations with more consistent regional physical properties (Figure 3.4d).

Among the fitted exponential functions in the four scenarios, that function in scenario 2 provides a better fit to the mean refractivity of the GPS stations. In addition, the 95% confidence interval of the fitted exponential function in this scenario incorporates the estimates of the mean refractivity at INUQ and IVKQ, although they were not included in the fitting process itself. The refractivity decay parameter computed in this scenario is equal to 0.121 km^{-1} and the mean value of refractivity is equal to 327.5 N-units (the radio refractivity).

In addition to the good matches of the mean value of refractivity to the value observed by Samsonov et al. (2014) for the altitudes below one km, 334 N-units, the estimated decay parameter also is in good agreement with the empirical value given by Bean & Thayer (1959). According to Bean & Thayer (1959), for elevations less than 9 km, the decay parameter for refractivity between 200 to 450 N-units ranges from 0.106 to 0.154 km^{-1} . Their decay parameter value of 0.122 km^{-1} corresponds to the mean refractivity 313 N-units, which is valid for mid-latitude regions.

Subsequently, in this paper, we only take into account the decay parameter, 0.121 km^{-1} , obtained from scenario 2. We use this value to calculate ZTD at each station in our study area. These results confirm that in the absence of radiosonde data, employing meteorological data will produce a reasonable estimate of the decay parameter for elevations below one km.

By substituting the estimated decay parameter and the refractivity computed at each GPS station in Equation 3.10, ZTD at each station can be computed.

3.3.3 Computing the elevation-dependent seasonal amplitude

Study of the seasonal fluctuation of ZTDs is important as they are mainly dependent on the variations of ZWD and therefore can provide significant information for monitoring of climate variations (Jin et al. 2007). Based on the model for computing the seasonal amplitude of ZTD in DInSAR data of Samsonov et al. (2014), we propose a model which can accurately estimate the local elevation-dependent seasonal amplitude of the differenced ZTD at each station relative to a reference station.

From Equation 3.10, the ZTD between the reference station and the other station can be computed as follow:

$$\Delta ZTD_{MET}(t, z_r, z_i) = 10^{-6} N_r(t) \int_{z_r}^{z_i} e^{-cz} dz \quad (3.11)$$

where, z_r and z_i are the elevations of reference station and the other station with respect to msl, respectively.

In order to compute the seasonal amplitude of ZTD, we expand Equation 3.11 and take into account the seasonal amplitude of refractivity instead of the time series of refractivity, as done by Samsonov et al. (2014), and we obtain

$$amp_{ZTDi}(z_r, z_i) = \left| \frac{10^{-6}(amp_{Nr})}{ce^{cz_r}} (1 - e^{-c(z_i - z_r)}) \right| \quad (3.12)$$

where, amp_{Nr} (N-units) is the average seasonal amplitude of refractivity at Earth's surface at the reference station, here station ACTO at 367.22 m above msl.

Because we consider the reference station at a greater altitude than that of the other stations in our study, $z_r \geq z_i$, we considered the absolute value of the resulting equation to prevent producing negative values for the amplitudes of the troposphere.

The amplitude of the refractivity at Earth's surface is computed as 18.93 N-units by fitting a simple annual sinusoidal function to the daily refractivity time series estimated at

station ACTO (Figure 3.3). In the next section, we compare the seasonal amplitudes of ZTD computed from the proposed model to the seasonal amplitudes of the differenced ZTD at every site. As noted by Li et al. (2006), the advantage of considering the differenced ZTD rather than absolute values is that the differenced ZTD values will reduce the impacts of the terrain elevation dependency of the ZTD and ZWD variations and provide more useful information.

3.3.4 Precipitable Water Vapor

The weather and climate changes that result in variations in atmospheric water vapor can be monitored through the measurement of PWV from observed ZTDs. Traditional techniques, such as radiosondes and radiometers, are expensive and have limited spatial coverage and temporal resolution. PWV is the vertical integration of the amount of water vapor from Earth's surface in the atmosphere and may be expressed either in g/cm^2 or in terms of the height of an equivalent vertical column of water vapor in centimeter. Therefore, employing the wet component of the ZTDs which is a function of temperature and water vapor pressure can provide an opportunity for retrieval of PWV (Karabatic et al. 2011).

As mentioned earlier, the ZHD can be computed accurately by employing a pressure dependent function. Removing this component from the total troposphere delay will result in ZWD. In this paper, we use the model developed by Saastamoinen (1973) to compute ZHD at each station as follow:

$$ZHD = \frac{0.002277P}{1-0.0026\cos^2\phi-0.00028H} \quad (3.13)$$

where, P is the air pressure at a GPS station (mbar), H is the elevation above msl in km, ϕ is the latitude of the station.

Note that the pressure in Equation 3.13 was measured at the weather station nearby the GPS station and computed at the GPS station using Equation 3.2.

Then PWV at each station can be computed from the obtained ZWD at each station by using the conversion factor proposed by Bevis et al. (1994) as follow (Equation 3.14):

$$PWV = 10^6 [R_V (-\frac{R_d}{R_V} k_1 + k_2 + \frac{k_3}{T_m})]^{-1} \times ZWD \quad (3.14)$$

where, R_V is the gas constant for water vapor, $461 \text{ K}^{-1}\text{kg}^{-1}$, and R_d is the gas constant for dry air, $287 \text{ JK}^{-1}\text{kg}^{-1}$, K_i are the physical refractivity constants given in section 3.2.1. T_m is the weighted mean surface temperature and can be calculated by employing the accepted formula proposed by Mendes et al. (2000) as

$$T_m = 50.4 + 0.789 T_s \quad (3.15)$$

where, T_s is the surface temperature in Kelvin.

It is worthwhile to mention that evaluation of the sensitivity of the obtained PWV to the surface temperature performed by Pikridas et al. (2014) and Liu et al. (2005) shows that the uncertainties of the surface temperature do not significantly influence the PWV estimates.

3.4 Results and Discussion

In this section, we discuss the GPS-ZTD and MET-ZTD obtained for each station. In addition, we compare the seasonal amplitude of ZTD computed by using the proposed elevation-dependent exponential model to the seasonal amplitude of the differenced ZTD at each station relative to station ACTO. The differenced ZTD is defined as the ZTD computed for the reference station, here station ACTO at the height of 367.22 m above msl, subtracted from the ZTD computed for each of the other stations. Moreover, we present the results of the computed PWV for every station in our study.

3.4.1 The comparison between GPS-ZTD and MET-ZTD

In order to compare the results of the computed GPS-ZTD and MET-ZTD at each station, we calculate the linear correlation coefficients between each pair of daily averaged ZTD time series based on Pearson Product Moment Correlation (PPMC) approach.

Figure 3.5 shows the correlogram, a visual presentation of the correlation matrix, created from the correlation of the ZTD time series. Each correlation coefficient is shown with a color. The variables in this matrix, from left to right, are sorted from low to high latitude

to satisfy the study of the pattern of dependency among variables. The low correlation coefficient between the observed GPS-ZTD and MET-ZTD at station IVKQ, as compared to the other stations (0.60, yellow color, Figure 3.5), is probably because the Cape Dorset weather station, which was employed to compute the MET-ZTD, is 213 km from IVKQ GPS station. Therefore, although the weather parameters corrected for the height difference between the weather station and GPS station, the resulting meteorological parameters cannot accurately reproduce the ZTD at station IVKQ. Horizontal interpolation of the meteorological data from the meteorological stations might produce a better match in the absence of nearby weather station (Gendt et al. 2004; Alshawaf et al. 2017).

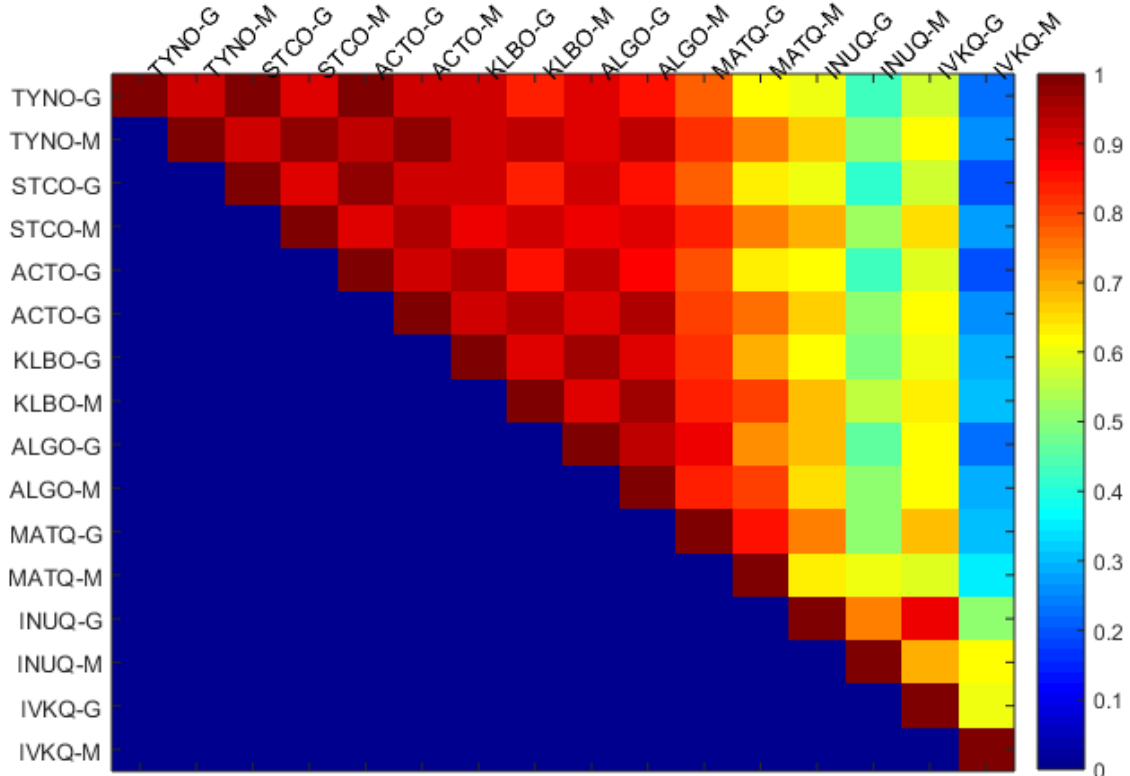


Figure 3.5. Correlogram of the Pearson's linear correlation coefficients between all pairs of ZTD time series calculated from the two strategies, using GPS data and meteorological data at all GPS stations. G and M stand for GPS data and meteorological data, respectively. The scale bar represents the correlation coefficient values. The variables from left to right are sorted for the stations from low to high latitude.

As shown in Figure 3.5, the ZTDs at stations in southeastern Ontario (lower latitude) have lower correlation with the ZTDs at stations in northwestern Québec (higher latitude). For example, as seen in the first row of the correlogram, the correlations between the GPS-ZTD at TYNO and the GPS-ZTD at other stations is decreasing from left to right, with increasing latitude.

The comparison between the mean of the daily averaged MET-ZTD and GPS-ZTD at each station in Table 3.2 shows that the estimated mean of MET-ZTD is greater than the mean of GPS-ZTD at all stations and ranges between 0 and 5 cm. Also, Table 3.2 represents the rms differences between daily averaged MET-ZTD and GPS-ZTD, that range between 3.78 and 11.01 cm.

3.4.2 The comparison between the elevation-dependent seasonal amplitude of ZTDs

In this paper, we consider station ACTO as the reference station. Therefore, all the ZTD time series computed from GPS data are subtracted by the GPS-ZTD computed for station ACTO as ΔZTD_{GPS} .

By fitting a simple annual sinusoidal function to the obtained ΔZTD_{GPS} at each station, we compute the seasonal amplitude at the corresponding station. In addition, we calculate the seasonal amplitude of the ZTD for every locations at an altitude between 0 and 1000 m above msl relative to station ACTO from Equation 3.12. These amplitudes are illustrated in Figure 3.6. As seen in this figure, the modeled seasonal amplitudes increase with above the elevation of the reference station, 367.22 m above msl. The results are in good agreement with those obtained from Samsonov et al. (2014) in which they considered a location at msl as a DInSAR reference point and observed an increase in the seasonal amplitude of ZTD with increasing height.

Figure 3.6 indicates the computed seasonal amplitudes of ΔZTD_{GPS} at each station (red star) relative to ACTO overlain with the modeled seasonal amplitudes (blue line). By substituting the altitude of each station in Equation 3.12, the seasonal amplitude of ZTD for the corresponding station relative to station ACTO is obtained. Comparison of the modeled and observed estimates shows that the seasonal amplitude of ΔZTD_{GPS} at all

stations, except those at stations INUQ and IVKQ, are within the 95% confidence interval of the modeled seasonal amplitudes.

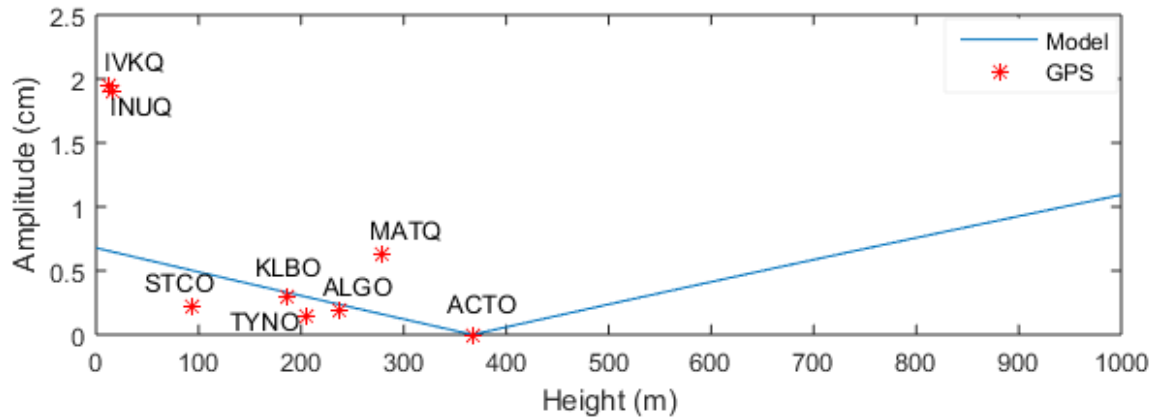


Figure 3.6. The vertical profile of the seasonal amplitude of the ΔZTD_{GPS} , obtained from the sinusoidal signal fitted to the difference between GPS-ZTD at each station and at station ACTO (red start) overlain with the seasonal amplitudes modeled by using Equation 3.12 for the points at altitudes between 0 and 1000 m msl (blue solid line).

From Table 3.2, the differences at all stations, again with the exception of stations INUQ and IVKQ range between -0.47 and 0.28 cm. The large difference, up to 1.3 cm, for INUQ and IVKQ probably relates to the low correlation between the ZTD at station ACTO and ZTDs at stations INUQ and IVKQ, discussed earlier. To verify the seasonal amplitudes of ΔZTD_{GPS} at GPS stations, we can compare them to the observed seasonal amplitudes of ZTD in the height time series of DInSAR points in the study carried out by Samsonov et al. (2014; see Figure 3.4) based on the parameters derived from the exponential fitting model for their radiosonde data and shown for points higher than 200 m above msl. We conclude that there is a good agreement for the results at stations MATQ and ALGO.

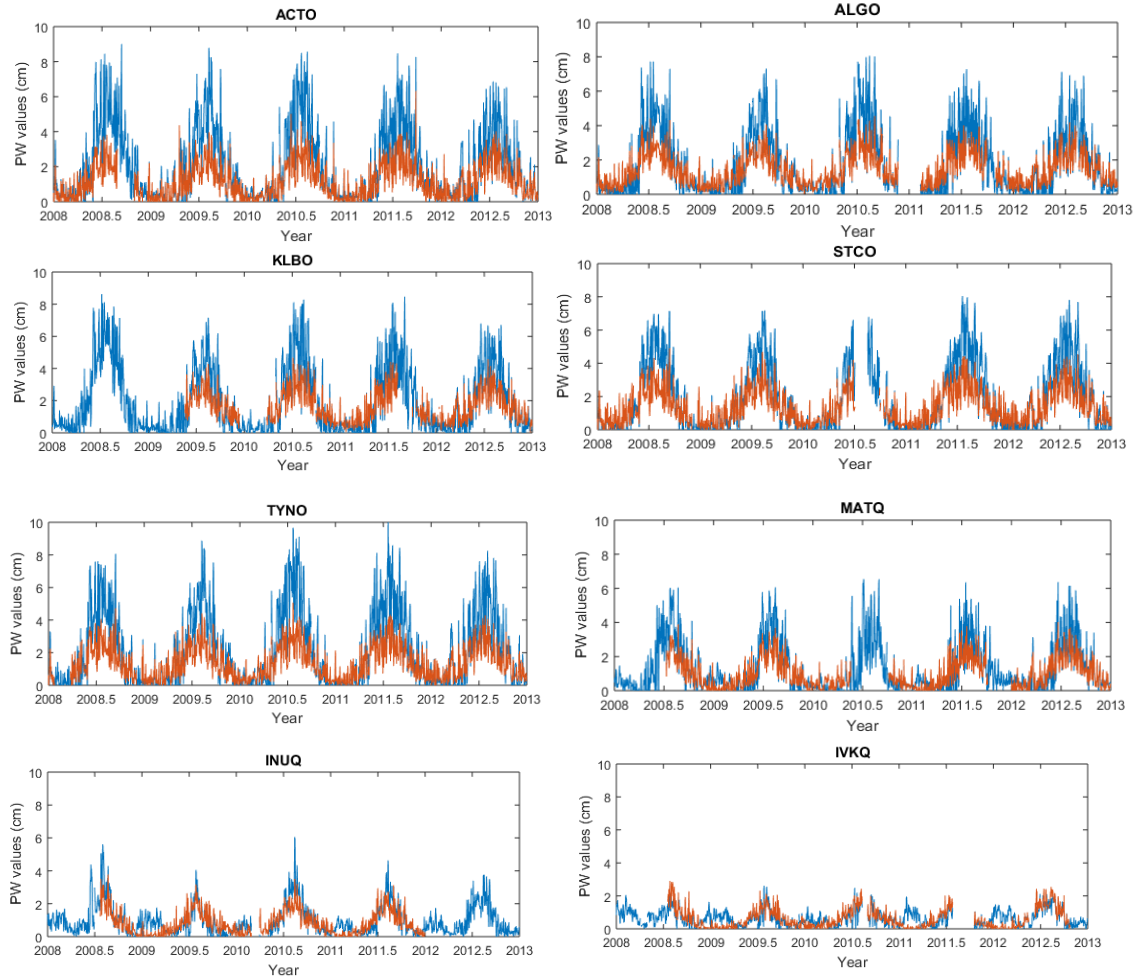


Figure 3.7. Comparison between daily GPS-PWV (red) and MET-PWV (blue) time series between 2008 and 2012.

3.4.3 The comparison between GPS-PWV and MET-PWV

Based on the pressure data at each GPS station and the latitude and elevation of the station, the ZHD can be computed by using Equation 3.13. Removing of the daily averaged of this component from the daily averaged MET-ZTD and GPS-ZTD at each station, produces MET-ZWD and GPS-ZWD, respectively. Then by substituting the MET-ZWD and GPS-ZWD in Equation 3.14 and using the relationships given in Equation 3.15 to compute the weighted mean surface temperature from the surface temperature, we can compute the MET-PWV and GPS-PWV at each station.

Figure 3.7 illustrates a comparison between the MET-PWV and GPS-PWV between 2008 and 2012. As this figure indicates, daily variations of these time series are similar to each other; the minimum occurs in winter and the maximum in summer. However, a large difference between the two time series at each station is noticeable between July and mid-September, when the winter snow begins to melt and the daily rainfall and perceptible water vapor increase. The research carried out by Joshi et al. (2013) also studied the PWV from GPS data and MODIS data and found that MODIS overestimates the amount of column water vapor in compare to the estimates from GPS data. They observed that the magnitude of the differences between PWV from MODIS and GPS data and the root-mean-square error (RMSE) of their residuals, systematically changes every season depending on the amount of water vapor.

This also can be seen in the mean values of MET-PWV which are greater than the mean values of GPS-PWV at all stations presented in Table 3.2. Their differences range between 0.05 and 0.89 cm in all five years between 2008 and 2012.

In order to validate the mean values of the PWVs at all stations, we compared them to the exponential function proposed by Reitan (1963) for computing PWV based on dew point temperature at each site:

$$PWV = \exp(aT + b) \quad (3.16)$$

where, PWV is in cm, T is the dew point temperature in degrees Fahrenheit, a is constant and is equal to 0.0393, b depends on the latitude and λ at each station and is computed as $(0.1133 - \ln(\lambda + 1))$ (Smith 1966), a , b and λ are unitless.

By using λ from Table 3.2 and T from Table 3.1 for each station, the mean annual PWV is estimated for the corresponding station. We obtained exponentially increasing values of the mean PWV, from 0.59 through 1.47 cm, by increasing the mean dew point temperature, from -9.56 ± 0.05 C° to 4.83 ± 0.05 C°. Comparison of the results of Equation 3.16 to the mean of both GPS-PWV and MET-PWV provides the difference in ranges: between -0.2 and 0.4 cm and -0.71 and -0.07 cm, respectively.

Again, the overestimated mean values of MET-PWVs at all stations also can be observed by comparing them to the results of Equation 3.16. The difference between the MET-PWV and GPS-PWV is very small at stations IVKQ and INUQ, located in a dry, cold area near Hudson Bay where the water vapor pressure and temperature are always low.

3.5 Conclusion

In this paper, we proposed a one-dimensional simplified model to compute the elevation-dependent seasonal amplitude of the local ZTD in GPS data in our study area, despite the fact that the variation in topography in this regions is not substantial. This model was based on the refractivity decay parameter with elevation and the meteorological data at a reference station's location. The modeled seasonal amplitudes at eight stations were compared to the seasonal amplitudes of ZTD computed by using PPP techniques at the corresponding stations.

Here, we produced the ZTD time series between 2008 and 2012 for eight GPS stations in eastern Ontario and western Québec using GPS data and local meteorological data, where all the GPS data were processed using the CSRS-PPP online service and the meteorological data were corrected for the height difference between the GPS station and the nearby weather station. Incorporating the meteorological data from near the GPS station provides a more accurate and high-resolution understanding of the weather condition at the GPS stations' locations.

Here, the refractivity at every GPS station in our study was computed based on the corrected meteorological data. Also, we elaborated on the high dependency of the mean refractivity on the partial water vapor pressure and temperature. We observed that the inconsistency of the refractivity at stations INUQ and IVKQ is a result of the lower water vapor pressure and temperature than expected, which is related to their location near Hudson Bay, which is cold and dry.

Moreover, we successfully computed a refractivity decay parameter of 0.121km^{-1} by fitting an exponential function to the estimates of the mean refractivity at all GPS stations, excluding INUQ and IVKQ, as a function of height. In addition to the fact that

the results are close to the given global empirical values and to the other studies for elevations below one km, the 95% prediction confidence intervals of the fitted exponential function also incorporates the estimates of the mean refractivity at INUQ and IVKQ, although they were not included in the fitting process.

Besides observing a positive correlation between the GPS-ZTD and MET-ZTD at every GPS station, we also observe that the ZTDs of the stations in southeastern Ontario are less correlated with the ZTDs of the stations in northeastern Québec. As determined by other researchers (Eamrdson et al. 2003), the correlation between ZTDs is highly dependent on the distance between them. This confirms the idea that studying the absolute ZTDs in an area with sparsely spaced GPS stations will provide more accurate information about the local weather conditions.

We produced a highly accurate estimate of mean ZTD obtained from CSRS-PPP that was compared with the results obtained from meteorological data. Although we found very close matches, from 0 to 5 cm, between the mean of the daily time series of the two ZTDs, the mean values of MET-ZTD are greater than the GPS-ZTD at all sites.

In this paper, we considered station ACTO as the reference station, and therefore the refractivity time series at the location of this station and the refractivity decay parameter estimated already are employed to estimate the elevation-dependent seasonal amplitudes of ZTDs at each station relative to station ACTO. As expected, the modeled seasonal amplitudes increase with altitude from the reference point's altitude, 367.22 m above msl. Good agreement between the estimates from the model and those observed from ΔZTD_{GPS} for all GPS stations except INUQ and IVKQ. The very large amplitudes observed for the seasonal fluctuations in ΔZTD_{GPS} at these two stations probably relate to the low correlation between their ZTD and the ZTD at station ACTO.

In this paper, we also studied the amount of the PWV in the atmosphere between 2008 and 2012 by using the GPS-ZWD and MET-ZWD obtained by removing the estimates of the hydrostatic component of troposphere delay from the total troposphere, GPS-ZTD and MET-ZTD, at each GPS station. The computed mean of daily time series of GPS-PWV and MET-PWV at all stations range between 0.61 ± 0.01 and 1.67 ± 0.02 cm and

between 0.66 ± 0.01 and 2.13 ± 0.05 cm, respectively. The PWVs are highly dependent on the water vapor pressure and humidity of the region. Between July and September, the daily humidity and rainfall increases with temperature and therefore result in abundant water vapor pressure during that period.

As suggested by Joshi et al. (2013), employing meteorological data in conjunction with the GPS analysis is a good technique for studying the monsoonal patterns and the weather conditions of a given region as well. In addition, these results indicate that the proposed model can accurately estimate the seasonal amplitude of ZTD on a local GPS network and are comparable with the seasonal amplitude of ZTD resulted from high precise positioning techniques. Moreover, by using the radiosonde data for estimating the decay parameter of refractivity or employing the estimates of decay parameter from other researches, the proposed model eliminates the need for the meteorological data at each individual station. Also, employing the proposed model can provide important information about the seasonal variations of the ZTD in the local scale. Hence, its combination with or its application instead of the low spatial resolution models such as those obtained from ECMWF can produce higher positioning accuracy at sub-millimeter levels. Finally, given the similarity of the effect of ZTD on both DInSAR and GPS data, the ZTD estimation method developed here may be applied to future studies for correcting DInSAR height time series.

3.6 References

- Alduchov, O.A., and Eskridge R.E. (1996), Improved Magnus form approximation of saturation vapor pressure, *J. Appl. Meteorol.*, 35 (4), 601-609. doi: 10.1175/1520-0450(1996)035<0601:IMFAOS>2.0.CO;2
- Alshawaf, F., Balidakis K., Dick G., Heise S., and Wickert J. (2017) Estimating trends in atmospheric water vapor and temperature time series over Germany
- Askne, J., and Nordius H. (1987), Estimation of tropospheric delay for microwaves from surface weather data. *Radio Science*, 1987, 22(3):379–386.

- Bai, Z., and Feng, Y. (2003), GPS water vapor estimation using interpolated surface meteorological data from Australian automatic weather stations. *Journal of Global Positioning Systems* 2, 83-89.
- Bar-Sever Y.E., Kroger, P.M., and Borjesson J.A. (1998), Estimating horizontal gradients of tropospheric path delay with a single GPS receiver. *J Geophys Res* 103(B3):5019–5035
- Bean, B.R., and Thayer G.D. (1959), Models of the atmospheric radio refractive index, *Proc. IRE*, 47, 740-755.
- Berg, R.E. and Holliday T. (2011), Precise Point Positioning Accuracy Analysis for Integrated Surveys. *Ontario Professional Surveyor*, Volume 54, No. 2, Spring 2011, pp. 32-37.
- Bernhardt, P.A., Selcher C.A., Basu S., Bust G., and Reising S.C. (2000), Atmospheric Studies with the Tri-Band Beacon Experiment on the COSMIC Constellation, *Terr. Atmos. Oceanic Sci.* 11(1): 291-312
- Bevis M., Businger S., Herring T.A., Rocken C., Anthes R.A., and Ware R.H. (1992), GPS meteorology: remote sensing of atmospheric water vapor using the Global Positioning System. *J Geophys Res* 97:15784–15801
- Bevis, M., Businger S., and Chiswell S. (1994), GPS meteorology: Mapping zenith wet delays on to Precipitable water, *J. Appl. Meteorol*, 33, 379 – 386.
- Bianchi, C. E., Mendoza L. P. O., Fernández L. I., Natali M. P., Meza A. M., and Moirano J. F. (2016), Multiyear GNSS monitoring of atmospheric IWV over Central and South America for climate studies. *Annales Geophysicae*, 34, 623-639, doi: 10.5194/angeo-34-623-2016.
- Boehm J., Niell A., Tregoning P., and Schuh H. (2006a), The Global Mapping Function (GMF): A new empirical mapping function based on data from numerical weather model data. *Geophysical Research Letters* 33 L07304
DOI:10.129/2005GL025546

- Boehm J., Werl, B., and Schuh H. (2006b), Troposphere mapping functions for GPS and very long baseline interferometry from European Centre for Medium-Range Weather Forecasts operational analysis data. *J Geophys Res.* 111 B02406 DOI: 10.1029/2005JB003629
- Bos M.S., and Scherneck, H.G. (2011), Free Ocean Tide Loading Provider URL <http://holt.oso.chalmers.se/loading>
- Celestino C.C., Sousa C.T., Yamaguti W., and Kuga H.K. (2007), Evaluation of Tropospheric and Ionospheric Effects on the Geographic Localization of Data Collection Platforms. *Mathematical Problems in Engineering – MPE*, volume 2007, Article ID 32514, 11 pages, doi:10.1155/2007/32514.
- CSRS-PPP (CSRS-PPP Canadian Spatial Reference System -Precise Point Positioning) service. http://www.geod.nrcan.gc.ca/products-produits/ppp_e.php (2013). Accessed 1 July 2017
- Danielson, E.W. (1969), The surface heat budget of Hudson Bay. McGill University, Marine Sciences Centre, Manuscript Report No. 9. 196 pp.
- Dousa J, and Elias, M. (2014), An improved model for calculating tropospheric wet delay, *Geoph. Res. Lett.* 41, doi:10.1002/2014GL060271
- Dousa, J., (2010), Precise near real-time GNSS analyses at geodetic observatory Pecny–precise orbit determination and water vapour monitoring (Report). *Acta Geod. Geomat.* 7, 7.
- Duan, J., Bavis M., Fang, P., Bock, Y., Chiswell, S., Businger, St., Rocken C., Solheim, F., van Hove, T., Ware, R., McClusky S., Herring, T.A., and King, R.W. (1996), GPS meteorology: Direct estimation of the absolute value of precipitable water, *J. Appl. Meteorol.*, 35, 830-838.
- Eaton, D.W., Adams J., Asudeh I., Atkinson G.M., Bostock M.G., Cassidy J.F., Ferguson I.J., Samson C., Snyder D.B., Tiampo K.F., and Unsworth, M.J. (2005),

Investigating Canada's lithosphere and earthquake hazards with portable arrays. *Eos* 86(17):169–176. doi:10.1029/2005EO170001

Elizabeth, J. P., Matt A.K., Philip M., and David A.L. (2010), A first look at the effects of ionospheric signal bending on a globally processed GPS network. *J Geod*, Vol. 84, pp. 491-499, DOI 10.1007/s00190-010-0386-2.

Elliott, W. P., and Gaffen D.J. (1993), Effects of conversion algorithms on reported upper-air dewpoint depressions, *Bull. Am. Meteorol. Soc.*, 74, 1323 – 1325, doi:10.1175/1520-0477(1993)0742.0. CO;2.

El-Mowafy, A. (2011), Precise Real-Time Positioning Using Network RTK. In S. Jin, *Global Navigation Satellite Systems: Signal, Theory and Applications* (pp. 161-187). Rijeka, Croatia: InTech.

Emardson, T. R., Simons M., and Webb F.H. (2003), Neutral atmospheric delay in interferometric synthetic aperture radar applications: Statistical description and mitigation. *J. Geophys. Res. Solid Earth*, 108 (2003), p. 2231 <http://dx.doi.org/10.1029/2002JB001781>

Flouzat M, Bettinelli P, Willis P, Avouac JP, Heriter T, and Gautam U. (2009), Investigating tropospheric effects and seasonal position variations in GPS and DORIS time series from the Nepal Himalaya. *Geophys J Int* 178(3):1246–1259

Fotiou, A., and Pikridas C. (2012), *GPS and Geodetic Applications*, 2nd edn, Ed. Ziti, Thessaloniki, Greece.

Gendt, G., Dick G., Reigber C., Tomassini M., Liu Y., and Ramatschi M. (2004), Near real time GPS water vapor monitoring for numerical weather prediction in Germany, *J. Meteorol. Soc. Jpn.*, 82, 361 – 370

Geng, J., Shi, C., Ge, M., Dodson, A.H., Lou, Y., Zhao, Q., and Liu, J. (2012), Improving the estimation of fractional-cycle biases for ambiguity resolution in precise point positioning, *J. Geod.*, 86, 579–589.

- Hoque, M.M., and Jakowski N. (2012), Ionospheric Propagation Effects on GNSS Signals and New Correction Approaches. In Tech. ISBN 978-953-307-843-4.
- Jin S, Park JU, Cho JH, Park PH. (2007), Seasonal variability of GPS-derived zenith tropospheric delay and climate implications. *J. Geophys. Res.* 112: D09110.
- Jin, S.G. (2012), GNSS Atmospheric and Ionospheric Sounding: Methods and Results, in S.G. Jin (Ed.), *Global Navigation Satellite Systems- Signals, Theory and Applications*, InTech-Publisher, Rijeka, Croatia, ISBN: 979-953-307-132-8, pp.359-380.
- Joshi, S., Kumar, K., Pande, B., and Pant, M.C., (2013), GPS-derived precipitable water vapour and its comparison with MODIS data for Almora, Central Himalaya, India. *Meteorol. Atmos. Phys.* 120 (3), 177–187.
- Karabatic, A., Weber, R., and Haiden, T., (2011), Near real-time estimation of tropospheric water vapour content from ground based GNSS data and its potential contribution to weather now-casting in Austria. *Adv Space Res* 47:1691–1703
- Katsougiannopoulos, S. (2008), Study of tropospheric effect on GNSS signals. Application to the European area. PhD thesis, Department of Geodesy and Surveying, Aristotle University of Thessaloniki, Greece
- Kim, B.C., and Tinin, M.V. (2011), Potentialities of multifrequency ionospheric correction in Global Navigation Satellite Systems, *J Geod.*, 85: 159. <https://doi.org/10.1007/s00190-010-0425-z>
- Klobuchar, J.A. (1996), Ionospheric Effects on GPS, In: *Global Positioning System: Theory and Applications*, Vol I, Parkinson, B. W. & Spilker, J. J. (Eds.), pp. 485-515, American Institute of Aeronautics & Astronautics, ISBN 156347106X
- Lahaye, F., Mireault, Y., Héroux, P., Tétreault, P. and Kouba, J. (2008) A New, Timely Service from Natural Resources Canada”, *GPS World*, Sept. 2008, accessed in June 2011 online: <http://sidt.gpsworld.com/gpssidt/article/articleDetail.jsp?id=549570>.

- Lawrence, M. G. (2005), The relationship between relative humidity and the dewpoint temperature in moist air: A simple conversion and applications, *Bull. Amer. Meteor. Soc.*, 86(2), 225–233, doi:10.1175/BAMS-86-2-225.
- Li, P.W., Wang X.Y., Chen Y.Q., and Lai S.T. (2005), Use of GPS signal delay for real-time atmospheric water vapor estimation and rainfall nowcast in Hong Kong, *The First International Symposium on Cloud-prone & Rainy Areas Remotes Sensing*, Chinese University of Hong Kong, October 6-8.
- Li, Z., Fielding E.J., Cross P., and Muller J.P. (2006a), Interferometric synthetic aperture radar (InSAR) atmospheric correction: MEdium Resolution Imaging Spectrometer (MERIS) and Advanced Synthetic Aperture Radar (ASAR) integration, *Geophys. Res. Lett.*, doi: 10.1029/2005GL025299.
- Li, Z., Muller J.P., Cross P., Albert P., Fischer J., and Bennartz R. (2006b), Assessment of the potential of MERIS near-infrared water vapour products to correct ASAR interferometric measurements, *Int J Remote Sens*, 27 (1-2), 349-365.
- Liu, J. Y., Chen C.H., Sun Y.Y., Tsai H.F., Yen H.Y., Chum J., Lastovicka J., Yang Q.S., Chen W.S., and Wen S., (2016), The vertical propagation of disturbances triggered by seismic waves of the 11 March 2011M9.0 Tohoku earthquake over Taiwan, *Geophys. Res. Lett.*, 43(4), 1759–1765
- Liu, J., Sun Z., Liang H., Xu X. , and Wu P. (2005), Precipitable water vapor on the Tibetan Plateau estimated by GPS, water vapor radiometer, radiosonde, and numerical weather prediction analysis and its impact on the radiation budget, *J. Geophys. Res.*, 110, D17106, doi:10.1029/2004JD005715.
- Martin, F., and Waldron C. (1961), A layered exponential model of radar refractivity, *J. Geophys. Res.*, 66(12), 4129–4135, doi:10.1029/JZ066i012p04129.
- Maxwell, J.B. (1986), A climate overview of the Canadian inland seas. In Martini, I.P., ed. *Canadian inland seas*. Amsterdam: Elsevier. 79–99.

- Mendes, V.B., Prates G., Santos L., and Langley R.B. (2000), An evaluation of the accuracy of models of the determination of the weighted mean temperature of the atmosphere. In: Proceedings of ION, 2000 national technical meeting, Jan 26–28, Pacific Hotel Disneyland, Anaheim, CA.
- Mendes, V.B., Collins P., and Langley R.B. (1995), The effect of tropospheric propagation delay errors in airborne GPS precision positioning. Proceedings of ION GPS-95, the 8th International Technical Meeting of the Satellite Division of The Institute of Navigation, Palm Springs, Calif., 12-15 September, pp. 1681-1689.
- Morland, J., Collaud Coen, M., Hocke, K., Jeannet, P., and Mätzler, C., (2009). Tropospheric water vapour above Switzerland over the last 12 years. *Atmospheric Chemistry and Physics*, 9(16), pp. 5975–5988.
- Musa TA, Amir S, Othman R., Ses, S., Omar, K., Abdullah, K., Lim, S., and Rizos, C., (2011), GPS meteorology in a low-latitude region: remote sensing of atmospheric water vapor over the Malaysian Peninsula. *J Atmos Sol Terr Phys* 73(16):2410–2422. doi:10.1016/j.jastp.2011.08.014
- Pikridas C., Katsougiannopoulos S., and Zinas N., (2014), A comparative study of zenith tropospheric delay and precipitable water vapor estimates using scientific GPS processing software and web based automated PPP service, *Acta Geodaetica et Geophysica*, June 2014, Volume 49, Issue 2, pp 177-188.
- Reitan, C.H., (1963), Surface dew point and water vapor aloft. *J. Appl. Meteorol.* 2, 776–779.
- Rueger, J. M. (2002), Refractive index formulae for radio waves." FIG XXII International Congress, International Federation of Surveyors (FIG), Washington, D.C., April 19–26. http://www.fig.net/pub/fig_2002/Js28/JS28_rueger.pdf.
- Saastamoinen, J., (1973), Contribution of the theory of atmospheric refraction, *Bulletin of Geodesique*, No. 105, pp. 279–298, No. 106, pp. 383–397, No. 107, pp. 13–34.

- Samadi Alinia, H., Tiampo K.F., James T.S., (2017), GPS coordinate time series measurements in Ontario and Québec, Canada, *J. Geodesy*, *J. Geodesy*. 31 pages. DOI 10.1007/s00190-016-0987-5.
- Samsonov, S.V., Trishchenko A.P., Tiampo K.F, González P.J., Zhang Y., and Fernández J. (2014), Removal of systematic seasonal atmospheric signal from interferometric synthetic aperture radar ground deformation time series, *Geophys. Res. Lett.*, 41, 6123–6130, doi:10.1002/2014GL061307.
- Schuler, T. (2001), On ground-based GPS tropospheric delay estimation, Doctor's Thesis, Studiengang Geodsie und Geoinformation, Universitt der Buundeswehr Munchen, Germany, Vol. 73, Neubiberg.
- Shrestha, S.M. (2003), Investigations into the Estimation of Tropospheric Delay and Wet Refractivity Using GPS Measurements (M.Sc. thesis), UCGE Report No. 20180.
- Smith, W. L. (1966), Note on the relationship between total precipitable water vapor and surface dew point, *J. Appl. Meteor.*, 5, 726–727.
- Sokolovskiy, S., Schreiner W., Rocken C., and Hunt D. (2008), Optimal Noise Filtering for the Ionospheric Correction of GPS Radio Occultation Signals, *J. Atmos. Oceanic Tech.* 26 (7), 1398-1403.
- Solheim, F.S., Vivekanandam J., Ware R.H., Rocken C. (1999), Propagation delays induced in GPS signals by dry-air, water vapor, hydrometeors and other particulates. *J. Geophys. Res.*, 104, 9663-9670.
- Steigenberger, P., Rothacher M., Dietrich R., Fritsche M., Ru'cke A., and Vey S. (2006), Reprocessing of a global GPS network. *J. Geophys. Res.*, 111, B05402, doi:10.1029/2005JB003747.
- Tregoning, P., and Watson C. (2009), Atmospheric effects and spurious signals in GPS analyses, *J. Geophys. Res.*, 114, B09403, doi:10.1029/2009JB006344.

Tregoning, P., and Herring, T.A. (2006), Impact of a priori zenith hydrostatic delay errors on GPS estimates of station heights and zenith total delays, *Geophys. Res. Lett.*, 33, L23303, doi:10.1029/2006GL027706.

Tregoning, P., Boers, R., O'Brien, D., and Hendy, M., (1998), Accuracy of absolute precipitable water vapor estimates from GPS observations, *J. Geophys. Res.*, 103, 28,701 – 28,710

Chapter 4

4 Modeling the elevation-dependent seasonal amplitude of tropospheric delays in GPS height time series using DInSAR and meteorology data³

In this work, I employ high-resolution DInSAR data to retrieve the local pattern of seasonal variations in ZTD and propose an elevation-dependent exponential model which provides the best fit to the amplitudes of all pixels. This model is based on the integration of the exponential refractivity function between the elevation of the DInSAR points and the DInSAR reference location. To achieve this, radiosonde data and meteorological data from a weather station collocated with the DInSAR reference location are utilized. The results show that the seasonal amplitudes increase exponentially from the elevation of the reference location. The study of the modeled seasonal amplitudes and the high frequency variations in differenced ZTD for each GPS station provides information about the variations of the water vapor pressure with height. The resulted rmse of the residuals decreases with growing elevation as the variability of the wet water vapor decreases with elevation. This confirms the high variability of water vapor at the lower altitudes regions. Our proposed approach has the potential to accurately estimate the seasonal amplitude of ZTDs in GPS data in areas of strong, local topographic relief that is not captured by low resolution weather models and without the need to acquire collocated meteorological observations to every GPS station.

³ A version of this chapter has been submitted to Geophysical Journal International. Samadi Alinia H., Tiampo, K.F., Samsonov, S.V., and González, P.J. (2017) Modeling the elevation-dependent seasonal amplitude of tropospheric delays in GPS height time series using DInSAR and meteorology data. *Geophys. J. Int* (under review)

4.1. Introduction

The troposphere is defined as the neutral, non-ionized layer of the atmosphere which extends from Earth's surface to an altitude of approximately 9-16 km. The lower part of this layer, below 10 km, results in a delay of the arrival of the signals in the radar frequency band and an increase in the range to the satellite of between 2 and 3 m (Spilker 1996; Klobuchar 1996). That delay can be divided into two main components, the hydrostatic (dry) and the wet component (Saastamoinen 1972). The hydrostatic component, a function of the dry gases in the atmosphere, causes approximately 90% of the total delay (Bevis et al. 1994; Fotiou & Pikridas 2012) and is computed from the surface air pressure measurements (Mendes & Langley 1994). The wet component constitutes the remaining effect of the delay and depends on the temperature and water vapor pressure, which are highly variable in space and time. This component has a larger contribution to the variations of the total delays in the radio signals (Bevis et al. 1994; Hanssen 1998; Fotiou & Pikridas 2012). The resulting biases in GPS vertical positioning imposed by ZTD can range over all wavelengths, with amplitudes of several centimeters. The wet component of delay is the major source of the seasonal variations in the total troposphere delay and it is highly dependent on the topography (Jin et al. 2007).

Several methodologies have been proposed to correct this error from GPS measurements. In general, these methods either use high-resolution meteorological data observed by the meteorological instruments at IGS GPS stations and NWP data from global weather forecasts such as ECMWF, which provides predicted components of delay at a grid spacing of $0.125^{\circ} \times 0.125^{\circ}$ (Bevis et al. 1992; Van Dam et al. 1994; Hofmann-Wellenhof et al. 2001; Foster et al. 2006; Fotiou & Pikridas 2012; Pikridas et al. 2014; Yuan et al. 2014), or standard models that are not dependent on the surface meteorological data (e.g., Hopfield model (Hopfield 1969), Saastamoinen model (Saastamoinen 1973) and modified Hopfield model (Goad & Goodman 1974). According to Jin et al. (2007), because of the strong dependency of the ZTD on the atmospheric parameters, ZTD obtained from non-meteorological data are not as accurate as the ZTDs obtained from meteorological data. However, the main issue is that only a few GPS stations have meteorological instrument to measure the weather parameters at the site (Vedel et al. 2001). Most recently, Lu et al.

(2016) conducted a study for providing a high-resolution tropospheric gradients and improvement in positioning accuracy by employing multi-GNSS processing.

Additionally, various studies have been carried out to mitigate the effect of troposphere delays in DInSAR data. These include those that consider cloud-free image pairs and average SAR interferograms (Zebker et al. 1997; Sandwell & Sichoix 2000), and employing the external data such as GPS measurements to take an advantage of the similar effects of the delay on both GPS and DInSAR signals (Bock & Williams 1997, Ge 2000, Hanssen 2001, Bonforte et al 2001; Ge et al. 2003; Tregoning & Van Dam 2005, Yu et al. 2017). Williams et al. (1998) suggested that sparse data such as GPS and ground-based meteorological data can be used to remove the long wavelength (low-frequency) components of atmospheric effects. In addition, some researchers use a combination of meteorological observations, GPS and digital elevation models (DEM) (Delacourt et al. 1998; Li et al. 2004) or apply a water vapor correction model integrated with GPS (Li et al. 2005; Onn & Zebker 2006; Samsonov et al. 2007). Li et al. (2005, 2006) proposed a novel approach to the tropospheric correction that uses a water vapor correction model with GPS data, and either the NASA Moderate Resolution Imaging Spectroradiometer (MODIS) data and/or ESA's Medium Resolution Imaging Spectrometer (MERIS) data. Elf-Darwich et al. (2012) proposed that employing mesoscale numerical meteorological models such as weather research and forecasting (WRF) leads to estimate high accuracy water vapor effects on DInSAR data and therefore it provides more accurate ground deformation measurements.

Foster et al. (2006) studied the impact of the topography of Hawaii on the atmosphere and removed the atmosphere delay in DInSAR data by using a high-resolution weather model called MM5 (NCAR-Penn State Mesoscale Model Version 5) (Grell et al. 1995). They employed three interferograms for pairs of dates between 2003 and 2005 to demonstrate that they do not record a discrete displacement event over a short time span and can be interpreted as the atmosphere path delay. For the relatively short time period between 29 Sep 2003 and 03 Nov 2003, the interferogram signals represent atmospheric delay and is in good agreement with that predicted by MM5 model, particularly for the high areas such as Mauna Loa and Mauna Kea (Foster et al. 2006).

Another approach to remove the seasonal component of troposphere error from DInSAR ground deformation time series was developed by Samsonov et al. (2014). They used meteorological and radiosonde data observed at the stations located in the Naples Bay region of Italy and computed the refractivity at Earth's surface and at altitude, respectively. Their study resulted in an elevation dependent exponential model that can be used to calculate the seasonal amplitude of ZTD. Their model provides the best fit to the amplitudes of seasonal variation of troposphere observed in DInSAR points at elevations between 200 to 700 m above msl, although the fit is not as good at higher elevations. They suggest that the deviation of their model from the variations in seasonal amplitude at higher elevations is due to either the spatial filtering applied to the interferograms or the use of simple sine function in calculating the amplitude of troposphere, which can underestimate the seasonal cycle of troposphere signals. They demonstrated that their proposed correction model could reduce the noises in DInSAR height time series by as much as 50% (Samsonov et al. 2014).

In this paper, we propose to employ high spatial resolution DInSAR data to model the local seasonal variations of troposphere signal in GPS data caused by the wet and hydrostatic components of the troposphere, which again is a function of water vapor pressure and temperature and air pressure

Modeling of ZTD is problematic in volcanoes or mountainous areas with large topographic relief, particularly in moist, heterogeneous tropical atmosphere like Mauna Loa, Hawaii (Jolivet et al. 2014). This is because there is a strong interaction between winds and high mountains influencing the pattern of local weather parameters, including water vapor pressure both horizontally and vertically (e.g., generating clouds on the windward side of the mountain and dry and clear skies on the leeward side of the mountain).

In this study, we take into account the area containing the Kilauea volcano and the east rift zone of Mauna Loa in the island of Hawaii (Figures 4.1). Data is available for both GPS and DInSAR. Initially, the seasonal fluctuations of ZTD in DInSAR data are estimated by fitting a sinusoidal signal with 1-year period to the height time series of all

pixels. Then motivated from Samsonov et al. (2014) we propose an elevation-dependent model, which provides a best fit to estimates of amplitudes of ZTD in DInSAR data. This model links to a meteorological and radiosonde data collected at a surface weather stations and a radiosonde station, respectively.

In order to evaluate the potential of the proposed correction model to observe seasonal amplitudes of troposphere delay in GPS data, we compare the seasonal variations of troposphere signals derived from the model and phase of 180° to the differenced ZTD at each station (Ge et al. 2003; Li et al. 2006). Differenced ZTD is defined as the ZTD computed for the reference station, here station PUKA at a height of 2999.8 m above msl, subtracted from the ZTD computed for each of the other stations. As demonstrated by Li et al. (2006), the upside of considering the differenced ZTD rather than absolute values is that the absolute values will reduce the terrain elevation dependency of the ZTD and ZWD variations.

In this study, we consider fourteen GPS stations inside the region imaged by DInSAR and eight GPS stations outside of this region for dates corresponding to the DInSAR observations. Data from each GPS station is processed using CSRS-PPP, available from NRCan (<https://webapp.geod.nrcan.gc.ca/geod/tools-outils/ppp.php>), resulting coordinates and ZTD. As a result of the comparison between the modeled ZTD and the differenced ZTD at each station, the RMSE of the residuals are computed and investigated in detail. We compare the modeled ZTD and the differenced ZTD at each station and compute the RMSE of the residuals.

An overview of the geology and meteorology of our study area is provided in section 2. In section 3, we discuss the data and processing. In the following section, we focus on the approaches employed for estimating the seasonal amplitude of ZTD, including a detailed explanation of the DInSAR height time series fitting and the computation of the refractivity from meteorological and radiosonde measurements to derive the elevation-dependent amplitudes of ZTD. In Section 5, we elaborate on the ZTD variations computed by using CSRS-PPP and estimation of the differenced ZTD for each GPS station. Interpretation and conclusions are presented in the final section.

4.2. Geologic setting

Hawaii is located in the Pacific Ocean, approximately 3379 km southwest of California. The six major Hawaiian Islands include Kauai, Oahu, Molokai, Lanai, Maui, and Hawaii (Big Island), where Kauai is the oldest, at ~5 Myr (millions of years), and Hawaii is the youngest at ~ 0.7 Myr, stretching from northwest to southeast. These islands were formed as a result of the activity of a static mantle plume currently centered beneath Hawaii Island, which is composed of five main volcanoes: Mauna Loa, Kilauea, Mauna Kea, Hualalai and Kohala (Clague & Sherrod 2014). Mauna Kea, at 4,207 m above msl, experienced its last eruption is approximately 4000 years ago, while Mauna Loa, at 4,169 m above msl, last erupted in 1984 (Peterson & Moore 1987, Trusdell & Swannell 2003, Clague & Sherrod 2014, USGS 2017a).

Kilauea is located on the southeast flank of Mauna Loa and rises 1,247 m above the sea level (USGS 2017b). This volcano has been erupting continuously for more than three decades at its summit and east rift zone locations. The summit crater hosts an active lava lake that has dramatic level fluctuations, dropping during deflation and rising during inflation (Wilson et al. 2008; USGS 2017b). This volcano has been affected by the shape of its neighbor, Mauna Loa, and has adopted a similar rift zone orientation (Fiske & Jackson 1972). However, recent research has revealed that Kilauea volcano has a separate magma plumbing system (Poland et al. 2012).

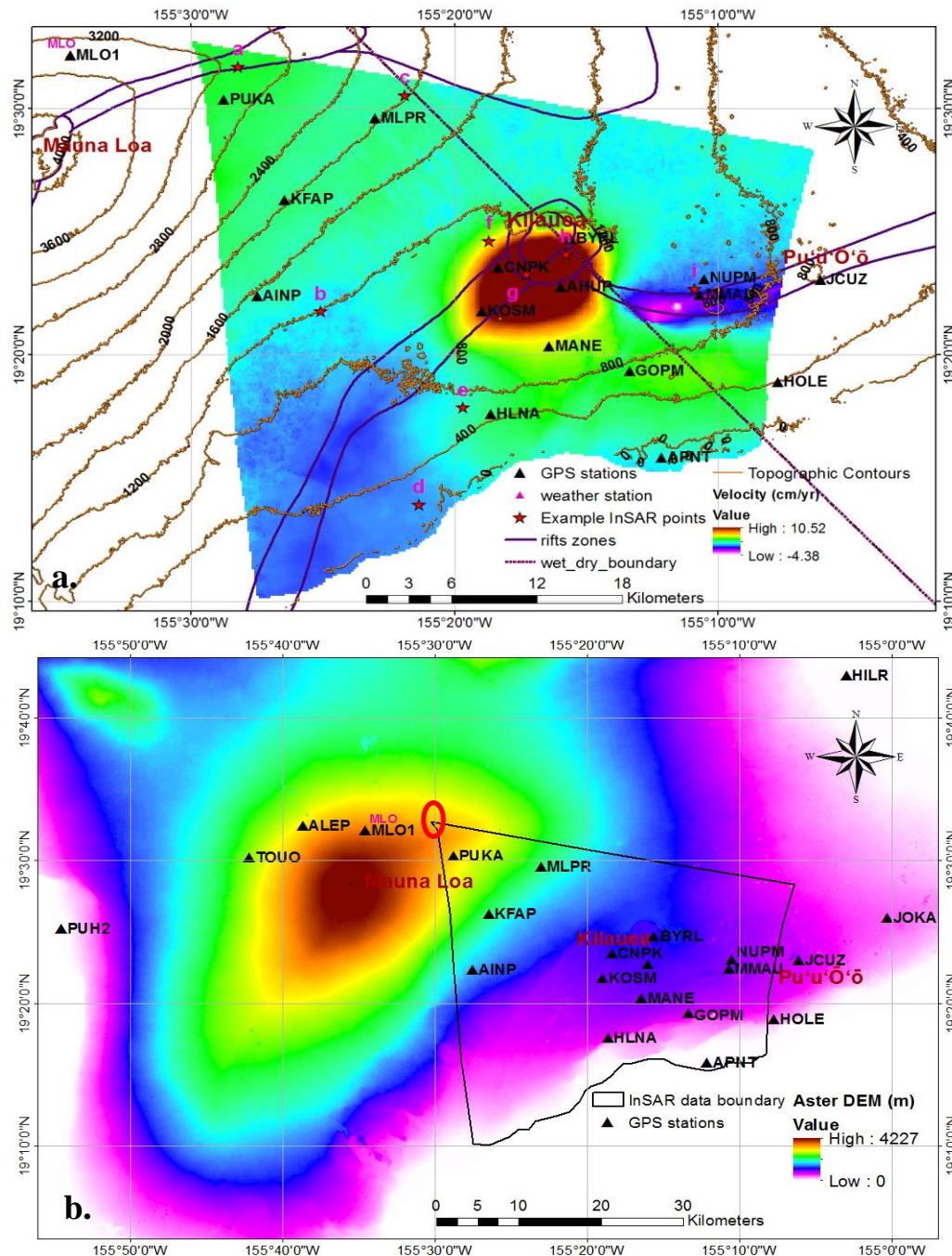


Figure 4.1. a) The map in the background is the velocity model (in cm/yr) calculated from the linear regression on the DInSAR data from 2014 to 2017. The brown contour lines show elevations spaced at 400 meter interval. The positions of sample DInSAR points are shown with red stars. The rift zones of Mauna Loa and Kilauea are shown in purple. A positive velocity value shows uplift. The DInSAR reference location is shown with red circle in the NW corner **b)** Distribution of the GPS stations inside and outside of the DInSAR data boundary. The map in the background is the ASTER DEM with 30 m per pixel resolution (<http://gdex.cr.usgs.gov/gdex/>).

The climate of different regions is directly affected by the wet/windward or dry/leeward sides of volcanic islands and are strongly dependent on the shape and the heights of the volcanic peaks (Longman et al. 2015). The windward side of Hawaii is on the eastern slope of Mauna Kea and on the southeast flank of Mauna Loa. This region is approximately perpendicular to the direction of the north-easterly trade winds which carry moisture in the atmosphere. Therefore, the prevailing trade winds make the windward side windier and wetter, which results in more rainfall per year (Zhang et al. 2016). As shown in Figure 4.2 (dashed line), we consider the separation line between dry and wet zones based on the breakpoints proposed by Gagné & Cuddihy (1990) for Dry-Mesic and Mesic-Wet boundaries, where 2500 mm of rainfall is received at 1000 m above msl.

Figure 4.2 also shows a map of averaged climate data, including air temperature, rainfall, water vapor pressure, relative humidity, and air pressure. The maps of air temperature, rainfall and relative humidity are at the resolution of 250 m; (<http://climate.geography.hawaii.edu/>; Giambelluca et al. 2014; Frazier et al. 2012).

The temperature map in Figure 4.2a indicates that higher elevations have lower temperatures that increase gradually toward sea level, ranging from 3.62 and 23.91 °C. The coldest zone of our study area is found symmetrically around the summit of Mauna Loa. Figure 4.2b illustrates the average annual rainfall, overlain with elevation contours. Values range between 204.09 mm to over 7629.16 mm. The rainfall is concentrated on the lower elevations on the east side of the Island. According to Colleen (2013), this is likely a result of the orientation of Mauna Loa volcano, parallel to the direction of the prevailing trade winds. This figure also shows that the tall mountain obstructs the trade winds on the leeward side of the island, resulting in less rainfall and drier conditions near the summit.

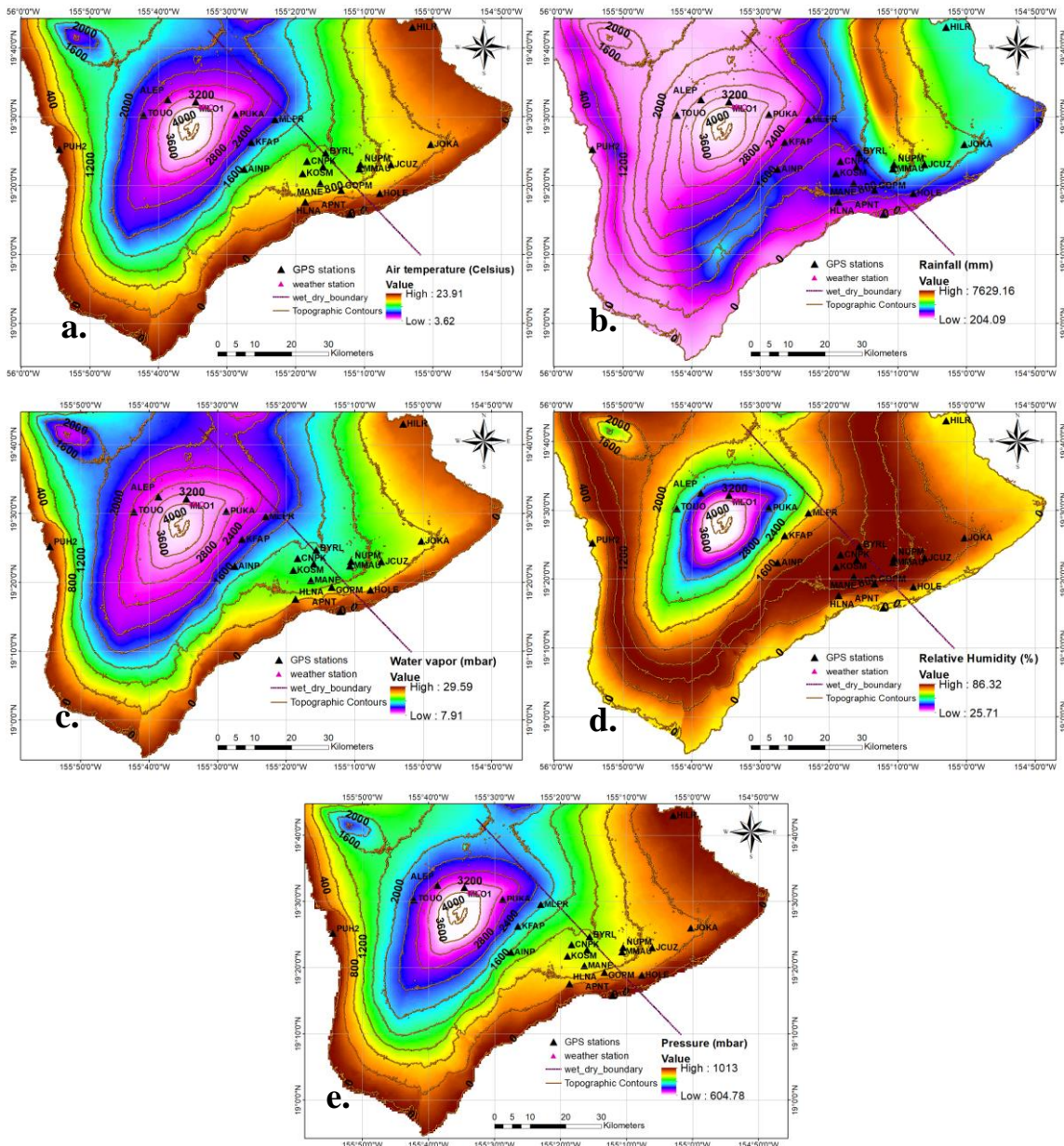


Figure 4.2. Climate data including a) air temperature b) rainfall, c) water vapor computed from the air temperature d) relative humidity e) air pressure computed from the expression proposed by Triplet & Roche (1983) and the ASTER-derived DEM (<http://gdex.cr.usgs.gov/gdex/>). Maps of air temperature, rainfall and relative humidity (<http://climate.geography.hawaii.edu/>; Giambelluca et al. 2014; Frazier et al. 2016) at 250 m resolution. The brown contour lines represent elevations spaced at 400 meter intervals. The windward/wet and leeward/dry side are separated with a dashed line.

As we will demonstrate later, water vapor pressure increases exponentially with temperature (Figure 4.2a, c). In Figure 4.2d, the high relative humidity of greater than 80% can be seen at lower elevations, between 400 and 1600 m above msl. It is worthwhile to mention that relative humidity in the Planetary Boundary Layer (PBL), the lowest layer of the troposphere where the wind is influenced by friction, approximately 1000 m above Earth's surface, increases with decreasing air temperature (Figure 4.2a, d).

In this paper, we estimated the air pressure from the DEM derived from ASTER Global DEM (GDEM), downloaded from the USGS Global Explorer website (<http://gdex.cr.usgs.gov/gdex/>) at a resolution of 30 m per pixel. We used the expression proposed by Triplet & Roche (1983):

$$P = P_0(1 - 0.0000226H)^{5.225} \quad (4.1)$$

where, P_0 is the pressure at msl, 1013 mbar (Houlié' et al. 2005), H is the elevation of each pixel in meter.

As shown in Figure 4.2e, due to the opposite relationship between the air pressure and altitude presented in Equation 4.1, the highest pressure value, 1013 mbar, is observed at the lowest elevation, at mean sea level. The air pressure values decrease exponentially with increasing altitudes, 604.78 mbar observed at the highest elevation in our study area, 4227 m above msl.

4.3. Data

For the DInSAR analysis, we collected 32 ascending Ultra-Fine 13 Wide (U13W2) images spanning 20140101-20170202 and 34 descending Ultra-Fine 16 Wide (U16W2) images spanning 20131213-20170303 from RADARSAT-2 satellite (Table 4.1). The considered time steps of these data are twelve days which provides high temporal resolution appropriate for observing the seasonal fluctuations of the tropospheric delay. Each SAR dataset was processed independently with the GAMMA software (Wegmuller and Werner, 1997). A single master for each set was selected and the remaining images were re-sampled into the master geometry. The interferograms were multilooked (10 in range and 10 in azimuth) and the topographic phase was removed using a 30 m resolution

Shuttle Radar Topography Mission (SRTM) DEM. Differential interferograms were filtered using the adaptive filtering with a filtering function based on the local fringe spectrum (Goldstein & Werner 1998) and unwrapped using the minimum cost flow algorithm (Costantini 1998). Minor interpolation of each interferogram was performed to improve the spatial coverage reduced by decorrelation. Then, ascending and descending interferograms were geocoded and resampled to a common latitude/longitude grid with a uniform spatial sampling of 30 m.

Table 4.1. SAR datasets used in MSBAS processing: RADARSAT-2 Ultra-Fine 13 and 16 Wide (U13W2, U13W2); time span (in YYYYMMDD format), azimuth θ° and incidence φ° angles, number of available SAR images N , and number of calculated interferograms M for each data set. ASC and DSC in the table stands for ascending and descending, respectively.

| DInSAR set | Time span | θ° | φ° | N | M |
|----------------|-------------------|----------------|-----------------|-----|-----|
| R2-U13W2 (ASC) | 20140101-20170202 | 349 | 40 | 32 | 300 |
| R2-U16W2 (DSC) | 20131213-20170303 | -169 | 42 | 34 | 372 |
| Total: | 20140101-20170202 | | | 64 | 672 |

The Multidimensional Small Baseline subset (MSBAS) (Samsonov & d'Oreye, 2012) technique was applied to ascending and descending datasets simultaneously to produce horizontal east-west and height time series and annual linear deformation rates. First order regularization with λ equal to 0.25 was employed and the reference region was selected in the NW corner, at elevation 3107 m above msl (red circle, Figure 4.1a) ensuring that the non-seasonal atmospheric component in the height time series is less significant.

Again, Figure 4.1a shows the average vertical velocity of all 1,257,000 DInSAR pixels between 2014 and 2017. The velocity values in our study area range between 4.4 cm/yr of subsidence in the eastern rift zone of Kilauea volcano, 8 km away from the volcanic

cone of Pu‘u‘Ō‘ō, to 10.5 cm/yr of uplift in the south of Kilauea volcano. As discussed above, Kilauea has been erupting continuously for more than three decades and is currently active at its summit and upper southeast rift zone.

We selected nine points, a through i, over our study area to provide examples of the DInSAR height time series (Figure 4.1a). The height time series of these points are presented in Figure 4.3 which are labeled accordingly. Figure 4.3a, b and c illustrate the height time series of points a, b and c, and show a low rate of subsidence in the east rift zone of the Mauna Loa over the time period between 2014 and 2017 as a result of the massive lava outpouring from the 1984 eruption of Mauna Loa (Clague & Sherrod 2014). Figure 4.3d and 4.3e show subsidence of 1.4 and 0.7 cm/yr, respectively, in the outer flank of the Kilauea rift-zone (Clague & Sherrod 2014). Figure 4.3 (f, g and h) show uplift of 1.0, 10.2 and 6.4 cm/yr. The vertical deformation time series of points ‘g’ and ‘h’ show uplift of approximately 30 cm occurred in the time span between 2014 and 2017 and is related to the ongoing eruption of Kilauea at the summit and at the Pu‘u‘Ō‘ō vent on the east rift zone. Deflation is observed on the upper side of east rift zone of Kilauea at location ‘i’ (Figure 4.3i). The vertical deformation here is related to numerous eruptions and inflation of the summit of Kilauea during this time period (Baker & Amelung 2015).

The height time series of the DInSAR data obtained from differential interferograms have not been corrected for the tropospheric differential phase so that the DInSAR derived seasonal fluctuations of differential ZTD, converted from the LOS direction, can be used for correcting ZTD error from the up component of the position time series of GPS stations referenced to a station. In order to validate this, here, the RINEX data of fourteen GPS stations in the same region as the DInSAR data and seven stations were selected. All these stations have observations during the same time period as the DInSAR data to ensure the consistency in analyzing the seasonal variations of ZTD signals. These stations belong to the Hawaii Volcano Observatory (HVO) network, supported by collaboration with University of Hawaii, Stanford University and United States Geological Survey (USGS). Time series with 30 second sampling rate are freely available on the UNAVCO website (<ftp://data-out.unavco.org/pub/rinex>). These stations are located inside and outside of the region of DInSAR data. They have been selected based on the availability

of the data between 2014 and 2017, variety of elevations and wide area coverage of the study region (Figure 4.1b). All the GPS measurements made with dual-frequency receivers such as Trimble NetRS and Javad TreG3th Sigma (Table 4.2). Table 4.2 presents the information for the GPS stations, including position of the sites, receiver types and the first and last dates of data availability. Every GPS station has data over the 2014 to 2017 time period, with the exception of station MLO1, that stopped collection on August 23, 2016.

The radiosonde data required to model the annual amplitude of troposphere are downloaded for 2014 from the only radiosonde station in Hawaii's Big Island, PHTO/Hilo (<http://weather.uwyo.edu/upperair/sounding.html>). This air station measures temperature, humidity and pressure parameters twice daily at altitudes from zero to as high as 3.5 km. We use these observations to compute the refractivity over different atmospheric heights. Moreover, we employ the *in situ* meteorological data (pressure, temperature and relative humidity) observed between 2014 and 2017 at MLO1 weather station, the closest weather station to our DInSAR reference point, 7.61 km, in order to take an advantage of the high temporal resolution of the local surface station to estimate the temporal variations of the refractivity over that time period (<https://www.esrl.noaa.gov/gmd/dv/data/index.php?category=Meteorology&type=Insitu>). The location of this weather station (-155.57° , 19.54° , 3395.81 m above msl) is shown in Figure 4.1a.

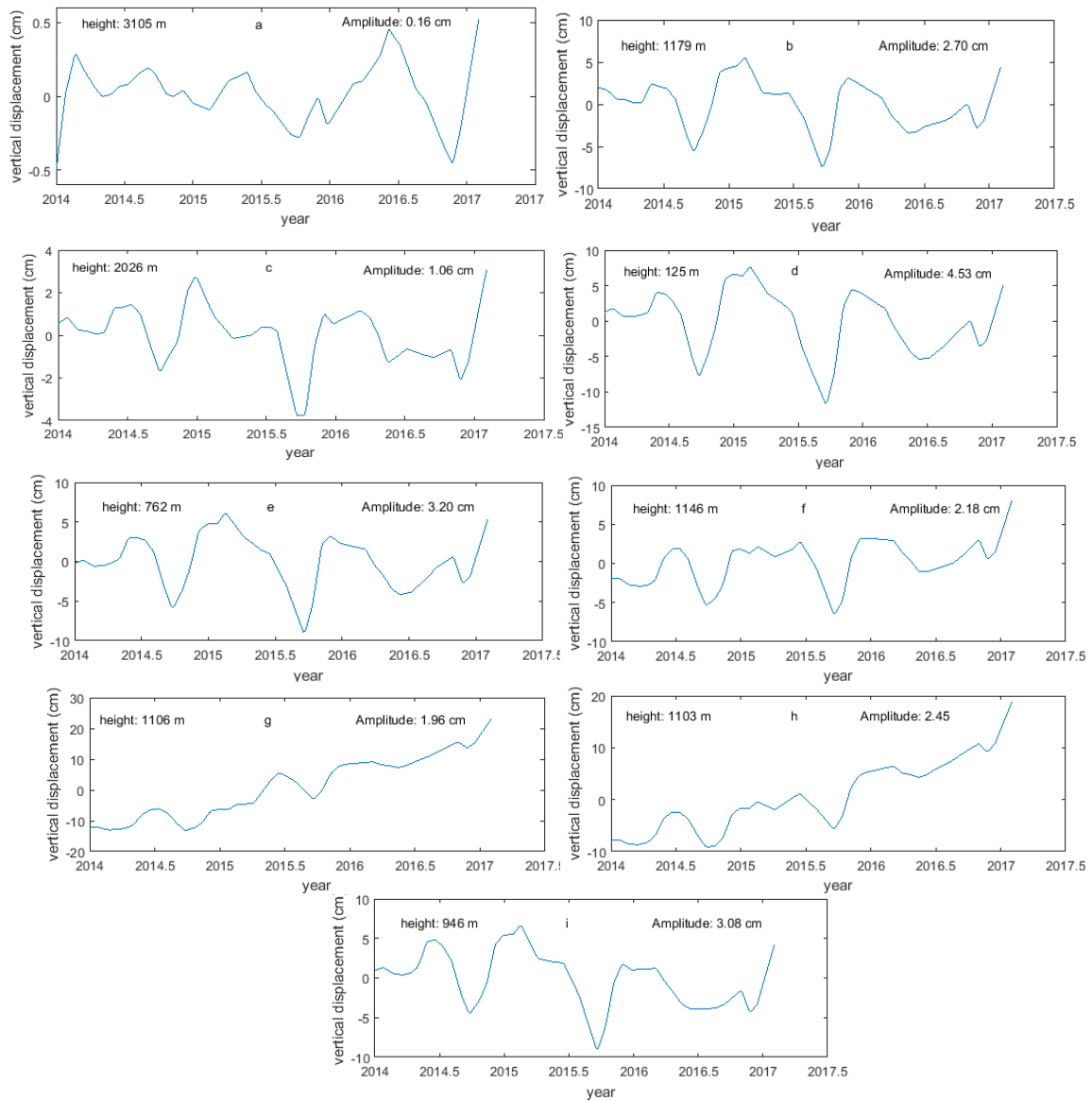


Figure 4.3. Example of DInSAR height time series of the specified points *a* through *i*, shown in Figure 4.1a. They all are referenced to a point at elevation 3107 m above msl. In addition to the elevation of each point derived from the ASTER Global DEM (GDEM) (<http://gdex.cr.usgs.gov/gdex/>), seasonal amplitudes estimated by fitting a sinusoidal signal to the height time series are given in each plot. Positive values indicate uplift.

Table 4.2. GPS stations details

| Station | Receiver | Longitude (degree) | Latitude (degree) | Altitude (m) above msl | Start date | End date |
|---------|---------------------|-----------------------|----------------------|------------------------------|------------|----------|
| AHUP | Trimble NetRS | -155.27 | 19.38 | 1082.92 | 1999 May | 2017 May |
| ALEP | Javad TreG3th Sigma | -155.64 | 19.54 | 2895.72 | 2004 July | 2017 May |
| BYRL | Trimble NetRS | -155.26 | 19.41 | 1076.74 | 2006 Feb. | 2017 May |
| CNPK | Trimble NetR9 | -155.31 | 19.39 | 1100.86 | 2008 June | 2017 May |
| GOPM | Trimble NetRS | -155.22 | 19.32 | 739.35 | 1999 May | 2017 May |
| HILNA | Trimble NetR9 | -155.31 | 19.29 | 677.11 | 1996 Aug. | 2017 May |
| HOLE | Trimble NetRS | -155.13 | 19.31 | 408.43 | 1999 May | 2017 May |
| JCUZ | Trimble NetRS | -155.10 | 19.38 | 808.80 | 2007 July | 2017 May |
| KFAP | Trimble NetRS | -155.44 | 19.44 | 2047.97 | 2004 July | 2017 May |
| MLPR | Trimble NetRS | -155.38 | 19.49 | 2015.90 | 2005 Aug. | 2017 May |
| NUPM | Trimble NetR9 | -155.18 | 19.38 | 913.30 | 1999 June | 2017 May |
| MANE | Trimble NetRS | -155.27 | 19.34 | 975.08 | 1999 May | 2017 May |
| JOKA | Trimble NetRS | -155.00 | 19.43 | 466.55 | 2007 Oct. | 2017 May |
| TOUO | Javad TreG3th Sigma | -155.70 | 19.50 | 2509.62 | 2004 July | 2017 May |
| AINP | Trimble NetRS | -155.46 | 19.37 | 1543.10 | 2005 Sept. | 2017 May |
| APNT | Trimble NetR9 | -155.20 | 19.26 | 23.74 | 1996 Sept. | 2017 May |
| PUH2 | Trimble NetRS | -155.91 | 19.42 | 29.45 | 2014 March | 2017 May |
| HILR | Trimble NetR8 | -155.05 | 19.72 | 12.84 | 2010 May | 2017 May |
| KOSM | Trimble NetRS | -155.32 | 19.36 | 967.70 | 1999 Aug. | 2017 May |
| MLO1 | Trimble NetR9 | -155.58 | 19.54 | 3402.71 | 2004 Dec | 2016 Aug |
| MMAU | Trimble NetRS | -155.18 | 19.37 | 929.71 | 2010 July | 2017 May |
| PUKA | Trimble NetRS | -155.48 | 19.51 | 2999.80 | 2005 March | 2017 May |

4.4. Amplitude of seasonal troposphere signal

4.4.1. DInSAR data

The seasonal fluctuation is apparent in the example height time series of the DInSAR data in the vertical direction presented in Figure 4.3, particularly in those time series at lower elevations, where the water vapor and temperature are at their highest levels (see, e.g., point d at 125 m above msl, Figure 4.1a). These fluctuations can be modeled reasonably well by fitting the first harmonic of the sinusoidal function to the height time series of each point as follow:

$$\Delta h(t_m) = a + b \times t_m + A \sin(\omega t_m + \phi) \quad (4.2)$$

To enhance the accuracy in determining the seasonal variations in the time series, we first removed the trend term and then employed a Fourier analysis. Since the data are sampled at m discrete time points, t_m , so the seasonal signal can be written as follows (Smith & Gomberg 2009):

$$A \sin(\omega t_m + \phi) = C \sin(\omega t_m) + D \cos(\omega t_m) \quad (4.3)$$

where,
$$A = \sqrt{(C^2 + D^2)}, \phi = \tan^{-1}\left(\frac{C}{D}\right), \omega = \frac{2\pi}{T}$$

and C and D are the frequency coefficients for annual perturbation.

We solved this function for the amplitude, A , and phase, ϕ , that maximizes the fit to the time series data. T is the period of the signal and is extracted from each height time series by employing a Fast Fourier Transform (FFT) technique.

The resulting analysis shows that the seasonal fluctuations of more than 99% of the DInSAR points are statistically significant, $r^2 \geq 0.2$ and $p - value \leq 0.05$, which confirms that these DInSAR height time series contain a seasonal component that can be used to accurately estimate the spatial seasonal ZTD signals. The estimated seasonal

amplitude of ZTD for all DInSAR points are shown in a raster format, overlain with the topographic maps in Figure 4.4a. As this figure clearly illustrates, the seasonal amplitude is higher at the coastal areas and lower at higher altitudes (e.g., Mauna Loa). This also can be seen in the example time series presented in Figure 4.3. According to Figure 4.3a and d, we estimated an amplitude of 4.53 cm for 125 m above msl and 0.16 cm for 3105 m above msl. As shown in Figure 4.4b, these estimated amplitudes increase exponentially with growing and lowering height from 3107 m above msl, elevation of the reference point. Comparing the estimated seasonal amplitude of ZTD with the atmospheric parameters, we can see that it is dependent on temperature, water vapor and pressure, again as expected, which are a function of height.

As mentioned earlier in this section, in addition to the seasonal amplitudes, the phase of the annual signals are estimated by fitting Equation 4.3 to the height time series. We found values range between -180° and 180° , clockwise from north. These values correspond to the shift of the signal from the beginning of the calendar year.

These estimated seasonal amplitudes of the DInSAR locations are suitable for use in deriving a model to determine the seasonal amplitudes as a function of height.

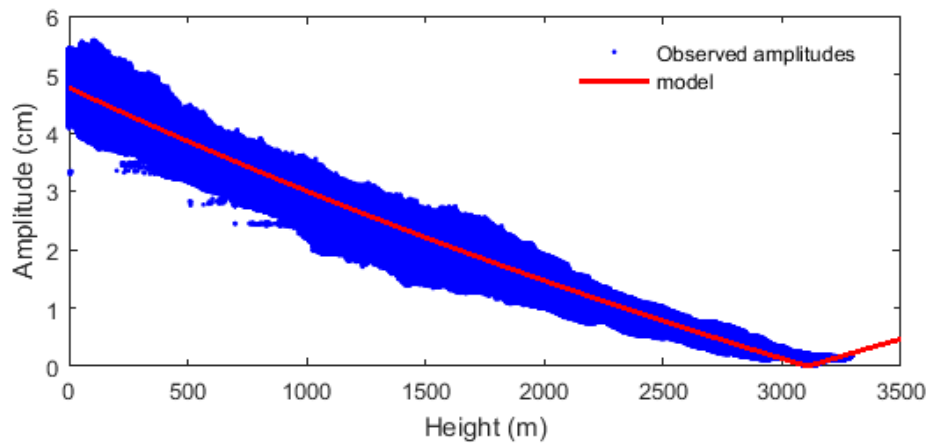
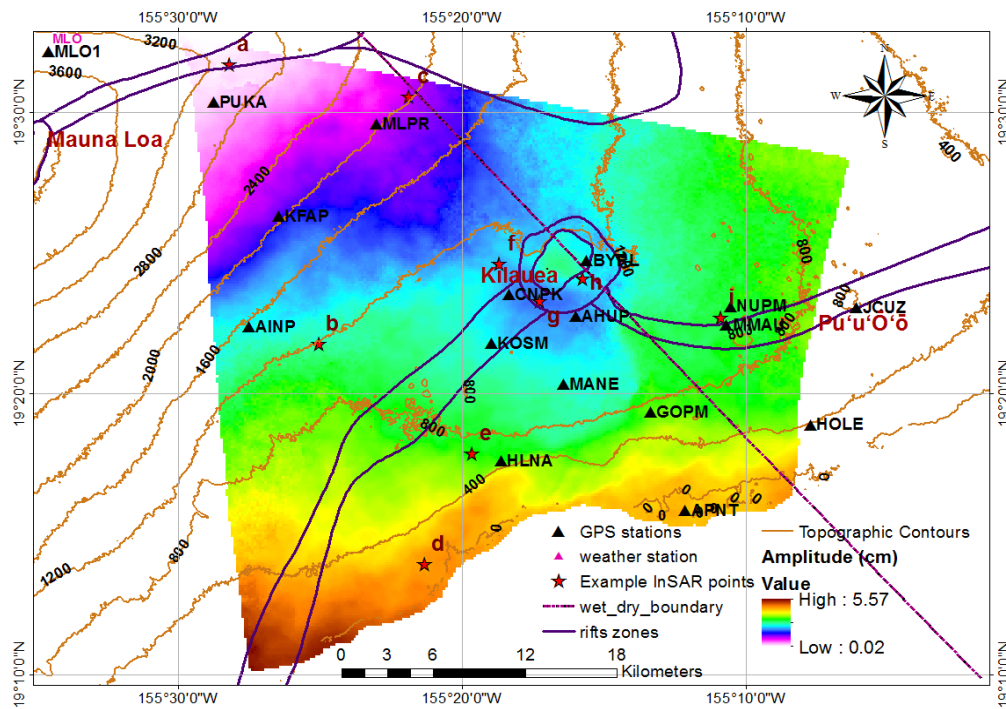


Figure 4.4. a) Map of the measured amplitudes of seasonal variations of troposphere signal in DInSAR data by adjusting a sinusoidal signal on the height time series of each point. In the raster maps the brown contour lines represent elevations spaced at 400 meter interval. The rift zones of Mauna Loa and Kilauea are shown as dark lines. The inflation areas at Kilauea's summit are shown as red circles. Separation between dry and wet regions are shown by the dashed line. b) The vertical profile of the measured amplitudes as a function of height (blue) overlain with the modeled amplitudes by employing Equation 4.9 (red).

4.4.2. Exponential refractivity model

The speed of radio signal propagation is dependent on the material through which it travels and it is slightly lower in the atmosphere than in a vacuum. The ratio of the speed of light in a vacuum to the speed of light in the atmosphere is termed the refractive index, n , which is more conveniently expressed as the refractivity N (Bean & Dutton 1968):

$$N = 10^6(n - 1) \quad (4.4)$$

N can be computed by its relationship with atmospheric parameters including pressure, temperature, and water vapor pressure proposed by Smith & Weintraub (1953):

$$N = K_1 \frac{P_d}{T} + K_2 \frac{e}{T} + K_3 \frac{e}{T^2} \quad (4.5)$$

In this equation, P_d is the partial pressure due to dry gases (hPa), K_i is the refractivity constants, e is the partial pressure of water vapor (hPa), and T is the absolute temperature (degrees Kelvin). The refractivity constants K_i were determined empirically in a laboratory. We adopt the refractivity constants computed in Rueger (2002) of $77.69 \text{ K mbar}^{-1}$, $71.29 \text{ K mbar}^{-1}$, and $375463 \text{ K}^2 \text{ mbar}^{-1}$ for the refractivity constants K_1 , K_2 , and K_3 , respectively. The partial water vapor pressure is estimated from the dew point temperature, calculated from its relationship with the relative humidity and temperature (Lawrence 2005) measured at the weather station. Proposed by Alduchov and Eskridge (1996) for dew point temperatures less than 50°C , the partial vapor pressure can be computed as follow:

$$E = 6.1037e^{17.641t/(243.27+t)} \quad (4.6)$$

where, t is the dew point temperature in degrees Celcius.

We use the surface measurements for pressure, water vapor pressure and temperature within the time span of 2014 to 2017 observed in situ at the MLO1 station located at Mauna Loa volcano, 3395.81 m, to estimate the refractivity time series at the surface from Equation 4.5. The seasonal cycle in refractivity of the atmosphere is apparent in

both the hourly and daily time series shown in Figure 4.5a. The amplitude of the seasonal variation of daily refractivity estimated from the best-fit sinusoid function is 18.94 (N-units). This seasonal cycle is due to the seasonal variations in the climate data primarily due to water vapor pressure and temperature (Ayantunji et al. 2011) in which the seasonal maximum occurs in the summer (June) and the minimum occurs in the winter (January) of each year. In addition to the surface weather observations, we used the radiosonde data measured at the radiosonde station PHTO/HILO and computed the refractivity of the points at elevations between 0 and 3.5 km above the surface of the earth. We present the vertical profile of the estimates of the refractivity in Figure 4.5b.

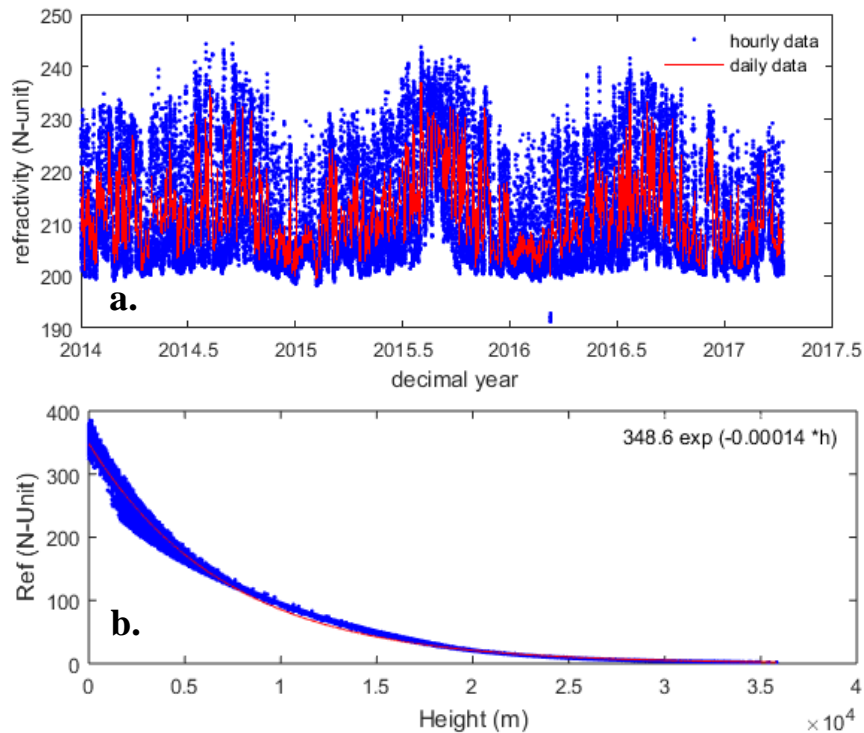


Figure 4.5. **a)** the hourly time series of the refractivity of atmosphere at the surface of Earth computed from the air pressure, water vapor pressure and temperature time series observed at the weather station MLO1 (in blue). The daily averaged refractivity time series computed from hourly data (in red). **b)** The vertical profile of the refractivity calculated from the atmospheric parameters (air pressure, water vapor pressure and temperature) observed at the radiosonde station PHTO/HILO. The fitted red line is the best fit exponential function.

As stated above, when a radio signal passes through the Earth's troposphere, it experiences bending and delay due to the variability of the refractivity index of the troposphere (Mendes 1999). That tropospheric delay is directly proportional to the refractivity and the effect of water vapor is highly significant, when compared to the effect of pressure and temperature.

The tropospheric delay can be calculated through an integration of refractivity along the vertical path in the troposphere as follows (Martin & Waldron 1961; Hopfield 1972):

$$d_{trop} = 10^{-6} \int_{path} N ds \quad , \quad (4.7)$$

Here, this delay is the integration of the refractivity in the range of elevations between the reference and measurement points:

$$d_{trop}(t, z_r, z_i) = 10^{-6} N_r(t) \int_{z_r}^{z_i} e^{-cz} dz \quad (4.8)$$

where, $N_r(t)$ is the refractivity time series computed from the temporal surface meteorological data measured at the weather station collocated with the reference point, c is the exponential decay parameter, z_r and z_i are the elevation of reference station and the measurement point, respectively. The elevation above sea level, in meters, is obtained from the ASTER-derived DEM (<http://gdex.cr.usgs.gov/gdex/>).

In this paper, the decay parameter is computed by fitting an exponential function to the vertical profile of refractivity of the points between 0 and 30 km above the ground (Figure 4.5b). This figure illustrates the exponentially decrease in the refractivity with height with a decay rate of 0.14 km^{-1} . This value is in good agreement with the empirical value given by Bean and Thayer (1959), 0.1424 km^{-1} , for elevations above 9 km. The computed parameters for the fitted exponential model are presented on the top right of this figure.

To take advantage of the relationship between the refractivity and tropospheric path delay, as done in Samsonov et al. (2014), we expanded Equation 4.8. Because we considered the reference station at a high elevation and the seasonal amplitudes increase

from the elevation of reference point, we considered the absolute value of the resulting equation (Equation 4.9, below) to fit the model amplitudes to the observed amplitudes from DInSAR data, as appropriate.

$$amp_{ZTDi}(z_r, z_i) = \left| \frac{10^{-6}(amp_{Nr})}{ce^{cz_r}} (1 - e^{-c(z_i - z_r)}) \right| \quad (4.9)$$

where, amp_{Nr} is the average seasonal amplitude of refractivity at Earth's surface, c is the refractivity decay computed from radiosonde data, z_i is the elevation of the measurement points and z_r is the elevation of the reference point, 3107 m above msl.

We compute the amplitude of the refractivity at the surface of Earth by fitting a simple Sinusoidal function to the daily averaged refractivity time series estimated at the in situ station, MLO1 (Figure 4.4a). The annual sinusoidal curve fitting to the refractivity time series provides an estimate of 18.94 N-units for the amplitude of its 1-year seasonal oscillation. From Equation 4.9, the seasonal amplitudes of ZTD are computed for the points at elevation between zero and 3500 m above msl shown in Figure 4.4b. As this figure indicates, this model is a good fit within the 90% confidence interval to the observed seasonal amplitudes of ZTD in the DInSAR data.

Examining the correlation between the observed seasonal amplitudes and the weather variables of Figure 4.2 shows that ZTD is positively correlated with temperature and water vapor pressure which is because the ZWD is more variable than ZHD based on these two weather variables. Also observed by Jin et al. (2007), the correlation between ZTD and ZWD variations is 0.95. The estimated seasonal amplitudes are proportional to the pressure data, which it is dependent on the elevation of the points.

Using the above analysis, we are able to model the seasonal variations imposed by ZTD at any location. In the next section, we use the derived seasonal correction model for twenty-one GPS stations distributed over the island of Hawaii. We also include stations from outside of the DInSAR data area to verify that our proposed seasonal ZTD correction model is not dependent on the location of the reference point.

4.5. ZTD correction to GPS data

The seasonal ZTD signal at any location can be estimated either by fitting the sinusoidal signal to the DInSAR height time series (Equation 4.3) or computing the elevation-dependent amplitudes by employing Equation 4.9 and the phase shift of 180° . Because the derived ZTDs are the values between the DInSAR points and a reference point, as discussed earlier, they can be used to remove the seasonal troposphere signals in the differenced GPS position time series relative to a reference station (Ge et al. 2003). Here, we compare the modeled seasonal variations to the relative ZTD at each individual site.

To calculate the differenced ZTD at each site relative to a reference station, we assume a GPS station close to the DInSAR reference point and then subtract it from the ZTD computed at the other stations at common epochs (Ge et al. 2003). Here, station PUKA at elevation 2999.8 m above msl and a distance of 4.79 km from the DInSAR reference point is considered as the reference in order to maintain consistency in interpreting the results. Table 4.3 presents information on the distances between the reference and the other stations, altitudes of each site and the modeled seasonal amplitudes of ZTD computed for each station by using Equation 4.9 and substituting the elevation of each GPS station for z_i and the elevations of the reference, 2999.8 m above msl, for z_r .

In this paper, the RINEX data for each GPS station are processed based on the PPP technique, which calculates the absolute position without attaching to a reference station. To do so, we use the online service from CSRS-PPP. The main advantage of the PPP approach is that, unlike the differential processing approaches, the ZTD is considered an unknown parameter and therefore is estimated along with the position.

Table 4.3. Altitude of the GPS stations from Table 4.2. The length is the distance between the reference station, PUKA, and each station. The modeled seasonal amplitudes between each station and PUKA are estimated from Equation 4.9. The rmse of the residuals is the difference between the observed high-frequency ΔZTD_{PPP} and the modeled seasonal component. The maximum, mean and minimum of the difference between the modeled seasonal variation and ΔZTD_{PPP} for each station are also presented. Stations are sorted based on altitude.

| Station | Altitude (m) | Length (km) | Amplitude (cm) | RMS of residual (cm) | Max difference (cm) | Mean difference (cm) | Min difference (cm) |
|---------|--------------|-------------|----------------|----------------------|---------------------|----------------------|---------------------|
| HILR | 12.84 | 50.80 | 4.61 | 5.97 | 9.35 | 0.43 | 0.03 |
| APNT | 23.74 | 39.55 | 4.59 | 5.38 | 8.65 | 0.17 | 0.06 |
| PUH2 | 29.45 | 46.02 | 4.57 | 3.46 | 10.47 | -0.10 | 0.05 |
| HOLE | 408.43 | 42.46 | 3.91 | 4.57 | 10.72 | 0.36 | 0.03 |
| JOKA | 466.55 | 50.46 | 3.78 | 4.66 | 7.69 | 0.15 | 0.02 |
| HLNA | 677.11 | 29.48 | 3.41 | 4.36 | 8.77 | 0.35 | 0.04 |
| GOPM | 739.35 | 33.76 | 3.3 | 3.98 | 10.08 | 0.29 | 0.05 |
| JCUZ | 808.80 | 41.87 | 3.19 | 3.93 | 9.33 | 0.18 | 0.02 |
| NUPM | 913.30 | 34.6 | 3.01 | 3.58 | 8.32 | 0.16 | 0.21 |
| MMAU | 929.71 | 34.82 | 2.98 | 3.28 | 6.93 | 0.30 | 0.12 |
| KOSM | 967.70 | 23.31 | 2.92 | 4.16 | 6.50 | 0.30 | 0.08 |
| MANE | 975.08 | 28.43 | 2.91 | 3.15 | 8.30 | 0.17 | 0.00 |
| BYRL | 1076.74 | 25.34 | 2.74 | 3.55 | 7.91 | 0.17 | 0.02 |
| AHUP | 1082.92 | 26.40 | 2.73 | 3.75 | 6.90 | 0.18 | 0.01 |
| CNPK | 1100.86 | 22.13 | 2.7 | 4.11 | 7.04 | 0.20 | 0.03 |
| AINP | 1543.10 | 14.89 | 2 | 2.38 | 4.10 | 0.18 | 0.02 |
| MLPR | 2015.9 | 10.15 | 1.31 | 1.61 | 5.85 | 0.12 | 0.07 |
| KFAP | 2047.97 | 8.50 | 1.26 | 1.81 | 10.03 | -0.04 | 0.05 |
| TOUO | 2509.62 | 23.49 | 0.63 | 0.24 | 8.25 | 0.05 | 0.00 |
| ALEP | 2895.72 | 17.76 | 0.13 | 0.78 | 1.90 | 0.01 | 0.00 |
| PUKA | 2999.80 | 0 | ----- | ----- | ----- | ----- | ----- |
| MLO1 | 3402.71 | 10.75 | 0.48 | 0.64 | 9.70 | -0.20 | 0.03 |

All the post-processed position solutions are in the International Terrestrial Reference Frame (ITRF) and are computed in the static mode using precise satellite orbits and clocks available at the time of submitting GPS data. One of the advantages of this service is that there is no minimum for a GPS observation session and longer observation period makes it possible to resolve the carrier phase ambiguities required to recover more accurate positions (CSRS-PPP guide, 2004; Geng et al. 2012). In addition to using the antenna phase center calibration value published by the International GNSS Service (IGS) and by the National Geodetic Survey (NGS) available at <http://www.ngs.noaa.gov/ANTCAL>, this service includes ocean loading corrections computed with OSO Chalmers grid model (Bos & Scherneck 2011). This service also uses an ionospheric-free linear combination of L1 and L2 of the code and phase observations to eliminate ionosphere delay.

It should be noted that the CSRS-PPP estimates ZTD by employing Global Mapping Function (GMF) which uses the Global Pressure and Temperature (GPT) for meteorological data (Boehm et al. 2007). As a result, its coefficients are computed based on the data from the European Centre for Medium-Range Weather Forecasts (ECMWF) numerical weather model (Kouba 2008).

The adapted form of this mapping function for both hydrostatic and wet mapping functions (Boehm et al. 2006a):

$$m(\varepsilon) = \frac{1 + \frac{a}{b}}{\sin\varepsilon + \frac{1+c}{a}} \frac{1 + \frac{a}{b}}{\sin\varepsilon + \frac{b}{\sin\varepsilon + c}} \quad (4.10)$$

where, a, b and c are constant coefficients. ε is the elevation cut-off angle and the value of 10° is applied in CSRS-PPP by default. This function is based upon the monthly average of pressure, temperature and relative humidity data on a $15^\circ \times 15^\circ$ global grid profile produced from the ECMWF numerical weather model data, 40 year reanalysis data (ERA40). Indeed, this function is the spherical harmonic expansion of VMF1 (Boehm et al. 2006b) parameters and requires the station coordinates and day of year as input parameters. The coefficient a for both hydrostatic and wet components is obtained

from spherical harmonics and are computed based on the same process as used in VMF1 (Boehm et al. 2006). This parameter, at any latitude at day of year t (referred to January 28), can be calculated as:

$$a = a_0 + A \cos\left(\frac{t-T_0}{365} \cdot 2\pi\right)$$

$$a_0 = \sum_{n=0}^9 \sum_{m=0}^n P_{nm}(\sin(\varphi)) \cdot [A_{nm} \cos(m\lambda) + B_{nm} \sin(m\lambda)] \quad (4.11)$$

where, constant a_0 and the annual amplitude A , on a global grid of monthly mean between September 1999 and August 2002 in a least-square adjustment. The coefficients b and c are estimated based on the empirical equations with a same strategy used in VMF1.

From the processing of the data of each GPS station by using CSRS-PPP, we estimated the precise coordinates and ZTD, so called ZTD_{PPP} , with a time step of 30-s, for the time period from 2014 to 2017. Then we perform the daily averaged method to obtain the daily time series and select those dates which match the DInSAR observation dates. The calculated ZTD_{PPP} time series at each GPS station are subtracted from the ZTD_{PPP} time series estimated for station PUKA at the common dates, so called ΔZTD_{PPP} . Figure 4.6 indicates the resulting differenced ZTD time series of all twenty-one stations relative to PUKA.

Comparing the modeled seasonal oscillations overlain with the ΔZTD_{PPP} for each station in Figure 4.6 shows that they are properly in phase such that the minimum occur in the winter and the maximum tropospheric delay occurs in the summer every year. The results show that the model produces seasonal amplitudes of as much as 5 cm for stations APNT, PUH2 and HILR referenced to PUKA. These stations are located at the lowest altitudes and are close to the ocean.

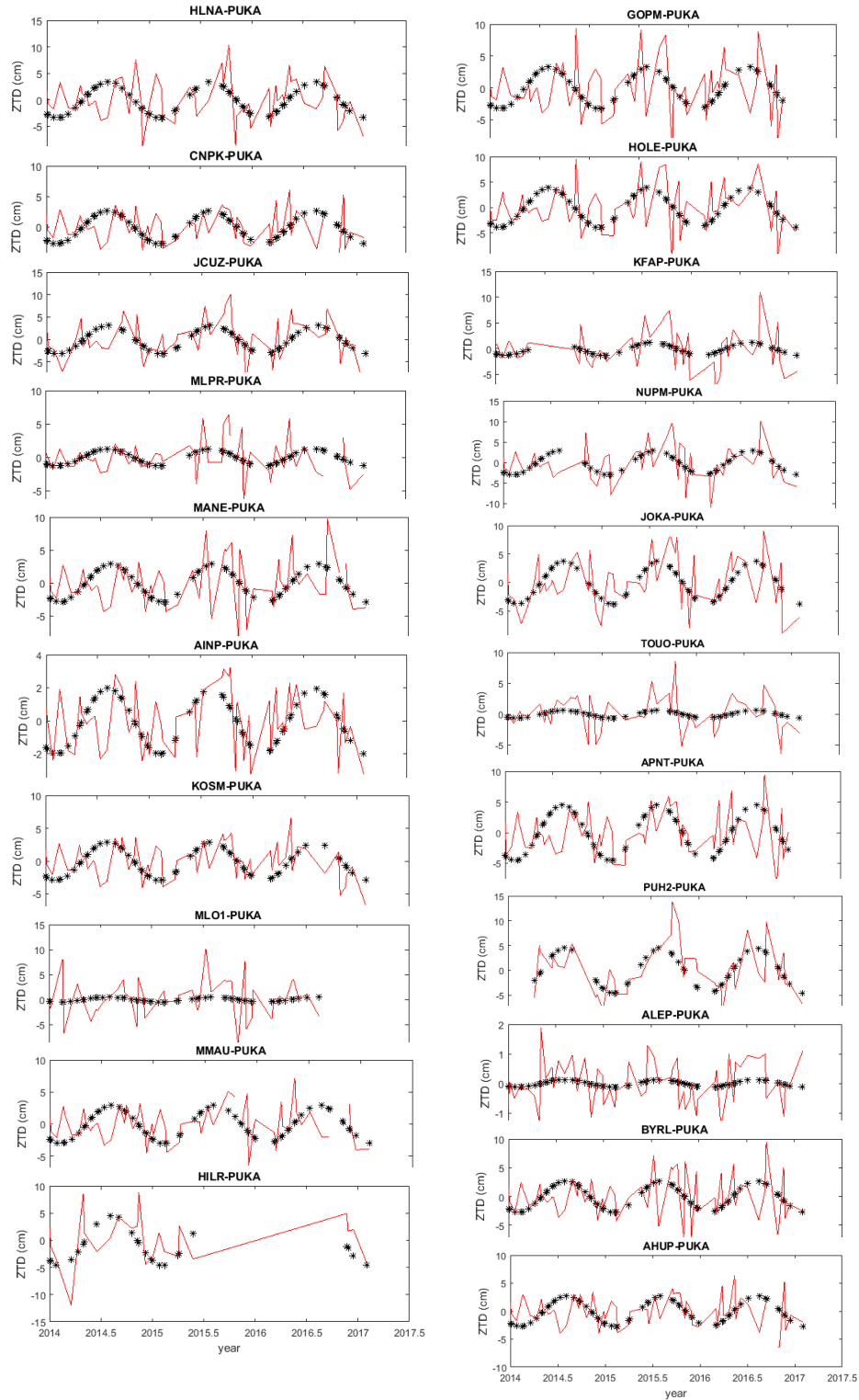


Figure 4.6. (red) ΔZTD_{PPP} time series for each GPS station relative to the reference station, PUKA (black) the modeled seasonal variation of ZTD in which the amplitudes estimated by using Equation 4.9.

The lower seasonal amplitudes, less than 1 cm, are observed for stations located on Mauna Loa summit area, e.g., TOUO, MLO1 and ALEP referenced to PUKA. In this area, the effective weather parameters including temperature, water vapor pressures and air pressure, are at their lowest values. According to Table 4.3, the modeled amplitudes computed for each GPS increase from the reference station such that, as it was expected from the elevation-dependent exponential model, the estimated amplitude for station MLO1, at height 3402.7 m above msl, is greater than the one estimated for station ALEP, at height 2895.71 m above msl.

As shown in Table 4.3, the computed rmse of the residuals between the modeled ZTD and estimated ΔZTD_{PPP} ranges from 0.24 to 5.97 cm for stations TOUO and HILR relative to PUKA, respectively. According to Jin et al. (2007), the unmodeled residuals reflect the high-frequency variations (short period) in the wet component of troposphere error and therefore change with altitude. We can see the highest value, 5.97 cm, for the station close to coast and in the windward side of the island, HILR, where the rainfall and relative humidity are at their highest values.

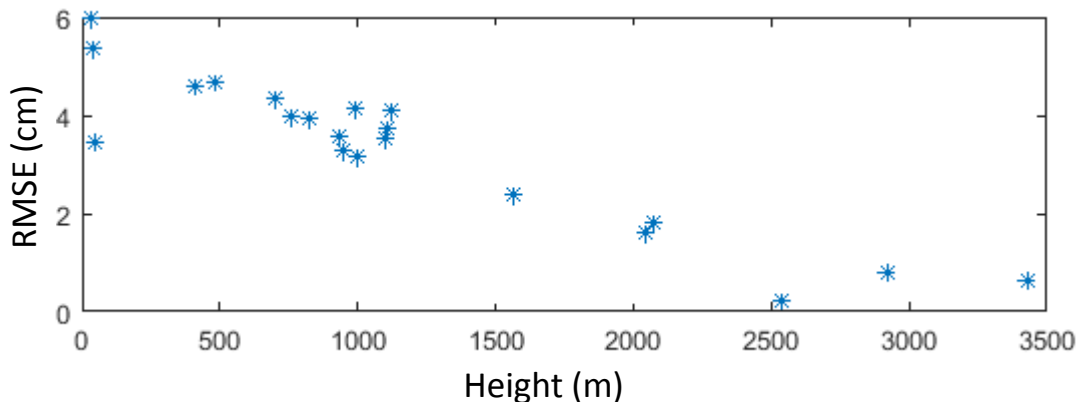


Figure 4.7. Vertical profile of the rmse of the residuals between the seasonal variations obtained from the modeled amplitudes of ZTD obtained from Equation 4.9 and the differenced ZTD, ΔZTD_{PPP} , obtained by subtracting the ZTD computed for the reference station from the ZTD computed for the other stations.

As shown in Figure 4.7, the rmse of the residuals decrease with increasing height as a result of decreasing the variability of the water vapor pressure and the wet component of the ZTD with increasing elevation. We estimated a value of less than 1 cm for the stations at heights greater than 2400 m, including TOUO, MLO1 and ALEP in the Mauna Loa summit area, where the variability of the wet component of troposphere is very low.

Furthermore, we calculate the differences between the modeled seasonal ZTD signals and the ΔZTD_{PPP} at each station to evaluate the potential of the modeled ZTD for correcting the GPS height time series for this error. Table 4.3 represents the estimated mean, maximum and minimum differences computed for each station. The mean difference is less than 0.2 cm for most of the stations. The observed mean, maximum and minimum differences of all stations are 0.16, 7.94 and 0.04 cm, respectively. The values of minimum and mean differences between the two ZTDs indicates that the best fit model to the amplitude of DInSAR data can compute the minimum and maximum of seasonal oscillations of the ZTD signals in GPS data, accurately.

4.6. Conclusion

In this paper, we could take advantage of the similarities of the effect of ZTD, a major source of positioning error in modern satellite geodesy, on both GPS and DInSAR data in order to model the local seasonal variations of ZTD on the GPS data by using high spatial resolution of DInSAR data in a high topographic relief area, the area surrounding the Kilauea volcano in Hawaii.

In this research, the DInSAR height time series obtained from the MSBAS processing of 66 SAR images taken from 2014 through 2017 with the time steps of twelve days, were analyzed by fitting a sinusoidal function. The estimates of the seasonal amplitudes range between 0.20 and 5.57 cm, which grow exponentially with increasing and decreasing elevation from the reference point at 3107 m above msl. The interpretation of the results demonstrates that the spatial variations of the observed seasonal amplitudes of ZTD, relates to the variations in the climate data particularly to the water vapor pressure and

temperature. The highest seasonal amplitudes of ZTD were found at the low altitude locations that are close to the coast area and the smallest seasonal amplitudes of ZTD were observed at the high elevations, Mauna Loa summit area.

Motivated by Samsonov et al. (2014), we proposed a model from the meteorological data observed at the surface weather station close to the DInSAR reference point and radiosonde data, PHTO/HILO. This model provides a best fit to more than 99% of the estimates of seasonal amplitudes of ZTDs in DInSAR height time series. We used the elevation-dependent correction model and considered phase shift of 180° , which leads the maximum of the amplitudes takes place in the summer (June), to compute the annual ZTD signals in GPS stations relative to the reference station. As a consequence of employing this model, we could successfully calculate the seasonal amplitude, ranging between 0.13 and 4.61 cm for twenty-one stations in Hawaii.

In order to validate our results, the RINEX data of all twenty-two considered GPS stations was processed using CSRS-PPP in static mode spanning a similar period as the DInSAR data, and then the variations of the differenced ZTD, ΔZTD_{PPP} (the difference between the ZTDs computed for each station and for the reference station, PUKA, obtained using CSRS-PPP application) were compared to the modeled seasonal variations obtained from the correction model, mentioned above. This comparison resulting an rmse of the residuals which reflects the high-frequency variations in ZTDs. We estimated 0.24 cm for station TOUO and 5.97 cm for HILR referenced to PUKA while decreasing from high to low elevations. This is because the variability of the wet component of troposphere is lower for the stations at the higher altitudes and in the volcano's summit area. The results show that the proposed correction model is capable of reducing the seasonal amplitude of ZTDs of up to 5.57 cm in the vertical component of GPS stations located at low elevations..

We also have computed the mean, maximum and minimum differences between the modeled ZTD and the ΔZTD_{PPP} for all stations as 0.16, 7.94 and 0.04 cm, respectively. The very low mean difference between the two ZTDs confirms that the seasonal

amplitudes computed from the correction model are in good agreement with the seasonal component of ΔZTD_{PPP} in the height time series of GPS stations referenced to PUKA.

These results suggest that an elevation-dependent model for the seasonal amplitude of ZTD derived from high-resolution DInSAR height time series can be used to estimate the seasonal variations of ZTD on local GPS data in a region of high variability in topography and climate. This model can be used in combination with, or in lieu of, the low spatial resolution corrections from numerical weather models in order to produce sub-centimeter level positioning accuracy. Finally, the results of this research also could be valuable in future studies of tropospheric variation in both space and time, in atmospheric water vapor.

4.7. References

- Alduchov, O.A., and Eskridge, R.E. (1996), Improved Magnus form approximation of saturation vapor pressure, *J. Appl. Meteorol.*, 35 (4), 601-609. doi: 10.1175/1520-0450(1996)035<0601:IMFAOS>2.0.CO;2
- Ayantunji, B.G., Okeke P.N. and Urama J.O. (2011), Diurnal and seasonal variation of surface refractivity over Niagara. *Progress in Electromagnetics Research B*, Vol. 30, 201-222.
- Baker, S., and Amelung, F. (2015), Pressurized magma reservoir within the east rift zone of Kīlauea Volcano, Hawai‘i: Evidence for relaxed stress changes from the 1975 Kalapana earthquake, *Geophys. Res. Lett.*, 42, doi:10.1002/2015GL063161.
- Bean, B. R., and Dutton, E. J., (1968), *Radar Meteorology*. Dover Publications, Inc., New York.
- Bevis, M., Businger, S., Chiswell, T., Herring, A., Anthes, R., Rocken, C., and Ware, R., (1994), GPS meteorology: Mapping zenith wet delays onto precipitable water, *J. Appl. Meteorol.*, 33, 379–386.

- Bevis, M., Businger S., Herring T., Rocken C., Anthes R., and Ware R. (1992), GPS meteorology: Remote sensing of atmospheric water vapor using the Global Positioning System, *J. Geophys. Res.*, 97(D14), 15,787–15,801, doi:10.1029/92JD01517.
- Bock, Y., and Williams, C.A. (1997), Integrated satellite interferometry in southern California, *EOS, TRANSACTIONS, AGU*, 78 (29), 299-300.
- Boehm J., Niell A., Tregoning, P., Schuh, H. (2006a), Global Mapping Function (GMF): A new empirical mapping function based on numerical weather model data. *Geophys Res Lett* 33:L07304, DOI 10.1029/2005GL025546
- Boehm J, Werl, B., Schuh, H. (2006b), Troposphere mapping functions for GPS and very long baseline interferometry from European Centre for Medium-Range Weather Forecasts operational analysis data. *J Geophys Res* 111:B02406. doi:10.1029/2005JB003629
- Boehm, J., Heinkelmann, R. and Schuh, H. (2007), A global model of pressure and temperature for geodetic applications. *J Geod*, 81(10), pp.679–83.
- Bonforte, A., Ferretti A., Prati C., Puglisi G., and Rocca F. (2001), Calibration of atmospheric effects on SAR interferograms by GPS and local atmospheric models: First results, *J. Atmos. Solar-Terrestrial Phys.*, 63, 1343 – 1357.
- Bos, M.S., Scherneck, H.G. (2011), Free Ocean Tide Loading Provider URL <http://holt.oso.chalmers.se/loading>
- Clague, D.A., Sherrod, D.R., (2014), Growth and degradation of Hawaiian volcanoes. Chapter 3. In: Poland, M.P., Takahashi, T.J., Landowski, C.M. (Eds.), *Characteristics of Hawaiian Volcanoes*. USGS Professional Paper 1801, pp. 97–146.

- Colleen, D., (2013), Spatial Distribution of Freshwater Resources on the Hawaiian Islands
- Costantini, M. (1998), A novel phase unwrapping method based on network programming. *IEEE Geosci Remote S*, 36(3):813–821.
- Decker, R.W., Hill, D.P., Wright, T.L., (1966), Deformation measurements on Kilauea Volcano, Hawaii: *Bulletin Volcanologique*, v. 29, p. 721-732.
- Delacourt, C., Briole, P., and Achache, J. (1998), Tropospheric corrections of SAR interferograms with strong topography. Application to Etna, *Geophys. Res. Lett.*, 25(15), 2849–2852, doi:10.1029/98GL02112
- Fiske, R. S., and Jackson, E. D., (1972), Orientation and growth of Hawaiian volcanic rifts: the effect of regional structure and gravitational stresses: *Royal Soc. [London] Proc.*,v. 329, p. 299- 326.
- Foster, J., Brooks B., Cherubini T., Shacat C., Businger S., and Werner, C., L., (2006), Mitigating atmospheric noise for InSAR using a high resolution weather model, *Geophys. Res. Lett.*, 33, L16304, doi: 10.1029/2006GL026781.
- Fotiou A., Pikridas C. (2012), *GPS and Geodetic Applications*, 2nd edition, (Eds.) Ziti, Thessaloniki, Greece.
- Frazier, A. (2012), Month-year rainfall maps of the Ha-waiian Islands. M.A. thesis. University of Hawai'i at Manoa, 81pp
- Gagné WC, Cuddihy LW. (1990), Vegetation. In: Wagner WL, Herbst DR, Sohmer SH. (Eds) *Manual of the Flowering Plants of Hawai'i*. University of Hawai'i Press; /Bishop Museum Press, Honolulu, 45–114.
- Ge, L. (2000), Development and testing of augmentations of continuously-operating GPS networks to improve their spatial and temporal resolution. UNISURV S-63, The University of New South Wales, Australia

- Ge, L and Chang, H.C. and Janssen, V. and Rizos, C. (2003), Integration of GPS, radar interferometry and GIS for ground deformation monitoring. Proc. 2003 Int. Symp. on GPS/GNSS, Toyko, Japan, 15-18 November 2003. pp. 465-472.
- Geng J, Shi C, Ge M, Dodson AH, Lou Y, Zhao Q, Liu J (2012), Improving the estimation of fractional-cycle biases for ambiguity resolution in precise point positioning. *J Geod* 86(8):579–589. doi:10.1007/s00190-011-0537-0
- Giambelluca, T.W., Shuai X., Barnes M.L., Alliss R.J., Longman R.J., Miura T., Chen Q., Frazier A.G., Mudd R.G., Cuo L., and Businger A.D. (2014), Evapotranspiration of Hawai‘i. Final report submitted to the U.S. Army Corps of Engineers—Honolulu District, and the Commission on Water Resource Management, State of Hawai‘i.
- Goad, C.C., and Goodman L. (1974), A modified Hopfield tropospheric refraction correction model. In: American Geophysical Union Annual Fall Meeting, 12-17 December 1974, San Francisco, California, USA (abstract EOS Trans. AGU 55, 1106).
- Goldstein R. M and Werner C. R. (1998), interferogram filtering for geophysical applications. *Geophys Res Lett*, 25(21):4035–4038.
- Grell, A.G., Dudhia, J., Stauffer, D.R., (1995). A Description of the Fifth-Generation Penn State/NCAR Mesoscale Model (MM5). NCAR Technical Note, NCAR/TN-398 STR. National Center for Atmospheric Research, Boulder, CO.
- Hanssen, R. F., (1998), Atmospheric heterogeneities in ERS tandem SAR interferometry DEOS Report No. 98.1, 136 pp, Delft University Press, Delft
- Hanssen, R.F., (2001), Radar Interferometry. Data Interpretation and Error Analysis, Kluwer.
- Hofmann-Wellenhof, B., Lichtenegger, H. and Collins, J. (2001), GPS. Theory and practice 5th Edition. Springer, New York, ISBN 3-211-83534-2, 384 pp.

- Hopfield, H.S. (1969), Two-quadratic tropospheric refractivity profile for correcting satellite data. *J Geophys Res*, Vol. 74, PP. 4487-4499.
- Hopfield, H. S. (1972), Tropospheric range error parameters: further studies. Applied Physics Laboratory Technical Memorandum TG1291, Johns Hopkins Univ., Baltimore, Md.
- Houlié N., Briole P. , Nercessian A., and Murakami M. (2005), Sounding the plume of the 18 August 2000 eruption of Miyakejima volcano (Japan) using GPS, *Geophys. Res. Lett.*, 32, L05302, doi:10.1029/2004GL021728
- Jin S., Park J.U., Cho J.H., Park P.H. (2007), Seasonal variability of GPS-derived zenith tropospheric delay (1994–2006) and climate implications, *Journal of Geophysical Research*, Vol. 112, No. D9, DOI: 10.1029/2006JD007772.
- Jolivet R., Agram P.S., Lin N., Simons M., Doin M., Peltzer G., Li, Z. (2014), Improving InSAR geodesy using Global Atmospheric Models, *J. Geophys. Res.*, 119, pp. 2324-2341, 10.1002/2013JB010588
- Klobuchar, J.A. (1996), Ionospheric effects on GPS, in: Parkinson, B.W. & J.J. Spilker (Eds.), *Global Positioning System: Theory and Applications Volume I*, Progress in Astronautics and Aeronautics, 163, AIAA, Washington, 485-515.
- Kouba, J. (2008), Implementation and testing of the gridded Vienna Mapping Function 1 (VMF1). *J Geodesy* 82(4):193–205. doi:10.1007/s00190-007-0170-0
- Lawrence, M. G. (2005), The relationship between relative humidity and the dewpoint temperature in moist air. *Bull. Am. Meteorol. Soc.* 86:225–233.
<http://dx.doi.org/10.1175/BAMS-86-2-225>.
- Leandro, R.F. (2009), Precise Point Positioning with GPS: A New Approach for Positioning, Atmospheric Studies, and Signal Analysis. Ph.D. dissertation, Department of Geodesy and Geomatics Engineering, Technical Report No. 267, University of New Brunswick, Fredericton, New Brunswick, Canada, 232 pp.

- Li Z., J. Muller, P. Cross, E. (2005), Fielding Interferometric synthetic aperture radar (InSAR) atmospheric correction: GPS, Moderate Resolution Imaging Spectroradiometer (MODIS), and InSAR integration J Geophys Res., 110 (2005), 10.1029/2004JB003446
- Li, Z., E. J. Fielding, P. Cross, and J.-P. Muller (2006), Interferometric synthetic aperture radar atmospheric correction: GPS topographydependent turbulence model, J. Geophys. Res., 111, B02404, doi:10.1029/2005JB003711
- Longman, R.J., Diaz H.F., Giambelluca, T.W. (2015), Sustained increases in lowertropospheric subsidence over the central tropical North Pacific drives adecline in high elevation rainfall in Hawai'i. J Clim.;28:8743–59.
- Lu C., Li X., Li Z., Heinkelmann R., Nilsson T., Dick G., Ge M., Schuh H. (2016), GNSS tropospheric gradients with high temporal resolution and their effect on precise positioning. J. Geophys. Res. Atmos.;121:912–930. doi: 10.1002/2015JD024255.
- Martin, F., and Waldron C. (1961), A layered exponential model of radar refractivity, J. Geophys. Res., 66(12), 4129–4135, doi:10.1029/JZ066i012p04129.
- Mendes, V. B. (1999), Modeling the neutral-atmosphere propagation delay in radiometric space techniques. Ph.D. dissertation, Department of Geodesy and Geomatics Engineering Technical Report No. 199, University of New Brunswick, Fredericton, New Brunswick, Canada, 353 pp
- Mendes, V. B. and Langley, R. B., (1994), A Comprehensive Analysis of Mapping Functions Used in Modeling Tropospheric Propagation Delay in Space Geodetic Data, International Symposium on Kinematic Systems in Geodesy, Geomatics and Navigations, Banff Canada
- NRCan GSD (Natural Resources Canada Geodetic Survey Division) (2004), On-line Precise Point Positioning Project-How To Use Document. V.1.1, 2004.

- Peterson, D.W., and Moore, R.B., (1987), Geologic history and evolution of geologic concepts, Island of Hawaii, chap. 7 of Decker, R.W., Wright, T.L., and Stauffer, P.H., eds., *Volcanism in Hawaii: USGS Professional Paper 1350*, v. 1, p. 149–189.
- Poland, M., Miklius A., Sutton J., and Thornber C. (2012), A mantle-driven surge in magma supply to Kīlauea Volcano during 2003–2007, *Nat. Geosci.*, 5, 295–300
- Saastamoinen, J. (1972), Atmospheric correction for the troposphere and stratosphere in radio ranging of satellites, in *The Use of Artificial Satellites for Geodesy, Geophys. Monogr*, vol. 15, pp. 247–251, AGU, Washington, D. C.
- Samsonov S., Tiampo K., Rundle J., Li Z., (2007), Application of DinSAR-GPS Optimization for Derivation of Fine-Scale Surface Motion Maps of Southern California. *IEEE Transactions on Geoscience and Remote Sensing*, 45 (2). doi: <http://dx.doi.org/10.1109/TGRS.2006.887166>.
- Samsonov S., and d'Oreye N., (2012), Multidimensional time series analysis of ground deformation from multiple InSAR data sets applied to Virunga Volcanic Province. *Geophysical Journal International*, 191(3):1095–1108, doi: 10.1111/j.1365-246X.2012.05669.x.
- Samsonov, S.V., Trishchenko, A.P., Tiampo, K., González, P.J., Zhang, Y., and Fernández, J. (2014), Removal of systematic seasonal atmospheric signal from interferometric synthetic aperture radar ground deformation time series, *Geophys. Res. Lett.*, 41, 6123–6130, doi:10.1002/2014GL061307.
- Sandwell, D., and Sichoix L. (2000), Topographic recovery from stacked ERS interferometry and a low resolution digital elevation model, *J. Geophys. Res.*, 105, 28,211 – 28,222.
- Smith, E.F., and Gomberg, J., (2009), A search in strainmeter data for slow slip associated with triggered and ambient tremor near Parkfield, California, *J. Geophys. Res.*, 114, B00A14, doi:10.1029/2008JB006040.

- Smith, E. K., and Weintraub, S., (1953), The constants in the equation for the atmospheric refractive index at radio frequencies, *Proc. IRE*, 41(8), 1035–1037.
- Spilker, J., (1996), Tropospheric effects on GPS. In *Global Positioning System: Theory and applications I*, vol. 163, edited by Parkinson BW and Spilker JJ, American Institute of Aeronautics and Astronautics, Washington, 517-546.
- Tregoning, P., and van Dam T. (2005), Atmospheric pressure loading corrections applied to GPS data at the observation level, *Geophys. Res. Lett.*, 32, L22310, doi:10.1029/2005GL024104.
- Triplet, J.P., and Roche, C., (1983), *Mdte'orologie grindtale*, 300 pp, Météo France
- Trusdell, F.A., and Swannell, P. (2003), Explosive deposits on Mauna Loa [abs.]: Cities on Volcanoes 3 meeting, Hilo, Hawaii, July 14–18, 2003, Abstracts Volume, p. 135.
- USGS (2017a), Hawaii Volcano Observatory, Volcano Hazards Program, visited July 07th.
- USGS (U.S. Geological Survey) (2017b), Hawaii Volcano Observatory, Active Volcanos of Hawaii, visited July 07th.
- van Dam, T. M., Blewitt G., and Heflin M. (1994), Detection of atmospheric pressure loading using the Global Positioning System, *J. Geophys. Res.*, 99, 23,939–23,950, doi:10.1029/94JB02122.
- Vedel, H., Mogensen, K. S., and Huang, X. (2001), Calculation of zenith delay from meteorological data: Comparison of NWP model, radiosondes and GPS delay, *Phys. Chem. Earth.*, 26, 497 – 502.
- Wegmuller U. and Werner C. (1997) GAMMA SAR processor and interferometry software. In *The 3rd ERS symposium on space at the service of our environment*, Florence, Italy.

- Williams S., Bock Y., Fang P. (1998), Integrated satellite interferometry: Tropospheric noise, GPS estimates and implications for interferometric synthetic aperture radar product. *J. Geophys. Res.*;103:27051–27068.
- Wilson, D., Elias T., Orr T., Patrick M., Sutton J., and Swanson D. (2008), Small explosion from new vent at Kilauea's summit, *Eos Trans. AGU*, 89, 203, doi:10.1029/2008EO220003.
- Yu, C., Penna, N.T., Li, Z. (2017) Generation of real-time mode high-resolution water vapor fields from GPS observations. *J. Geophys. Res.*, 122, 2008–2025.
- Yuan, Y., Zhang, K., Rohm, W., Choy, S., Norman, R., Wang, C. (2014), Real-time retrieval of precipitable water vapor from GPS precise point positioning. *J Geophys Res Atmos* 119:10044–10057
- Zebker, H.A., Rosen P.A., Hensley S. (1997), Atmospheric effect in interferometric synthetic aperture radar surface deformation and topographic maps. *J. Geophys. Res.* 102 (B4), 7457–7563.
- Zhang C., Wang Y., Hamilton K, and Lauer A., (2016), Dynamical Downscaling of the Climate for the Hawaiian Islands. Part II: Projection for the Late Twenty-First Century, *J Cli* 29 (8), 3027-3048

Chapter 5

5 General Conclusions

5.1. Summary and Conclusions

The goal of this research was to employ state-of-art approaches to produce more precise GPS location estimates in order to accurately monitor surface deformations induced by the physical processes on a regional and local scale. In the first phase of this work, I processed GPS data in different network configurations in order to determine the most reliable sub-networks for regional surface deformation measurements. In addition, I applied a noise analysis model and characterized the noise characteristics of the position time series, and developed a technique that produces a simplified elevation-dependent model which can accurately estimate the seasonal variations of local ZTD on GPS height time series.

In the first work, I studied the horizontal and vertical surface deformation of eastern Ontario and western Québec, which are primarily due to GIA processes. Different subsets of GPS stations from a network of seven permanent cGPS stations operated by NRCan plus seven stations from the POLARIS network were processed using double-differencing techniques in BSW5.0 for one year of GPS data. The two most reliable sub-networks of GPS stations were selected which result in the most accurate GPS position time series between 2008 and 2012. In addition to analyzing the position changes time series of the GPS stations from the selected sub-network over five years, the time series of fifty-five additional stations over a similar time period from a global solution was employed to compare GPS-constrained surface deformation to GIA model predictions. The observed horizontal velocity of the GPS stations in the study area shows that the GPS stations are rotating counterclockwise from south, near the Great Lakes, to north, near Hudson Bay, ranging from 0.67 mm/yr to 1.50 mm/yr. The estimated vertical velocities reveal that there is a significant difference between the velocity of the GPS stations in the southern region, -1.93 ± 0.46 mm/yr, and the northern region, 10.92 ± 1.12 mm/yr.

A complex noise model which is the combination of white noise and power law noise were employed to analyze the GPS time series using Hector software and the MLE method. The amplitude and spectral index of the GPS position time series were estimated for all three components assuming annual and semi-annual signal. The estimates of the mean spectral index obtained from the best fit spectral of white noise and power law noise estimated using MLE for the Bernese and global solution times series were approximately -1.01 ± 0.09 and -0.79 ± 0.07 , respectively, indicating the presence of flicker noise in the time series. The similarity of the spectral indices estimated from the power law noise showed that almost all GPS stations in this study are affected by an identical noise type, flicker noise, which is mainly due to the instabilities of the geodetic monuments. The estimates of the horizontal and vertical velocity uncertainties from this analysis were examined and we found that less than 40% of the vertical velocity errors in the GPS stations considered in this study relates to the surface mass loading effects and this value is less than 17% for the horizontal velocities uncertainties.

Significant variation in the direction of the horizontal component of the velocities of the stations in the southern and northern regions was observed, ranging between 0.67 and 1.50 mm/yr. The observations of the horizontal velocities vectors indicate that the stations near the Great Lakes are directed south-southeast while the stations on the shoreline of Hudson Bay are oriented toward the Bay. Study of the vertical component of the GPS time series reveals a subsidence of approximately 1.93 ± 0.46 mm/yr. in the south and uplift of approximately 10.92 ± 1.12 mm/yr. in the north.

The results show that the vertical velocities provide a better fit to the vertical velocities predicted by the GIA models and help to constrain the viscosity profile in the lower and upper mantle. The horizontal velocities, although an order of magnitude smaller than the vertical, are in good agreement with the predicted models of the stations in the southern region, although none of the models could reproduce the horizontal directions of the stations in the north, INUQ and IVKQ.

In the second work, I studied the local ZTD and PWV for the same GPS stations as in the previous study, in eastern Ontario and western Québec. I employed the observations of

atmospheric parameters from the weather stations near each GPS station. Because the atmospheric parameters are more sensitive to the topography, I corrected them for the height difference using interpolation methods. Subsequently, ZTD and PWV at the location of each GPS station were calculated. It is worthwhile to mention that the errors in the interpolated temperature and pressure do not significantly change the accuracy of the obtained results.

As the seasonal amplitude of ZTD has higher effect on the position accuracy and they could be modeled properly as a function of height. I proposed a model to compute the seasonal amplitude of ZTD between each station and a reference station. This model is based on the decay parameter of refractivity, which I computed from the best fitting exponential function to the mean refractivity at all GPS stations and the seasonal amplitude of refractivity at the reference station. To evaluate the accuracy of the model, the ZTD time series between 2008 and 2012 was computed for each GPS station using the CSRS-PPP application, which employs global weather prediction models to correct for tropospheric error. The rms difference between the ZTD estimated from GPS data processing and that computed from meteorological data range between 3.8 and 11.1 cm.

Comparing the modeled seasonal amplitudes and the observed seasonal amplitudes of ZTD between each station and ACTO reveals a good agreement for all stations, with an exception of stations INUQ and IVKQ. The large seasonal amplitude observed for these two stations is probably due to their low correlations with station ACTO. As we observed, the correlation coefficients between the ZTD at stations in the south (lower latitude) and the ZTD at other stations decrease by increasing the latitude. The results of this study demonstrated that the proposed model can accurately estimate the seasonal variations of ZTD as well as the seasonal amplitude of ZTD computed using precise point positioning technique, for a local GPS network with small differences in regional topographic height.

In addition, I observe a positive correlation between the absolute ZTD time series obtained from the integration of refractivity computed from meteorological data and GPS processing at all stations. The comparison between the mean of the daily time series of

the two ZTDs, indicates that the mean values of MET-ZTD are greater than the GPS-ZTD at all sites. Also, I computed the local PWVs at all stations from the two strategies. Similar daily variations between the GPS-PWV and MET-PWV were observed, with the largest differences identified between July and September, when the humidity and water vapor pressure increase in the local atmosphere.

Computing the seasonal variations of ZTD in volcanic areas, where the local weather conditions change significantly with elevation, is a challenging issue. Therefore, in the last stage of this work, I employed high spatial resolution DInSAR data in an area surrounding Kilauea volcano on the island of Hawaii. All the DInSAR data in LOS direction are converted to the vertical direction by dividing by cosine of incidence angle, the mapping function commonly used in DInSAR data. By employing MSBAS processing approach, the east-west and height components of deformation were produced, the horizontal north-south component are ignored because its contribution is very small. Then we observed the seasonal variations of ZTD at every pixel. The proposed model is based on radiosonde and meteorological data from a weather station collocated with the location of a DInSAR reference point, estimating the best fit to the vertical profile of the seasonal amplitudes of ZTD in the vertical time series of all DInSAR pixels.

Results show that the magnitude of the seasonal amplitude of ZTD increases exponentially from the altitude of that reference location. The accuracy of the proposed model is evaluated by comparing the sinusoidal seasonal variations obtained from the modeled seasonal amplitude to the variation of the PPP-derived local ZTD, using CSRS-PPP online application, on twenty-one GPS stations distributed throughout the island, relative to the reference station. Although in the GPS processing the GMF mapping functions are employed to produce ZTD and the troposphere gradient in the north and east directions are estimated along with ZTD, the estimated minimum and mean differences, close to zero, indicate that the proposed model accurately estimates the seasonal fluctuations of ZTD on local GPS network. Also, based on that comparison, the root mean square error (rmse) of the residual, reflecting the variations of the local water vapor pressure, was computed for every GPS station. The estimated rmse values

decreased with increasing height. The lowest (0.24 cm) and highest (5.97 cm) rmse values were observed for the stations at the lowest and highest altitudes, respectively.

All the GPS data on Kilauea were processed using the CSRS-PPP application, which employs GMF and global weather parameters. The results indicate that the proposed model can be used in high accuracy positioning applications. The main advantage of using the proposed model is that it eliminates the need for the meteorological data at the location of each GPS station and it can be used in local networks in lieu of the low spatial resolution of numerical weather prediction models. Finally, this model can accurately estimate the seasonal amplitude of ZTD on a local scale at any arbitrary elevation.

5.2. Future Studies

Possible avenues for future studies can be outlined as follows:

The Bernese software used in the first study models the tropospheric effects based on the NMF mapping function. Employing an updated version of Bernese that uses mapping functions such as VMF1 and GMF, which better take into account the measurements of atmospheric parameters, is recommended for future work.

Also, in the first study I used five years data of GPS stations, which can be used to provide a more accurate crustal velocity field at a smaller spatial resolution to constrain the predicted motions by GIA models. However, processing of longer time series would be beneficial to achieve a better estimate of surface velocity in both horizontal and vertical directions, and potentially allow for inversion of the parameters of the different GIA models.

The results of the second study provide important information regarding the seasonal changes of the local ZTD which could be valuable for observing the temporal and spatial variations of water vapor pressure on local and regional scales in the future.

Taking advantage of the similarities of the effects of ZTD on both DInSAR data and GPS data, the methods proposed in this research for computing the local ZTD on GPS data can be used to correct the DInSAR data by employing different interpolation approaches. In

addition, it is recommended to integrate DInSAR derived ZTDs with cGPS derived ZTDs in the future work.

The proposed model to compute the elevation-dependent seasonal variations of ZTD is based on the seasonal amplitude of refractivity at the reference station. Employing the actual time series of refractivity from that reference station reproduces the ZTD time series between the measurement and the reference sites estimated by using CSRS-PPP application.

It is recommended to employ the proposed simplified refractivity model obtained from high spatial resolution of DInSAR data instead of using the low resolution global weather prediction models and to evaluate the accuracy of the positioning estimates at better spatial resolutions in future studies of GPS data in different regions, including tectonically active basins such as the Wasatch Range or the Sierra Nevada mountains.

In this dissertation, Hector software was employed to identify the noise type in the GPS position time series. It may be possible to use this software to evaluate the error on DInSAR time series, although the time-dependent noise in the DInSAR observations is different from those which are dominant in the GPS observations (e.g., the monument instabilities which results in flicker noise and walker noise)

The DInSAR data in LOS direction were converted to the zenith direction by dividing by the cosine of the satellite incidence angle, the mapping function. It is recommended to evaluate that relationship and other mapping functions and their associated uncertainties in future studies.

Appendices

A GPS data processing using Bernese V.5

In this paper, RINEX data for GPS stations spanning 2008 to 2012 (Table A-1) are processed using the Bernese Processing Engine (BPE) (Beutler et al. 2007) and a double-differencing technique. Table A-1 contains all information related to the GPS RINEX data in this analysis, including position of the sites, monuments, receiver and antenna types, the first date of data availability, length and end date. The offset dates for the considered time interval are shown as well.

The updated precise orbit information and the Earth Orientation Parameter (EOP) spanning of our GPS campaign are introduced into the program to create the standard orbit files. In the preprocessing phase, the code observation files are used to synchronize the receiver clock with the GPS times and then the baselines are created based on the zero-difference observation files. In addition, at this stage, the cycle-slips and outliers are detected and removed by considering the RMS value of the observations and multiple ambiguities are added for the phase observations using the triple-combination approach.

Table A.1. GPS station information for stations from the POLARIS network and those operated by Canadian Geodetic Survey (CGS), Natural Resources Canada. All coordinates are based on WGS84. The subscript star is Stations operated by Canadian Geodetic Survey (CGS), Natural Resources Canada.

| Site | Monument | Lat. | Lon. | Start Date | Length (year) | Offset | End date | Location | Receiver Type | Antenna Type |
|-------|-------------------------|-----------------|-----------------|------------|---------------|-------------------------------|---------------|--------------------------------------|--------------------|---------------|
| ALGO* | Stainless steel pillars | N45° 57' 20.85" | W78° 04' 16.91" | 2001 Jun. | 4.79 | 2012 Dec. 20 | 2012 Dec. 31 | Algonquin Park, ON, Canada | AOA BENCHMAR K ACT | AOAD/M _T |
| ACTO | Concrete pier | N43° 36' 31.32" | W80° 03' 44.64" | 2004 Nov. | 4.75 | ----- | 2012 Dec. 20 | Acton, ON, Canada | NOVATEL1 | NOV702 |
| TYNO | Concrete pier | N43° 05' 42" | W79° 52' 12.72" | 2004 Nov. | 4.72 | ----- | 2012 Dec. 31 | Tyneside, ON, Canada | NOVATEL2 | NOV702 |
| STCO | Concrete pier | N43° 12' 34.56" | W79° 10' 13.8" | 2005 Apr. | 4.75 | ----- | 2012 Dec. 24 | Saint Catharines, ON, Canada | NOVATEL3 | NOV702 |
| KLBO | Stainless steel pillars | N45° 21' 23.76" | W80° 12' 47.52" | 2009 May | 3.02 | ----- | 2012 June 29 | Killbear Provincial Park, ON, Canada | NOVATEL4 | NOV702 |
| MATQ | Stainless steel pillars | N49° 45' 32.25" | W77° 38' 15.16" | 2008 Jul. | 4.48 | ----- | 2012 Dec. 31 | Matagami La Palce, QC, Canada | TRIMBLE NETRS | TRM4124 9.00 |
| IVKQ | Stainless steel pillars | N62° 25' 52.35" | W77° 54' 39.37" | 2008 Jul. | 4.21 | ----- | 2012 Oct. 24 | Ivujivik, QC, Canada | TRIMBLE NETRS | TRM4124 9.00 |
| INUQ | Stainless steel pillars | N58° 27' 3.76" | W78° 7' 6.11" | 2008 Jul. | 3.72 | ----- | 2010 April 12 | Inukjuak, QC, Canada | TRIMBLE NETRS | TRM4124 9.00 |
| KUUJ* | Concrete pier | N55° 16' 42.10" | W77° 4' 43.56" | 2002 Jul. | 4.97 | 2010 July 30 2012 Sept. 06 | 2012 Dec. 31 | Kuujuuarapi k, QC, Canada | TPS NETG3 | TPSCR.G 3 |
| VALD* | Concrete pillar | N48° 05' 49.41" | W77° 3' 5.1" | 2001 Nov. | 4.77 | 2009 July 18 2010 Feb. 15 | 2012 Dec. 31 | Val D'Or, QC, Canada | TPS NETG3 | TPSCR.G 3 |
| CAGS* | Pillar | N45° 35' 06" | W75° 48' 26.28" | 2000 Feb. | 4.87 | 2011 July 12 | 2012 Dec. 31 | Gatineau, QC, Canada | TRIMBLE NETRS | ASH7009 36D_M |

The ionospheric delay signals are eliminated using ionosphere free linear combination (L3) of carrier phase measurements. The effect of the higher order ionosphere has not been considered as they have less than 1 mm effects (Hernández-Pajares et al. 2007; Petrie et al. 2010). The tropospheric effects are modeled by applying the Niell (1996) mapping function for both the dry and the wet part which maps the zenith troposphere delay to the satellite-station direction. The benefit of using this model is that the calculation of the wet and dry mapping functions does not depend on the local surface meteorology and it gives an accurate positions for stations located in the latitude range 43-75°N for minimum elevation angle of three degrees.

Here, we considered the minimum elevation angle equal to five degrees that minimizes multipath errors. The ocean tidal loading effects that cause crustal deformation and therefore site displacement are corrected from the horizontal and vertical components by introducing a GOT00.2 model containing eleven coefficients for each particular site to the program. This file contains the magnitude of the ocean loading effect for a subset of IGS stations so that the amplitude and phase shifts values for other stations in our study were obtained from Bos & Scherneck (2011). These values were not corrected for the center of mass motion so that our frame origin is in the solid earth centre (CM).

Next, all baselines are processed separately and the ambiguities are resolved by the Quasi-Ionosphere-Free (QIF) Ambiguity Resolution Strategy. New coordinates and troposphere parameters files are introduced and the results consist of two parts. The first part refers to the solution where the ambiguities are estimated as real-valued measurement biases whereas the second part reports the results after resolving the ambiguity parameters to integer values. It is important to know that the ambiguities larger than the specified RMS could not be resolved.

Then, the final network solution is implemented in which the correlation between the observations is considered and the ambiguities that have been resolved already are introduced as known parameters. In this way, the free network or the minimum constraint solution, in which no station is fixed to its a priori coordinates, is carried out in this paper. This approach is optimal for defining the geodetic datum with a

minimum number of constraints where there are inconsistencies in the reference stations coordinates. Then, the coordinates obtained from the last solution are compared to the a priori coordinates for the IGS core sites so that the stations with the residual more than the considered threshold, 15 mm for north and east directions and 30 mm for up direction, would be rejected in the datum definition. In this phase, seven transformation parameters are calculated by comparing the two sets of coordinates, the output coordinates from the last step to the first input file containing stations coordinates in IGS08, in the Helmert transformation program. Then the repeatability of the coordinate solution is checked to report the difference of each individual coordinate set to the mean value. In the final solution at each epoch, the troposphere parameters have to be pre-eliminated and to avoid singularities, all station coordinates have to be constrained. The station coordinates obtained in the last step are introduced here.

Subsequently, the obtained daily GPS position time series spanning approximately 5 years are analyzed to estimate the velocities of the GPS sites. The outliers are eliminated as follows: first coordinates with jumps of more than 300 mm are removed manually, then the Hampel filter (Hampel 1974) is employed. In this method, if a point differs from the mean by more than three times the standard deviation it is replaced by the median of the window containing the six surrounding points.

We employed the sigma averaging (SIGAVG) method presented by Goudarzi et al. (2012) in the GPS interactive time series analysis (GITSA) software (Goudarzi et al., 2012) to detect jumps and discontinuities in the position time series. This approach divides the time series into different segments based on the introduced threshold, here set at 3 mm, and detects discontinuities at the border of adjacent segments without jumps.

The rate uncertainties and the linear trends are then determined by employing Hector software (Bos et al., 2013). A Maximum Likelihood Estimation (MLE) approach is used to calculate the noise in the time series (Williams et al., 2004) by computing the parameters of the noise model, including the amplitude and spectral index. This software also computes the constant velocity, offsets which may occur due to GPS equipment changes, annual and semi-annual variations and velocity uncertainties. Here, the

combination of the power-law noise (colored noise) and white noise is taken into account as source of noises in the time series. In addition, the AmmarGrag method is employed for the likelihood computation because the percentage of missing data is less than 50% of the total time series length. The covariance matrix which represents the time-dependent positions is computed from (William 2008) (Equation A.1):

$$C = a_w^2 I + b_v^2 J_v \quad (\text{A.1})$$

where, a_w and b_v are the white and power-law amplitudes, respectively. These depend on the variance of the noise, innovation noise, σ^2 . I is the unit matrix with $n \times n$ dimension and J_v is the covariance matrix for the power-law noise with spectral index ν .

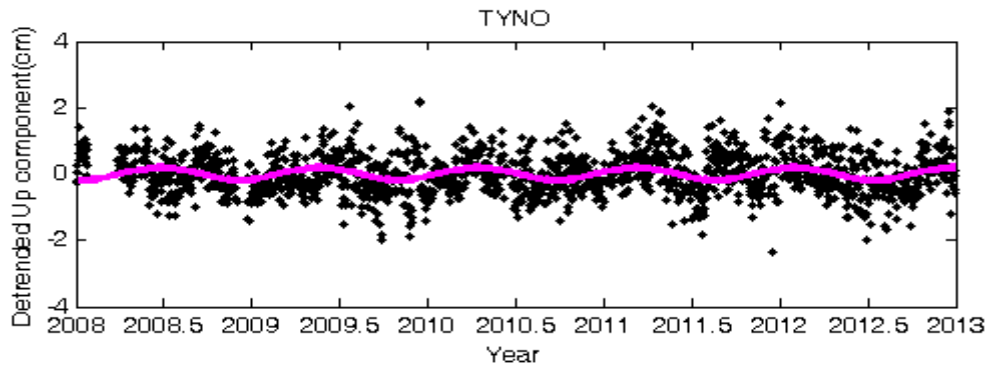


Figure A.1. Detrended position changes time series at station TYNO in eastern Ontario. The pink line corresponds to the best fit annual sinusoidal function.

Figure A.1 illustrates the daily vertical position time series for station TYNO and its corresponding fitted sine function.

To verify the correctness of choice of the noise model, the power spectra analysis is carried out by fitting the combination of white plus power-law noise model to the computed spectrum for the GPS observations. This analysis represents the difference between observations minus the estimated linear trend and additional offsets and periodic signals. Figure A.2 shows the Power Spectral Density (PSD) plot for the vertical position time series of station TYNO. At high frequencies the fitted model is flat, which is representative of the white noise. At lower frequencies the fitted model obeys power-law

noise with a slope of approximately one, which implies the presence of flicker noise in the time series.

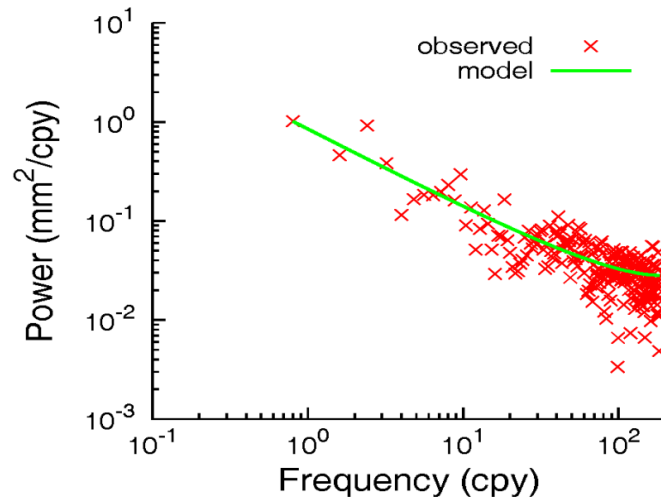


Figure A.2. The computed power spectral density of the residuals for the up component for station TYNO. The fitted white plus power-law noise model is shown by the solid green line. The red “x” is the calculated spectrum for the observations.

A.1 References

Beutler G, Bock H, Dach R, Fridez P, Gade A, Hugentobler U, Jaggi A, Meindl M, Mervart L, Prange L, Schaer S, Springer T, Urschl C, and Walser P (2007), Bernese GPS Software Version 5.0. In: Dach R, Hugentobler U, Fridez P, and Meindl M (eds) Astronomical Institute University of Bern, Bern

Bos, M.S., and Scherneck, H.G. (2011), Free ocean tide loading provider. <http://holt.oso.chalmers.se/~loading>

Bos, M.S., Fernandes, R.M.S., Williams, S.D.P., and Bastos, L. (2013), Fast error analysis of continuous GNSS observations with missing data. *J Geodesy* 87(4):351–360. doi:10.1007/s00190-012-0605-0

Goudarzi M.A., Cocard M., Santerre R., and Woldai T. (2013), GPS interactive time series analysis software. *GPS Solut* 17: 595–603. doi:10.1007/s10291-012-0296-

- Hampel F.R. (1974), The influence curve and its role in robust estimation. *J Am Stat Assoc* 69(346):383–393
- Hernández-Pajares M, Juan JM, Sanz J, and Orus R (2007), Second-order ionospheric term in GPS: implementation and impact on geodetic estimates. *J Geophys Res* 112(B08417):2007. doi:10.1029/1178-2006JB004707
- Niell, A.E. (1996) Global mapping functions for the atmosphere delay at radio wavelengths. *J Geophys Res* 101:3227–3246
- Petrie EJ, King MA, Moore P, and Lavallée DA (2010), A first look at the effects of ionospheric signal bending on a globally processed GPS network. *GPS Solut* 14:491–499. doi:10.1007/s00190-010-0386-2
- Williams, S.D.P. (2008), Cats: GPS coordinate time series analysis software. *GPS Solut* 12(2):147–153. doi:10.1007/s10291-007-0086-4
- Williams, S.D.P., Bock Y., Fang P., Jamason P., Nikolaidis R.M., Prawirodirdjo L., Miller M., and Johnson, D.J. (2004), Error analysis of continuous GPS position time series. *J Geophys Res* 109 (B03412). doi:10.1029/2003JB002741

B GPS data processing using GIPSY/OASIS-II software

The time series of GPS stations on the NGL website (<http://geodesy.unr.edu/>), were processed using GIPSY/OASIS-II software (Webb & Zumberge 1997) and made available by Jet Propulsion Laboratory (JPL). The precise point positioning (PPP) technique (Zumberge et al. 1997) was applied to the ionosphere-free carrier phase and pseudo-range data. The daily GPS coordinate time series are produced using GPS satellite orbit, GPS satellite clock and satellite antenna calibration models. The elevation cut-off angle was set at seven degrees. Troposphere effects were modeled using the Global Mapping Function (GMF) proposed by Boehm et al. (2006) and horizontal gradients were estimated using a random walk stochastic process at every five minutes

(Bar-Sever et al. 1998). The first order of ionosphere effect was removed with the ionosphere-free carrier phase and pseudo-range data combination. As the higher order ionosphere effect has very low amplitude, less than 1mm, it was not considered in the process (Hernández-Pajares et al. 2007). Non-tidal atmospheric loading model was not applied and only the effects of ocean loading were corrected by using the FES2004 tidal model (Lyard et al., 2006) which was provided by <http://holt.oso.chalmers.se/loading> (Scherneck 1991). The ocean loading effect was modeled in the CM frame (Blewitt 2003; Fu et al. 2012). In addition, the integer ambiguities for every station were solved using the wide lane and phase bias (WLPB) approach (Bertiger et al. 2010). The resulted coordinates were obtained in the frame of JPL's fiducial-free orbit so that they were transformed into reference frame IGS08 employing a seven-parameter transformation computed with JPL's orbit products (Blewitt 2014).

A similar time series analysis was performed for the time series obtained from this solution to estimate the velocities, velocity uncertainties and spectral index associated with the power-law noise.

B.1 References

- Bar-Sever, Y.E., Kroger, P.M., and Borjesson, J.A. (1998), Estimating horizontal gradients of tropospheric path delay with a single GPS receiver. *J Geophys Res* 103(B3):5019–5035
- Bertiger, W., Desai, S.D., Haines, B., Harvey, N., Moore, A.W., Owen, S., Weiss, J.P. (2010), Single receiver phase ambiguity resolution with GPS data. *J Geodesy* 84:327–337. doi:10.1007/s00190-010-0371-9
- Blewitt, G. (2003), Self-consistency in reference frames, geo-center definition, and surface loading of the solid Earth. *J Geophys Res* 108(B2). doi:10.1029/2002JB002082
- Blewitt, G. (2014), Nevada Geodetic Laboratory (NGL), Position time series. Nevada Geodetic Laboratory, Reno, NV <http://geodesy.unr.edu/index.php>. Accessed 1 July 2014

- Boehm, J., Niell, A.E., Tregoning, P., and Schuh, H. (2006), The global mapping function (GMF): a new empirical mapping function based on data from numerical weather model data. *J Geophys Res.* 10.1029/2005GL025546
- Fu, Y., Freymueller, J.T., and Jensen, T. (2012), Seasonal hydrological loading in southern Alaska observed by GPS and GRACE. *Geophys Res Lett* 39(L15310). doi:10.1029/2012GL052453
- Hernández-Pajares M, Juan JM, Sanz J, and Orus R (2007), Second-order ionospheric term in GPS: implementation and impact on geode-1177 tic estimates. *J Geophys Res* 112(B08417):2007. doi:10.1029/1178 2006JB0047071179
- Lyard F, Lefèvre F, Letellier T, and Francis O (2006), Modelling the global ocean tides: a modern insight from FES2004. *J Ocean Dyn* 56: 394-415
- Scherneck H.G. (1991), A parameterized solid Earth tide model and ocean tide loading effects for global geodetic baseline measurements. *J Geophys* 106:677–694
- Webb, F.H., and Zumberge, J.F. (1997), An introduction to GIPSY/OASIS II. JPL Publication D-11088
- Zumberge, J.F., Heflin, M.B., Jefferson, D.C., Watkins, M.M., and Webb, F.H. (1997), Precise point positioning for the efficient and robust analysis of GPS data from large networks. *J Geophys Res* 102:5005–5017

C Glossary

| | |
|--------|---|
| NL | Narrow-Lane |
| ZTD | Zenith Tropospheric Delay |
| GPS | Global Positioning System |
| DInSAR | Differential Interferometric Synthetic Aperture Radar |
| GIA | Glacial Isostatic Adjustment |
| PPP | Precise Point Positioning |
| NRCan | Natural Resource Canada |
| SBAS | Spaced Based Augmentation System |
| GFIF | Geometry-Free and Ionosphere-Free |
| PRN | Pseudo-Random Noise |
| SNR | Signal-to-Noise Ratio |
| MWWL | Melbourne-Wübbena Wide-Lane |
| NGS | National Geodetic Survey |
| IGS | International GPS Service |
| CODE | Center for Orbit Determination in Europe |
| TEC | Total Electron Contents |
| PWV | Precipitable Water Vapor |
| ZHD | Zenith Hydrostatic Delay |
| ZWD | Zenith Wet Delay |
| NMF | Niell Mapping Function |
| cGPS | continuous GPS |

| | |
|-------------|---|
| QIF | Quasi Ionosphere Free |
| UMV | Upper Mantle Viscosity |
| RMSE | Root-Mean-Square Error |
| PPMC | Pearson Product Moment Correlation |
| IGS | International GNSS Service |
| OSO | Onsala Space Observatory |
| NGS | National Geodetic Survey |
| TPS | Topcon Positioning System |
| AOA | Allen Osborne Associates |
| CORS | Continuously Operating Reference Stations |
| SCIGN | Southern California Integrated GPS Network |
| ASAR | Advanced Synthetic Aperture Radar |
| MERIS | MEDium Resolution Imaging Spectrometer |
| MODIS | Moderate Resolution Imaging Spectroradiometer |
| ERA-Interim | European Center for Medium-Range Weather Forecasts Reanalysis |
| APD | Atmospheric Path Delay |
| GPT | Global Pressure and Temperature Model |
| LMV | Lower Mantle Viscosity |
| NGL | Nevada Geodetic Laboratory |
| ITRF | International Terrestrial Reference Frame |
| NWP | Numerical Weather Prediction |
| DoY | Day Of Year |
| AFB | Air Force Base |

| | |
|-----------|--|
| MEO | Medium Earth Orbit |
| LOS | Line-of-Sight |
| VMF | Vienna Mapping Function |
| VMF1 | Vienna Mapping Function 1 |
| GNSS | Global Navigation Satellite System |
| GMF | Global Mapping Function |
| CGS | Canadian Geodetic Survey |
| WRF | Weather Research and Forecasting |
| NOAM | North American |
| PBL | Planetary Boundary Layer |
| PENNDOT | Pennsylvania Department of Transportation |
| NYSDOT | New York State Department of Transportation |
| ODOT | Ohio Department of Transportation |
| PLI | Precision Laser and Instrument |
| CONNDOT | Connecticut Department of Transportation |
| MDOT | Michigan Department of Transportation |
| NRCan GSD | Natural Resources Canada, Geodetic Survey Division |
| msl | Mean Sea Level |
| SOSZ | Southern Ontario Seismic Zone |
| WQSZ | Western Québec Seismic Zone |
| CSZ | Charlevoix Seismic Zone |
| LSZ | Lower St. Lawrence Zone |
| BUZ | Boothia Ungava Zone |

| | |
|---------------------------|---|
| VM | Viscosity Model |
| GDEM | Global Digital Elevation Model |
| USGS | United States Geological Survey |
| HVO | Hawaii Volcano Observatory |
| MET-ZTD | ZTD computed from meteorological data |
| GPS-ZTD | ZTD computed from GPS processing |
| ZTD_{PPP} | zenith tropospheric delay estimated from precise point positioning technique |
| ΔZTD_{PPP} | Subtraction of ZTD_{PPP} computed for the reference station from the ZTD_{PPP} for the other stations |
| POLARIS | Portable Observatories for Lithospheric Analysis and Research Investigating Seismicity |
| CSRS | Canadian Spatial Reference System |
| ERA40 | European Centre for Medium-Range Weather Forecasts 40-year re-analysis |
| P-code | Precise code |
| NOAA-ESRL | National Oceanic Atmospheric-Earth System Research Laboratory |
| K_1 , K_2 , and K_3 | refractivity constants |
| BSW5.0 | Bernese GPS Software Version 5.0 |
| MSBAS | Multidimensional Small Baseline Subset |
| N | refractivity |
| SRTM | Shuttle Radar Topography Mission |
| C/A | Coarse Acquisition |

D Computer Code

Codes that I have written in chapters 2.

%Compute the plate velocities

```

    %% Calculate Plate velocities
    velocitiesngl= 'coordinates.xls';
    [velocities,txt,row] = xlsread(velocitiesngl,1);
    lon= velocities(:,1);
    lat = velocities(:,2);
    alt=velocities(:,3);
    r = 6378137;%Radius of the Earth
    %% ITRF2008 (N-PGR) components
    wx= 0.035;
    wy= -0.662;
    wz= -0.1;
    w_plate=sqrt(wx^2+wy^2+wz^2);%rad/yr Pole Rotation Rate
    w_degoverma=(0.184+0.003)*(pi/180)*10^-6;%rad/yr

%upper band
lat_plate=-7.9+0.8;
lon_plate=-88+0.7;

eulervector=[w_degoverma*cosd(lat_plate)
             w_degoverma*cosd(lat_plate)*sind(lon_plate)
             w_degoverma*sind(lat_plate)];

VNS_up=r*w_degoverma*cosd(lat_plate)*sind(lon- lon_plate)
for i=1:size(lon)
VEW_up(i,1)=r*w_degoverma*(((cosd(lat(i)))*sind(lat_plate))-
((sind(lat(i)))*(cosd(lat_plate))*(cosd(lon(i)-lon_plate))))
end
%lower band
w_degoverma=(0.184-0.003)*(pi/180)*10^-6;%rad/yr

lat_plate=-7.9-0.8; %rad
lon_plate=-88-0.7; %rad

eulervector=[w_degoverma*cosd(lat_plate)
             w_degoverma*cosd(lat_plate)*sind(lon_plate)
             w_degoverma*sind(lat_plate)];

VNS_low=r*w_degoverma*cos(lat_plate)*sin(lon- lon_plate)
for i=1:size(lon)
VEW_low(i,1)=r*w_degoverma*(((cosd(lat(i)))*sind(lat_plate))-
((sind(lat(i)))*(cosd(lat_plate))*(cosd(lon(i)-lon_plate))))
End

%med
w_degoverma=(0.184)*(pi/180)*10^-6;%rad/yr

lat_plate=-7.9; %degree

```

```

lon_plate=-88; %degree

eulervector=[w_degoverma*cosd(lat_plate)
             w_degoverma*cosd(lat_plate)*sind(lon_plate)
             w_degoverma*sind(lat_plate)];

VNS_med=r*w_degoverma*cosd(lat_plate)*sind(lon- lon_plate)
for i=1:size(lon)
VEW_med(i,1)=r*w_degoverma*((cosd(lat(i)))*sind(lat_plate))-
((sind(lat(i)))*(cosd(lat_plate))*(cosd(lon(i)-lon_plate)))
end

% converting utm to geodetic coordinates

stationsble= 'stations.xlsx';
a= 6378137.0;
e2=298.257222101;
[stations,txt,raw] = xlsread(stationsble);
[lat,lon]=utm2ell(stations(:,2),stations(:,1),17,a,e2,1cm);
lat2=lat*180/pi;
lon2=lon*180/pi;

% analyzing the GPS coordinates

%% load the position changes time series produced by Bernese
%% load the position changes time series from NGL
load Algofiltered.mat
load Algonevada.mat
load Actofiltered.mat
load Actonevada.mat
load Stcofiltered.mat
load Stconevasda.mat
load Tynofiltered.mat
load Tynonevada.mat
load Klbofiltered.mat
load Matqfiltered.mat
load Matqnevada.mat
load Inuqfiltered.mat
load Inuqnevada.mat
load Ivkqfiltered.mat
load Ivkqnevada.mat
load Paryfiltered.mat
load Parynevada.mat

%% the following steps are employed for all stations and components
x = Actonevada(:,1);
y2= Actofiltered(:,5);
y1= Actonevada(:,2);
e= Actofiltered(:,8);

date=Actofiltered(:,1:3);
y=[y1 y2];
% estimate the linear velocities of time series
p2= polyfit(date(:,1),y1,1);

```

```

veleast_nevada=p2(1)*100
p= polyfit(date(:,1),y2,1);
veleast_bernese=p(1)*100

%# normalize: (y-min)/(max-min) ==> [0,1]
yy = bsxfun(@times, bsxfun(@minus,y,min(y)), 1./range(y));
subplot(222), plot(x,yy(:,1), x,yy(:,2))
title('minmax')

%# standarize: (y - mean) / std ==> N(0,1)
yy = zscore(y);
[Z,mu,sigmaacx] = zscore(y);

%%% removing the outliers using hampel function

DX = 3*median(x(2:end)-x(1:end-1));
T=3;
Threshold = 0;
[YY, I, Y0, ~, UB, ADX, NO] = hampel(x,yy(:,2), DX, T,
'adaptive',Threshold)

% convert dates to mjd to input the times series to Hector software

vel_date= 'hector-input-data.xlsx';
[status,sheets]=xlsfinfo(vel_date);
for i=1:57
[table,txt,row] = xlsread(vel_date,i, 'A:C');
for j=1:length (table(:,1))
yearmjd(j,i)= floor(365.25*(table(j,1) - 1970) + 40587 + 0.1) -0.5;
yearmjd_round(j,i)= round(yearmjd(j,i));
end
end

*****

Codes that I have written in chapters 3.

I have done the following steps for all weather stations to estimate the ZTD from
meteorological data at the GPS stations' locations

%%input the meteorological data from excel to matlab
Weathermeasurment= 'hourly-weather_measurements_inuq.xlsx';
[inuq,txt,row] = xlsread(Weathermeasurment);
dyinuq = decyear(inuq(:,1),inuq(:,2),inuq(:,3),inuq(:,4),0,0);

%% correct the GPS meteorological data for the height difference

H_GPS= 16.532; % GPS height above msl
H_MET=25.750; % weather station height

```

```

TMSL=(inuq(:,6)+273.16)+(0.0065*H_MET);
TGPS_inuq=(TMSL)-(0.0065*H_GPS); %According to Equation 2 in dousa
elias

partial_watervapor=6.1037*(exp(17.641*inuq(:,7)./(243.27+inuq(:,7))));

Pmsl=inuq(:,10)/(1-(0.0000226*H_MET))^5.225;
PGPS_inuq=Pmsl*(1-(0.0000226*H_GPS))^5.225; %According to Equation 2 in
dousa elias

emsl=partial_watervapor/(((1-(0.0000226*H_MET))^5.225)^(2.79+1));
%According to Equation 2 in dousa elias and smith 1966, for the decay
rate of partial water vapor pressure.
annaullanda=2.79;
EGPS_inuq=emsl*(((1-(0.0000226*H_GPS))^5.225)^(annaullanda+1));

```

%% calculate refractivity time series

```

for i=1:size(dyinuq,1)
    refractinuq(i,1)=77.69*(PGPS_inuq(i,1)-
EGPS_inuq(i,1))/(TGPS_inuq(i,1))+71.29*(EGPS_inuq(i,1))/(TGPS_inuq(i,1)
)+375463*(EGPS_inuq(i,1))/((TGPS_inuq(i,1))^2);
end

```

%% plot the refractivity

```

figure;
scatter(dyinuq,refractinuq,6,'MarkerEdgeColor',[0.04,0.52,0.78])
avgrefrinuq=nanmean(refractinuq)

hold on
plot(dyinuq,ones(size(dyinuq,1),1)*avgrefrinuq,'--r')
xlabel('Year')
ylabel('Refractivity (N-Unit)')
str1 = 'Inukjuak to INUQ = 4km';
text(2008.3,370,str1)
ylim([250 400])
title('INUQ')

```

%%%% calculate MET-ZTD

```

C=0.000121;%1/km

syms z
f=exp(-C*z)
inuq_met=(10^-6)*refractacto*double(int(f, H_GPS,Inf));
[ztdmet_inuq,dyinuqdai] = dailyavgmet(inuq,inuq_met);

```

%%%%% calculate PWV at each station

```
[PGPS_dai,dyinuqdai2] = dailyavgmet(inuq,PGPS_inuq);

F=(1-0.00266*cos(2*58.451)-0.00028*(16.532/1000))
ZHD=0.002277*PGPS_dai/F %%meter

ZWD_inuq=ztdmet_inuq-ZHD; % compute wet component of ZTD

% convert hourly temperature to daily

[Tsmet_inuq,dyinuqdai3] = dailyavgmet(inuq,TGPS_inuq);

Tm=50.4+0.789*(Tsmet_inuq);

inuq_factor=10^6*(461*((-287/461)*77.60+71.59+375000./Tm)).^-1;
PW_met_inuq=inuq_factor.*ZWD_inuq/10;

avgpw=nanmean(PW_met_inuq);
figure;
plot(dyinuqdai2,PW_met_inuq*100) %cm
ylim([0 10])
hold on

%% plot the computed amplitudes at each station overlain with the
modeled amplitudes

zr=367.22; %elevation of station ACTO, reference station
C=0.000121;
z=[0:1000];
amplitudrefract=18.93;
amplitude2=abs((10^-6)*(amplitudrefract)*(1-exp((-C)*(z-
zr)))/((C)*exp((C)*zr))) %meter
figure;
plot(z,amplitude2*100)
ylabel('Amplitude (cm)')
xlabel('Height (m)')

elev= [205.102 94.169 367.217 185.574 237.184 279.705 16.532 12.234];

GPSamp3=[0.15 0.22 0 0.3 0.19 0.63 1.9 1.95]; %%GPS % the seasonal
amplitudes of deltaZTD at each station relative to station ACTO.

plot(elev,GPSamp3,'*r')
hold on
legend('Model','GPS')

text(elev(2),GPSamp3(2),'STCO',...
'horiz','center','vert','bottom')
hold on

text(elev(1),GPSamp3(1),'TYNO',...
'horiz','center','vert','bottom')
```

```

hold
text(elev(3),GPSamp3(3),'ACTO',...
     'horiz','left','vert','bottom')
hold on

text(elev(4),GPSamp3(4),'KLBO',...
     'horiz','center','vert','bottom')
hold on
text(elev(4),GPSamp3(5),'ALGO',...
     'horiz','center','vert','TOP')
hold on
text(elev(6),GPSamp3(6),'MATQ',...
     'horiz','center','vert','bottom')
hold on
text(elev(7),GPSamp3(7),'INUQ',...
     'horiz','right','vert','bottom')
hold on

text(elev(8),GPSamp3(8),'IVKQ',...
     'horiz','center','vert','bottom')
% ylim([0 15])

%%
%%
% meanrefract=[nanmean(refractinuq) nanmean(refractivkq)
nanmean(refractstco) nanmean(refracttyno) nanmean(refractpary) ...
% nanmean(refractalgo) nanmean(refractmatq) nanmean(refractacto)];

%% plot the exponential decay fits

% amplitudfinalresults='amplitudfinalresults2.xlsx';
% [results,txt,row] = xlsread(amplitudfinalresults,6);
% heights= results(:,1);
%%%%%%%%%%%%%%%%%%%%%%%%%%%%%%%%%%%%%%%%%%%%%%%%%%%%%%%%%%%%%%%%%%%%%%%%
heights=[16.532;12.234;94.169;205.102;185.574;237.184;279.705;367.217];
figure;
plot(heights(1:end),meanrefract(1:end),'*')
% hold on
hold on
exponfit1 = fit(heights(1:end),meanrefract(1:end),'exp1')
plot(exponfit1,'m')%scenario 1

p21 = predint(exponfit1,heights,0.95,'functional','off');
hold on, plot(heights,p21,'m--')

hold on

exponfit2 = fit(heights(3:end),meanrefract(3:end),'exp1')
plot(exponfit2,'k') %scenario 2

p21 = predint(exponfit2,heights,0.95,'functional','off');
hold on, plot(heights,p21,'k--')

```



```

heights3=[16.532;12.234;94.169;205.102;185.574;237.184;367.217];
% meanrefract3=[nanmean(refractinuq) nanmean(refractivkq)
nanmean(refractstco) nanmean(refracttyno) nanmean(refractpary) ...
% nanmean(refractalgo) nanmean(refractacto)];

exponfit3 = fit(heights3(3:end),meanrefract3(3:end)','exp1')
hold on
plot(exponfit3,'g') %scenario 3

p21 = predint(exponfit3,heights,0.95,'functional','off');
hold on, plot(heights,p21,'g--')

heights4=[-23.771;-20.355;200.897;239.945];
meanrefract4=[319.83 316.80 318.74 312.83];

hold on
exponfit4 = fit(heights4,meanrefract4','exp1')
plot(exponfit4,'b') %scenario 4
p21 = predint(exponfit4,heights,0.95,'functional','on');
hold on, plot(heights,p21,'b--')

grid on
%%
xlabel('Height (m)')
ylabel('Refractivity (N-Unit)')
legend('GPS stations','scenario 1',' ','scenario 2',' ','scenario
3',' ','scenario 4')

text(heights(2),meanrefract(2) ','IVKQ',...
'horiz','center','vert','bottom')
hold on

text(heights(1),meanrefract(1) ','INUQ',...
'horiz','center','vert','bottom')
hold
text(heights(3),meanrefract(3) ','STCO',...
'horiz','left','vert','bottom')
hold on
text(heights(4),meanrefract(5) ','KLBO',...
'horiz','center','vert','TOP')
hold on

text(heights(4),meanrefract(4) ','TYNO',...
'horiz','center','vert','bottom')
hold on

text(heights(8),meanrefract(8) ','ACTO',...
'horiz','center','vert','bottom')
hold on

text(heights(6),meanrefract(6) ','ALGO',...
'horiz','center','vert','bottom')

```

```

        hold on

text(heights(7),meanrefract(7) , 'MATQ',...
      'horiz','right','vert','bottom')
ylim([290 350])

% loading the ZTD computed by PPP to MATLAB

% computing GPS-PWV

% The following steps have been carried out for all GPS stations

%ACTO
load('ACTO')
dybernhourly=deyear(ACTO(:,2),ACTO(:,3),ACTO(:,4),ACTO(:,5),ACTO(:,6),
ACTO(:,7));
    figure;
    hold on
plot(dybernhourly(:,1), ACTO(:,8),'.')
[ztdbern_acto,dyactobern] = dailyavgberb(ACTO); % convert 30s to
%daily
hold on
plot(dyactobern, ztdbern_acto,'.')

%%%%%%%% calculate PWV
[PGPS_dai,dyactodai2] = dailyavgmet(acto,PGPS_acto);

F=(1-0.00266*cos(2*43.609)-0.00028*(367.22/1000))
ZHD_acto=0.002277*PGPS_dai/F %%meter

% calculate ZWD at each station
ZWD_acto=ztdbern_acto-ZHD_acto;

[Tsmet_acto,dyactodai3] = dailyavgmet(acto,TGPS_acto);

Tm=50.4+0.789*(Tsmet_acto);

acto_factor=10^6*(461*((-287/461)*77.60+71.59+375000./Tm)).^-1;
PW_bern_acto=acto_factor.*ZWD_acto/10;

avgpw=nanmean(PW_bern_acto);
% figure;
hold on
plot(dyactodai3,PW_bern_acto*100)
ylabel('PW values (cm)')
xlabel('Year')
title('ACTO')

%% compute correlation between each pair of ZTDs

```

```

cor=[ztdbern_tyno ztdmet_tyno ztdbern_stco ztdmet_stco ztdbern_acto
ztdmet_acto ztdbern_klbo ztdmet_klbo ztdbern_algo ztdmet_algo
ztdbern_matq ztdmet_matq ztdbern_inuq ztdmet_inuq ztdbern_ivkq
ztdmet_ivkq]

[R,PValue] =corrplot(cor
,'varNames',{'TB','TM','SB','SM','AB','AM','KB','KM','AB','AM','MB','MM
','InB','InM','IvB','IvM'}, 'type','Pearson','testR','on',
'rows','pairwise')
    hfig = gcf;
    haxes = findobj(hfig, 'Type', 'Axes');
    arrayfun(@(ax) xlim(ax, [2:3]), haxes); %to change all the axes limit
    arrayfun(@(ax) ylim(ax, [2:3]), haxes); %to change all the axes limit
n=size(R,1)
set(gca, 'XTick', 1:n); % center x-axis ticks on bins
set(gca, 'YTick', 1:n); % center y-axis ticks on bins

%%%%%%%%
%% Correlogram

    figure;
    imagesc(triu(R))
    colormap('jet')
    colorbar;
    labelNames = {'TYNO-G'; 'TYNO-M'; 'STCO-G'; 'STCO-M'; 'ACTO-G'; 'ACTO-
G'; 'KLBO-G'; 'KLBO-M'; 'ALGO-G'; 'ALGO-M'; 'MATQ-G'; 'MATQ-M'; 'INUQ-
G'; 'INUQ-M'; 'IVKQ-G'; 'IVKQ-M'};
n=size(R,1)
set(gca, 'color', 'm')
set(gca, 'XTick', 1:n, 'XAxisLocation', 'top'); % center x-axis ticks on
bins
set(gca, 'YTick', 1:n); % center y-axis ticks on bins
set(gca, 'XTickLabel', labelNames); % gca gets the current axis
set(gca, 'YTickLabel', labelNames); % gca gets the current axis
xticklabel_rotate([1:n], 45, {'TYNO-G'; 'TYNO-M'; 'STCO-G'; 'STCO-M'; 'ACTO-
G'; 'ACTO-M'; 'KLBO-G'; 'KLBO-M'; 'ALGO-G'; 'ALGO-M'; 'MATQ-G'; 'MATQ-
M'; 'INUQ-G'; 'INUQ-M'; 'IVKQ-G'; 'IVKQ-M'}, 'interpreter', 'none')
%%
%% Plot the weather parameters

elev=[-23.77 -20.35 57.32 168.30 177.00 200.90 239.94 367.22]';

meantTemp=[nanmean(TGPS_inuq) nanmean(TGPS_ivkq) nanmean(TGPS_stco)
nanmean(TGPS_tyno) nanmean(TGPS_pary) nanmean(TGPS_algo)
nanmean(TGPS_matq) nanmean(TGPS_acto)]';
meantEpress=[nanmean(EGPS_inuq) nanmean(EGPS_ivkq) nanmean(EGPS_stco)
nanmean(EGPS_tyno) nanmean(EGPS_pary) nanmean(EGPS_algo)
nanmean(EGPS_matq) nanmean(EGPS_acto)]';
meanDewtemp=[nanmean(inuq(:,7)) nanmean(ivkq(:,7)) nanmean(stco(:,7))
nanmean(tyno(:,7)) nanmean(pary(:,7)) nanmean(algo(:,7))
nanmean(matq(:,7)) nanmean(acto(:,7))];

figure;
plot(elev,meantTemp, '-b') %air temperature

```

```

    hold on
    [AX,H1,H2]=plotyy(elev,meanDewtemp,elev,meantEpress,'plot')
    set(get(AX(1),'Ylabel'),'String','Dew point temperature (°C)')
    set(get(AX(2),'Ylabel'),'String','Partial water vapor pressure (mbar)')
    set(H1,'LineStyle','--')
    set(H2,'LineStyle','-')
    xlabel('Height (m)')
    ylim([-15 10])

    hold on
    text(elev(2),meanDewtemp(2),'IVKQ',...
        'horiz','center','vert','bottom')
    hold on

    text(elev(1),meanDewtemp(1),'INUQ',...
        'horiz','center','vert','bottom')
    hold
    text(elev(3),meanDewtemp(3),'STCO',...
        'horiz','left','vert','bottom')
    hold on

    text(elev(4),meanDewtemp(4),'TYNO',...
        'horiz','center','vert','bottom')
    hold on
    text(elev(4),meanDewtemp(5),'KLBO',...
        'horiz','center','vert','TOP')
    hold on
    text(elev(6),meanDewtemp(6),'ALGO',...
        'horiz','center','vert','bottom')
    hold on
    text(elev(7),meanDewtemp(7),'MATQ',...
        'horiz','right','vert','bottom')
    hold on

    text(elev(8),meanDewtemp(8),'ACTO',...
        'horiz','center','vert','bottom')
    % ylim([0 15])
    legend('GPS stations','mean dew point temperature','mean air
    temperature','partial water vapor pressure')
    %% Compute the PWV from the formula given by Smith (1966)

    a=-1.33;
    b=0.04;
    Td=[4.34    %dew point temperature
    4.83
    3.73
    2.77
    0.35
    -2.92
    -6.72
    -9.56]
    Td_F = Td * 1.8 + 32;
    PWV_ashlewf =exp(b*Td_F +a)
    %%%
    landa=[2.78

```

```

2.78
2.78
2.78
2.78
2.78
2.79
2.41];
Td_F = Td * 1.8 + 32;
PWV_smith =exp(0.0393*Td_F +(0.1133-log(landa+1)))

```

% The function I have written to convert hourly data to daily

```

% function [ tableavgdaytzdmeteo,tabledeciyeameteo] = dailyavgmet(
tablemet,APD)
metk=1;
d=1;
for y=2008:2012

    [metidx,c]= find(tablemet(:,1)==y);
    for m=1:12
        [metidx2,c2]= find(tablemet(metidx,2)==m);
        metindx= metidx(metidx2);

        for d=1:31
            [metidx2,c]= find(tablemet(metindx,3)==d);
            metavg(d,m)= mean(APD(metindx(metidx2),1));
            dymetdaily2(d,m)=decyear(y,m,d);%decimal year
            daymet(d,m)=d;
            yearmet(d,m)=y;
        end
    end
    metavgday(:,metk)=metavg(:);
    dymeteo(:,metk)=dymetdaily2(:);
    daymeteo2(:,metk)=daymet(:);
    yearmeteo2(:,metk)=yearmet(:);
    metk=metk+1;
end
tableavgdaytzdmeteo=metavgday(:);%daily Tropospheric Zenith delay
computed through meteo data
tabledeciyeameteo=dymeteo(:);%decimal year
tabledaymeteo=daymeteo2(:);%day
tableyearmeteo=yearmeteo2(:);%year
end

```

Codes that I have written in chapters 4.

```

load('timeseries1')
numberyear=[10:2:136];
% for i=1:size(numberyear,2)
yearfrac=timeseries1(1,numberyear);

for f=577899
    f
    d(f,1:64)= timeseries1(f+1,numberyear);

    [fit, gof] = createFitacto(yearfrac, d(f,1:64));

```

```

    r2(f)=gof.rsquare;
% sse(f)=gof.sse;% adjrsquare(f)=gof.adjrsquare;
rmse(f)=gof.rmse;
Amplitude(f)=sqrt((fit.a1)^2+((fit.b1)^2));
Phase(f)=(atan2(fit.b1,fit.a1))*180/pi;
t(f)= (sqrt(r2(f)).*sqrt(64-2))./(sqrt(1-r2(f)));
v=64;
tdist2T = @(t,v) (1-betainc(v/(v+t^2),v/2,0.5));
% tdist1T = @(t,v) 1-(1-tdist2T(t,v))/2;
p_value(f)=1-tdist2T(t(f),v);
end

%% import DInSAR vertical time series to matlab

filename = 'MSBAS_TIME_SERIES_2.txt';
delimiterIn = ' ';
headerlinesIn = 1;
A = importdata(filename,delimiterIn,headerlinesIn);
timeseries2=A.data;
long = -155.3713309 + timeseries2(:,1)*0.000278;
lat = 19.526898 -timeseries2(:,2)*0.000278 ;
%%
load('timeseries2')
numberyear=[8:2:640];
% for i=1:size(numberyear,2)
    yearfrac=str2double(A.textdata(1,numberyear));

    for f=174456:315292
        f
        d(f,1:317)= timeseries2(f,numberyear);

        [fit, gof] = createFitacto(yearfrac, detrend(d(f,1:317))); %compute
% the seasonal amplitudes
        r2(f)=gof.rsquare;
% sse(f)=gof.sse;
% adjrsquare(f)=gof.adjrsquare;
rmse(f)=gof.rmse;
Amplitude(f)=sqrt((fit.a1)^2+((fit.b1)^2));
Phase(f)=(atan2(fit.b1,fit.a1))*180/pi;
t(f)= (sqrt(r2(f)).*sqrt(317-2))./(sqrt(1-r2(f)));
        f
v=317;
tdist2T = @(t,v) (1-betainc(v/(v+t^2),v/2,0.5));
% tdist1T = @(t,v) 1-(1-tdist2T(t,v))/2;
p_value(f)=1-tdist2T(t(f),v);
    end
%% plot amplitude of timeseries2 as function of height

serdata= 'timeseries2_height.xls';
timeseries2_height= [xlsread(serdata,1)
    xlsread(serdata,2)
    xlsread(serdata,3)
    xlsread(serdata,4)
    xlsread(serdata,5)
    xlsread(serdata,6)
    xlsread(serdata,7)

```

```

        xlsread(serdata,8)
        xlsread(serdata,9)];

figure;
plot(timeseries2_height(:,13),timeseries2_height(:,8),'.r')
hold on
plot(timeseries2_height(1:33169,13),Amplitude(:,1:33169),'.b')
data= [timeseries2(1:33169, 1:2), long(1:33169), lat(1:33169),
timeseries2(1:33169, 5:6), Amplitude(1:33169)', Phase(1:33169)',
r2(1:33169)',rmse(1:33169)', p_value(1:33169)'];
filename = 'myfile.xls';
xlswrite(filename,data)

%%%%%%

%%
filename = 'MSBAS_TIME_SERIES3.txt';
delimiterIn = ' ';
headerlinesIn = 1;
A = importdata(filename,delimiterIn,headerlinesIn);
timeseries3=A.data;
long=-155.5343939+0.000278*timeseries3(:,1);
lat=19.5563432-0.000278*timeseries3(:,2);
%%
load('timeseries3')
numberyear=[8:2:134];
% for i=1:size(numberyear,2)
    yearfrac=str2double(A.textdata(1,numberyear));

    example=[40552 278197 506153 543460 649037 706133 783133 860224
1105620];
    for i=4
        f=example(i)
        % for f= 12222
            f
            d(f,1:64)= timeseries3(f,numberyear);
        % figure;
        % subplot(2,1,1)
            [fit, gof] = createFitacto(yearfrac, detrend(d(f,1:64)));
            hold on
            plot(yearfrac, d(f,1:64)-mean(d(f,1:64)))
            text(2014.5,0.5,'height:',...
                'horiz','center','vert','bottom')
            hold on
            text(2017,0.5,'Amplitude:',...
                'horiz','right','vert','bottom')
            hold on
            text(2015.5,0.5,'d',...
                'horiz','right','vert','bottom')

        % legend({'Actual timeseries' 'seasonal fluctuation'})

ylabel('vertical displacement (cm)')
xlabel('year')

```

```

end

    r2(f)=gof.rsquare;
% sse(f)=gof.sse;
% adjrsquare(f)=gof.adjrsquare;
rmse(f)=gof.rmse;
Amplitude(f)=sqrt((fit.a1)^2+((fit.b1)^2));
Phase(f)=(atan2(fit.b1,fit.a1))*180/pi;
t(f)= (sqrt(r2(f)).*sqrt(64-2))./(sqrt(1-r2(f)));
v=64;
tdist2T = @(t,v) (1-betainc(v/(v+t^2),v/2,0.5));
% tdist1T = @(t,v) 1-(1-tdist2T(t,v))/2;
p_value(f)=1-tdist2T(t(f),v);
end

%% import the amplitudes and their heights from detrended time series
from ascii to matlab
    filename = 'timeseries3_height_allpoints_detrended';
% filename = 'timeseries3_goodpoint_heightpablo';

delimiterIn = ' ';
headerlinesIn = 1;
A2 = importdata(filename,delimiterIn,headerlinesIn);
timeseries3_height=A2.data;

figure;
plot(timeseries3_height(:,15),timeseries3_height(:,10),'.b')

%calculate refractivity time series and its amplitude
MLO = 'MLO_weather_station.xlsx';
table = xlsread(MLO,1);

dymldata = decyear(table(:,1),table(:,2),table(:,3),table(:,4),0,0);

figure;
plot(dymldata,table(:,18),'.')
%%

[correctrefract,idx,outliers] = deleteoutliers(table(:,18),0.05,1);
[correctrepress,idx,outliers] = deleteoutliers(table(:,8),0.05,1);

[indexind,c2] = find(~isnan(correctrefract(:,1)));
refractfilt=correctrefract(indexind,1);

[indexind2,c2] = find(~isnan(correctrepress(:,1)));
pressfilt=correctrepress(indexind2,1);

figure;
plot(dymldata(indexind),refractfilt,'-b')

figure;
plot(dymldata(indexind2),pressfilt,'-b')

```



```

ye=table(indexind,1);
mon=table(indexind,2);
da=table(indexind,3);
%%

metk=1;
d=1;
for y=2014:2018

    [metidx,c]= find(ye==y);
    for m=1:12
        [metidx2,c2]= find(mon(metidx,1)==m);
        metindx= metidx(metidx2);
        for d=1:31
            [metidx2,c]= find(da(metindx,1)==d);
            refavg(d,m)= mean(refractfilt(metindx(metidx2),1));
            dymon(d,m)=decyear(y,m,d);
            day(d,m)=d;
            year(d,m)=y;
        end
    end
    refavgmon(:,metk)=refavg(:);

    dayavg2(:,metk)=dymon(:);

    metk=metk+1;
end
refracmonth=refavgmon(:);%monthly refractivity
dyfinal=dayavg2(:);
hold on
plot(dyfinal,refracmonth,'-r')
ylabel('refractivity (N-unit)')
xlabel('decimal year')

ampref=peak2peak(refracmonth)/2;
legend({'hourly data' 'daily data'})

%%

zr=3107; %PUKA
z=0:1:3500;%PUKA
C=0.0001406;
amplitudrefract=18.94; % Amplitude of sinsoidal fit to the refractivity
time series
ampAPD=abs((10^-6)*(amplitudrefract)*(1-exp((-C)*(z-
zr)))/(C)*exp((C)*zr)); %meter
hold on
plot(z,ampAPD*100,'r')

ylabel('Amplitude (cm)')
xlabel('Height (m)')

legend({'Observed amplitudes' 'model'})

```

```

%% compare the modeled seasonal ZTD time series to those obtained from
PPP

    d2=d(f,1:64)+3105;
figure;
plot(yearfrac,d(f,1:64))

zr=3107; %PGF1
z=d2;%PGF1
C=0.0001406;
% c=200;
% 348.6
amplitudrefract=18.94; % Amplitude of sinsoidal fit to the refractivity
time series
amplitude=abs((10^-6)*(amplitudrefract)*(1-exp((-C)*(z-
zr)))/((C)*exp((C)*zr))); %meter

phase=180;
for i=1:size(amplitude,2)
APD_computed(i)=(amplitude(i)*sin((2*pi*yearfrac(i))+phase));

end
    subplot(2,1,2)
hold on
plot(yearfrac,APD_computed) % (cm)

year=fix(yearfrac);
day=yearfrac-year;
ly = leapyear(year);
ly2 = double(ly);
for i=1:64
    if ly2(i)==1;
datestr(datum(year(1,i),1,1)+day(i)*366)
    end
    if ly2(i)==0;
datestr(datum(year(1,i),1,1)+day(1,i)*365)
    end
end

    str = sprintf(formatSpec,A1,A2,A3)
ly = leapyear(year)
% gpsdata = 'GPS_data.xlsx';

gpspositions = 'gps_stations_positions.xls';

for ii=1:21
    table = xlsread(gpsdata,ii);
    table2 = xlsread(gpspositions);

%% convert day of year and year into decimal year

x_table=decyear(table(:,2),table(:,3),table(:,4),table(:,5),table(:,6),
table(:,7));

```

```

metk=1;
d=1;
for y=2014:2017

    [metidx,c]= find(table(:,2)==y);
    for m=1:12
        [metidx2,c2]= find(table(metidx,3)==m);
        metindx= metidx(metidx2);

        for d=1:31
            [metidx2,c]= find(table(metindx,4)==d);
            tzdavg(d,m)= nanmean(table(metindx(metidx2),16));
            heightavg(d,m)= nanmean(table(metindx(metidx2),28));
            dytabledaily2(d,m)=decyear(y,m,d);%decimal year
            daytable(d,m)=d;
            yeartable(d,m)=y;
        end
    end
    tzdavgday(:,metk)=tzdavg(:);
    heightavgtable(:,metk)= heightavg(:);
    dytable(:,metk)=dytabledaily2(:);
    dayavg2(:,metk)=daytable(:);
    yearavg2(:,metk)=yeartable(:);
    metk=metk+1;
end
tableavgdaytz=tzdavgday(:);%daily Tropospheric Zenith delay
computed through meteo data
tableavgday=heightavgtable(:);
Ndecimals = 4;
f = 10.^Ndecimals;
tabledeci=dytable(:);%decimal year
tableday=dayavg2(:);%day
tableyear=yearavg2(:);%year
x2_ii = round(f*tabledeci)/f;
%%
[napu,rr]=find(~isnan(tableavgday));
tableavgdaytzd=tableavgdaytz(napu);
tableavgdayheight=tableavgday(napu);
tabledeciyea=tabledeci(napu);
x2=x2_ii(napu);

%% find intersect of the corrected ANIP with PUKA

[xinter,idain,idpuk]=intersect(x2,x_puka2)

%% calculate dhir corrected
dhanhi=tableavgdayheight(idain)-pukaavgdayheight(idpuk); % corrected dh
ppp (m)
[aindpukadiff,idx,outliers] = deleteoutliers(dhanhi,0.05,1)
aindpukadiff2=(aindpukadiff-nanmean(aindpukadiff))*1000;

% figure;
% plot(xinter,aindpukadiff2,'-r')%mm

[nanbo,cc]=find(~isnan(aindpukadiff2));%important id (final ids)

```

```

ylabel('mm')
title('dh corrected PPP AINP-PUKA')

%% convert zenith delay to slant delay

lattable = table2(ii,1)*(pi/180);%latitude of station in radians
H= table2(ii,3);%meter
longtable=table2(ii,2)*(pi/180);%longtitude of station in radians
yearmjd= floor(365.25*(xinter(nanbo) - 1970) + 40587 + 0.1) -0.5;
dmjd= round(yearmjd);
e=10*(pi/180)% zenith distance in radians
for i=1:size(dmjd,1)
[gmfh(i),gmfw(i)] = gmf_f_hu (dmjd(i),lattable,longtable,H,e);
table_std(i)=0.12*gmfw(i)*tableavgdaytzd(nanbo(i))+0.88*gmfh(i)*tableav
gdaytzd(nanbo(i));
end

tablematr=[tableavgdayheight(nanbo) table_std'];

table_raw=tablematr(:,1)+table_std';
trendstd=mean(table_std'-detrend(table_std'));

figure;
plot(xinter(nanbo),table_std(nanbo))

%% find difference between slant delays at phu2 and PUKA
dstd_aipuk=puka_std(nanbo) '-table_std';
[dstd_aipuk2,idx,outliers] = deleteoutliers(dstd_aipuk,0.05,1)

dstd_aipuk3=(dstd_aipuk2-nanmean(dstd_aipuk2))*1000;

figure;
% [ca,ra]=find(~isnan(dstd_aipuk3))
plot(xinter(nanbo),dstd_aipuk3, '-r') %mm

dhuncorre_aipuk=table_raw-puka_raw(nanbo);
[dhuncorre_aipuk2,idx,outliers] =
deleteoutliers(dhuncorre_aipuk,0.05,1)

dhuncorre_aipuk3=(dhuncorre_aipuk-nanmean(dhuncorre_aipuk))*1000;%mm
[dhuncorre_aipuk_estimate_amp,idx,outliers] =
deleteoutliers(dhuncorre_aipuk,0.05,1)

figure;
plot(xinter(nanbo),dhuncorre_aipuk3/10, '-b')

%% compute the seasonal signal

vertunc=table_raw; %'PPP-uncorrected'

```

```

        %%%%% Simple exponential refractivity
        zr=puka_raw(nanbo);
        C=0.0001406;
        amplitudrefract=18.94; % Amplitude of sinsoidal fit to the refractivity
        time series

        phase=180;
        for kk=1:size(vertunc,1)
            Amplitude(kk)=abs((10^-6)*(amplitudrefract)*(1-exp(-
            (C)*(vertunc(kk)-zr(kk)))))/(C*exp(C*zr(kk)))); %centimeter

        APD_computed(kk)=(Amplitude(kk)*sin((2*pi*xinter(nanbo(kk))+phase)));
        end
        amp(ii)=nanmean(Amplitude)*100;

        %%

        correct=detrend(dhunccorre_aipuk3/10)-APD_computed'*100;
        trend=dhunccorre_aipuk3/10-detrend(dhunccorre_aipuk3/10);
        figure;
        plot(xinter(nanbo),correct+trend,'-r')
        hold on
        plot(xinter(nanbo),dhunccorre_aipuk3/10,'-b')
        hold on
        plot(xinter(nanbo),APD_computed*100,'*k')
        xlabel('year')
        ylabel('ZTD (cm)')
        title('MMAU-PUKA')
        xlim([2014 2017.5])

        rms_uncorrect(ii)=rms(detrend(dhunccorre_aipuk3/10))
        rms_correct(ii)=rms(correct)

        [cc,rr]=find(~isnan(dstd_aipuk3))

        [r2(ii) rmse(ii)] = rsquare(-
        dstd_aipuk3(cc)/10,APD_computed(cc)'*100)%mm
        n= size(APD_computed(cc)',1);
        sigma(ii)=nanstd(-dstd_aipuk3/10);% mm
        dstdstd=-dstd_aipuk3/10;
        for i=1:n
            dif(i)=( dstdstd(cc(i))-
            (APD_computed((cc(i)))*100))^2/(sigma(ii)^2);
        end
        chi_square(ii)= (1/(n-1))*sum(dif,2)

        clear vertunc
        clear APD_computed
        clear correctable2
        clear remeancor_insar_table
        clear removmean_raw
        clear nanbo
        clear table_std
        end

```

```
%% plot the rmse
gpspositions = 'gps_stations_positions.xls';
    table3 = xlsread(gpspositions,2);

figure;
plot (table3(1:21,3), table3 (1:21,11),'*')
ylabel('RMS of ZTD (cm)')
xlabel('Height (m)')
```

Curriculum Vitae

Hadis Samadi Alinia

Post-Secondary Education and Degrees

K.N. Toosi University of Technology, Tehran, Iran 2002-2007
B.Sc. in Geomatics Engineering

The University of Tehran, Tehran, Iran 2007-2010
M.Sc. in Geospatial Information System

The University of Western Ontario, London, ON, Canada 2012-2017
PhD. in Geophysics

Honors and Awards

Best research master thesis award from research center, ministry of interior of Iran, 2012
Western Graduate Research Scholarships (WGRS) 2012-2017
Canadian Exploration Geophysical Society (KEGS) Award, 2014
Canadian Exploration Geophysical Society (KEGS) Scholarship, 2015

Related work experience

2012-2017, Research Assistant, the University of Western Ontario
2012-2016, Teaching Assistant, the University of Western Ontario 2009,
Geomatics Engineer, MS Co., Tehran, Iran 2007-2012

Professional Membership

AGU, CGU, PDAC

Publications

Samadi Alinia H., Tiampo, K.F., and James, T.S. (2017) "GPS coordinate time series measurements in Ontario and Québec", Canada, *Journal of Geodesy*. 91(6), pp. 653-683. DOI 10.1007/s00190-016-0987-5.

Samadi Alinia H., Tiampo, K.F., and Samsonov, S.V. (2017) Simplified one-dimensional methodology to retrieve the seasonal amplitude of zenith tropospheric delay on GPS data, *Radio Science Journal*. (under review)

Samadi Alinia H., Tiampo, K.F., Samsonov, S.V., and González, P.J. (2017) Modeling the elevations-dependent seasonal amplitude of tropospheric delay in GPS height time series using DInSAR and meteorology data, *Geophysical Journal International*. (under review)